

Doctoral Dissertation

博士論文

X-ray study of the accretion flow  
onto highly magnetized neutron stars

(X線観測による強磁場中性子星への質量降着流の研究)

A Dissertation Submitted for the Degree of Doctor of Philosophy

December 2022

令和4年12月博士（理学）申請

Department of Physics, Graduate School of Science,

The University of Tokyo

東京大学大学院理学系研究科

物理学専攻

Tsubasa Tamba

丹波 翼

## Abstract

Accreting neutron stars provide unique environments where the accreting matter experiences physical processes under strong gravity and magnetic fields. The X-ray emission from an accreting neutron star reflects the effects of such unique physical processes. The X-ray emission from accreting neutron stars exhibits time variability due to anisotropic emission caused by three-dimensional structures of the accretion flow and the neutron star, and the reprocess by the circumstellar medium. However, the relation between observational time variabilities and these physical conditions has not been deeply investigated since the time variability emerges as a consequence of a complicated mixture of these effects.

We studied the X-ray spectral variabilities of two luminous accreting neutron stars, Cen X-3 and Her X-1, with NuSTAR and NICER observation data in order to investigate the three-dimensional structures of the accretion flow and the effects of the circumstellar medium. We analyzed archival data of these two sources, and also performed a long-time observation of Cen X-3 covering two consecutive orbits, which is the longest observation ever, to comprehensively study the time variability. We adopted a radical approach in which the spectra, light curves, and pulse profiles were comprehensively analyzed, focusing on both the orbital- and spin-phase variabilities. The analysis results derived from the observation data were compared with three-dimensional physical models.

We first investigated the orbital-phase variability of Cen X-3 from the broadband X-ray data covering 0.6–78 keV in order to reveal the effects of the circumstellar medium on the X-ray emission from the neutron star. The 4–78 keV luminosity ranges from  $3.7 \times 10^{35}$  erg s<sup>−1</sup> to  $4.5 \times 10^{37}$  erg s<sup>−1</sup> along the orbital phase. The orbital-phase spectral variability is characterized by the photon index variation from −0.37 to 1.72. The low-flux phases are synchronized by hard photon indices, enhanced equivalent widths of the Fe line, and drops in 3–5 keV pulse fraction. We also found that these orbital-phase variabilities are preserved even when we focus on a specific spin phase. These observational properties can be explained by a unified picture that the intrinsic emission from the neutron star is stable and the flux variability is caused by the obscuration due to a clumpy stellar wind. The typical size and hydrogen number density of the clumps are roughly estimated to be  $R_c \sim 8 \times 10^{10}$  cm and  $n_c \sim 1 \times 10^{13}$  cm<sup>−3</sup>, respectively. The low-energy spectral variability is explained by a partial obscuration of the accretion disk, which emits two blackbody radiations with temperatures of  $kT \sim 0.1$  keV and  $kT \sim 0.5$  keV and luminosities of  $\sim 10^{36}$  erg s<sup>−1</sup>. We successfully nailed down these physical pictures of the circumstellar medium of Cen X-3 owing to the statistically rich observation data and detailed study on the time variability, which could not be resolved by conventional spectral analysis. We also investigated the orbital-phase variability of Her X-1, but the 3–78 keV flux varies by only 2.8%, suggesting a stable accretion flow and circumstellar medium.

We then investigated the spin-phase variabilities of Cen X-3 and Her X-1 in order to reveal the three-dimensional structure of the accretion flow. The energy dependence

of the spin-phase variability is characterized by a monotonic increase in pulse fraction for both sources. The pulse profiles of Cen X-3 display a gradual shift from a flat peak to a sharp peak around the pulse maximum as energy increases. The pulse profiles of Her X-1 exhibit more characteristic features around the pulse maximum, in which a split double-peaked shape gradually shifts to a sharp peak as energy increases. We constructed a simulation-based three-dimensional model of a highly magnetized accretion flow onto a neutron star, and reproduced energy-resolved pulse profiles of these two sources based on bulk and thermal Comptonization inside the column. By comparing the observation and simulation, we successfully limited the geometry of the accretion column and gave physical interpretations to the spin-phase variability of the X-ray emission. We showed that both Cen X-3 and Her X-1 have elongated accretion columns with a height-to-radius ratio of  $h/r_0 \sim 10$ . The X-ray emission is mostly composed of the fan beam and the reflection from the neutron star surface, and the reflection gradually becomes dominant over the fan beam as energy increases. The difference between Cen X-3 and Her X-1 is explained by the angle between the magnetic axis and line of sight. Cen X-3 has a misaligned configuration of the two axes with  $> 10^\circ$  while Her X-1 has an aligned configuration with  $< 10^\circ$ . Our results imply that the variety in pulse profiles of X-ray pulsars is made by the difference in line of sight with respect to the neutron star.

# Contents

<b>1</b>	<b>Introduction</b>	<b>1</b>
<b>2</b>	<b>Reviews of accretion onto highly magnetized neutron stars</b>	<b>4</b>
2.1	Overview . . . . .	4
2.2	Classification of neutron stars based on observation . . . . .	5
2.2.1	Three classes of neutron stars . . . . .	6
2.2.2	Classification of X-ray pulsars . . . . .	8
2.3	Observational appearances of X-ray pulsars . . . . .	10
2.3.1	Coherent pulsation . . . . .	11
2.3.2	Luminosity . . . . .	12
2.3.3	Energy spectrum . . . . .	13
2.3.4	Time variability . . . . .	18
2.4	Physics of accretion flow . . . . .	20
2.4.1	Geometry of accretion flow . . . . .	20
2.4.2	Radiative processes in accretion column . . . . .	22
2.4.3	Formation of radiation spectrum . . . . .	26
2.4.4	Application to observation data . . . . .	29
<b>3</b>	<b>Instrumentation</b>	<b>30</b>
3.1	NuSTAR . . . . .	30
3.1.1	Overview . . . . .	30
3.1.2	Optics . . . . .	31
3.1.3	Mast . . . . .	33
3.1.4	Focal Plane Modules (FPMs) . . . . .	33
3.2	NICER . . . . .	34
3.2.1	Overview . . . . .	34
3.2.2	Optics and detectors . . . . .	36
3.2.3	Background estimation . . . . .	37



<b>4</b>	<b>Broadband X-ray variability of Cen X-3 studied with short-time NuS-TAR observation</b>	<b>39</b>
4.1	Overview of Cen X-3 . . . . .	39
4.2	Observation and data reduction . . . . .	40
4.3	Orbital-phase variability . . . . .	42
4.3.1	Energy-resolved light curve . . . . .	42
4.3.2	Spectral fitting on orbital-phase-resolved spectra . . . . .	43
4.4	Spin-phase variability . . . . .	48
4.4.1	Energy-resolved pulse profile . . . . .	48
4.4.2	Ratio spectrum . . . . .	51
4.4.3	Spectral fitting on spin-phase-resolved spectra . . . . .	51
4.5	Doubly-phase-resolved analysis . . . . .	56
4.5.1	Energy- and spin-phase-resolved light curve . . . . .	56
4.5.2	Energy- and orbital-phase-resolved pulse profile . . . . .	57
4.6	Summary . . . . .	60
<b>5</b>	<b>Broadband X-ray variability of Cen X-3 studied with long-time NuS-TAR observation</b>	<b>62</b>
5.1	Observation and data reduction . . . . .	63
5.1.1	Rough estimation of orbital parameters . . . . .	63
5.1.2	Precise estimation of orbital parameters . . . . .	64
5.1.3	Definition of orbital intervals . . . . .	67
5.2	Orbital-phase variability . . . . .	68
5.2.1	Energy-resolved light curve . . . . .	68
5.2.2	Spectral fitting on orbital-phase-resolved spectra . . . . .	71
5.3	Spin-phase variability . . . . .	76
5.3.1	Energy-resolved pulse profiles . . . . .	76
5.3.2	Spectral fitting on spin-phase-resolved spectra . . . . .	80
5.4	Doubly-phase-resolved analysis . . . . .	83
5.4.1	Orbital-phase variability of pulse profiles . . . . .	83
5.4.2	Doubly-phase-resolved spectroscopy . . . . .	86
5.5	Summary . . . . .	91
<b>6</b>	<b>Soft X-ray variability of Cen X-3 studied with NICER observation</b>	<b>92</b>
6.1	Observation and data reduction . . . . .	92
6.2	Spectroscopy . . . . .	93
6.3	Pulse profile . . . . .	98
6.4	Summary . . . . .	99

<b>7</b>	<b>Discussions on the circumstellar medium of Cen X-3</b>	<b>100</b>
7.1	Stellar wind obscuration as the main cause of the orbital-phase variability .	100
7.2	Stellar wind model . . . . .	103
7.3	Physical origins of X-ray emission in eclipse phase . . . . .	104
7.4	Physical origins of X-ray variability in out-of-eclipse phase . . . . .	108
7.4.1	Physically-motivated spectral model . . . . .	108
7.4.2	Physical interpretation of spectral model . . . . .	112
7.4.3	Independence of spin phase . . . . .	115
7.4.4	Joint fitting on NuSTAR and NICER spectra . . . . .	117
7.5	Physical pictures of circumstellar medium of Cen X-3 . . . . .	121
7.5.1	Summary of emission geometry . . . . .	121
7.5.2	Clumpy stellar wind . . . . .	122
7.5.3	Accretion disk . . . . .	123
7.5.4	Stability of accretion flow . . . . .	124
<b>8</b>	<b>Broadband X-ray variability of Her X-1 studied with NuSTAR obser-</b>	
	<b>vation</b>	<b>126</b>
8.1	Overview of Her X-1 . . . . .	126
8.2	Observation and data reduction . . . . .	127
8.3	Orbital-phase variability . . . . .	129
8.3.1	Energy-resolved light curve . . . . .	130
8.3.2	Orbital-phase-resolved spectroscopy . . . . .	131
8.4	Spin-phase variability . . . . .	134
8.4.1	Energy-resolved pulse profile . . . . .	134
8.4.2	Spin-phase-resolved spectroscopy . . . . .	136
8.5	Variability of pulse profile . . . . .	140
<b>9</b>	<b>Discussions on the accretion flow onto highly magnetized neutron stars</b>	<b>142</b>
9.1	Summary of pulse profile properties of Cen X-3 and Her X-1 . . . . .	142
9.1.1	Pulse maximum . . . . .	143
9.1.2	Asymmetry around pulse maximum . . . . .	144
9.1.3	Emission from dipole configuration . . . . .	146
9.2	Physical model of X-ray emission from accretion column . . . . .	147
9.2.1	Simulation setup . . . . .	147
9.2.2	Simulation parameters . . . . .	149
9.2.3	Energy spectrum . . . . .	152
9.3	Modeling of pulse profile . . . . .	153
9.3.1	Effects of reflection from neutron star surface . . . . .	153
9.3.2	Generation of pulse profile . . . . .	155

9.3.3	Modeling of Her X-1 pulse profiles . . . . .	156
9.3.4	Modeling of Cen X-3 pulse profiles . . . . .	159
9.4	Three-dimensional structures of accretion flow . . . . .	161
9.4.1	Summary of pulse profile modeling . . . . .	161
9.4.2	Origin of CRSF . . . . .	162
<b>10</b>	<b>Conclusions</b>	<b>165</b>

# List of Figures

2.1	Pulsar distribution in the $P - \dot{P}$ diagram. . . . .	6
2.2	Illustration of wind-fed and disk-fed accretion . . . . .	10
2.3	Relation between the spin period and binary orbital period of X-ray pulsars	10
2.4	Spin-up trends of X-ray pulsars . . . . .	12
2.5	Typical energy spectra of X-ray pulsars . . . . .	15
2.6	Diversity and variability of CRSF . . . . .	17
2.7	Example of superorbital modulation . . . . .	19
2.8	Example of QPO . . . . .	20
2.9	Schematic view of the accretion flow onto a highly magnetized neutron star	21
2.10	Schematic picture of accretion column . . . . .	24
2.11	Her X-1 spectrum fitted by accretion column model . . . . .	29
3.1	Illustration of NuSTAR in deployed and stowed configurations . . . . .	31
3.2	Effective area of NuSTAR compared to other X-ray observatories . . . . .	32
3.3	Reduction in NuSTAR effective area due to vignetting effect . . . . .	33
3.4	Picture of NuSTAR FPM . . . . .	34
3.5	Illustration of NICER onboard ISS . . . . .	35
3.6	Photo of co-aligned NICER XRCs . . . . .	36
3.7	Photo of a NICER XRC and cross-section illustration (right) . . . . .	37
3.8	Effective area of NICER compared to XMM-Newton pn . . . . .	37
4.1	Cen X-3 NuSTAR 1: Energy-resolved light curves and hardness ratios . . .	43
4.2	Cen X-3 NuSTAR 1: MCMC calculation of parameter coupling between photon index and cut-off energy . . . . .	46
4.3	Cen X-3 NuSTAR 1: Orbital-phase variations of best-fit spectral parameters	47
4.4	Cen X-3 NuSTAR 1: Relation between flux and $N_{\text{H}}$ along orbital phase . .	48
4.5	Cen X-3 NuSTAR 1: Energy-resolved pulse profiles . . . . .	50
4.6	Cen X-3 NuSTAR 1: Pulse fraction and Fourier coefficients as a function of energy . . . . .	50
4.7	Cen X-3 NuSTAR 1: Spin-phase-resolved spectra and ratio spectra . . . .	52
4.8	Cen X-3 NuSTAR 1: Fitting results of spin-phase-resolved spectroscopy . .	54

4.9	Cen X-3 NuSTAR 1: Spin-phase variation of spectral parameters as a function of continuum flux . . . . .	54
4.10	Cen X-3 NuSTAR 1: Normalized light curves resolved by energy and spin phase . . . . .	57
4.11	Cen X-3 NuSTAR 1: Orbital-phase variability of pulse profile parameters .	59
5.1	Cen X-3 NuSTAR 2: Binary modulation of spin period . . . . .	64
5.2	Cen X-3 NuSTAR 2: Variations of $Z_2^2$ values for orbital parameters . . . .	66
5.3	Cen X-3 NuSTAR 2: Variation of pulse peak phase over the observation . .	67
5.4	Cen X-3 NuSTAR 2: 3–78 keV light curve with definitions of orbital-phase eclipse phases . . . . .	68
5.5	Cen X-3 NuSTAR 2: Energy-resolved light curves and hardness ratios . . .	70
5.6	Cen X-3 NuSTAR 2: Hardness ratios as a function of 3–78 keV count rate .	71
5.7	Cen X-3 NuSTAR 2: Orbital-phase variability of best-fit spectral parameters	74
5.8	Cen X-3 NuSTAR 2: Relations between flux and continuum parameters along orbital phase . . . . .	75
5.9	Cen X-3 NuSTAR 2: Relations between absorbed fluxes of different energy bands and photo index along orbital phase . . . . .	75
5.10	Cen X-3 NuSTAR 2: Relations between flux and Fe line parameters along orbital phase . . . . .	76
5.11	Cen X-3 NuSTAR 2: Energy-resolved pulse profiles . . . . .	78
5.12	Cen X-3 NuSTAR 2: Analysis results of energy-resolved pulse profiles . . .	79
5.13	Cen X-3 NuSTAR 2: Peak phases of energy-resolved pulse profiles . . . . .	79
5.14	Cen X-3 NuSTAR 2: Spin-phase variability of best-fit spectral parameters .	81
5.15	Cen X-3 NuSTAR 2: Relations between flux and continuum parameters along spin phase . . . . .	82
5.16	Cen X-3 NuSTAR 2: Relation between flux and Fe line parameters along spin phase . . . . .	82
5.17	Cen X-3 NuSTAR 2: Relation between flux and CRSF parameters along spin phase . . . . .	83
5.18	Cen X-3 NuSTAR 2: Variations of pulse profiles along orbital phase . . . .	85
5.19	Cen X-3 NuSTAR 2: Relations between 3–5 keV pulse fraction and continuum spectral parameters . . . . .	86
5.20	Cen X-3 NuSTAR 2: Definition of spin-phase intervals for doubly-phase-resolved spectroscopy . . . . .	88
5.21	Cen X-3 NuSTAR 2: Reduced chi-square values of doubly-phase-resolved spectroscopy . . . . .	88
5.22	Cen X-3 NuSTAR 2: Variabilities of fluxes along orbital and spin phases .	89

5.23	Cen X-3 NuSTAR 2: Variabilities of continuum parameters along orbital and spin phases . . . . .	90
5.24	Cen X-3 NuSTAR 2: Relation between continuum flux and photon index along orbital and spin phases . . . . .	90
6.1	Cen X-3 NICER: Light curve as a function of orbital phase . . . . .	93
6.2	Cen X-3 NICER: Definition of orbital intervals . . . . .	95
6.3	Cen X-3 NICER: Fitting results on orbital-phase-resolved spectra . . . . .	96
6.4	Cen X-3 NICER: Energy dependence of pulse fraction . . . . .	98
7.1	Cen X-3 Discussion: Column density as a function of orbital phase, calculated from simple stellar wind model . . . . .	104
7.2	Cen X-3 Discussion: Emission mechanism during eclipse phase . . . . .	106
7.3	Cen X-3 Discussion: Illustration of simulation setup for Compton scattering by stellar wind . . . . .	107
7.4	Cen X-3 Discussion: Fitting results of eclipse phase spectra . . . . .	107
7.5	Cen X-3 Discussion: Example of spectral fitting based on physically-motivated model . . . . .	110
7.6	Cen X-3 Discussion: Fitting results of orbital-phase-resolved spectra with physically-motivated spectral model . . . . .	111
7.7	Cen X-3 Discussion: Relations among spectral parameters along orbital phase	112
7.8	Cen X-3 Discussion: Relation between 3–5 keV pulse fraction and blackbody flux ratio . . . . .	114
7.9	Cen X-3 Discussion: Fitting results of doubly-phase-resolved spectra with physically-motivated spectral model . . . . .	116
7.10	Cen X-3 Discussion: Relations among spectral parameters derived from double-phase-resolved spectroscopy . . . . .	117
7.11	Cen X-3 Discussion: Results of joint fitting on NuSTAR and NICER spectra	119
7.12	Cen X-3 Discussion: Schematic illustration of X-ray emission geometry of Cen X-3 . . . . .	121
7.13	Cen X-3 Discussion: Relation between Fe line intensity and blackbody luminosity . . . . .	124
8.1	Her X-1 NuSTAR: MAXI light curve of Her X-1 . . . . .	128
8.2	Her X-1 NuSTAR: Variations of $Z_2^2$ values for orbital parameters . . . . .	129
8.3	Her X-1 NuSTAR: Variation of pulse peak phase over the observation . . . . .	129
8.4	Her X-1 NuSTAR: Energy-resolved light curves and hardness ratios . . . . .	130
8.5	Her X-1 NuSTAR: Fitting result of phase-averaged spectra . . . . .	132
8.6	Her X-1 NuSTAR: Orbital-phase variability of spectral parameters . . . . .	133
8.7	Her X-1 NuSTAR: Energy-resolved pulse profiles . . . . .	135

8.8	Her X-1 NuSTAR: Analysis results of energy-resolved pulse profiles . . . .	136
8.9	Her X-1 NuSTAR: Fitting results of spin-phase-resolved spectroscopy . . .	138
8.10	Her X-1 NuSTAR: Spin-phase variability of CRSF parameters . . . . .	140
8.11	Her X-1 NuSTAR: Variations of pulse profiles along orbital phase . . . . .	141
9.1	Discussion: Energy dependence of pulse profiles of Cen X-3 and Her X-1 . .	143
9.2	Discussion: Symmetrical degrees of pulse profiles . . . . .	145
9.3	Discussion: Difference in Her X-1 pulse profiles along superorbital phase . .	146
9.4	Discussion: Schematic illustration of simulation setup . . . . .	149
9.5	Discussion: Emission profiles from flat and elongated columns . . . . .	152
9.6	Discussion: Comparison of energy spectra between observation and simulation	153
9.7	Discussion: Emission profiles with reflection components . . . . .	155
9.8	Discussion: Geometrical configuration among spin axis, magnetic axis, and line of sight . . . . .	156
9.9	Discussion: Results of pulse profile modeling on Her X-1 . . . . .	158
9.10	Discussion: Results of pulse profile modeling on Cen X-3 . . . . .	160
9.11	Discussion: Schematic illustration of emission mechanism from accretion column . . . . .	162
9.12	Discussion: Schematic illustration of CRSF generation on the neutron star surface . . . . .	164

# List of Tables

0	Abbreviation list . . . . .	x
4.1	Cen X-3 NuSTAR 1: Orbital parameters of Cen X-3 . . . . .	42
4.2	Cen X-3 NuSTAR 1: Best-fit parameters derived from spin-phase-resolved spectroscopy . . . . .	55
4.3	Cen X-3 NuSTAR 1: Statistical parameters characterizing orbital-phase variability of pulse profile parameters . . . . .	60
5.1	Cen X-3 NuSTAR 2: Orbital parameters of Cen X-3 . . . . .	66
5.2	Cen X-3 NuSTAR 2: Count rates of different orbital intervals . . . . .	70
6.1	Cen X-3 NICER: Best-fit parameters of spectral fitting . . . . .	97
7.1	Cen X-3 Discussion: Spectral parameters for intrinsic emission from neutron star . . . . .	102
7.2	Cen X-3 Discussion: Best-fit parameters of spectral fitting on eclipse phases	108
7.3	Cen X-3 Discussion: Best-fit parameters of joint spectral fitting . . . . .	120
8.1	Her X-1 NuSTAR: Orbital parameters of Her X-1 . . . . .	128
8.2	Her X-1 NuSTAR: Statistical parameters of energy-resolved light curves . .	131
8.3	Her X-1 NuSTAR: Best-fit parameters of phase-averaged spectrum . . . . .	133
8.4	Her X-1 NuSTAR: Best-fit parameters of spin-phase-resolved spectroscopy	139
9.1	Discussion: Parameters of pulse profile obscuration . . . . .	145
9.2	Discussion: Free parameters of Her X-1 pulse profile modeling . . . . .	157
9.3	Discussion: Free parameters of Cen X-3 pulse profile modeling . . . . .	159



Table 0: Abbreviation list

Abbreviation	Definition
BeXRB	Be/X-Ray Binary
BH	Black Hole
Cen X-3	Centaurus X-3
CRSF	Cyclotron Resonance Scattering Feature
Her X-1	Hercules X-1
HMXB	High Mass X-ray Binary
IMXB	Intermediate Mass X-ray Binary
IXPE	Imaging X-ray Polarimetry Explorer
ISS	International Space Station
LMC	Large Magellanic Cloud
LMXB	Low Mass X-ray Binary
NS	Neutron Star
RXTE	Rossi X-ray Timing Explorer
SMC	Small Magellanic Cloud
ULX	Ultra-Luminous X-ray source
WD	White Dwarf
XRB	X-Ray Binary
XRP	X-Ray Pulsar

# Chapter 1

## Introduction

Neutron stars, formed after the death of normal stars, are celestial objects with the highest density in the universe except for black holes. They provide unique laboratories to investigate physical processes under strong gravity, high density, and strong magnetic fields. When a neutron star is accompanied by a main-sequence star, the strong gravity induces mass transfer from the companion star, and the gravitational energy is converted to intense electromagnetic radiation. The considerable energy release from an accreting neutron star enables us to investigate the neutron star itself and the highly magnetized accreting matter by observing interactions between them. The rich information about neutron stars leads to solving fundamental questions in astrophysics, such as the equation of state, formation mechanism, and evolution processes of neutron stars. Moreover, the accreting neutron star is the only environment in the universe where we can directly observe physical processes of general relativity, dense matter, and highly magnetized plasma simultaneously.

Since the discovery of X-rays from a neutron star (Giacconi et al., 1962), X-ray observations have played an important role in unveiling the accretion mechanism of neutron stars since the converted gravitational energy is mainly released as photons in this band. X-ray observatories have discovered more than 100 accreting neutron stars bright in X-rays, which are classified as “X-ray pulsars”. They are mostly accompanied by strong magnetic fields of  $\sim 10^{12}$  G and accretion flows from massive companion stars. In recent years, the launch of the hard X-ray observatory NuSTAR in 2012 has made further progress in the research of X-ray pulsars. The highly improved capability in the hard X-ray band allows us to investigate the broadband X-ray radiation from the accretion flow and directly measure the magnetic field strength via cyclotron resonance scattering feature (CRSF).

The accumulating observational properties of X-ray pulsars discovered by X-ray observations let us construct a unified picture of the accretion flow. The most prevailing theory is the accretion column model (Basko & Sunyaev, 1976; Becker, 1998). In this model, the

accretion flow is channeled along the magnetic field lines and falls onto the magnetic poles, leading to a formation of optically thick plasma columns above the magnetic poles. The falling accretion flow is decelerated either by collision or radiation pressure. When the neutron star luminosity exceeds  $\sim 10^{37}$  erg s $^{-1}$  (Mushtukov et al., 2015), the radiation-dominated shock is formed inside the accretion column, which decelerates the accretion flow via Compton scattering. The observed spectra in this class of X-ray pulsars are interpreted as generated from bulk and thermal Comptonization in the accretion column with substantial modification of scattering cross sections due to the presence of strong magnetic field (Daugherty & Harding, 1986; Mushtukov et al., 2016; Schwarm et al., 2017; Suleimanov et al., 2022). Becker & Wolff (2007) constructed the most widely-used one-dimensional model, which reproduces the phase-averaged spectra of luminous X-ray pulsars based on these physical processes.

However, the constructed models up to date are mostly based on one-dimensional views along the magnetic axis, and the understanding of the emission mechanism based on three-dimensional pictures is still underway. The effects causing anisotropic radiation, such as the geometry of the accretion column, the obscuration or reflection by the neutron star, and the rotation of the neutron star, have not been fully considered in the interpretation of the observation data. The reprocessing by the circumstellar medium renders another anisotropy and makes the observed spectrum even more complicated. These anisotropy emerges in the observation data as time variabilities in spectra depending on various timescales, but they are hardly explained by reasonable interpretations based on physical processes. Moreover, the lack of understanding of three-dimensional pictures could lead to wrong estimations of fundamental parameters such as luminosity, accretion rate, and spectral energy distribution because the anisotropy of the emission is not taken into account.

The most effective way to approach the three-dimensional picture of X-ray pulsars is to analyze the time variability of the X-ray emission. Most X-ray pulsars display complex spectral variabilities induced by mixtures of the variability in the accretion rate, the anisotropic emission, and reprocessing by the circumstellar medium. Odaka et al. (2014) successfully interpreted the spectral variability in a wind-fed X-ray pulsar Vela X-1 based on a three-dimensional physical model of the accretion column. They proved that the variability of the spin-phase-averaged spectrum was a consequence of the time-variable structure of the accretion column induced by the change in the accretion rate. However, the highly transient accretion rates and long spin periods in such wind-fed sources make it difficult to investigate the spin-phase variability, from which we can estimate the effects of the spin motion and the obscuration or reflection by the neutron star. In order to fully investigate the three-dimensional picture, we need to observe X-ray pulsars with more stable accretion rates and short spin periods, which can be achieved by disk-fed X-ray pulsars. The high luminosities of disk-fed X-ray pulsars also help us perform a detailed

study on the spectral variability along the orbital and spin phases.

In this thesis, we investigate the three-dimensional picture of the accretion flow onto disk-fed X-ray pulsars by analyzing X-ray observation data and applying the same physical model as Odaka et al. (2014). We picked up two disk-fed X-ray pulsars, Cen X-3 and Her X-1, because of their high luminosities and relatively close distances to the earth, providing rich photon counts. The high luminosities of the two sources also indicate the presence of radiation-dominated accretion columns. They are the most studied X-ray pulsars, and the well-known properties of these sources, such as orbital and spin periods and binary properties, would also help us investigate the X-ray variability. Since we need broadband observation data with rich photon counts, we analyzed NuSTAR and NICER archival data covering soft to hard X-ray bands. We also proposed a NuSTAR observation of Cen X-3 over two consecutive orbits, which enables us to perform a comprehensive study on the spectral variabilities along the orbital and spin phases. We carefully analyzed the spectra, light curves, and pulse profiles obtained from the observation data, in order to evaluate spectral variabilities from multiple different perspectives. We tried, for the first time, to give physical interpretations on X-ray variabilities of X-ray pulsars based on a physical model reproducing emission processes in the highly magnetized accretion flow.

The present thesis is organized as follows. We review the observational properties and physics of accretion onto highly magnetized neutron stars in Chapter 2, and describe the X-ray instrumentation in Chapter 3. In the following chapters, we investigated X-ray variabilities of Cen X-3 and Her X-1 and discussed three-dimensional pictures of these sources. While Cen X-3 displays large spectral variabilities along the orbital and spin phases, Her X-1 is stable along the orbital phase and only shows variability along the spin phase. Therefore, we first discuss the orbital-phase variability of Cen X-3, and then discuss the spin-phase variabilities of the two sources together. In Chapter 4, we present the analysis results of Cen X-3 data obtained from a NuSTAR observation in 2015. Since this set of archival data was not sufficient to construct a physical picture, we conducted another long-time observation with NuSTAR in 2022. We report the analysis results of the long-time observation in Chapter 5. The soft X-ray variability of Cen X-3 studied by NICER is presented in Chapter 6. In Chapter 7, we summarize our analysis results in Chapters 4–6 and give physical pictures of the circumstellar medium of Cen X-3. We then analyzed Her X-1 observation data, mainly focusing on the spin-phase variability, which is presented in Chapter 8. In Chapter 9, we discuss the structure of the accretion flows in Cen X-3 and Her X-1, combining the observation data with our simulation-based model. Finally, Chapter 10 gives our conclusions.

# Chapter 2

## Reviews of accretion onto highly magnetized neutron stars

### 2.1 Overview

Neutron stars are a class of compact stellar objects formed after core-collapse supernovae of massive stars with  $M > 9M_{\odot}$  (Heger et al., 2003). Along with other compact objects like white dwarfs (WDs) and black holes (BHs), they provide unique environments in the universe with strong gravity, high density, and extreme magnetic field. The typical mass and radius of the neutron star are  $1.4M_{\odot}$  and 12 km, respectively. This configuration gives a gravitational redshift of  $z \sim 0.24$  at the surface of the neutron star, where the effects of general relativity are non-negligible. The volume-averaged density of a neutron star is  $4 \times 10^{14} \text{ g cm}^{-3}$ , which exceeds the normal nuclear density. In the central region of a neutron star, generally, the density is several times higher than the nuclear density, where physical processes would be different from what we know. The highly magnetized environment is formed as a result of a core-collapse supernova. Since the radius of the star becomes  $\sim 1/1000$  in the collapse, the magnetic field strength is enhanced to  $10^{11}$ – $10^{15}$  G due to the conservation of the magnetic flux ( $BR^2 = \text{const}$ ). Such extreme conditions provide us with unique laboratories to investigate the physics of strong gravity, dense matter, and strong magnetic fields.

Neutron stars are generally observed as “pulsars”, exhibiting coherent pulsations due to their steady spin modulations. Since the discovery of a pulsating radio source in 1967 (PSR J1919+2153; Hewish et al., 1968), more than 3000 pulsars have been discovered in radio, optical, X-ray, and gamma-ray bands (Manchester et al., 2005). The observational properties, such as the spin period, luminosity, spectrum, and time variability, reveal a considerable variety of neutron stars. While most neutron stars emit photons in the radio band, those associated with high temperature, strong magnetic field, or strong gravity have bright luminosities in the X-ray or gamma-ray bands. When a neutron star

is accompanied by a main-sequence star, mass accretion from the companion onto the highly magnetized neutron star generates high-energy X-ray emission with a coherent pulsation. Such objects are generally called X-ray pulsars (XRPs) and constitute a large population of neutron stars bright in X-rays. The present thesis focuses on the physical processes in the accretion flow of X-ray pulsars. In this chapter, we first review the classification of neutron stars and how X-ray pulsars are different from other classes. We then review the observational properties of X-ray pulsars discovered in the X-ray band. Finally, we describe a widely agreed physical picture of the accretion flow in a highly magnetized environment.

## 2.2 Classification of neutron stars based on observation

Recent observation techniques have enabled us to discover thousands of neutron stars. The observational properties of neutron stars show vast diversity. Since neutron stars are generally observed as pulsars, the observational features can be roughly classified by their periods ( $P$ ) and period derivatives ( $\dot{P}$ ). Figure 2.1 shows the  $P - \dot{P}$  diagram of the observationally confirmed neutron stars. They distribute in a wide range in the diagram. The spin period ranges from 1 ms to 10 s, while the period derivative ranges from  $10^{-21} \text{ s s}^{-1}$  to  $10^{-9} \text{ s s}^{-1}$ .

Assuming the observed pulsation is due to pure dipole magnetic radiation, the spin period and its derivative can be replaced with physical parameters, that is, the magnetic field strength and the age of the pulsar. The typical magnetic field strength is given by the dipole magnetic field strength on the surface of the neutron star,  $B_d$ . It is given by

$$\begin{aligned} B_d &= \sqrt{\frac{3c^3 I}{2\pi^2 R_{\text{ns}}^6} P \dot{P}} \\ &= 1.0 \times 10^{14} \text{ G} \left( \frac{P}{1 \text{ s}} \right)^{1/2} \left( \frac{\dot{P}}{10^{-11} \text{ s s}^{-1}} \right)^{1/2}, \end{aligned} \quad (2.1)$$

where  $c$ ,  $I$ , and  $R_{\text{ns}}$  are the speed of light, the moment of inertia, and the radius of the neutron star, respectively. The cyan lines in Figure 2.1 represent the contours of the dipole magnetic field. The typical age of a pulsar is given by the “characteristic age”  $\tau_c$ , calculated by

$$\tau_c = \frac{P}{2\dot{P}}. \quad (2.2)$$

The definition of the characteristic age is based on the observational properties of the spin period evolution, approximated by

$$\dot{\Omega} \propto -\Omega^3, \quad (2.3)$$

where  $\Omega = 1/P$  is the spin frequency of the pulsar. The orange lines in Figure 2.1 denote the contours of the characteristic age.

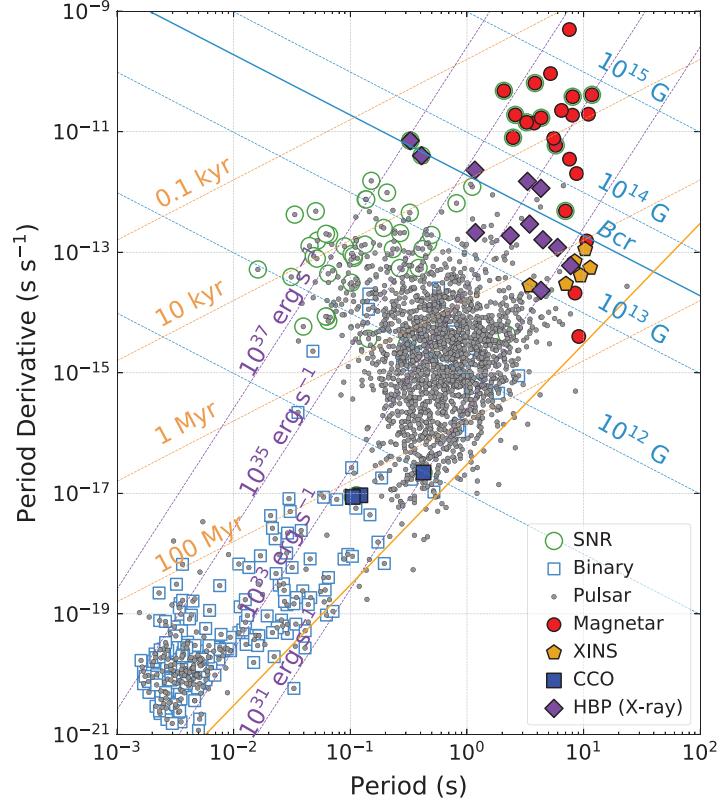


Figure 2.1: Pulsar distribution in the  $P - \dot{P}$  diagram. Constant lines of the dipole magnetic field and characteristic ages are shown by cyan and orange lines, respectively. The figure is taken from Enoto et al. (2019). The data are originally taken from the Australia Telescope National Facility (ATNF) pulsar catalogue (version 1.60) for pulsars and McGill magnetar catalogue for magnetars (Manchester et al., 2005; Olausen & Kaspi, 2014).

### 2.2.1 Three classes of neutron stars

In general, neutron stars are classified into three classes according to their likely energy sources. The classification is based on observational properties such as the spin period evolution and luminosity of the source. The three classes consist of rotation-powered, magnetically-powered, and accretion-powered neutron stars.

The first class, rotation-powered neutron stars, accounts for most of the discovered neutron stars, represented by gray dots in Figure 2.1. They dissipate their rotational energy by emitting electromagnetic radiation and spin down at steady rates. They are mainly detected in the radio frequency, while some sources are detected in the optics, X-

rays, and gamma-rays. These sources are characterized by fast spins and low luminosities. The typical spin period of rotation-powered neutron stars is 0.01–1 s. The luminosity of a rotation-powered neutron star is sufficiently lower than the decay of the rotational energy. The loss rate of the rotational energy is referred to as the spin-down luminosity, calculated by

$$L_{\text{sd}} = -\frac{d}{dt} \left( \frac{1}{2} I \Omega^2 \right) = \frac{4\pi^2 I \dot{P}}{P^3}. \quad (2.4)$$

Assuming a typical neutron star with a mass and radius of  $1.4M_{\odot}$  and 12 km, the spin-down luminosity is

$$L_{\text{sd}} \sim 6.35 \times 10^{35} \left( \frac{P}{1 \text{ s}} \right)^{-3} \left( \frac{\dot{P}}{10^{-11} \text{ s s}^{-1}} \right) \text{ erg s}^{-1} \quad (2.5)$$

The typical luminosity of a rotation-powered pulsar estimated by observations is  $< 1\%$  of the spin-down luminosity, and the loss of the rotational energy can sufficiently supply the energy emitted by photons. These objects are recognized as “ordinary” pulsars, to which the simple expressions of dipole magnetic field strength or characteristic age (equations 2.1 and 2.2) can be applied.

The second class, magnetically-powered neutron stars, is an exceptional class of isolated neutron stars usually called “magnetars”. They have long spin periods of 1–10 s and large spin-down rates of  $10^{-15}$ – $10^{-9} \text{ s s}^{-1}$ , as represented by red filled circles in Figure 2.1. The apparent dipole magnetic field calculated from  $P$  and  $\dot{P}$  exceeds the critical field,

$$B_{\text{cr}} = \frac{m_e^2 c^3}{\hbar e} = 4.4 \times 10^{13} \text{ G}, \quad (2.6)$$

where  $m_e$  is the electron mass. In such an extreme magnetic field, the nonlinear effects of QED could affect the emission. These sources are mainly observed in X-rays with frequent bursting activities, presumably due to the transformation of the magnetic field structure. Because the X-ray luminosity of a magnetar is comparable to or higher than its spin-down luminosity, the most likely energy source is its magnetic energy.

The last class, the accretion-powered neutron stars, requires a companion star and resides in a binary system, which is different from the former two classes. More than 100 sources are detected up to date (e.g., Walter & Ferrigno, 2017). In such systems, the gravitational energy of the accreting matter is converted into the emission energy. Since the emitted photons are mainly in X-rays, these neutron stars are called “X-ray pulsars”. The mass accretion rate  $\dot{M}$  is an important parameter to characterize the system, and related to the luminosity by

$$L = \frac{GM_{\text{ns}}\dot{M}}{R_{\text{ns}}}, \quad (2.7)$$



where  $G$  is the gravitational constant. The accretion luminosity generally has an upper limit, called the Eddington luminosity, due to a balance between the gravitational energy and radiation pressure. In a spherically symmetric case, the Eddington luminosity is

$$\begin{aligned} L_{\text{Edd}} &= \frac{4\pi G M_{\text{ns}} m_{\text{p}} c}{\sigma_{\text{T}}} \\ &= 1.3 \times 10^{38} \text{ erg s}^{-1} \left( \frac{M_{\text{ns}}}{M_{\odot}} \right), \end{aligned} \quad (2.8)$$

where  $m_{\text{p}}$ ,  $\sigma_{\text{T}}$ ,  $M_{\odot}$  are the mass of a proton, the Thomson scattering cross section, and the mass of the sun, respectively. The observed X-ray luminosities of accretion-powered neutron stars typically range from  $10^{32}$  to  $10^{38} \text{ erg s}^{-1}$ , highly dependent on the type of the companion star. The spin-down model of the dipole magnetic field does not account for the spin period evolution of these objects because these neutron stars show spin-up trends due to mass accretion.

### 2.2.2 Classification of X-ray pulsars

The X-ray binaries (XRBs) indicate a binary system hosting an optical companion and a compact star. The compact star is either a neutron star or a black hole. The XRBs are generally classified into two sub-classes according to the mass of the companion star. One is the high mass X-ray binaries (HMXBs), where companion stars are young and have masses of  $\gtrsim 8M_{\odot}$ , and the other is the low mass X-ray binaries (LMXBs), where the companion stars are older and have masses of  $\lesssim 2M_{\odot}$ . Most X-ray pulsars are contained in HMXBs, and those in LMXBs are very rare. This is because the typical ages of LMXBs are  $\gtrsim 10^9$  years and too old to keep a strong magnetic field to emit X-rays, as it would decay by Ohmic processes and Hall evolution (Igoshev et al., 2021). Even so, there are several exceptional X-ray pulsars that are contained in LMXBs, such as Her X-1. X-ray pulsars, most formed in HMXBs, are roughly classified into three sub-classes according to the type of the companion star.

The first sub-class is associated with Be stars, called the Be/X-ray binaries (BeXRBs). The Be star is non-supergiant B star whose spectrum has hydrogen emission lines. This type of companion stars has masses of  $\sim 10 - 20M_{\odot}$ . The orbits in Be systems have long periods of  $\gtrsim 15$  days with large eccentricities of  $e \gtrsim 0.1$ . As a result, BeXRBs show strong flux variabilities and relatively low persistent luminosities (e.g., V 0332+53). The mass accretion is realized by the capture of matter from the decretion disk of the companion star, but the detailed mechanism is still an open issue (e.g., Martin et al., 2014).

The second sub-class is associated with massive early-type stars, that is, the OB supergiants. This class is called the supergiant X-ray binaries (SGXBs). In these objects, the companion stars are massive giants with masses of  $\gtrsim 20M_{\odot}$ . The orbits in such systems have short periods of 1.5–10 days and small eccentricities. In an SGXB, the

neutron star emits X-rays via capture of a part of the stellar wind from the companion star. Therefore, these objects are called “wind-fed” sources. The schematic view of the wind-fed accretion is shown in the left panel of Figure 2.2. Since the capture of stellar wind is an inefficient way of mass accretion, the optical component needs to emit a substantial stellar wind. The typical mass loss rate is  $10^{-6}$ – $10^{-8} M_{\odot} \text{ yr}^{-1}$  and the wind is accelerated by radiation from the massive star with a terminal velocity up to  $2000 \text{ km s}^{-1}$ . The mass accretion rate is higher than BeXRBs, which results in a high persistent luminosity of  $\sim 10^{36} \text{ erg s}^{-1}$ . Vela X-1 is the most studied wind-fed X-ray pulsar (McClintock et al., 1976).

The last sub-class is similar to the second one but has a different mechanism of mass accretion. The companion stars are massive early-type stars, but the mass accretion is realized via accretion disks rather than the capture of stellar wind. The different mechanism of mass accretion is due to the closeness between the neutron star and the companion star. When the companion star is large and the binary separation is small, the companion star can fill its Roche lobe, which is a region around a star where matter is gravitationally bound to that star. In this situation, the accretion flow directly falls onto the neutron star via the inner Lagrangian point, forming an accretion disk by conservation of angular momentum (Roche lobe overflow). These objects are called “disk-fed” sources to distinguish them from wind-fed sources. The illustration is shown in the right panel of Figure 2.2. Generally, the mass accretion via an accretion disk leads to a more stable accretion rate with a higher luminosity of  $10^{36}$ – $10^{38} \text{ erg s}^{-1}$  than the wind-fed accretion. Only several sources are categorized into this class (e.g., Cen X-3, LMC X-4, SMC X-1, Her X-1).

Figure 2.3 shows the distribution of the three classes of X-ray pulsars on the plane of the neutron star spin period versus the binary orbital period (Corbet diagram; Corbet, 1986). The Roche-lobe filling sources, namely the last sub-class, have short orbital and spin periods. The present thesis focuses on the physics and surrounding conditions of the accretion flows onto highly magnetized neutron stars. The approach we take is the investigation of the spectral variability along both the orbital and spin phases. The disk-fed sources are suitable for this purpose because they have bright luminosities, stable accretion rates, and short orbital periods.

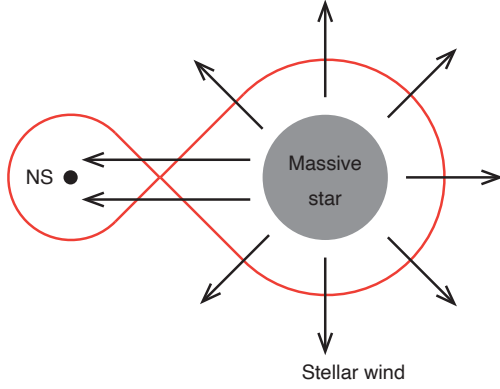
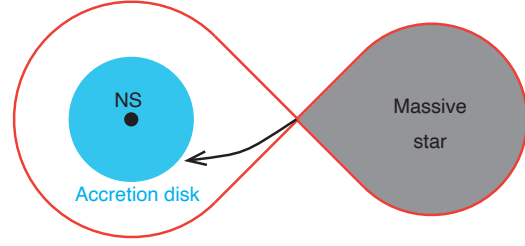
**Wind-fed accretion****Disk-fed accretion**

Figure 2.2: Illustration of wind-fed (left) and disk-fed (right) accretion. Red lines represent the boundaries of Roche lobes.

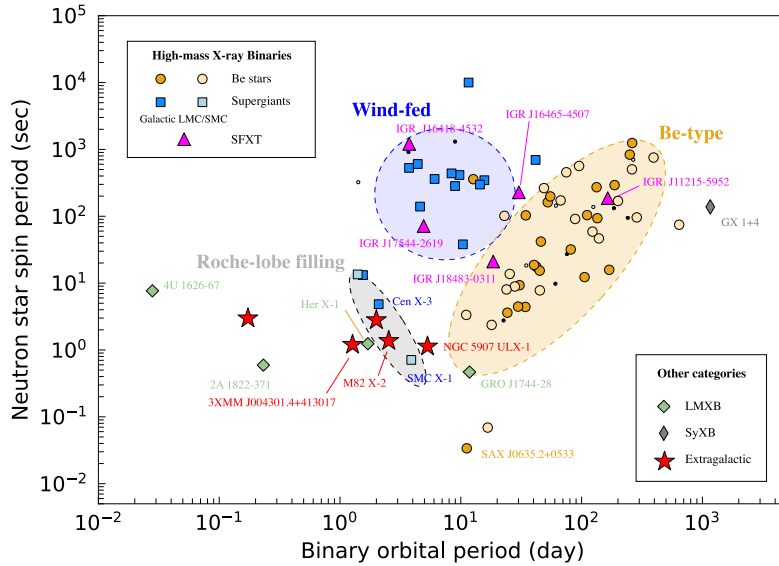


Figure 2.3: Relation between the spin period and binary orbital period for discovered X-ray pulsars (called the Corbet diagram; Corbet, 1986). Three classes of X-ray pulsars are presented. Taken from Enoto et al. (2019).

## 2.3 Observational appearances of X-ray pulsars

X-ray pulsars show a lot of characteristic observational properties. In this section, we review important properties of X-ray pulsars, particularly focusing on the disk-fed SGXBs. The description in this section is based on recent reviews of X-ray pulsars: Mushtukov & Tsygankov (2022); Walter et al. (2015); Paul & Naik (2011).

### 2.3.1 Coherent pulsation

Coherent pulsations of the observed flux are naturally explained by a misalignment between the rotation and magnetic axes of a neutron star. The shapes of pulsations are characterized by light curves folded by spin periods, that is, pulse profiles. While the pulse profile of an ordinary radio pulsar typically has a sharp peak within a narrow range of the spin phase, that of an X-ray pulsar has a large duty cycle ( $\sim 50\%$ ), and emission never drops to zero intensity even at the pulse minimum. The pulse profile in an X-ray pulsar has a complex morphology, which differs from source to source. Moreover, the pulse profile is highly dependent on the energy band and luminosity, possibly reflecting the differences in physical processes and surrounding conditions. No convincing model has been established up to date that can explain the energy and luminosity dependence of pulse profiles. A comprehensive study on the pulse profiles of X-ray pulsars in a phenomenological way was carried out by Alonso-Hernández et al. (2022).

In general, disk-fed X-ray pulsars track gradual spin-up trends due to the angular momentum exchange between the neutron stars and accretion flows. Figure 2.4 presents the long-term variations of the spin periods of Cen X-3 and Her X-1, which are both disk-fed X-ray pulsars. The spin-period evolution is highly stochastic, far from a stable evolution with a constant spin-up rate, because of the variability of the accretion rate and the complex mechanism of angular momentum transfer. Simultaneous measurements of the spin-period evolution and luminosity are used to probe the physics of the accretion flow and surrounding conditions.

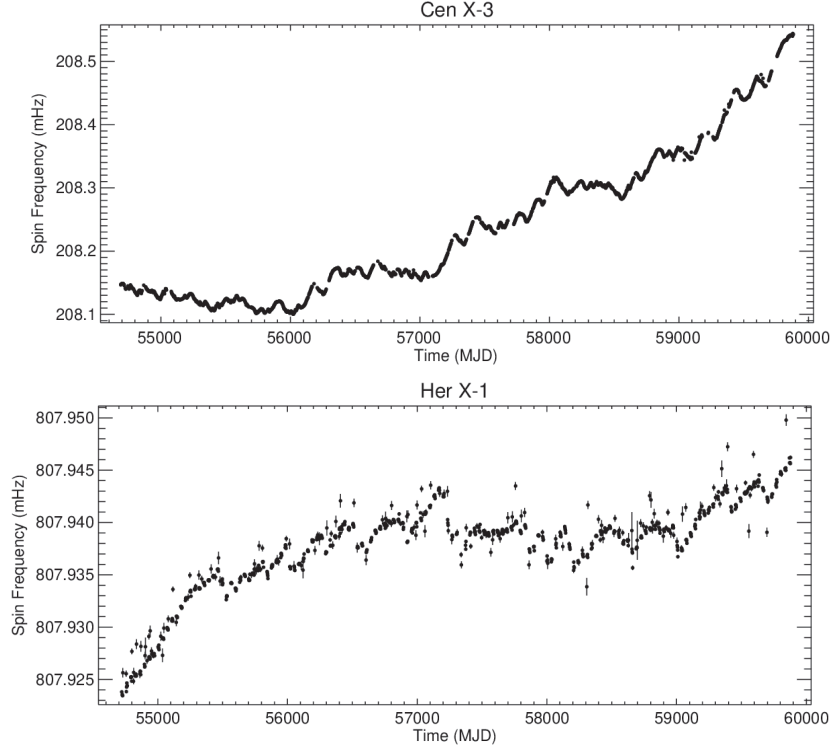


Figure 2.4: Long-term variations in the spin frequencies of Cen X-3 (top) and Her X-1 (bottom). Generated from Fermi/GBM accreting Pulsars Program (<https://gammaray.nsstc.nasa.gov/gbm/science/pulsars.html>)

### 2.3.2 Luminosity

The luminosity of an X-ray pulsar can be estimated from the observed X-ray flux only when one knows the distance to the source, the beaming factor, and the spectral distribution. These parameters cause significant uncertainties in the measurement of luminosity. The measurement of distances generally has large uncertainties, often with errors as large as 50%. However, thanks to the Gaia observatory (Gaia Collaboration et al., 2016), the distances to a substantial number of X-ray pulsars are measured with about 10% accuracy. The beaming factor is another problematic factor in the measurement of luminosity. It reflects the anisotropic radiation of X-rays due to the geometrical effects of the accretion flow, which leads to either overestimation or underestimation of the luminosity. Even so, the beaming factor is difficult to know, and the luminosity is usually determined with the assumption of isotropic radiation. Since the luminosity can be directly related to the accretion rate via equation (2.7), one should recognize that the calculated accretion rate does not necessarily reflect the actual situation, particularly for bright X-ray pulsars where the beaming factor could be significant (e.g., King et al., 2017; Mushtukov et al., 2021).

The apparent luminosity of X-ray pulsars typically ranges from  $10^{32}$  to  $10^{38}$  erg s $^{-1}$ . In several sources, the apparent luminosity exceeds the Eddington luminosity (equation 2.8) and reaches  $\sim 10^{41}$  erg s $^{-1}$ . Such sources are called ultra-luminous X-ray sources (ULXs; Bachetti et al., 2014; Israel et al., 2017). The discovery of neutron stars in the ULXs challenges the conventional picture of mass accretion based on the Eddington limit, and implies unknown mechanism of mass accretion onto highly magnetized neutron stars.

### 2.3.3 Energy spectrum

The effective temperature in X-ray pulsars can be estimated from the luminosity  $L$  and the area of emission region  $S$ , which is

$$T_{\text{eff}} = \left( \frac{L}{\sigma_{\text{SB}} S} \right)^{1/4} \quad (2.9)$$

$$= 5.6 \text{ keV} \left( \frac{L}{10^{37} \text{ erg s}^{-1}} \right)^{1/4} \left( \frac{S}{1 \text{ km}^2} \right)^{-1/4}. \quad (2.10)$$

Here,  $\sigma_{\text{SB}}$  denotes the Stefan-Boltzmann constant. If we assume a typical luminosity of  $L = 10^{37}$  erg s $^{-1}$  and emission area of 1000 km $^2$ , which roughly corresponds to the neutron star surface, the effective temperature would be  $\sim 1$  keV. This naturally explains why most X-ray pulsars mainly emit in the X-ray band. However, the actual spectral distribution of X-ray pulsars is far from a pure thermal emission due to the complex physical processes of the accretion flow. In the following, we describe the phenomenological features for typical spectral components.

### Continuum spectrum

The continuum spectra of bright X-ray pulsars ( $L > 10^{35}$  erg s $^{-1}$ ) are similar to each other. They are approximated by phenomenological functions rather than physically-motivated models. As shown in Figure 2.5, the typical spectra can be roughly described with a power-law with a high-energy cut-off, called the “highecut” model (White et al., 1983; Nagase, 1989). The expression of the model function is given by

$$\frac{dN}{dE} \propto \begin{cases} E^{-\Gamma} & (E \leq E_c) \\ E^{-\Gamma} \exp\left(-\frac{E - E_c}{E_f}\right) & (E > E_c), \end{cases} \quad (2.11)$$

where  $E_c$  and  $E_f$  represent the cut-off energy and the folding energy, respectively. When  $E_c \rightarrow 0$ , the function approaches a simple cut-off power law. Although the highecut model well reproduces energy spectra of X-ray pulsars, the function could cause an artificial bias around the cut-off energy because the first derivative of the function is discontinuous at  $E = E_c$ . When one needs to avoid such a bias, two models are widely used to explain the spectra.

The first is the Negative Positive Exponential (NPEX) model (Mihara, 1995; Makishima et al., 1999). The expression of the model function is given by

$$\frac{dN}{dE} = (A_1 E^{-\Gamma_1} + A_2 E^{\Gamma_2}) \exp\left(-\frac{E}{E_f}\right), \quad (2.12)$$

where  $\Gamma_1 > 0$  and  $\Gamma_2 > 0$  are two photon indices characterizing the negative and positive power laws. For the positive power-law component,  $\Gamma_2 = 2$  is often adopted because it gives a good approximation of the low-energy tail of a blackbody function (e.g., Mihara et al., 1998).

The other model is the Fermi-Dirac cut-off power law (Tanaka, 1986). The model expression is given by

$$\frac{dN}{dE} \propto \frac{E^{-\Gamma}}{\exp\left(\frac{E-E_c}{E_f}\right) + 1}, \quad (2.13)$$

where  $E_c$  and  $E_f$  are the cut-off and folding energy, respectively. The shape of the function is similar to equation (2.11) but has a smooth turnover around  $E_c$ . The function and its derivative are continuous at any point, and thus artificial biases can be removed. The mathematical meanings of  $E_c$  and  $E_f$  are different from those in equation (2.11), and direct comparison of the parameters should not be made.

None of these models gives physical interpretations about the emission mechanism and spectral formation of X-ray pulsars. For luminous X-ray pulsars (especially SGXBs), the energy spectra can be physically interpreted as consequences of non-thermal processes in the so-called accretion columns. Because the accretion flow is accelerated to a comparable velocity to the speed of light when it reaches the surface of the neutron star, bulk and thermal Comptonization play a crucial role in forming non-thermal X-ray emission. A physically-motivated model based on the bulk and thermal Comptonization was established to reproduce the spectral shapes of X-ray pulsars (Becker & Wolff, 2007), which we review in Section 2.4.

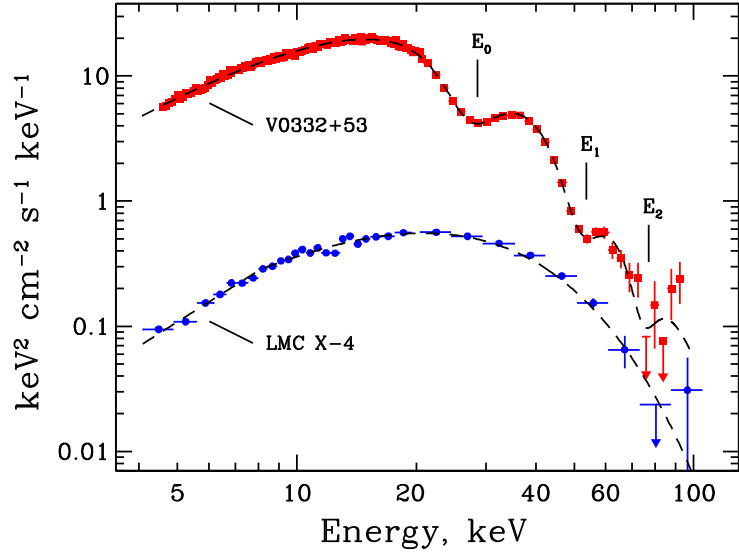


Figure 2.5: Typical energy spectra of X-ray pulsars. X-ray spectra of V 0332+53 and LMC X-4 are presented by red and blue points, respectively. Taken from Walter et al. (2015).

### Cyclotron resonance scattering feature

Many X-ray pulsars display broad absorption-like features in the hard X-ray band. This absorption line is called the cyclotron resonance scattering feature (CRSF), made by a physical process near the neutron star surface. In a strong magnetic field of  $B \sim 10^{12}$  G, electrons are trapped by the magnetic field, and their energies are quantized to the Landau levels. The energy transitions between the Landau levels take place by absorbing or emitting photons that have the corresponding energy to the transition. The resonance scattering generates absorption-like features of the spectrum at specific energies. The CRSF energies are given by

$$E_{\text{cyc}} = \frac{\hbar e B}{m_e c} n = n \times 11.6 \text{ keV} \left( \frac{B}{10^{12} \text{ G}} \right), \quad (2.14)$$

where  $n$  is a positive integer, and  $n = 1$  corresponds to the fundamental cyclotron line induced by electron transition between the ground and the first excited level. If we consider the effect of the gravitational redshift  $z$ , the absorption energies are modified by

$$E_{\text{cyc}} = \frac{n}{1+z} \times 11.6 \text{ keV} \left( \frac{B}{10^{12} \text{ G}} \right). \quad (2.15)$$

The CRSF was predicted in the 1970s (Gnedin & Syunyaev, 1974) and discovered shortly after that by the observation of Her X-1 (Truemper et al., 1978). Since then, it has been utilized for the direct measurements of the magnetic fields of neutron stars.



Currently, CRSFs are detected in about 30 X-ray pulsars (Staubert et al., 2019). In several sources, higher harmonics are detected, which strongly supports that the origin of the absorption line is the resonance scattering. In Figure 2.5, we show a spectrum of an X-ray pulsar V 0332+53 (red points), in which multiple cyclotron lines are detected. LMC X-4 (blue points), on the other hand, does not have such features. The CRSF generally displays a broad absorption line with a few-keV line width due to either or both of the magnetic field structure and the thermal motion of electrons. The upper panel of Figure 2.6 shows CRSF energies and line widths for multiple X-ray pulsars. The most extreme cases show the central energies at  $\sim 60$  keV and the line widths of  $> 10$  keV. Due to the relatively small effective areas of X-ray observatories in the hard X-ray band, as well as the broad line widths of CRSFs, its measurement could be difficult and highly dependent on the modeling of the continuum spectrum.

The CRSFs show variabilities in many ways. For example, the central energy could either positively or negatively correlate with the luminosity, as shown in the lower panels of Figure 2.6. The change in the accretion flow geometry could be the cause, but still, a lot of models are trying to explain such variabilities (e.g., Bykov & Krasil'Shchikov, 2004). In some X-ray pulsars, the CRSF shows spin-phase variability or emerges only in a narrow range of the spin phase (e.g., Lutovinov et al., 2015, 2017). This is considered to be a consequence of the complex mixture of the geometry of the emission region and magnetic field strength and structure (Mushtukov et al., 2015). A continuous decay of CRSF energy over ten years is also reported (e.g., Her X-1: Staubert et al., 2020).

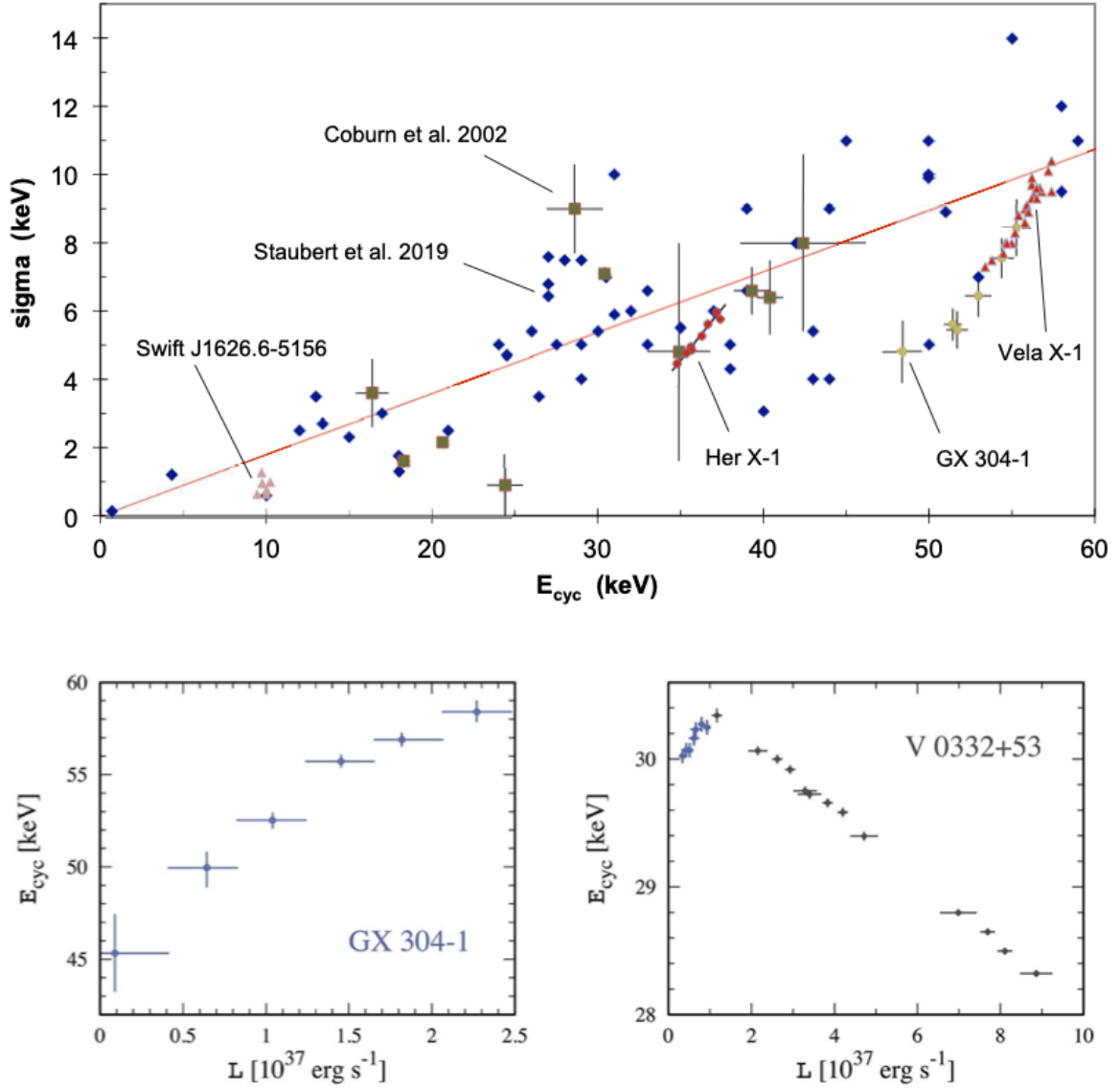


Figure 2.6: (top) Scattering plot of detected CRSFs on the plane of central energy and line width, taken from Staubert et al. (2020). (bottom) Variability of central energies of CRSFs with luminosities for GX 304-1 and V 0332+53, taken from Mushtukov & Tsygankov (2022).

### Emission lines

The fluorescent lines are often detected from X-ray pulsars. The most prominent is the Fe  $K\alpha$  lines from both neutral and highly ionized irons. The emission lines originate from the reflection of the neutron star radiation by surrounding matters, such as the accretion disk and the stellar wind (e.g., Inoue, 1985). If the companion star has a highly ionized stellar wind, the fluorescent lines other than Fe emission lines are detected, such as Ne, Mg, and Si (e.g., Cen X-3: Wojdowski et al., 2003; Vela X-1: Watanabe et al., 2006). These

emission lines also exhibit variabilities in the equivalent width and intrinsic intensity with the orbital and spin phases. Especially, the line emission becomes more dominant in the eclipse phases when the direct emission from the neutron star is suppressed. The emission lines and their variabilities can be utilized to probe the three-dimensional distribution and the ionization state of surrounding matters.

### 2.3.4 Time variability

#### Aperiodic variability

The X-ray pulsars are characterized by their variabilities in the observed luminosities with timescales other than coherent pulsations. The majority of X-ray pulsars are transient sources with flux variabilities larger than an order of magnitude, demonstrating dramatic variations in X-ray luminosity with time scales from weeks to months. Even for the persistent sources, the flux variabilities are significant, often characterized by “high state” (high luminosity) and “low state” (low luminosity). The variability of the X-ray flux is usually interpreted as the change in the accretion rate. However, the geometry or beam pattern could be changed when the accretion rate increases or decreases. Therefore, the luminosity variability does not exactly replicate the change in the mass accretion rate. Variations of beam pattern, changes in geometries of accretion flow or accretion disk, and obscuration by stellar wind constitute possible origins of the aperiodic flux variability (e.g., Klein et al., 1996).

#### Superorbital modulation

In several luminous X-ray pulsars, the observed fluxes show periodic modulations of typically 30–60 days, much longer than the orbital or spin periods. This variability is called the “superorbital modulation”. These objects showing superorbital modulations are SMC X-1 (Wojdowski et al., 1998), LMC X-4 (Heemskerk & van Paradijs, 1989), and Her X-1 (Petterson, 1975), all of which are disk-fed sources. Figure 2.7 shows an example of superorbital modulation by the observed count rate variability of SMC X-1. We can see a clear modulation in the observed count rate with a  $\sim 55$  day cycle. Indeed, the period of the superorbital modulation in SMC X-1 ranges from 40 to 65 days (Ribó et al., 2001; Trowbridge et al., 2007).

The physical origin of the superorbital modulation is not fully understood. The most supported scenario is the precession of a warped accretion disk seen from edge on (Wijers & Pringle, 1999). In this model, the accretion disk is tilted from the binary plane by the radiation of the neutron star. As a result, the precession occurs at the superorbital period and the accretion disk obscures the X-rays from the neutron star at the low-flux phases. There are many other hypotheses on the superorbital modulation, such as a tidal force

from the donor star and magnetic warping (Pfeiffer & Lai, 2004).

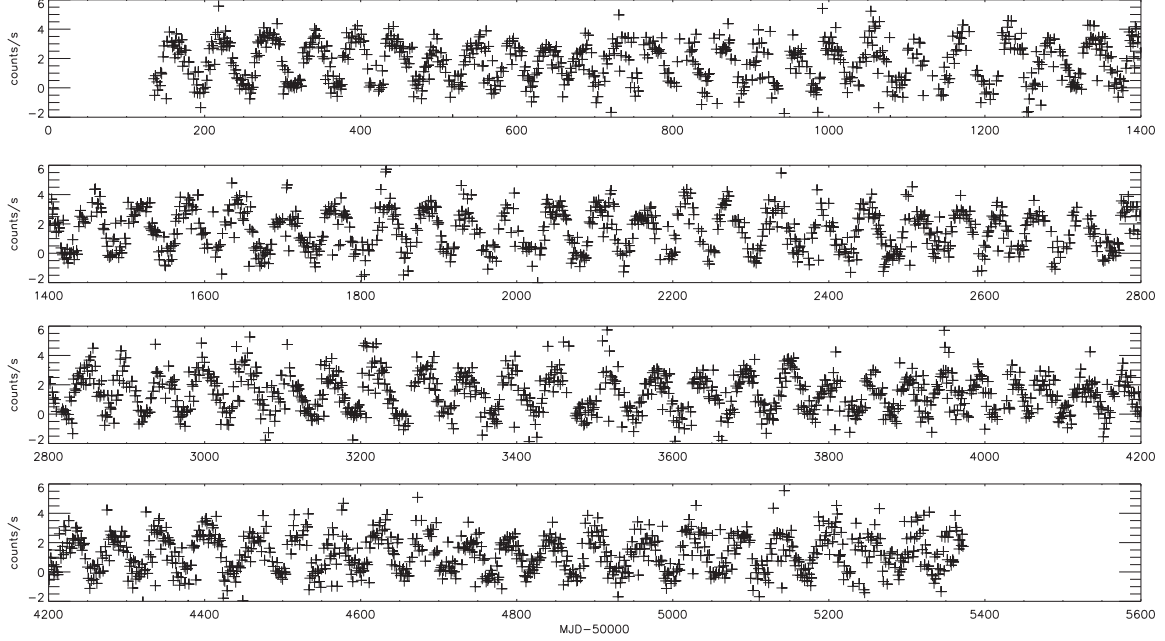


Figure 2.7: Superorbital modulation of SMC X-1 observed by RXTE All Sky Monitor, taken from Hu et al. (2011).

### Quasi-periodic oscillation

The power spectrum analysis of X-ray pulsars gives the frequency dependence of the flux variability. The power spectra of several X-ray pulsars show broad peaks at 10–100 mHz, which is called quasi-periodic oscillation (QPO). The origin of QPO is thought to be the inhomogeneity in the inner accretion disk. The presence of QPO features is known for both transient and persistent X-ray pulsars. Figure 2.8 shows an example of QPO in Cen X-3. The broad peaked feature at  $\sim 40$  mHz (green dashed line) is the QPO component. Since Cen X-3 does not exhibit a clear superorbital modulation, the detection of QPO is one of the observational features that support the existence of an accretion disk (Takeshima et al., 1991; Raichur & Paul, 2008a).

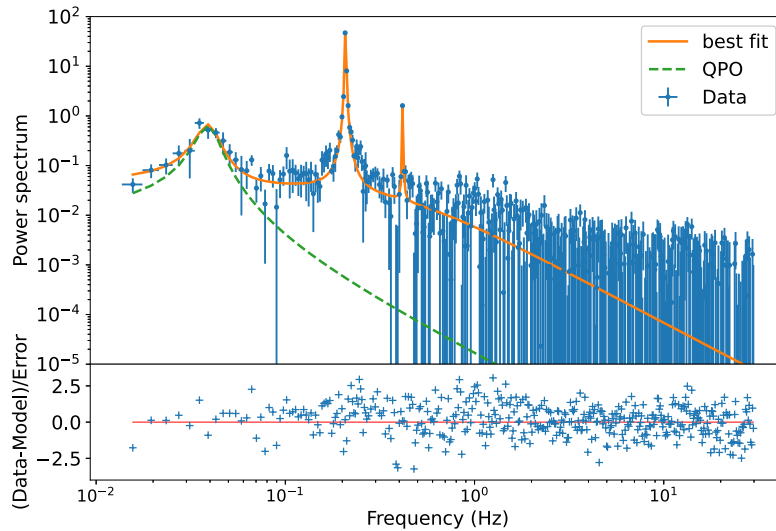


Figure 2.8: Example of QPO seen in the power spectrum of Cen X-3, taken from Liu et al. (2022). The green dashed line denotes the QPO component.

## 2.4 Physics of accretion flow

The spectral formation of X-ray pulsars is often treated by phenomenological models, as mentioned in Section 2.3.3. However, there are also models based on physical interpretations. The most widely supported model is that developed by Becker & Wolff (2007), in which the spectral formation is explained by the bulk and thermal Comptonization in the dense region formed just above the magnetic pole. This region is called the “accretion column” (Basko & Sunyaev, 1976), where radiation-dominated shock decelerates the accretion flow. In this section, we review this model and also describe the physical processes of the accretion flow. The description is based on Becker & Wolff (2007), and its previous researches: Becker & Wolff (2005); Becker (1998, 1992).

### 2.4.1 Geometry of accretion flow

In the accretion site of a highly magnetized neutron star, the magnetic pressure plays a crucial role in determining the geometry of accretion flow. When the magnetic pressure is negligible, the accreting matter falling towards the neutron star moves based on the gravitational potential and conservation of angular momentum. However, after the accreting matter reaches a point where magnetic pressure balances the gravity, it no longer “directly falls” onto the neutron star. Instead, the accreting matter is channeled along the magnetic field and only moves along it. The position where the magnetic pressure

equalizes the gravity is called the Alfvén radius (Lamb et al., 1973), given by

$$\begin{aligned}
 R_m &= \left( \frac{1}{8G} \right)^{1/7} \left( \frac{R_{\text{ns}}^{12} B_0^4}{M \dot{M}^2} \right)^{1/7} \\
 &= 2.4 \times 10^8 \text{ cm} \left( \frac{B_0}{10^{12} \text{ G}} \right)^{4/7} \left( \frac{R_{\text{ns}}}{10 \text{ km}} \right)^{12/7} \left( \frac{\dot{M}}{10^{17} \text{ g s}^{-1}} \right)^{-2/7} \left( \frac{M_{\text{ns}}}{M_\odot} \right)^{-1/7} \quad (2.16)
 \end{aligned}$$

This radius virtually represents the inner edge of the accretion disk.

The accretion flow channeled along the magnetic field falls onto narrow regions around the polar caps of the neutron star. The accreting matter is once accelerated to almost the speed of light but decelerated by radiation pressure from the neutron star surface. Consequently, an optically thick plasma with a high density is formed just above the magnetic pole. This region is the accretion column, where the emissions of X-ray pulsars are generated via inverse Compton scattering by the dense plasma. The coherent pulsations of X-ray pulsars are evidence of narrow emission regions, which correspond to the accretion columns.

Figure 2.9 shows a schematic view of the accretion flow onto a highly magnetized neutron star in a disk-fed source. The accretion disk starts at  $R_{\text{sp}}$ , which is the binary separation. The magnetic field disrupts the accretion disk at  $R_m$  by the magnetic pressure. Inside the Alfvén radius, the accretion flow moves along the magnetosphere and finally reaches the polar cap forming an accretion column.

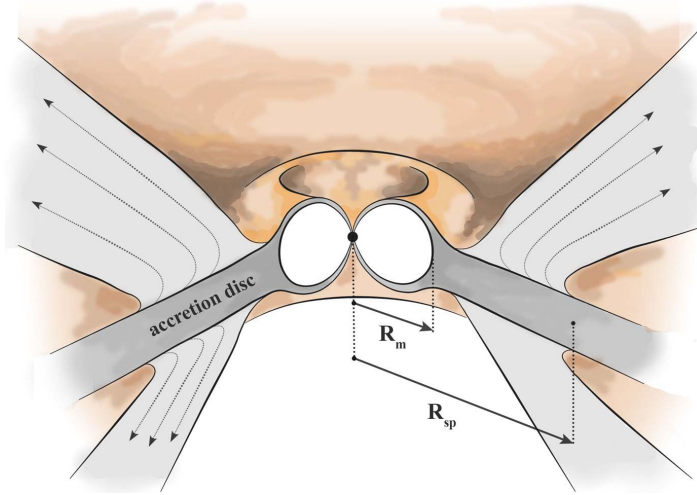


Figure 2.9: Schematic view of the accretion flow onto a highly magnetized neutron star, taken from Mushtukov & Tsygankov (2022).  $R_m$  and  $R_{\text{sp}}$  represent the Alfvén radius (see equation 2.16) and the binary separation, respectively.

## 2.4.2 Radiative processes in accretion column

### Magnetic effect

In the accretion column, the flow is channeled by the strong magnetic field of  $B \sim 10^{12}$  G, and the presence of the magnetic field has crucial effects on the photons propagating through the plasma. The most noticeable effect is the suppression of the scattering cross section by the magnetic field. In such a strong magnetic field, the cross section of the Compton scattering is also dependent on the polarization mode. The two modes of polarization consist of the ordinary and extraordinary modes. In the ordinary mode, the electric field vector of a photon is located in the plane formed by the magnetic field and photon propagation direction. In the extraordinary mode, on the other hand, the electric field vector is perpendicular to this plane. According to Arons et al. (1987), the cross sections of these two modes are given by

$$\begin{aligned}\sigma_{\text{ord}}(\epsilon, \varphi) &= \sigma_{\text{T}} [\sin^2 \varphi + k(\epsilon) \cos^2 \varphi], \\ \sigma_{\text{ext}}(\epsilon, \varphi) &= \sigma_{\text{T}} k(\epsilon) + \sigma_l \phi_l(\epsilon, \epsilon_{\text{cyc}}, \varphi),\end{aligned}\tag{2.17}$$

where  $\epsilon$  and  $\varphi$  represent the photon energy and the propagation angle with respect to the magnetic field, respectively.  $k(\epsilon)$  represents the suppression of the cross section by the magnetic field given by

$$k(\epsilon) = \begin{cases} 1 & (\epsilon \geq \epsilon_{\text{cyc}}) \\ (\epsilon/\epsilon_{\text{cyc}})^2 & (\epsilon \leq \epsilon_{\text{cyc}}), \end{cases}\tag{2.18}$$

where  $\epsilon_{\text{cyc}}$  is the fundamental cyclotron energy defined by equation (2.14) with  $n = 1$ .  $\sigma_l$  is the cross section of the resonant scattering given by

$$\sigma_l = \frac{\pi m_e c^2}{\alpha_F \epsilon_{\text{cyc}}} \sigma_{\text{T}} = 1.9 \times 10^4 \sigma_{\text{T}} \left( \frac{B}{10^{12} \text{ G}} \right)^{-1}.\tag{2.19}$$

$\alpha_F$  is the fine-structure constant.  $\phi_l$  is the unity-normalized line profile function resonant at  $\epsilon = \epsilon_{\text{cyc}}$ . Detailed derivations of the above equations are written in Canuto et al. (1971) and Ventura (1979).

In the calculation of the Comptonized spectrum, it is important to know the cross sections of photons propagating parallel and perpendicular to the magnetic field. If a photon travels parallel to the magnetic field, that is, ascending to the top of the accretion column, the cross sections of the two polarization modes are given by setting  $\varphi = 0.0$ ,

$$\begin{aligned}\sigma_{\text{ord}}(\epsilon, \varphi = 0) &= \sigma_{\text{T}} k(\epsilon), \\ \sigma_{\text{ext}}(\epsilon, \varphi = 0) &= \sigma_{\text{T}} k(\epsilon) + \sigma_l \phi_l(\epsilon, \epsilon_{\text{cyc}}, \varphi = 0).\end{aligned}\tag{2.20}$$

On the other hand, if a photon travels perpendicular to the magnetic field, that is, trying to escape from the wall of the accretion column, the cross sections are given by setting

$$\varphi = \pi/2,$$

$$\begin{aligned}\sigma_{\text{ord}}(\epsilon, \varphi = \pi/2) &= \sigma_{\text{T}}, \\ \sigma_{\text{ext}}(\epsilon, \varphi = \pi/2) &= \sigma_{\text{T}}k(\epsilon) + \sigma_{\text{I}}\phi_{\text{I}}(\epsilon, \epsilon_{\text{cyc}}, \varphi = \pi/2).\end{aligned}\quad (2.21)$$

Therefore, we can roughly estimate  $\sigma_{\parallel}$  and  $\sigma_{\perp}$ , which are the cross sections of photons propagating parallel and perpendicular to the magnetic field, respectively. They are given by

$$\begin{aligned}\sigma_{\parallel} &\simeq \sigma_{\text{T}} \left( \frac{\bar{\epsilon}}{\epsilon_{\text{cyc}}} \right)^2, \\ \sigma_{\perp} &\simeq \sigma_{\text{T}},\end{aligned}\quad (2.22)$$

where we ignore the effect of resonant scattering and  $\bar{\epsilon}$  is the mean energy of the propagating photons. Equation (2.22) shows that the opacity of the low-energy photons traveling along the magnetic field is substantially reduced.

### Radiation-dominated flow

Figure 2.10 shows a schematic picture of an accretion column. The X-ray emission is formed by inverse Compton scattering of soft seed photons generated at the neutron star surface or inside the accretion column. Since the accretion flow is accelerated by releasing its gravitational potential to the free-fall velocity  $v_{\text{ff}} = \sqrt{2GM_{\text{ns}}/R_{\text{ns}}} \sim 0.5c$  near the neutron star surface, a sufficient luminosity is needed to decelerate it by radiation pressure. This deceleration mechanism is called the radiation-dominated shock, formed by continuous variations of the density and pressure. It is different from an ordinary gas-dominated shock, which has a discontinuous profile at the sonic point. The critical luminosity for the formation of the accretion column with radiation-dominated shock is given by

$$L_{\text{crit}} = \frac{2.72 \times 10^{37} \sigma_{\text{T}}}{\sqrt{\sigma_{\perp} \sigma_{\parallel}}} \left( \frac{M_{\text{ns}}}{M_{\odot}} \right) \left( \frac{r_0}{R_{\text{ns}}} \right) \text{ erg s}^{-1}, \quad (2.23)$$

where  $\sigma_{\perp}$  and  $\sigma_{\parallel}$  are energy-averaged scattering cross sections for photons propagating perpendicular and parallel to the magnetic field (see equation 2.22), respectively, and  $r_0$  is the radius of the accretion column (Becker, 1998; Basko & Sunyaev, 1976). Since  $r_0/R_{\text{ns}} \sim 1/100$  and  $\sigma_{\text{T}}/\sqrt{\sigma_{\perp} \sigma_{\parallel}} \sim 100$ , X-ray pulsars with luminosities of  $\gtrsim 10^{37} \text{ erg s}^{-1}$  naturally form accretion columns and radiation-dominated shocks. In such a mechanism, the gravitational energy of an accreting matter is first converted to kinetic energy and then transformed to X-ray radiation via Comptonization.

The velocity profile of a radiation-dominated flow can be determined by the conservation of mass, momentum, and energy fluxes inside the accretion column. The derivation



in Becker (1998) gives the velocity profile inside the accretion column by

$$v(z) = -v_{\text{ff}} \left[ 1 - \left( \frac{7}{3} \right)^{-z/z_{\text{sp}}} \right], \quad (2.24)$$

where  $z$  denotes the vertical distance from the neutron star surface and  $z_{\text{sp}}$  represents the altitude of the sonic point given by

$$z_{\text{sp}} = \frac{r_0}{2\sqrt{3}} \left( \frac{\sigma_{\perp}}{\sigma_{\parallel}} \right)^{1/2} \ln \frac{7}{3}. \quad (2.25)$$

The velocity of the accretion flow is  $-v_{\text{ff}}$  at the upper region of the column, while it is decelerated to 0 at the surface of the neutron star. The density of the accretion column can be calculated by the accretion rate and the conservation of mass flux.

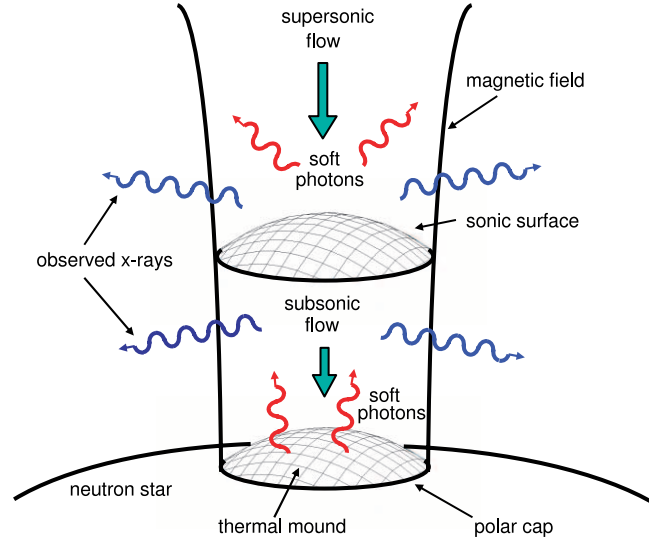


Figure 2.10: Schematic picture of an accretion column, taken from Becker & Wolff (2007).

### Thermal equilibrium

Since a proton has a larger mass than an electron by a factor of  $\sim 2000$ , protons and electrons may have different temperatures in a plasma. Due to the difference in mass, protons carry most kinetic energy. Electrons are cooled by Comptonization with X-rays carrying away their kinetic energy, and also gain energy from protons via Coulomb collisions. The thermal equilibrium is realized if the timescale of the Coulomb collision is sufficiently short compared to that of Comptonization and free fall. The calculation in Arons et al. (1987) gives the Coulomb collision timescale by

$$t_{\text{ei}} \sim 10^{-11} \left( \frac{\rho}{0.01 \text{ g cm}^{-3}} \right)^{-1} \left( \frac{T_e}{10^7 \text{ K}} \right)^{3/2} \text{ s}, \quad (2.26)$$

where  $\rho$  and  $T_e$  are the mass density and the electron temperature, respectively. In the accretion column, these values are typically  $\rho \sim 10^{-4} - 10^{-2} \text{ g cm}^{-3}$  and  $T_e \sim 10^6 - 10^7 \text{ K}$ , which result in  $t_{\text{ei}} \sim 10^{-13} - 10^{-9} \text{ s}$ . The timescale of Comptonization is given by

$$t_{\text{IC}} \sim 10^{-6} \left( \frac{\bar{\sigma}}{10^{-3} \sigma_{\text{T}}} \right)^{-1} \left( \frac{r_0}{1 \text{ km}} \right)^2 \left( \frac{L}{10^{37} \text{ erg s}^{-1}} \right)^{-1} \text{ s}, \quad (2.27)$$

where  $\bar{\sigma}$  denotes the average cross section of Comptonization. In an ordinary X-ray pulsar, this results in  $t_{\text{IC}} \gtrsim 10^{-8} \text{ s}$ . The timescale of free fall is given by

$$t_{\text{dyn}} \sim \frac{R_{\text{ns}}}{v_{\text{ff}}} = \left( \frac{R_{\text{ns}}^3}{2GM_{\text{ns}}} \right)^{1/2} = 10^{-4} \left( \frac{R_{\text{ns}}}{10 \text{ km}} \right)^{3/2} \left( \frac{M_{\text{ns}}}{M_{\odot}} \right)^{-1/2} \text{ s}. \quad (2.28)$$

The typical value is  $t_{\text{dyn}} \sim 10^{-4} \text{ s}$ . The comparison among these three timescales shows that the Coulomb collision timescale is sufficiently short compared to the Comptonization or free-fall timescale. Therefore, the plasma in an accretion column reaches a thermal equilibrium, and we can safely treat it as a mono-temperature plasma.

### Bulk and thermal Comptonization

Since the plasma in the accretion column basically moves vertically due to the gravity and magnetic field, it is an ideal site for first-order Fermi energization, which is called bulk Comptonization. In this process, photons gain energy efficiently since the scattering center is involved in the converging flow (e.g., Laurent & Titarchuk, 1999). The efficiency is characterized by the spatial derivative of the accreting matter velocity. The bulk Comptonization generates a power-law-like spectrum without any cut-off features (Becker & Wolff, 2005). However, many X-ray pulsars show spectra with a flattening in the soft X-ray band and a quasi-exponential cut-off in the hard X-ray band. Both of these effects cannot be reproduced by bulk Comptonization. Instead, they can be reproduced by including the effect of thermal Comptonization, which is the inverse Compton scattering by thermal electrons. Thermal Comptonization is the second-order Fermi energization, in which photons gain energy inefficiently by stochastic motions (Sunyaev & Titarchuk, 1980). This process is characterized by the electron temperature. Since the inflow speed of the accretion flow is much larger than the typical thermal velocity, bulk Comptonization dominates over thermal Comptonization in an ordinary X-ray pulsar.

### 2.4.3 Formation of radiation spectrum

#### Transport equation

The one-dimensional radiative transport equation in an accretion column is given by

$$\begin{aligned} \frac{\partial f}{\partial t} + v \frac{\partial f}{\partial z} = & \frac{dv}{dz} \frac{\epsilon}{3} \frac{\partial f}{\partial \epsilon} + \frac{\partial}{\partial z} \left( \frac{c}{3n_e \sigma_{\parallel}} \frac{\partial f}{\partial z} \right) - \frac{f}{t_{\text{esc}}} \\ & + \frac{n_e \bar{\sigma} c}{m_e c^2} \frac{1}{\epsilon^2} \frac{\partial}{\partial \epsilon} \left[ \epsilon^4 \left( f + kT_e \frac{\partial f}{\partial \epsilon} \right) \right] + \frac{Q(z, \epsilon)}{\pi r_0^2}, \end{aligned} \quad (2.29)$$

where  $f(z, \epsilon)$  is the photon distribution function at position  $z$  and energy  $\epsilon$ . The number density  $n(z)$  and energy density  $U(z)$  can be calculated from  $f(z, \epsilon)$  by

$$\begin{aligned} n(z) &= \int_0^\infty \epsilon^2 f(z, \epsilon) d\epsilon, \\ U(z) &= \int_0^\infty \epsilon^3 f(z, \epsilon) d\epsilon. \end{aligned} \quad (2.30)$$

The left-hand side of equation (2.29) represents the time derivation of the photon density in the co-moving reference frame. Each term in the right-hand side of equation (2.29) represents a corresponding physical process as follows.

- The first term represents the bulk Comptonization characterized by the velocity derivative along  $z$ -axis ( $dv/dz$ ). The velocity profile is given by equation (2.24).
- The second term describes the diffusion of photons along the vertical axis.
- The third term represents the photon escape from the wall of the accretion column. This term is characterized by the photon escape timescale  $t_{\text{esc}}$ . This term is used for the calculation of the observed X-ray spectrum.
- The fourth term represents the thermal Comptonization characterized by the electron temperature ( $kT_e$ ). This term resembles the Kompaneets equation (Kompaneets, 1957), which describes the spectrum of repeated Compton scattering in a thermal plasma.
- The last term accounts for the injection of seed photons.  $Q(z, \epsilon)$  denotes the photon source distribution at position  $z$ .  $\epsilon^2 Q(z, \epsilon) d\epsilon dz$  gives the number of seed photons injected per unit time between  $z$  and  $z + dz$  with energy between  $\epsilon$  and  $\epsilon + d\epsilon$ .

Equation (2.29) can be solved analytically by utilizing the separation of variables and the Green's function method. The separated differential equations have corresponding eigenvalues, and a linear combination of the eigenfunctions gives the exact solution. The exact form of the solution is too long to write down because it includes complex forms

of mathematical functions such as gamma functions, hypergeometric functions, Laguerre polynomials, and Whittaker functions (see Section 4 of Becker & Wolff, 2007).

The altitude-dependent spectrum can be derived from the escaping photons through the column wall. The phase density of photons escaping from the wall per unit time per unit energy is given by

$$\dot{N}_\epsilon(z, \epsilon) = \frac{\pi r_0^2 \epsilon^2}{t_{\text{esc}}(z)} f(z, \epsilon), \quad (2.31)$$

where the escape time  $t_{\text{esc}}$  is given by

$$\begin{aligned} t_{\text{esc}}(z) &= \frac{r_0 \tau_\perp(z)}{c} = \frac{r_0^2 n_e(z) \sigma_\perp}{c} \\ &= \frac{\dot{M} \sigma_\perp}{\pi m_p c |v(z)|}. \end{aligned} \quad (2.32)$$

Here,  $\tau_\perp$  denotes the optical thickness from the column center to the wall. The observed spectrum can be calculated by

$$\Phi_\epsilon(\epsilon) = \int_0^\infty \dot{N}_\epsilon(z, \epsilon) dz. \quad (2.33)$$

### Seed photons and source distributions

The seed photons of Comptonization originate from three ways of physical processes inside the accretion column. These are thermal bremsstrahlung (free-free emission), blackbody radiation, and cyclotron radiation. We denote these three processes as ff, bb, and cyc, respectively.  $Q(z, \epsilon)$  in equation (2.29) is the summation of the photon source distributions of the three processes, namely,

$$Q(z, \epsilon) = Q^{\text{ff}}(z, \epsilon) + Q^{\text{bb}}(z, \epsilon) + Q^{\text{cyc}}(z, \epsilon). \quad (2.34)$$

The first process, thermal bremsstrahlung, is induced by free electrons and ions in optically-thin regions. Based on equation (5.14b) in Rybicki & Lightman (1979), the photon production rate per unit volume per unit energy is given in cgs units by

$$\dot{n}_\epsilon^{\text{ff}} = 3.68 \times 10^{36} \rho^2 T_e^{-1/2} \epsilon^{-1} \exp(-\epsilon/kT_e) \quad (2.35)$$

The source distribution function is given by

$$\begin{aligned} Q^{\text{ff}}(z, \epsilon) &= \frac{\pi r_0^2}{\epsilon^2} \dot{n}_\epsilon^{\text{ff}} \\ &= 1.16 \times 10^{37} r_0^2 \rho^2 T_e^{-1/2} \epsilon^{-3} \exp(-\epsilon/kT_e). \end{aligned} \quad (2.36)$$

Since bremsstrahlung is observed in optically-thin regions, the position corresponding to this process is

$$z_{\text{th}} < z < \infty, \quad (2.37)$$

where  $z_{\text{th}}$  is the position of the “thermal mound”, under which the accretion flow becomes optically thick. This position is represented by

$$\alpha_{\text{R}}^{\text{ff}}(z_{\text{th}})r_0 = 1, \quad (2.38)$$

where  $\alpha_{\text{R}}^{\text{ff}}$  denotes the Rosseland-mean of free-free absorption coefficient expressed by (Rybicki & Lightman, 1979)

$$\alpha_{\text{R}}^{\text{ff}} = 6.1 \times 10^{22} T_{\text{th}}^{-7/2} \rho^2. \quad (2.39)$$

Here,  $T_{\text{th}}$  represents the temperature of the thermal mound that is computed separately from the electron temperature  $T_e$ , although these two temperatures are expected to be comparable. Typically, the thermal mound is very close to the neutron star surface ( $z_{\text{th}}/z_{\text{sp}} < 10^{-4}$ ), and thus we can treat the thermal bremsstrahlung as originating from the entire accretion column (see Section 5.1 of Becker & Wolff, 2005).

The second process, blackbody radiation, occurs at the surface of the thermal mound. The intensity of a blackbody radiation with a temperature  $T_{\text{th}}$  is given by

$$B_{\epsilon}(\epsilon) = \frac{2\epsilon^3}{c^2 h^3} \frac{1}{\exp(\epsilon/kT_{\text{th}}) - 1}. \quad (2.40)$$

Since the solid angle for the surface radiation is  $\pi$ , and this process only occurs at  $z = z_{\text{th}}$ , the source distribution function can be written by

$$Q^{\text{bb}}(z, \epsilon) = \frac{\pi^2 r_0^2}{\epsilon^3} B_{\epsilon}(\epsilon) \delta(z - z_{\text{th}}) \quad (2.41)$$

$$= \frac{2\pi^2 r_0^2}{c^2 h^3} \frac{\delta(z - z_{\text{th}})}{\exp(\epsilon/kT_{\text{th}}) - 1}. \quad (2.42)$$

As the location of the thermal mound is very close to the neutron star surface, the blackbody radiation can be virtually treated as emission from the neutron star surface.

The third process, cyclotron radiation, occurs under a strong magnetic field. This process is induced by the energy transition of electrons between Landau levels. Thus, the emitted photons always have the cyclotron energy  $\epsilon_{\text{cyc}}$  (equation 2.14). Based on Arons et al. (1987), the photon production rate per unit volume per unit energy is given

$$\dot{n}_{\epsilon}^{\text{cyc}} = 2.10 \times 10^{36} \rho^2 B_{12}^{-3/2} H \left( \frac{\epsilon_{\text{cyc}}}{kT_e} \right) \exp(-\epsilon_{\text{cyc}}/kT_e) \delta(\epsilon - \epsilon_{\text{cyc}}), \quad (2.43)$$

where

$$H \left( \frac{\epsilon_{\text{cyc}}}{kT_e} \right) = \begin{cases} 0.41 & \epsilon_{\text{cyc}}/kT_e \geq 7.5 \\ 0.15 \sqrt{\epsilon_{\text{cyc}}/kT_e} & \epsilon_{\text{cyc}}/kT_e \leq 7.5. \end{cases} \quad (2.44)$$

$B_{12}$  represents the magnetic field strength in unit of  $10^{12}$  G. The source distribution function can be calculated by

$$\begin{aligned} Q^{\text{cyc}}(z, \epsilon) &= \frac{\pi r_0^2}{\epsilon^2} \dot{n}_{\epsilon}^{\text{cyc}} \\ &= 1.92 \times 10^{52} r_0^2 \rho^2 B_{12}^{-7/2} H \left( \frac{\epsilon_{\text{cyc}}}{kT_e} \right) \exp(-\epsilon_{\text{cyc}}/kT_e) \delta(\epsilon - \epsilon_{\text{cyc}}). \end{aligned} \quad (2.45)$$

#### 2.4.4 Application to observation data

Several studies successfully fitted the observed spectra of X-ray pulsars by the accretion column model. Figure 2.11 shows an example, in which the broadband spectrum of Her X-1 is fitted by the model (Wolff et al., 2016). Among the three processes, the thermal bremsstrahlung is the most dominant process that mostly explains the observed spectrum. Similar trials were performed by West et al. (2017) and Thallhammer et al. (2021) for Her X-1, Cen X-3, and LMC X-4.

Although the accretion column model is the first model that gives physical interpretations of the observed spectra of X-ray pulsars, many effects are not taken into account because of the simplification. For example, the accretion flow is assumed to consist of a fully ionized hydrogen plasma. The electron cross sections are only treated for the mean photon energy. A constant magnetic field and constant radius through the entire column are also simplified assumptions. When one uses this model to fit the observed spectrum, it is necessary to keep these simplifications in mind.

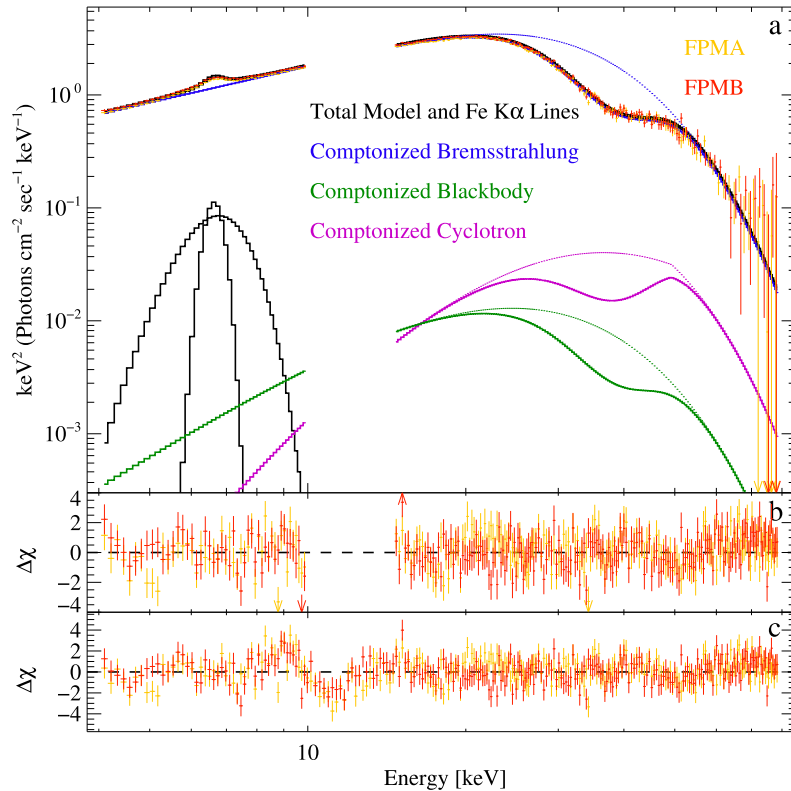


Figure 2.11: Her X-1 spectrum fitted by accretion column model, taken from Wolff et al. (2016). Blue, green, and purple lines denote Comptonized spectra of bremsstrahlung, blackbody, and cyclotron radiation, respectively.

# Chapter 3

## Instrumentation

In this thesis, we investigate the X-ray spectral variability of X-ray pulsars by utilizing observation data obtained with X-ray observatories. It requires observatories with large effective areas, good timing resolutions, and broadband coverages ranging from soft to hard X-ray bands. In this chapter, we describe the overview of two X-ray observatories, NuSTAR and NICER, which we utilized in this thesis.

### 3.1 NuSTAR

#### 3.1.1 Overview

The Nuclear Spectroscopic Telescope Array (NuSTAR; Harrison et al., 2013) is a space observatory launched on 2012 June 13. It is the first in-orbit observatory capable of focusing high-energy X-rays and operates in a wide energy band of 3–79 keV. Until the launch of NuSTAR, the focusing method was only valid for the soft X-ray band. The coded aperture technology was mainly used for hard X-ray observatories, such as INTEGRAL (Winkler et al., 2003), RXTE (Bradt et al., 1993; Swank, 1999), and BeppoSAX (Boella et al., 1997). However, it generally leads to a limited sensitivity and high background. Utilizing the focusing technique in the hard X-ray band greatly improved the effective area and reduced background. The highly improved hard X-ray capability of NuSTAR enables detailed investigations of high-energy emissions from X-ray objects.

Figure 3.1 presents illustrations of NuSTAR in the deployed and stowed configurations. It consists of two co-aligned optics modules, which focus onto two independent focal plane detectors utilizing total and Bragg reflection by multilayer-coated X-ray mirrors. An extendible mast of 10.14 m instrument focal length enables the focusing of hard X-rays, which have very shallow reflection angles. The instrument star trackers and metrology lasers are used to reconstruct the instantaneous alignment and pointing direction of the instrument. The focal plane module consists of a solid state CdZnTe (CZT) pixel detector

surrounded by a CsI anti-coincidence shield.

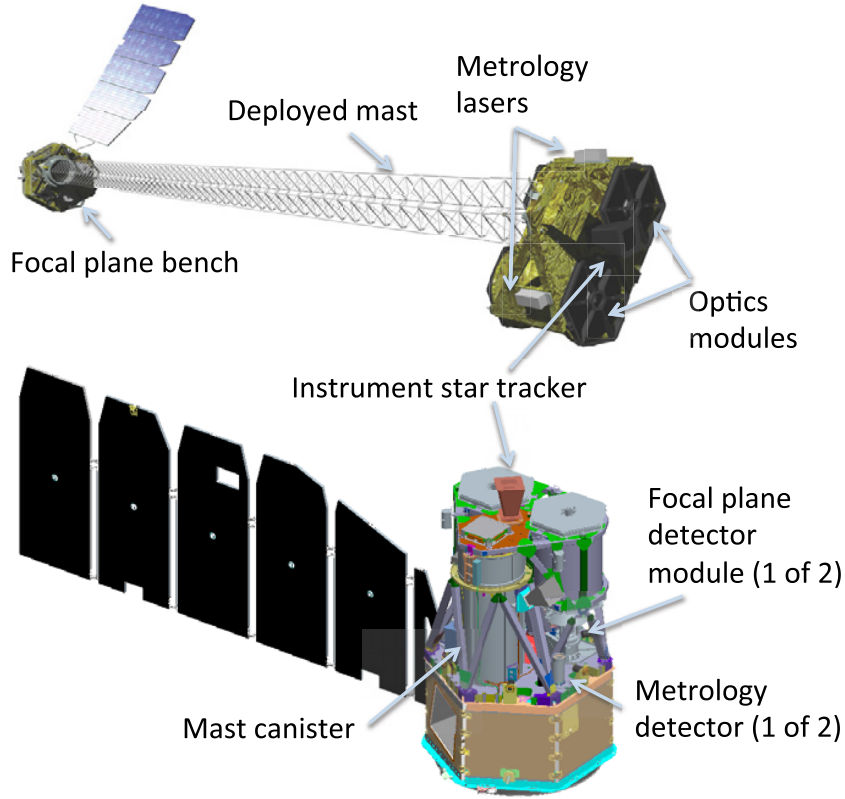


Figure 3.1: Illustration of NuSTAR in the deployed (top) and stowed (bottom) configurations (Harrison et al., 2013).

### 3.1.2 Optics

The NuSTAR observatory has two co-aligned hard X-ray grazing telescopes that point at celestial targets. Each optics module contains 133 nested grazing incidence shells in a conical approximation to a Wolter-I geometry (Petre & Serlemitsos, 1985). The inner 89 shells are coated with depth-graded Pt/C multilayers, capable of reflecting efficiently below the Pt K-absorption edge at 78.4 keV. The outer 44 are coated with W/Si, reflecting below the W K-absorption edge at 69.5 keV. The multilayer coating has the advantage of creating enhanced reflectivity due to a high contrast of density, which enables NuSTAR to collect hard X-ray photons up to 78.4 keV. Figure 3.2 shows the effective area of NuSTAR compared to those of other observatories. The effective area of NuSTAR is significantly large, especially in the hard X-ray band, with other observatories dropping their effective areas at  $\sim 10$  keV. The NuSTAR effective area drops at 69.5 keV and 78.4 keV, corresponding to the K-absorption edge of W and Pt, respectively.

Due to the optics configuration, the observed photons by NuSTAR track smaller graze



angles compared to soft X-ray telescopes. It leads to vignetting losses significant above an off-axis angle of  $2'$ . Figure 3.3 shows the reduction in the effective area as a function of the off-axis angle. Since higher energy photons have shallower graze angles, the drops of effective areas are more rapid for higher energy photons. The effective FoV is  $10'$  at 10 keV and  $6'$  at 68 keV, defined by the position with 50% effective area of the on-axis.

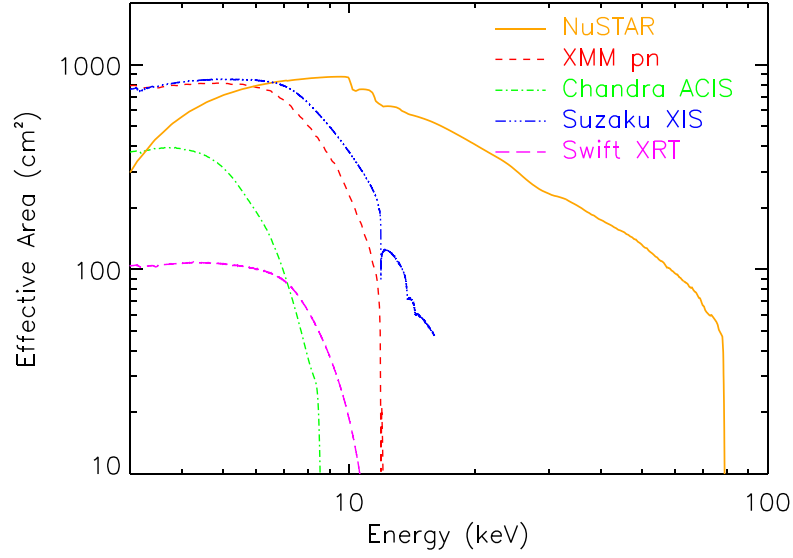


Figure 3.2: Effective area of NuSTAR compared with other observatories, taken from Harrison et al. (2013).

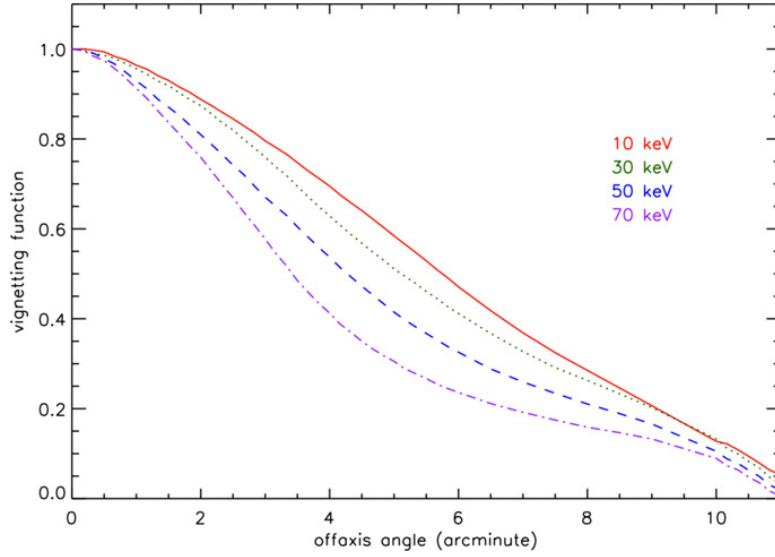


Figure 3.3: Reduction in the NuSTAR effective area due to the vignetting effect. Effective areas of different energies are plotted as a function of the off-axis angle. Taken from Harrison et al. (2013).

### 3.1.3 Mast

Because of the shallow reflection angles of hard X-rays, the focusing telescopes require long focal lengths. NuSTAR is equipped with a 10.14 m mast extending between the optics and the focal plane detectors. It is made up of carbon fiber, aluminum, and steel components and is designed to be isothermal to minimize the distortions of the structure. Since the mast is much longer than the size of the rocket, it was launched in the stowed configuration and deployed in orbit after the launch.

Despite the low net coefficient of thermal expansion, the optical axis and the X-ray focal point could be deflected due to the orbital day/night extremes. The deflection is typically 1 mm per orbit and a few mm in the worst case. The mast motion is tracked by a metrology system consisting of two IR lasers on the optics bench. The star tracker mounted to the optics bench also contributes to the correction of the mast motion.

### 3.1.4 Focal Plane Modules (FPMs)

Each of the two telescopes has its own focal plane module, consisting of a solid-state CdZnTe (CZT) pixel detector and a CsI anti-coincidence shield. These modules are called FPMA and FPMB. Figure 3.4 shows a picture of FPM. It consists of a  $2 \times 2$  array of CZT pixel detectors, each with  $32 \times 32$  pixels with pitches of 0.6 mm. The high atomic number (48 for Cd and 52 for Te) and wide band gap of  $\sim 1.5$  eV enable a good

detection efficiency of hard X-rays and the operation at room temperature, respectively. The energy resolution defined by FWHM is 400 eV at 10 keV and 900 eV at 68 keV. Each pixel subtends  $12''.3$  and each detector provides a  $12'$  FoV. The incident events are recorded with a time accuracy of  $2\ \mu\text{s}$ .

A CsI anti-coincidence shield is placed around the focal plane detectors to reduce background events. An incident event that produced energy deposits simultaneously in the anti-coincidence shield and the detector is rejected as a background event. Since the opening angle of the shield is large ( $15^\circ$  FWZI) and the blocking by the optics bench is not perfect, stray light from nearby objects may contaminate the observation data. Extremely bright X-ray sources of  $> 100$  mCrab within 1 to 5 degrees from a target would be a source of stray light. Such an effect becomes a serious problem, particularly when one observes objects in the galactic center. Since the formation of stray light is highly dependent on the pointing angle of the detector, one can avoid it by carefully selecting the observation date.

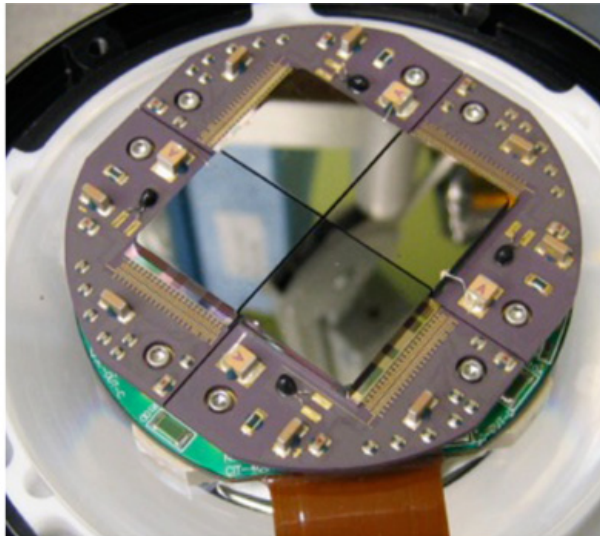


Figure 3.4: Picture of NuSTAR FPM, taken from Harrison et al. (2013).

## 3.2 NICER

### 3.2.1 Overview

The Neutron Star Interior Composition Explorer (NICER; Gendreau et al., 2012) is a NASA X-ray space observatory launched on 2017 June 3. This mission was designed to explore the interiors of neutron stars, where gravitational, electromagnetic, and nuclear-physics environments are extreme. The main goal of the mission is to constrain the

equation of state of neutron stars by utilizing spin-phase-resolved spectroscopy of thermal and non-thermal emissions from rotation-powered neutron stars. The extremely large effective area up to  $\sim 2300 \text{ cm}^2$ , high sensitivity in the soft X-ray band (0.2–12 keV), and good timing resolution of  $< 300 \text{ ns}$  compared to previous observatories are keys to probing such problems.

As illustrated in Figure 3.5, NICER is attached to one of the International Space Station’s (ISS) zenith-side ExPRESS Logistics Carriers (ELC), unlike other X-ray observatories solely orbiting the earth. This leads to the advantage of sufficient power supply, telemetry, and high-resolution GPS connection. Even though there are certain obscurations by ISS components and interruptions due to ISS operations, NICER achieves an entire hemisphere of sky coverage with high viewing efficiency. Moreover, NICER provides a rapid-response capability for targeting transient sources, which enables detailed investigations in X-ray timing astrophysics after the previous RXTE observatory.

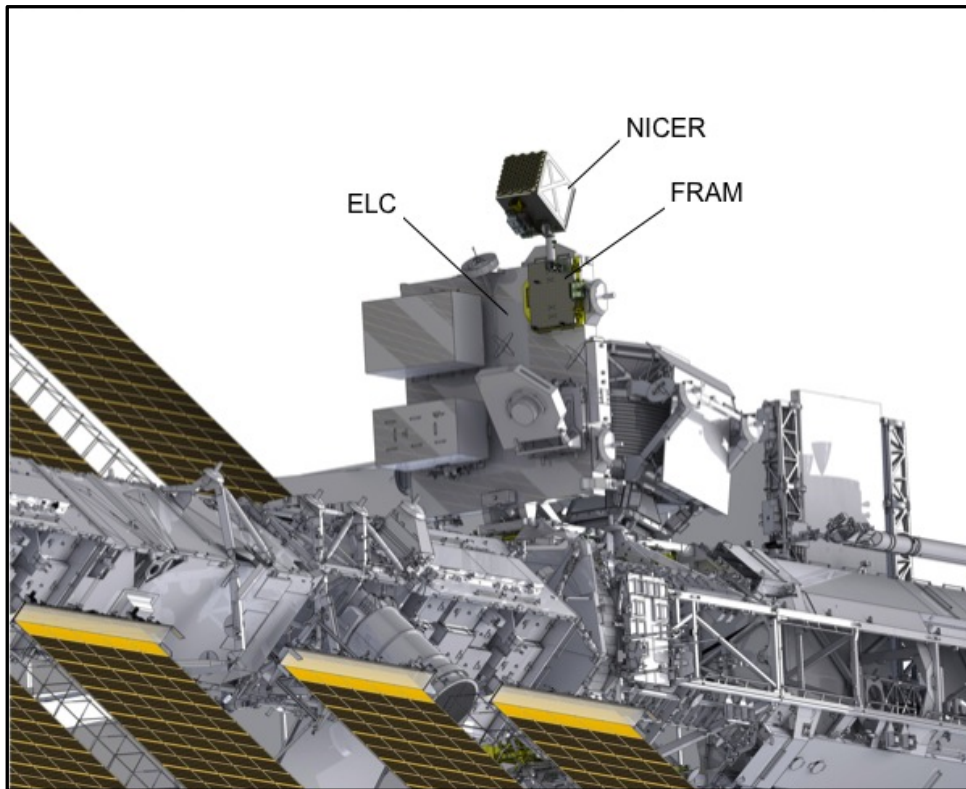


Figure 3.5: Illustration of NICER onboard the International Space Station (ISS), taken from Gendreau et al. (2012).

### 3.2.2 Optics and detectors

NICER optics are composed of co-aligned 56 separate mirror modules, each focusing X-rays on their own silicon drift detector (SDD), as shown in Figure 3.6. The mirrors are called the X-ray concentrator (XRC) and utilize Wolter I grazing incidence optics. The picture and schematic illustration of a single XRC are presented in Figure 3.7. Each mirror consists of 24 mirror shells and has a focal length of 1.085 m. X-ray mirrors usually employ both parabolic and hyperbolic mirrors to focus incident photons, but NICER only utilizes parabolic ones because it does not require imaging capability. It achieves a compact structure and reduces costs and weight. The only function of the mirrors is to narrow the field of view and focus X-rays on smaller detectors. These minimize noise and background contamination, and achieve a large effective area. Figure 3.8 shows the effective area of NICER compared to that of XMM-Newton pn (Jansen et al., 2001; Strüder et al., 2001). It shows an order of magnitude improvement from the previous observatory. The peak of the effective area is  $\sim 2300 \text{ cm}^2$  at  $\sim 1.5 \text{ keV}$ .

The focal plane detectors are composed of 56 silicon drift detectors (SDDs) aligned in a  $7 \times 8$  structure. The advantage of these detectors is a low background and a high timing resolution. The detectors are cooled to  $-55^\circ\text{C}$  to minimize the background induced by dark current. The high timing resolution is obtained by minimizing the size of each detector to  $25 \text{ mm}^2$  and reducing the uncertainties in the charge drift time. This minimization is achieved by installing an aperture on the top of the detector. Consequently, the timing resolution of NICER is  $< 300 \text{ ns}$ . The SDD also provides a moderate energy resolution typical of silicon-based detectors, approaching the Fano limit. The energy resolution is 3% at 6 keV and 8% at 1 keV.

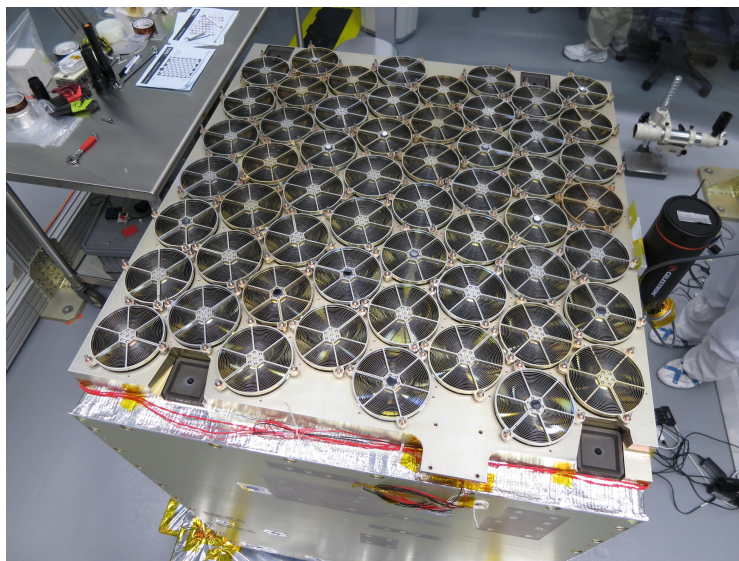


Figure 3.6: Photo of the 56 co-aligned NICER XRCs (Okajima et al., 2016).

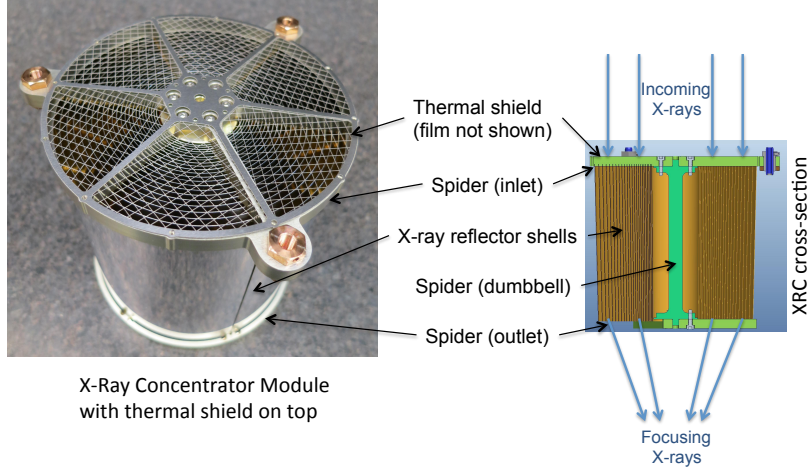


Figure 3.7: Photo of a NICER XRC (left) and cross-section illustration (right), taken from Okajima et al. (2016).

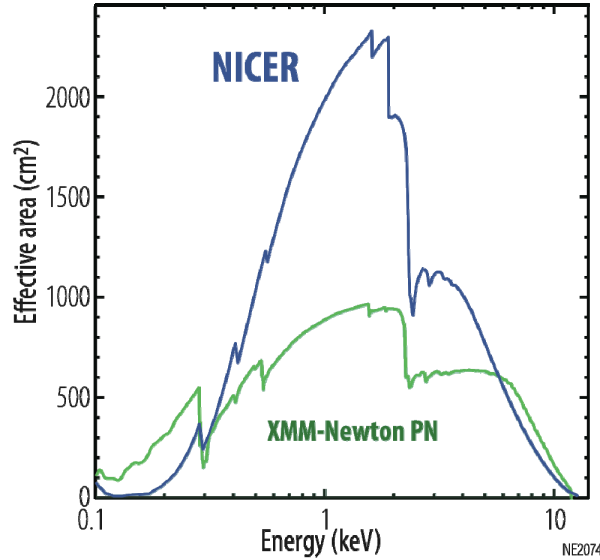


Figure 3.8: Effective area of NICER compared to XMM-Newton pn (Gendreau et al., 2012).

### 3.2.3 Background estimation

Since NICER is a non-imaging observatory, any incident photons entering the  $5' \times 5'$  FoV is treated as source photons. Therefore, it is impossible to generate background spectra from an off-source region on the detector. Instead, several models have been developed



to estimate a background spectrum within a specific observation. In the spectral or temporal analysis of the observation data, one needs to generate background spectra, especially when the source is faint. Even when the source is bright, it is necessary to carefully treat the low-energy and high-energy end of the NICER energy band, where the signal-to-noise ratio becomes much worse. For now, two types of such background generators are available.

One of the background estimators is `nicer.bkg_estimator`. It utilizes environmental data of a specific observation to estimate the background. The environmental data consist of the orientation of the spacecraft, its position in the earth magnetosphere, and the space weather. The orientation of the spacecraft is used to estimate the stray light from the sun, which can induce significant background at the low energy band. The magnetosphere information is essential to calculate the magnetic cut-off rigidity, which is modeled based on the International Geomagnetic Reference Field (Thébault et al., 2015). The space weather is also important to determine the background level, which is described by the planetary Kennziffer Index (Kp index; Bartels et al., 1939). It ranges from 0 to 9, where low values indicate calm space weather and high values indicate geomagnetic storms. The Kp is updated every three hours by a worldwide network of magnetometers.

The other background estimator is `nibackgen3C50` (Remillard et al., 2022). It is a phenomenological model in which the background spectrum of each observation is described by three parameters, namely “3C”. The modeling is constructed by utilizing observation data with seven point directions that are void of detectable sources. The three parameters are defined as “ibg”, “hrej”, and “nz”. The ibg denotes 15–18 keV events “in focus”, which is beyond the effective area of the optics and unlikely to be focused by the X-ray mirrors. The hrej represents events near the detector edge, which are rejected as particles. The nz is the low-energy event below 0.2 keV, likely caused by noise of the detectors. `nibackgen3C50` combines these three effects and generates a suitable background spectrum for an arbitrary observation data set.

# Chapter 4

## Broadband X-ray variability of Cen X-3 studied with short-time NuSTAR observation

### 4.1 Overview of Cen X-3

Centaurus X-3 (Cen X-3) is one of the most studied X-ray pulsars in our galaxy. It is the best target to investigate the relation between spectral variability and physical conditions. This is because it is a representative source of disk-fed X-ray pulsars, which generally have stable accretion streams compared to transient wind-fed X-ray pulsars. In such an object, it is more straightforward to distinguish the intrinsic variability of the accretion stream and the effects of the extrinsic stellar wind through the orbital- and spin-phase-resolved analysis. Moreover, the well-studied binary properties and X-ray spectral features allow us to perform a detailed analysis without many uncertain assumptions.

Cen X-3 is the first binary pulsar discovered in X-rays (Chodil et al., 1967; Giacconi et al., 1971), and one of the brightest X-ray pulsars in our galaxy, located  $6.4_{-1.4}^{+1.0}$  kpc from the earth (Arnason et al., 2021). The luminosity is estimated to be  $\sim 5.0 \times 10^{37}$  erg s $^{-1}$  in the energy band of 2–10 keV (Suchy et al., 2008), which strongly supports the mass accretion via an accretion disk rather than the mere capture of stellar wind. The existence of an accretion disk is also suggested by the variability of the optical light curve (Tjemkes et al., 1986) and quasi-periodic oscillations at  $\sim 40$  mHz (Takeshima et al., 1991; Raichur & Paul, 2008a; Liu et al., 2022). In the binary system, a neutron star with a mass of  $1.34_{-0.14}^{+0.16} M_{\odot}$  (van der Meer et al., 2007) is orbiting a giant O6–8 III counterpart V779 Cen with a mass and radius of  $20.5 \pm 0.7 M_{\odot}$  and  $12 R_{\odot}$  respectively (Schreier et al., 1972; Krzeminski, 1974; Hutchings et al., 1979). The orbital period is  $\sim 2.08$  days (Bildsten et al., 1997), of which  $\sim 20\%$  is eclipsed by the companion star. From the length of the eclipse is a high inclination angle of  $70.2 \pm 2.7$  deg estimated (Ash et al., 1999). The



neutron star is spinning with a period of  $\sim 4.8$  s, first discovered by the X-ray observation of Uhuru (Giacconi et al., 1971). It is followed by the discovery of a gradual and stochastic spin-up feature presumably due to the mass accretion (e.g., Tsunemi et al., 1996).

The spin-phase-averaged spectrum of Cen X-3 was well studied by previous studies. It is characterized by a power law with a photon index of  $\sim 1.0$  with a quasi-exponential cut-off at  $\sim 15$  keV (e.g., White et al., 1983). Several additional components were reported, such as the soft excess below  $\sim 3$  keV, multiple Fe emission lines, and the cyclotron resonance scattering feature (CRSF) at  $\sim 27$  keV. The Fe K-emission line was first observed by Ginga (Day et al., 1993) followed by the detection of three lines at  $\sim 6.4$  keV,  $\sim 6.7$  keV, and  $\sim 7.0$  keV, which were resolved by ASCA (Ebisawa et al., 1996). These lines correspond to neutral, He-like, and H-like emission lines, respectively. The CRSF was first reported by Ginga observation (Nagase et al., 1992) and later confirmed by BeppoSAX (Santangelo et al., 1998), indicating a surface magnetic field of  $B \sim 3 \times 10^{12}$  G. The spin-phase variability of the CRSF was also reported (Burderi et al., 2000). Since the discovery of the object, both the orbital- and spin-phase variabilities in the X-ray band have been studied by multiple observatories (Chandra: Wojdowski et al., 2003; Iaria et al., 2005; RXTE: Raichur & Paul, 2008b; Suzaku: Naik et al., 2011; XMM-Newton: Sanjurjo-Ferrín et al., 2021). Most recently, the spin-phase variability of the polarization was investigated with IXPE to determine the emission geometry as displaced from antipodal configuration (Tsygankov et al., 2022), consistent with the results of the pulse deconstruction analysis performed by Kraus et al. (1996). However, no consensus has been reached about the relation between the spectral variability and physical conditions such as the stability of the accretion stream or the structure of the stellar wind.

In this work, we aim to comprehensively study the orbital- and spin-phase spectral variabilities of Cen X-3 by giving physical interpretations. It requires observation data with sufficient statistics, a good timing resolution, and broadband capability ranging from the soft to hard X-rays, and NuSTAR is the best facility for our study. In this chapter, we present the analysis results derived from 39 ks NuSTAR archival data of Cen X-3, focusing on the orbital- and spin-phase variabilities. The chapter refers to the results in Tamba et al. (2022).

## 4.2 Observation and data reduction

Cen X-3 was observed by NuSTAR from 2015 November 30 to December 1 with an elapsed time of 38.7 ks (ObsID: 30101055002). For general data reduction, we followed “NuSTAR Data Analysis Software Guide”<sup>1</sup> and used `nupipeline` and `nuproducts` contained in `HEASoft` 6.29, which is a standard analysis tool for X-ray astronomy provided by NASA.

---

<sup>1</sup>[https://heasarc.gsfc.nasa.gov/docs/nustar/analysis/nustar\\_swguide.pdf](https://heasarc.gsfc.nasa.gov/docs/nustar/analysis/nustar_swguide.pdf)

The source and background regions were defined as a circle with a radius of  $180''$  from the source center and a rectangle in the off-source region, respectively, extracted by DS9 (Joye & Mandel, 2003). The barycentric correction was also applied to the arrival times in the data reduction process. As a result of general data reduction, the net exposures of FPMA and FPMB were 21.4 ks and 21.6 ks, respectively. After the data reduction, barycentric corrected event data were generated, from which spectra and light curves can be extracted. All of the temporal and spectral analyses in this chapter were carried out utilizing Xronos 6.0 and XSPEC 12.12.0, which are contained in HEASoft. The uncertainties are given at  $1\sigma$  confidence levels unless stated otherwise.

Before temporal or spectral analysis of X-ray binaries, it is necessary to correct the arrival times of observation data for the binary motion. Generally, the spin period of a binary system  $P_{\text{spin}}$  is affected by the Doppler shift originating from the binary motion, and shifts to a different value  $P_{\text{Doppler}}$ . When the eccentricity of the binary system is ignored, the apparent spin period can be written by

$$P_{\text{Doppler}}(t) = P_{\text{spin}} \{1 - A \sin(2\pi\Phi)\}, \quad (4.1)$$

where  $t$  is the time from the start of the observation and  $\Phi$  denotes the orbital phase expressed by

$$\Phi(t) = \Phi_{\text{start}} + \frac{t}{P_{\text{orb}}}. \quad (4.2)$$

In this work, we defined the zero point of  $\Phi$  as the mid-eclipse of the system.  $P_{\text{orb}}$  and  $\Phi_{\text{start}}$  represent the orbital period and the orbital phase at the start time of the observation, respectively. The amplitude of the sinusoidal function  $A$  is given by

$$A = \frac{2\pi a_x \sin i}{c P_{\text{orb}}}, \quad (4.3)$$

where  $a_x \sin i$  and  $c$  are the projected semi-major axis of the binary system and the speed of light, respectively. The arrival times of the observed photons should be converted to those in the rest frame of the binary system, referring to the orbital parameters. The correction can be made by

$$t_{\text{binary}} = t_{\text{solar}} - \frac{a_x \sin i}{c} \cos(2\pi\Phi), \quad (4.4)$$

where  $t_{\text{binary}}$  and  $t_{\text{solar}}$  are the photon arrival times of the solar system and binary system, respectively.

We divided the whole observation data of Cen X-3 into 20 pieces, with each piece having a duration of 2 ks, to examine the spin period variation due to the binary motion. The 20 spin periods displayed a variability due to the binary modulation. We applied a simple fitting to the spin period variation using equation (4.1) to determine the orbital

parameters. Here, the small eccentricity of the system ( $e < 0.0016$ ; Bildsten et al., 1997) is neglected.  $P_{\text{orb}}$ ,  $P_{\text{spin}}$ ,  $\Phi_{\text{start}}$ , and  $\Phi_{\text{start}}$  consist of the fitting parameters, among which  $P_{\text{orb}}$  was fixed to  $P_{\text{orb}} = 2.087$  days (Bildsten et al., 1997) because of the limited observation duration compared to the whole orbital period. Table 4.1 presents orbital parameters derived from the fitting compared to those yielded by previous X-ray observations (Bildsten et al., 1997; Falanga et al., 2015). All of the orbital parameters are consistent with previous observations.  $\Phi_{\text{start}} = 0.199$  means that the 38.7 ks continuous observation with NuSTAR covers an orbital interval of  $\Phi = 0.199\text{--}0.414$ . We then applied the binary correction to the arrival times of event data, using equation (4.4). Hereafter, all the temporal and spectral analyses are based on the binary corrected arrival times ( $t_{\text{binary}}$ ).

Table 4.1: Orbital parameters of Cen X-3.<sup>a</sup>

Reference	$P_{\text{orb}}$ (days)	$P_{\text{spin}}$ (s)	$a_{\text{x}} \sin i$ (lt-s)	$\Phi_{\text{start}}$
This work	2.087 (fixed)	4.8026(4)	39.5(20)	0.199(4)
Bildsten et al. (1997)	2.087113936(7) <sup>b</sup>	4.8	39.6612(9)	-

<sup>a</sup> For definition of parameters, see text.

<sup>b</sup> At the time of 50506.788423(7) MJD.

## 4.3 Orbital-phase variability

In order to investigate the orbital-phase variability, we divided the 38.7 ks observation data into 78 pieces, each of which has a duration of 500 s. We denote the orbital intervals by  $\Phi_i$  ( $1 \leq i \leq 78$ ), which indicates the orbital phase at the middle of  $i$ -th orbital interval. Therefore, it is given by

$$\Phi_i = \Phi_{\text{start}} + \frac{500 \text{ s}}{P_{\text{orb}}} (i - 0.5), \quad (4.5)$$

where we used values listed in Table 4.1 for  $\Phi_{\text{start}}$  and  $P_{\text{orb}}$ . As the orbital-phase-resolved analysis, we first investigated the variability of pure count rates in multiple bands, that is, the light curve analysis. We then analyzed the energy spectrum extracted from each orbital interval. In both analyses, 18 out of 78 orbital intervals were excluded because of very short exposures of  $< 30$  s, and the remaining 60 orbital intervals are valid.

### 4.3.1 Energy-resolved light curve

The energy dependence of the orbital-phase variability can be examined by energy-resolved light curves. We divided the effective energy range of NuSTAR (3–78 keV) into four separate bands and generated light curves of these bands for the orbital intervals  $\Phi_1\text{--}\Phi_{78}$ . The left panel of Figure 4.1 shows light curves of 3–5 keV, 5–10 keV, 10–20

keV, and 20–78 keV as well as the summation of the four bands (3–78 keV). We can see that lower energy bands show more variations than higher energy bands. The typical variation degree of a light curve can be quantified by  $\sigma/\mu$ , where  $\sigma$  and  $\mu$  denote the standard deviation and average of the count rate, respectively. The  $\sigma/\mu$  value is 0.43 (10.5/24.5), 0.21 (17.7/83.6), 0.12 (6.62/54.8), and 0.09 (0.54/5.80) for 3–5 keV, 5–10 keV, 10–20 keV, and 20–78 keV light curve, respectively. The variation degree shows a monotonic decrease with the energy, which indicates that low-energy photons are more responsible for the count rate variability.

We employed another barometer to evaluate the count rate variation, that is, the hardness ratio. It is defined for two specific bands and calculated by dividing the count rate of the higher energy band by that of the lower energy band. The right panel of Figure 4.1 presents hardness ratio among 3–5 keV, 5–10 keV, 10–20 keV, and 20–78 keV, as a function of the total (3–78 keV) count rate. Except for the constant hardness ratio of 20–78 keV / 10–20 keV, all the hardness ratios show clear negative correlations with the total count rate. The nearly monotonic decreases of hardness ratios with the count rate indicate that the light curves of different energy bands are highly synchronized, with low energy bands more variable than high energy bands.

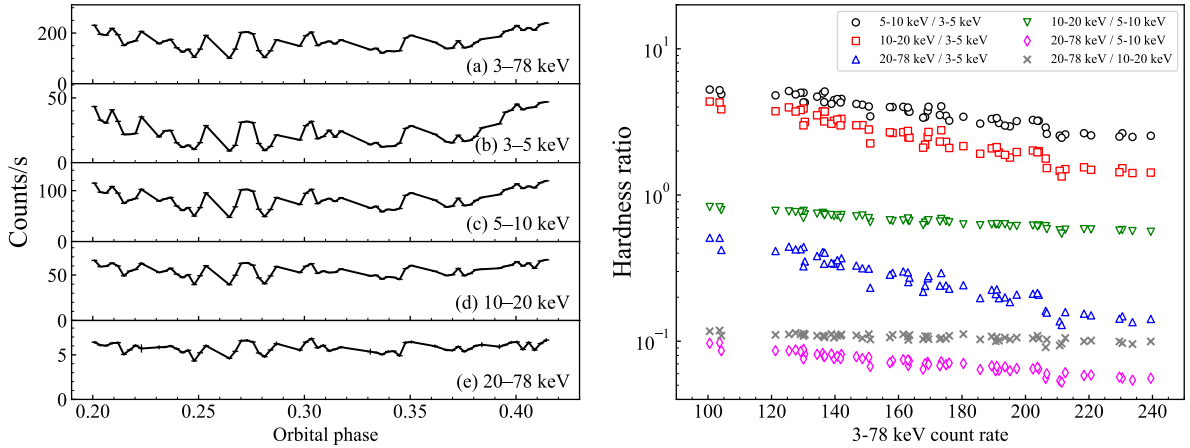


Figure 4.1: (left) Energy-resolved light curves of (a) 3–78 keV, (b) 3–5 keV, (c) 5–10 keV, (d) 10–20 keV, and (e) 20–78 keV. Each point corresponds to an orbital interval of 500 s. FPMA and FPMB counts are added. (right) Hardness ratios among different energy bands as a function of 3–78 keV count rate, calculated from energy-resolved light curves.

### 4.3.2 Spectral fitting on orbital-phase-resolved spectra

In order to quantify the orbital-phase spectral variability, we performed spectral fitting to the spectra extracted from the 60 valid orbital intervals. Here, we employed a phenomenological spectral model that can be applied to the resolved spectra. FPMA and

FPMB spectra were extracted separately and analyzed simultaneously by joint fitting.

The phase-averaged X-ray spectrum of Cen X-3 is roughly expressed by an absorbed power law with a quasi-exponential cut-off around  $\sim 15$  keV. Several additional components were reported, such as a soft excess described by a blackbody of  $\sim 0.1$  keV, three Fe emission lines in 6–7 keV, and the CRSF around 30 keV (Burderi et al., 2000; Naik et al., 2011; Tomar et al., 2021). For the continuum component, we adopted Fermi-Dirac cut-off power law (Tanaka, 1986), which is defined as

$$f_{\text{FDcut}}(E) = \frac{E^{-\Gamma}}{\exp\left(\frac{E-E_c}{E_f}\right) + 1}, \quad (4.6)$$

where  $E$ ,  $\Gamma$ ,  $E_c$ , and  $E_f$  represent the photon energy, the photon index, the cut-off energy, and the folding energy, respectively. The photoelectric absorption was reproduced by **phabs** model in **XSPEC**, which is expressed by

$$f_{\text{phabs}}(E) = \exp\left[-(N_{\text{H}}^{\text{IM}} + N_{\text{H}}) \sigma_{\text{abs}}(E)\right], \quad (4.7)$$

where  $N_{\text{H}}^{\text{IM}}$ ,  $N_{\text{H}}$ , and  $\sigma_{\text{abs}}(E)$  denote the hydrogen column density of the interstellar medium, that of the stellar wind, and the photoelectric cross section based on Verner et al. (1996), respectively. We employed a simplified model spectrum for the additional components because of the low statistics of each orbital-phase-resolved spectrum. The soft excess and CRSF were neglected, and three Fe emission lines were reduced to a single Gaussian line profile, which is

$$f_{\text{gauss}}(E) = \frac{I_{\text{Fe}}}{\sqrt{2\pi}\sigma_{\text{Fe}}} \exp\left[-\frac{(E - E_{\text{Fe}})^2}{2\sigma_{\text{Fe}}^2}\right], \quad (4.8)$$

where  $I_{\text{Fe}}$ ,  $E_{\text{Fe}}$ , and  $\sigma_{\text{Fe}}$  are the normalization factor, the central energy, and the line width of the Fe line. Therefore, the model spectrum as a whole can be written as

$$\frac{dN(E)}{dE} \propto f_{\text{phabs}} \times [f_{\text{FDcut}} + f_{\text{gauss}}]. \quad (4.9)$$

We carried out spectral fitting based on equation (4.9) applying several constraints on the parameters. The first one is  $N_{\text{H}}^{\text{IM}} = 1.1 \times 10^{22} \text{ cm}^{-2}$ , which is based on the galactic hydrogen column density towards the source (HI4PI Collaboration et al., 2016). The second constraint is  $\sigma_{\text{Fe}} = 0$  and  $E_{\text{Fe}} = 6.4$  keV, which come from the limited capability of NuSTAR to resolve the Fe emission lines. It is assumed that the neutral Fe emission line is dominant over the H-like or He-like Fe emission lines (e.g., Naik et al., 2011), and the line width is small compared to the energy resolution of NuSTAR. The energy range used for fitting is 4–78 keV, rather than the NuSTAR band 3–78 keV. We excluded 3–4 keV since this band could be affected by the soft excess component, which is generally described by a  $\sim 0.1$  keV blackbody (Burderi et al., 2000).

For the photon index, we tried two ways of analysis. We set  $\Gamma$  as a free parameter in one analysis and fixed it to  $\Gamma = 1.21$  in the other analysis. The fixed value of the photon index is chosen based on the phase-averaged analysis by Tomar et al. (2021). The latter case of analysis was carried out due to the strong parameter coupling between  $\Gamma$  and  $E_c$ , which may prevent us from yielding correct best-fit values of the photon index. The strong coupling between the two parameters demonstrated by MCMC (Markov Chain Monte Carlo) method is presented in Figure 4.2, where we picked up two orbital intervals with hardest ( $\Phi_{25}$ ) and softest ( $\Phi_{36}$ ) photon indices.

In Figure 4.3, we show the best-fit parameters at each orbital interval, derived from 4–78 keV spectral fitting. Two cases of analysis, free- and fixed-photon-index cases, are plotted by red and blue lines, respectively. The fitting results of the former analysis returned acceptable reduced chi-squares with an average value of 1.12. In the latter case of analysis, the average value of reduced chi-squares was 1.14, which is slightly worse than the free-photon-index case. As a result of fixing  $\Gamma$ , other parameters such as  $E_c$ ,  $E_f$ , and the equivalent width of the Fe line become much more robust to the orbital phase. Here, we do not rule out either case and define the former as Case 1 (free photon index) and the latter as Case 2 (fixed photon index).

In both of the cases,  $N_H$  shows the largest variability among the spectral parameters, as shown in Figure 4.3. It ranges from 0 to  $2.2 \times 10^{23} \text{ cm}^{-2}$  and from 0 to  $2.8 \times 10^{23} \text{ cm}^{-2}$  for Case 1 and 2, respectively. Figure 4.4 shows the relation between  $N_H$  and flux. In both of the analysis cases,  $N_H$  is negatively correlated with the absorbed flux (Figure 4.3a), while it has no significant correlation with the unabsorbed flux (Figure 4.3b). This result suggests that the flux variation is mainly caused by different degrees of absorption. The result is also consistent with the light curve analysis presented in Section 4.3.1 because the count rate of low energy photons is more likely affected by the absorption.

From the variability of the absorbed and unabsorbed flux, we can estimate the effect of stellar wind on the flux variability. Here, we evaluate the typical flux variation degree by the standard deviation divided by the average flux, calculated from the 60 orbital intervals. The variation degrees of the absorbed flux were 14.9% for both of the analysis cases. The variation degree of the unabsorbed flux was 10.3% and 8.6% for Case 1 and 2, respectively, which can be regarded as intrinsic variability of the source. Assuming the intrinsic and extrinsic variabilities are independent, the flux variation caused by stellar wind absorption is 10.8% and 12.2% for Case 1 and 2, respectively. Therefore, for the NuSTAR energy band, the effect of the stellar wind on the flux variability is comparable to the intrinsic variability.

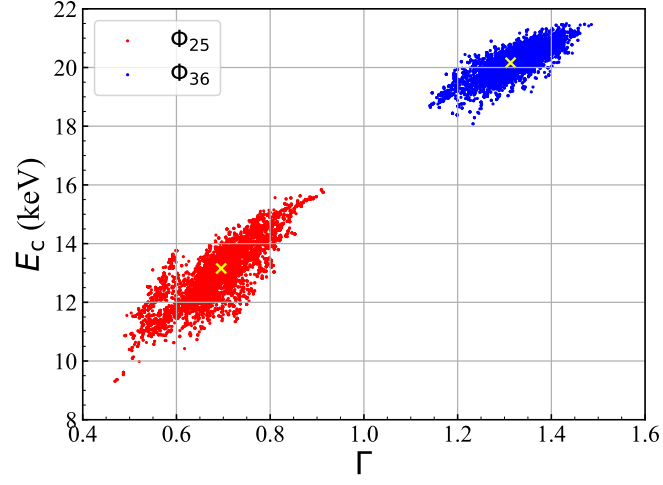


Figure 4.2: Parameter coupling between photon index ( $\Gamma$ ) and cut-off energy ( $E_c$ ) reproduced by 10000-step MCMC. The first 1000 steps were discarded beforehand as an initial burn-in phase. Red and blue plots represent orbital intervals with hardest ( $\Phi_{25}$ ) and softest ( $\Phi_{36}$ ) photon indices, respectively.

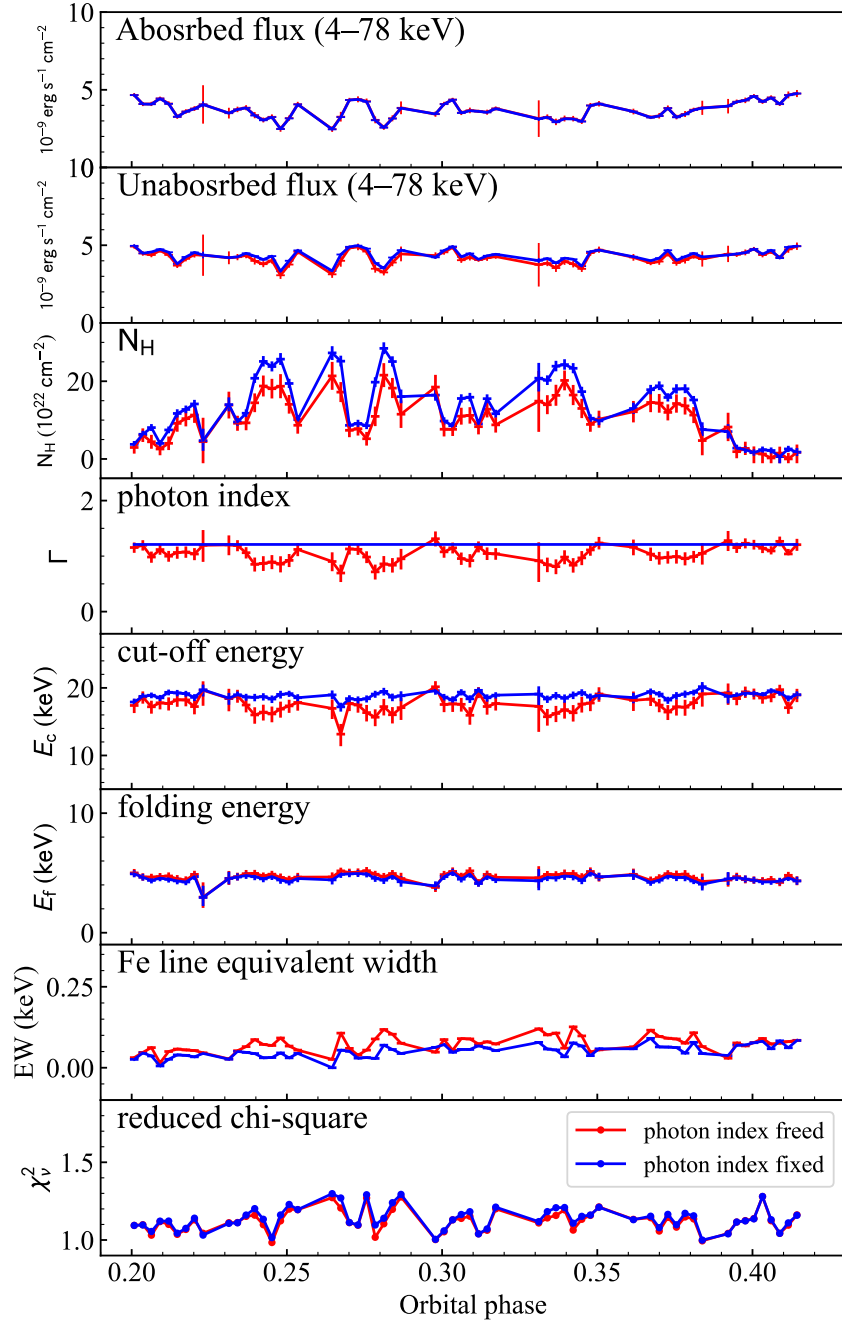


Figure 4.3: Orbital-phase variations of the best-fit spectral parameters derived from 4–78 keV orbital-phase-resolved spectra. The model expression is given in equation (4.9). Free- and fixed-photon-index cases of spectral analysis are plotted by red and blue lines, respectively. Error bars represent 90% confidence levels.



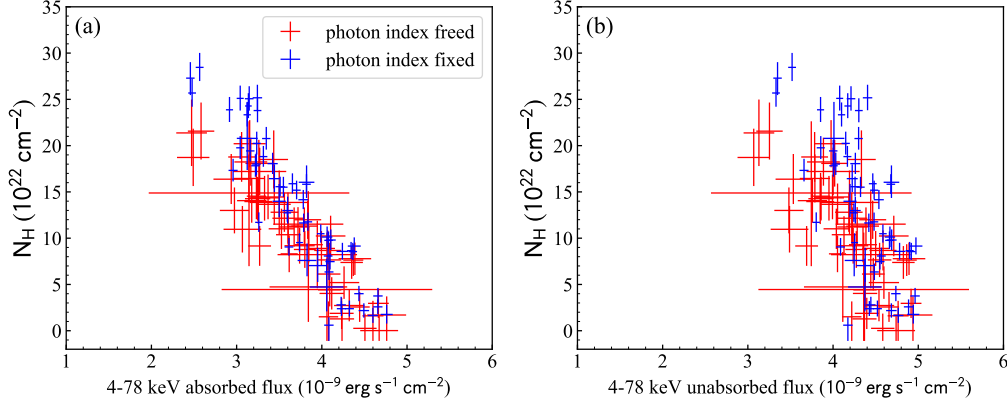


Figure 4.4: Relation between (a) 4–78 keV absorbed flux and  $N_{\text{H}}$ , (b) 4–78 keV unabsorbed flux and  $N_{\text{H}}$ , derived from the orbital-phase-resolved spectroscopy. Free- and fixed-photon-index cases of spectral analysis are plotted by red and blue lines, respectively. Error bars represent 90% confidence levels.

## 4.4 Spin-phase variability

In this section, we describe the spin-phase variability, which reflects the spectral variability within  $P_{\text{spin}} = 4.8026$  s (see Table 4.1). In order to quantify the short-term variability, we investigated energy-resolved pulse profiles and spin-phase-resolved spectra. We denote the spin phase as  $\phi$  ( $0.0 \leq \phi < 1.0$ ) so that we can distinguish it from the orbital phase  $\Phi$ .

### 4.4.1 Energy-resolved pulse profile

The spin-phase variability can be examined by pulse profiles. We divided the NuSTAR 3–78 keV band into 18 bands and generated energy-resolved pulse profiles by folding light curves with the spin period  $P_{\text{spin}}$ . The zero point of the spin phase was set so that  $\phi = 0.0$  at  $t_{\text{binary}} = 57360.0$  MJD. Figure 4.5 shows the 18 pulse profiles, and all of them show apparent pulsations with a gradual change of morphology as energy increases. As a fundamental trend, the pulsation gradually gets sharp, and the shape changes from double-peaked to single-peaked as energy increases. The same trend is already reported by Tomar et al. (2021).

In order to evaluate these trends qualitatively, we tried a more detailed analysis on the energy-resolved pulse profiles using Fourier transform. We calculated the rms pulse fraction  $\text{PF}_{\text{rms}}$  based on the Fourier coefficients. It is defined by

$$\text{PF}_{\text{rms}} = \frac{2\sqrt{\sum_{k=1}^{k_{\text{max}}} ((a_k^2 + b_k^2) - (\sigma_{a_k}^2 + \sigma_{b_k}^2))}}{a_0}, \quad (4.10)$$

where  $a_k$  and  $b_k$  are Fourier coefficients written by

$$\begin{aligned} a_k &= \frac{1}{N} \sum_{j=1}^N p_j \cos\left(\frac{2\pi k j}{N}\right), \\ b_k &= \frac{1}{N} \sum_{j=1}^N p_j \sin\left(\frac{2\pi k j}{N}\right), \end{aligned} \quad (4.11)$$

and  $\sigma_{a_k}^2$  and  $\sigma_{b_k}^2$  are defined by

$$\begin{aligned} \sigma_{a_k}^2 &= \frac{1}{N^2} \sum_{j=1}^N \sigma_{p_j}^2 \cos^2\left(\frac{2\pi k j}{N}\right), \\ \sigma_{b_k}^2 &= \frac{1}{N^2} \sum_{j=1}^N \sigma_{p_j}^2 \sin^2\left(\frac{2\pi k j}{N}\right). \end{aligned} \quad (4.12)$$

$N$ ,  $p_j$ , and  $\sigma_{p_j}$  denote the number of bins, the photon count rate at the  $j$ -th bin, and the Poisson variance at the  $j$ -th bin, respectively. The contribution of the  $k$ -th Fourier component can be calculated by

$$c_k = \sqrt{a_k^2 + b_k^2}. \quad (4.13)$$

The definition of  $\text{PF}_{\text{rms}}$  includes the correction terms described by  $\sigma_{a_k}$  and  $\sigma_{b_k}$ . It leads to a robust and accurate quantification of a pulse profile even with a noisy data set (see An et al., 2015). The detailed derivation of the equations is presented in Tendulkar et al. (2015), and Appendix 1 of An et al. (2015).

We applied the above analysis on each energy-resolved pulse profile, setting the number of bins to  $N = 64$ . Figure 4.6 presents the results of the detailed Fourier analysis. The increase in the sharpness of pulse profiles with energy was quantified by the calculation of the pulse fractions presented in Figure 4.6(a). The pulse fraction monotonically increases with the energy in the range of 3–45 keV, with two exceptional bands. They are 6–7 keV and 25–30 keV, which correspond to the Fe emission line band ( $\sim 6.4$  keV) and CRSF band ( $\sim 27$  keV), respectively. Figure 4.6(b) shows the contributions of the 1st and 2nd Fourier components compared to the 0-th (phase-averaged) Fourier component. The 1st and 2nd Fourier coefficients are comparable at lower energy bands, while the 1st Fourier component gets dominant over the 2nd as energy goes up. This is consistent with the single-peaked pulse profiles at higher energy bands. Therefore, qualitative trends seen in pulse profiles were quantified by analyzing the pulse fraction and Fourier coefficients as a function of energy.

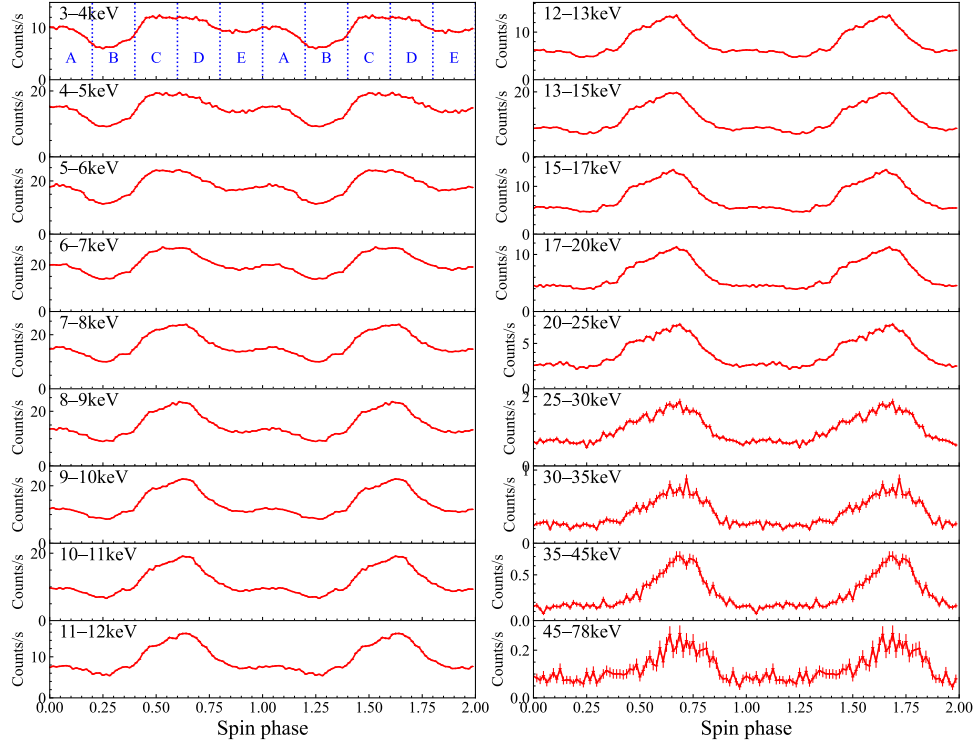


Figure 4.5: Energy-resolved pulse profiles generated for 18 energy bands. The summation of FPMA and FPMB counts are plotted. The definitions of spin phase A–E are presented as well.

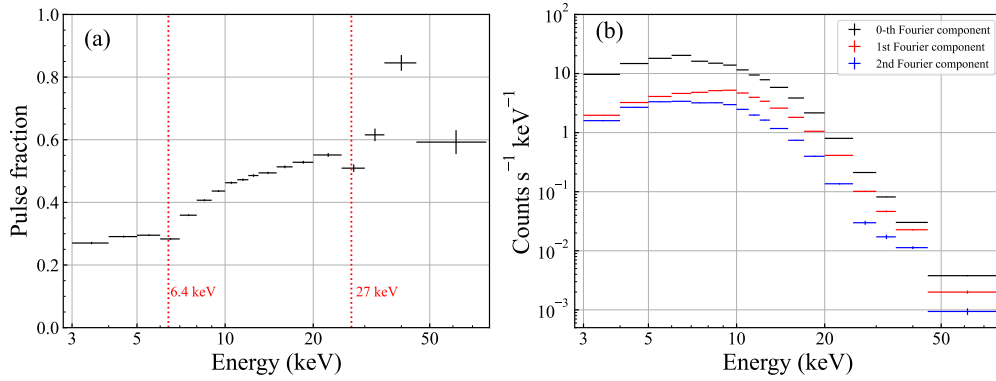


Figure 4.6: (a) Pulse fraction  $PF_{\text{rms}}$  as a function of energy, calculated using equation (4.10). The energies corresponding the Fe emission line and CRSF are presented by red dotted lines. (b) Contribution of the 1st (red) and 2nd (blue) Fourier components as a function of energy, compared to the 0-th (phase-averaged, black) Fourier component (see equations 4.11 and 4.13).

### 4.4.2 Ratio spectrum

In order to track more detailed energy dependence of the spin-phase variability, we employed “ratio spectrum” as an indicator to evaluate it. This barometer is used in Kondo et al. (2021), which presents a spin-phase-resolved analysis of Her X-1. We denote  $S(E; \phi_1, \phi_2)$  as the count spectrum of a spin-phase interval ranging from  $\phi_1$  to  $\phi_2$ . We also define  $S_{\text{ave}}(E) = S(E; 0.0, 1.0)$  as the phase-averaged spectrum. The ratio spectrum can be expressed as a ratio between these two spectra,

$$R(E; \phi_1, \phi_2) = \frac{S(E; \phi_1, \phi_2)}{S_{\text{ave}}(E)}. \quad (4.14)$$

If the source emission were completely stable along the spin phase, the ratio spectrum would equal unity, namely,  $R(E; \phi_1, \phi_2) = 1$ . The ratio spectrum was calculated after the FPMA and FPMB spectra were added.

We divided the whole spin phase into five intervals and investigated the spin-phase variability. Hereafter in this chapter, we denote five spin-phase intervals as phase A ( $\phi = 0.0\text{--}0.2$ ), B ( $\phi = 0.2\text{--}0.4$ ), C ( $\phi = 0.4\text{--}0.6$ ), D ( $\phi = 0.6\text{--}0.8$ ), and E ( $\phi = 0.8\text{--}1.0$ ). These definitions are also presented in the 3–4 keV pulse profile of Figure 4.5. The spin phase D corresponds to the pulse maximum and B to the minimum, as seen from Figure 4.5. Figure 4.7(a) shows the five spin-phase-resolved spectra, and Figure 4.7(b) presents the ratio spectra of the five spin-phase intervals. The ratio spectra show more significant variability in higher energy bands, suggesting the spectrum gets harder at high-flux phases. Besides the variability of the continuum, the energy bands corresponding to emission and absorption lines appear to show characteristic features in the ratio spectra. The count ratios around the Fe emission line ( $\sim 6.4$  keV) and CRSF ( $\sim 27$  keV), presented by red dotted lines in Figure 4.7(b), get close to unity compared to the nearby bands.

We also generated ratio spectra with finer spin-phase intervals. Figure 4.7(c) presents the scatter plot of 20 ratio spectra, each of which covers a spin-phase interval of  $\Delta\phi = 0.05$ . The higher variability in higher energy bands and lower variabilities around Fe line and CRSF bands, seen in Figure 4.7(b), still hold even when the spin-phase division becomes finer. These results are consistent with the energy-resolved pulse profile analysis (Section 4.4.1) because the pulse fraction gets higher at the high-energy bands and has dented features around the Fe line and CRSF energies.

### 4.4.3 Spectral fitting on spin-phase-resolved spectra

We have examined the qualitative features of spin-phase variability through energy-resolved pulse profiles (Section 4.4.1) and ratio spectra (Section 4.4.2). It has been revealed that the spectrum has a harder photon index at high-flux phases and softer at low-flux phases, as well as characteristic features around the Fe emission line and CRSF

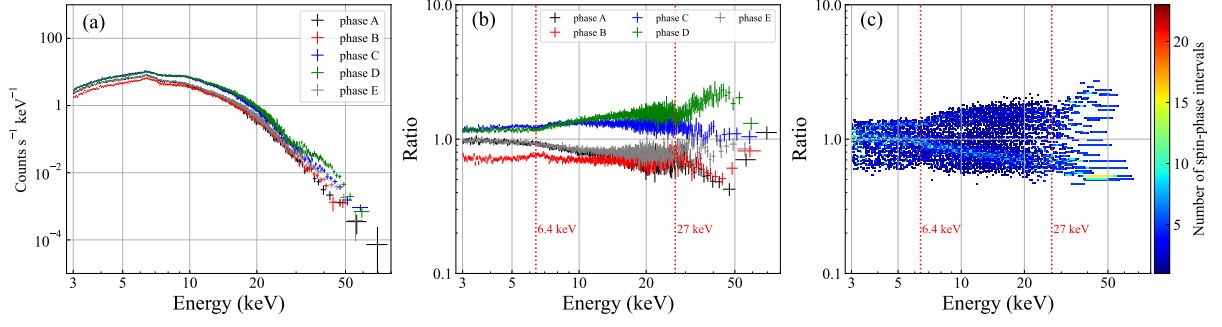


Figure 4.7: (a) Spin-phase-resolved spectra of FPMA at spin phase interval A (black), B (red), C (blue), D (green), and E (gray). (b) Ratio spectra of spin-phase intervals A–E. (c) Scatter plot of 20 ratio spectra, each covering a spin-phase interval of  $\Delta\phi = 0.05$ . The color bar represents the number of ratio spectra that have a specific value at each energy. The energies corresponding to the Fe emission line and the CRSF are shown by dotted red lines.

bands. In order to examine these properties more quantitatively, we performed spectral fitting to the spin-phase-resolved spectra. We utilized the spin-phase intervals A–E defined in Section 4.4.2 and tracked the variations of spectral parameters along the spin phase.

The spectral model we adopted here is the same as that of orbital-phase-resolved analysis (equation 4.9), but we added a Gaussian absorption line component (**gabs** in XSPEC) to investigate the variability of the CRSF. Therefore, the spectral model can be expressed as

$$\frac{dN(E)}{dE} \propto f_{\text{phabs}} \times (f_{\text{FDCut}} + f_{\text{gauss}}) \times f_{\text{gabs}}, \quad (4.15)$$

where  $f_{\text{gabs}}$  denotes the absorption line feature and is expressed by

$$f_{\text{gabs}}(E) = \exp \left\{ -\tau_{\text{cyc}} \exp \left[ -\frac{(E - E_{\text{cyc}})^2}{2\sigma_{\text{cyc}}^2} \right] \right\}. \quad (4.16)$$

$f_{\text{FDCut}}$ ,  $f_{\text{phabs}}$ , and  $f_{\text{gauss}}$  are defined in equations (4.6), (4.7), and (4.8), respectively.  $\tau_{\text{cyc}}$ ,  $E_{\text{cyc}}$ ,  $\sigma_{\text{cyc}}$  are parameters determining the CRSF structure, representing the optical depth at the line center, the central energy, and the line width, respectively. All of the parameters were set free except that  $N_{\text{H}}^{\text{IM}} = 1.1 \times 10^{22} \text{ cm}^{-2}$  (HI4PI Collaboration et al., 2016) and  $N_{\text{H}} = 3.74 \times 10^{22} \text{ cm}^{-2}$ . The latter constraint is based on the average  $N_{\text{H}}$  calculated by the orbital-phase-resolved spectroscopy with a fixed photon index (see Section 4.3.2). We set a common  $N_{\text{H}}$  over the whole spin phase because we assume the absorption by stellar wind or surrounding matters is independent of the spin phase. The parameters regarding the Fe emission line are set free owing to the rich photon counts of each spectrum, which were fixed in the orbital-phase-resolved spectroscopy. FPMA and FPMB spectra were

analyzed simultaneously by joint fitting, setting a cross-normalization factor as another fitting parameter. The valid energy range for the fitting is 4–78 keV, the same as the orbital-phase-resolved spectroscopy.

Figure 4.8 shows the fitting results of the five spectra, corresponding to the spin-phase intervals A–E, respectively. The residuals have no distinct structures, and the CRSFs are well reproduced in all the five spectra. The best-fit parameters are presented in Table 4.2. All the five spectra returned acceptable  $\chi^2_\nu$  values of 1.09–1.30. The table shows variations of spectral parameters along the spin phase, especially differences between the pulse maximum (phase D) and the pulse minimum (phase B). We picked up several spectral parameters and investigated their correlations with the continuum flux. The flux dependence of  $\Gamma$ ,  $I_{\text{Fe}}$ ,  $\text{Eqw}_{\text{Fe}}$ ,  $E_{\text{cyc}}$ ,  $\sigma_{\text{cyc}}$ , and  $\tau_{\text{cyc}}$  are shown in Figure 4.9.

The photon index  $\Gamma$  is an important parameter that measures the spectral hardening due to Comptonization inside the accretion column. Because the cut-off energy  $E_c$  and folding energy  $E_f$  do not show any significant variation along the spin phase,  $\Gamma$  is the only parameter that is responsible for the change of the spectral shape. Referring to Figure 4.9(a), one can see the parameter varies from 0.72 to 1.16 and has a clear negative correlation with the continuum flux. The harder spectra at the high-flux phases (phase C, D) and softer ones at the low-flux phases (phase A, B, E) are consistent with qualitative trends of pulse profiles (Section 4.4.1) and ratio spectra (Section 4.4.2), both of which suggested more significant variability in higher energy bands.

The Fe emission line shows a distinct variability along the spin phase. As can be seen in Figure 4.9(b) and (c), both the intensity and equivalent width are negatively correlated with the continuum flux. This feature is also seen in the pulse profiles and ratio spectra as low variability around  $\sim 6.4$  keV. At the pulse maximum, the intensity and equivalent width of the Fe line reach  $\sim 60\%$  and  $\sim 35\%$  of the pulse minimum, respectively. This is strong evidence that the Fe line originates from different emission regions from the pulsed continuum. The natural candidate for the origin of the Fe line is the reprocessing by surrounding materials, such as accretion stream, accretion disk, and stellar wind.

The CRSF also presents interesting variability along the spin phase, as shown in Figure 4.9(d), (e), and (f). The high-flux phases (C, D) have significantly higher central energy  $E_{\text{cyc}}$  and larger line width  $\sigma_{\text{cyc}}$  than the low-flux phases (A, B, E). The variation degrees of  $E_{\text{cyc}}$  and  $\sigma_{\text{cyc}}$  are  $\sim 10\%$  and  $\sim 25\%$ , respectively. The optical depth  $\tau_{\text{cyc}}$ , on the other hand, does not show significant variation along the spin phase because of large uncertainties. However, its positive correlation with the continuum flux can be suggested by the pulse fraction (Figure 4.6a) and ratio spectra (Figure 4.7), because both of them show low variations around the CRSF band. These results are evidence for the existence of a stronger magnetic field and deeper optical depth in the direction of the magnetic pole, if we naturally assume that the magnetic pole is on the line of sight at the timing of the pulse maximum.

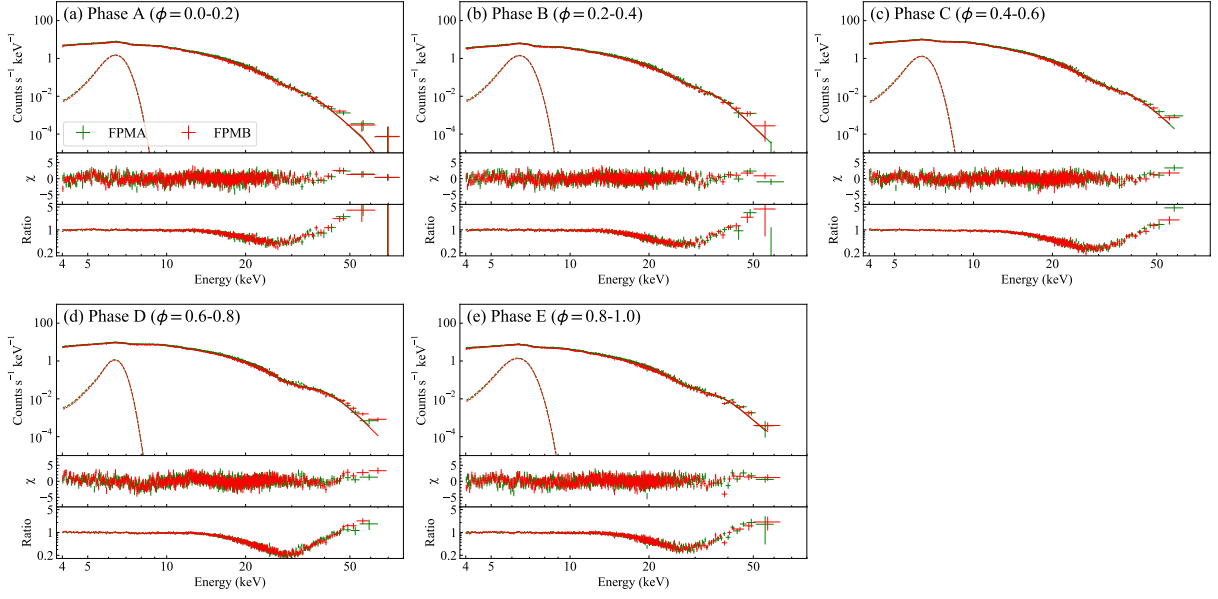


Figure 4.8: 4–78 keV fitting results of spin-phase-resolved spectra. The model expression is given by equation (4.15). The contributions of emission lines are plotted by dashed lines. The middle panels show residuals between the data and model. The bottom panels show the contributions of the CRSF by plotting ratios between data and model without CRSF.

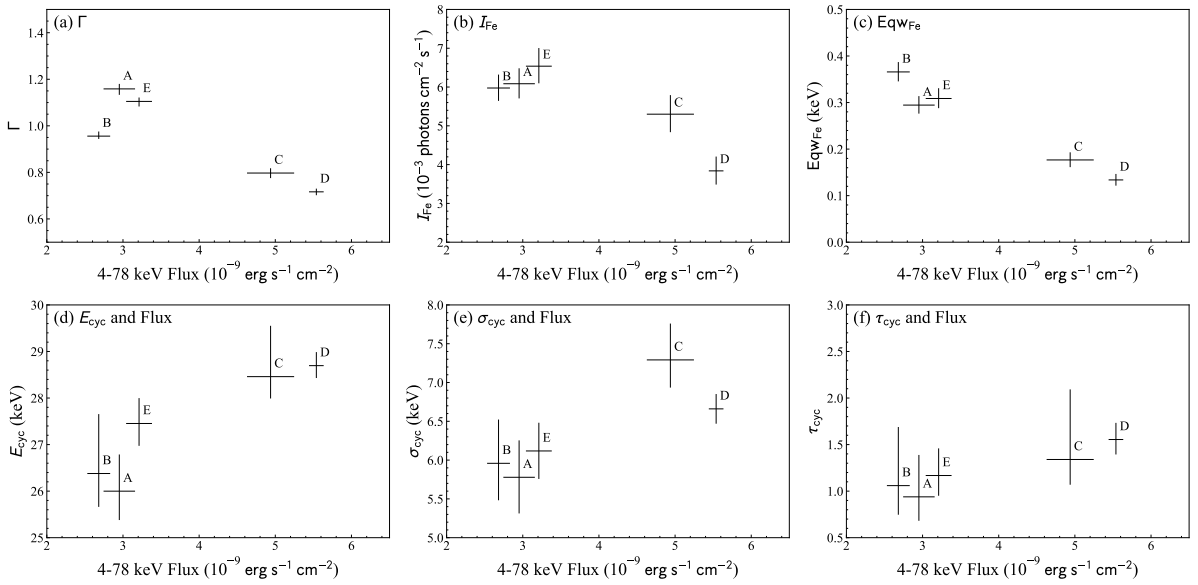


Figure 4.9: Spin-phase variations of spectral parameters as a function of 4–78 keV continuum flux, derived from spin-phase-resolved spectroscopy. Error bars denote 90% confidence levels.

Table 4.2: Best-fit parameters derived from spin-phase-resolved spectroscopy.<sup>a</sup>

Parameter <sup>b</sup>	phase A ( $\phi = 0.0\text{--}0.2$ )	phase B ( $\phi = 0.2\text{--}0.4$ )	phase C ( $\phi = 0.4\text{--}0.6$ )	phase D ( $\phi = 0.6\text{--}0.8$ )	phase E ( $\phi = 0.8\text{--}1.0$ )
$N_{\text{H}}^{\text{IM}}$ ( $10^{22} \text{ cm}^{-2}$ )			1.1 (fixed)		
$N_{\text{H}}$ ( $10^{22} \text{ cm}^{-2}$ )			3.74 (fixed)		
$\Gamma$	$1.16^{+0.02}_{-0.03}$	$0.96^{+0.02}_{-0.01}$	$0.80 \pm 0.02$	$0.72 \pm 0.01$	$1.10 \pm 0.02$
$E_c$ (keV)	$24^{+3}_{-2}$	$25^{+4}_{-2}$	$24^{+5}_{-2}$	$27 \pm 1$	$26 \pm 2$
$E_f$ (keV)	$4.4^{+0.4}_{-0.7}$	$4.1^{+0.5}_{-0.8}$	$4.9^{+0.4}_{-1.0}$	$5.1^{+0.3}_{-0.3}$	$5.0^{+0.4}_{-0.5}$
$E_{\text{Fe}}$ (keV)	$6.39^{+0.02}_{-0.03}$	$6.42 \pm 0.02$	$6.35 \pm 0.04$	$6.36 \pm 0.03$	$6.33 \pm 0.03$
$\sigma_{\text{Fe}}$ (keV)	$0.42 \pm 0.03$	$0.44 \pm 0.03$	$0.41^{+0.05}_{-0.04}$	$0.32 \pm 0.04$	$0.49 \pm 0.04$
$I_{\text{Fe}}$ ( $10^{-3}$ photons $\text{cm}^{-2} \text{ s}^{-1}$ )	$6.1 \pm 0.4$	$6.0 \pm 0.3$	$5.3 \pm 0.5$	$3.8 \pm 0.4$	$6.5^{+0.5}_{-0.4}$
$\text{Eqw}_{\text{Fe}}^c$ (keV)	$0.29 \pm 0.02$	$0.37 \pm 0.02$	$0.18 \pm 0.02$	$0.13 \pm 0.01$	$0.31 \pm 0.02$
$E_{\text{cyc}}$ (keV)	$26.0^{+0.8}_{-0.6}$	$26.4^{+1.3}_{-0.7}$	$28.5^{+1.1}_{-0.5}$	$28.7 \pm 0.3$	$27.5 \pm 0.5$
$\sigma_{\text{cyc}}$ (keV)	$5.8 \pm 0.5$	$6.0^{+0.6}_{-0.5}$	$7.3^{+0.5}_{-0.4}$	$6.7 \pm 0.2$	$6.1 \pm 0.4$
$\tau_{\text{cyc}}$	$0.9^{+0.5}_{-0.3}$	$1.1^{+0.6}_{-0.3}$	$1.3^{+0.8}_{-0.3}$	$1.6 \pm 0.2$	$1.2^{+0.3}_{-0.2}$
Flux <sup>d</sup> ( $10^{-9} \text{ erg s}^{-1} \text{ cm}^{-2}$ )	$3.0 \pm 0.2$	$2.7 \pm 0.2$	$4.9 \pm 0.3$	$5.5 \pm 0.1$	$3.2 \pm 0.2$
$\chi^2_{\nu}$ (d.o.f.)	1.15 (1000)	1.07 (1001)	1.09 (1117)	1.30 (1173)	1.16 (1033)

<sup>a</sup> Errors denote 90% confidence levels.

<sup>b</sup> For the definitions of the parameters, see equations (4.6), (4.7), (4.8), (4.15), and (4.16).

<sup>c</sup> The equivalent width of the Fe line.

<sup>d</sup> 4–78 keV absorbed flux.



## 4.5 Doubly-phase-resolved analysis

In Sections 4.3 and 4.4, we have investigated the orbital- and spin-phase variability, respectively. In this section, we examine the orbital- and spin-phase variabilities simultaneously. This analysis was carried out to support the validity of the orbital- and spin-phase-resolved analysis by showing that these two variabilities do not affect each other. We examined the relation between these two ways of variabilities through light curves and pulse profiles for multiple energy bands. Since the light curve represents the orbital-phase variability, we resolved it by the spin phase to see both orbital- and spin-phase variability. Similarly, as the pulse profile represents the spin-phase variability, we resolved it by the orbital phase.

### 4.5.1 Energy- and spin-phase-resolved light curve

We first generated light curves resolved by both energy and the spin phase to examine the dependency of orbital-phase variability on the spin phase. For the energy axis, the NuSTAR coverage of 3–78 keV band is divided into four energy bands, which are 3–5 keV, 5–10 keV, 10–20 keV, and 20–78 keV. For the spin-phase axis, we employed the spin-phase intervals A–E defined in Section 4.4.2 and divided the whole spin phase into five intervals. The comparison among light curves of different spin phases was carried out by “normalized light curve”, which we defined by

$$L_{\text{norm}}(\Phi; E_i, \phi_j) = \frac{L(\Phi; E_i, \phi_j)}{\frac{1}{T} \int_{\Phi} L(\Phi; E_i, \phi_j) d\Phi}, \quad (4.17)$$

where  $L(\Phi; E_i, \phi_j)$  denotes the light curve function at the energy band  $E_i$  and spin phase  $\phi_j$ , and  $T$  is the net exposure time. By normalizing each light curve with its average value over the orbital phase, one can compare the spin-phase deviation of light curves at each orbital phase.

Figure 4.10 shows the normalized light curves for different energy bands and spin phases. The differences among spin-phase-resolved light curves can be evaluated from it. For every energy band, the spin-phase deviations of light curves appear small, and five light curves track almost the same trajectories. One can evaluate spin-phase variation of light curves at a given orbital phase  $\Phi_i$  and energy band  $E_j$  by

$$\Delta L_{\text{norm}}(\Phi_i; E_j) = \frac{\max_{\phi \in A-E} |L_{\text{norm}}(\Phi_i; E_j, \phi) - L_{\text{norm,ave}}(\Phi_i; E_j)|}{L_{\text{norm,ave}}(\Phi_i; E_j)}, \quad (4.18)$$

where

$$L_{\text{norm,ave}}(\Phi_i; E_j) = \frac{1}{5} \sum_{\phi \in A-E} L_{\text{norm}}(\Phi_i; E_j, \phi). \quad (4.19)$$

The average of  $\Delta L_{\text{norm}}$  is 6.1%, 7.9%, 6.2%, 7.2%, and 10.8% for 3–78 keV, 3–5 keV, 5–10 keV, 10–20 keV, and 20–78 keV, respectively. Therefore, we can conclude that the

light curves of different spin phases track very similar variability with variation rates of  $\lesssim 10\%$ . The 24th orbital interval ( $\Phi_{24} = 0.265$ , red dashed line in Figure 4.10) might be an exceptional orbital phase. It has the most prominent  $\Delta L_{\text{norm}}$  in all the energy bands, which means it is an orbital phase with the most spin-phase variation. At this orbital phase,  $\Delta L_{\text{norm}}$  is 25%, 25%, 27%, 26%, and 36% for 3–78 keV, 3–5 keV, 5–10 keV, 10–20 keV, and 20–78 keV, respectively. Despite the extremely high variability along the spin phase, the orbital-phase-resolved spectrum of this interval does not show any characteristic features compared to those of other orbital intervals.

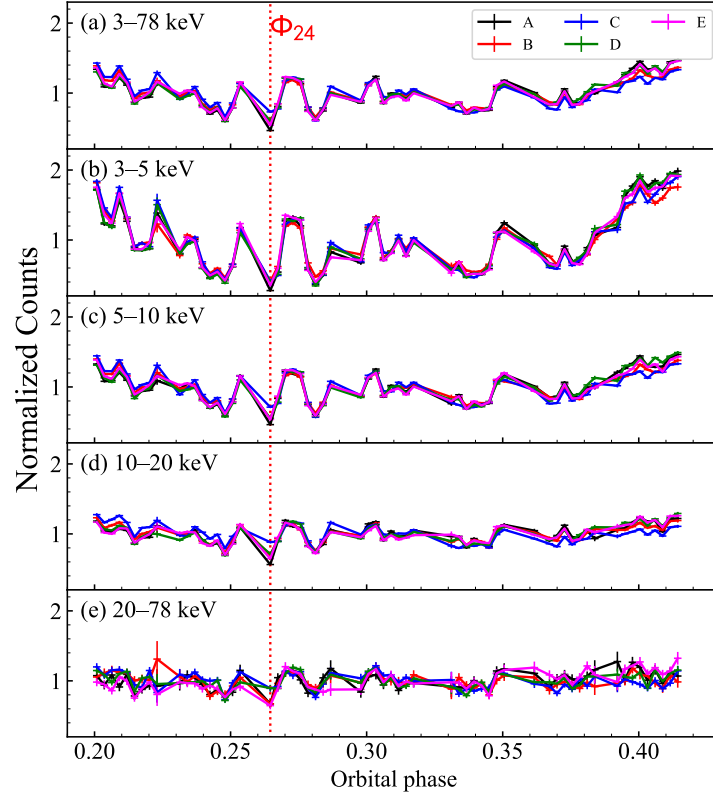


Figure 4.10: Normalized light curves ( $L_{\text{norm}}$ ) resolved by energy and spin phase. Each panel corresponds to a specific energy band, and different colors represent different spin phase intervals. The orbital phase with the most light curve variation is represented by the red dotted line.

#### 4.5.2 Energy- and orbital-phase-resolved pulse profile

Similar to Section 4.5.1, one can investigate the dependency of the spin-phase variability on the orbital phase by analyzing orbital-phase-resolved pulse profiles. We generated pulse profiles resolved by different energy bands and orbital phases. For the energy axis, we adopted the same division as the light curve analysis, which is 3–5 keV, 5–10 keV, 10–20 keV, and 20–78 keV. For the orbital-phase axis, we utilized the same orbital intervals as

used in Section 4.3, defined by  $\Phi_i$  ( $1 \leq i \leq 78$ ). The evaluation of the variability of pulse profiles can be performed through the Fourier transform. We employed four barometers that characterize the shape of pulse profiles. One of them is the rms pulse fraction  $\text{PF}_{\text{rms}}$ , defined by equation (4.10). The other three barometers are the ratio among Fourier coefficients (equation 4.13), composed of 1st to 0-th ( $c_1/c_0$ ), 2nd to 0-th ( $c_2/c_0$ ), and 2nd to 1st ( $c_2/c_1$ ).

Figure 4.11 presents the orbital-phase variability of the four parameters,  $\text{PF}_{\text{rms}}$ ,  $c_1/c_0$ ,  $c_2/c_0$ , and  $c_2/c_1$  for the four energy bands. Statistical parameters that denote orbital-phase variability, such as the average value (mean), standard deviation ( $\sigma$ ), variation degree ( $\sigma/\text{mean}$ ), and reduced chi-square value with respect to the best-fit constant model, are shown in Table 4.3. Referring to the variation degrees and reduced chi-square values, there were significant variations in  $\text{PF}_{\text{rms}}$ ,  $c_1/c_0$ ,  $c_2/c_0$ , while we did not detect significant variations in  $c_2/c_1$ . The variation degrees of the 1st and 2nd Fourier components are comparable at all the energy bands. The variation degree of the  $\text{PF}_{\text{rms}}$  above 5 keV is roughly  $\sim 10\%$ , which is consistent with the average light curve variability of 5–10% along the spin phase derived in Section 4.5.1. For 3–5 keV, the variation degrees are  $\sim 20\%$ , which is significantly larger than the other bands. From these results, we conclude that the pulse profiles are highly stable along the orbital phase with variation degrees of 10% for  $> 5$  keV and  $\sim 20\%$  for 3–5 keV.  $\Phi_{24}$  (red dashed line in Figure 4.11) might be an exception because it shows extremely high pulse fractions compared to other orbital intervals, which is consistent with the spin-phase-resolved light curve analysis (Section 4.5.1).

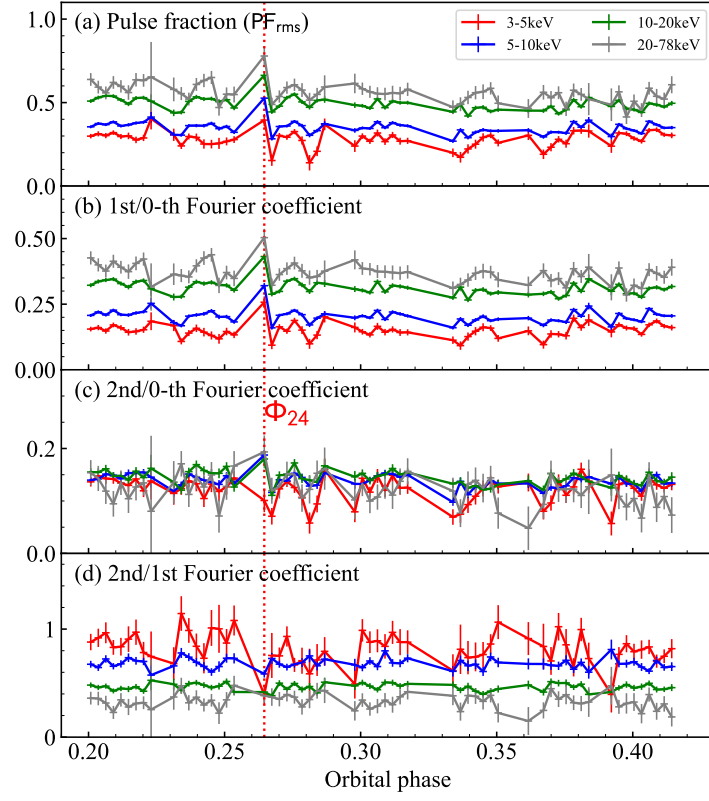


Figure 4.11: Parameters of energy and orbital-phase-resolved pulse profiles. Each panel denotes (a) Pulse fraction ( $PF_{rms}$ ), (b) ratio of 1st/0th Fourier coefficient ( $c_1/c_0$ ), (c) 2nd/0th ( $c_2/c_0$ ), and (d) 2nd/1st ( $c_2/c_1$ ), respectively. Different colors represent different energy bands. The orbital phase with the most pulse fraction ( $\Phi_{24}$ ) is plotted by the red dotted line.

Table 4.3: Statistical parameters that characterize orbital-phase variability of pulse profiles.

	band	mean	$\sigma^a$	$\sigma/\text{mean}$	$\chi_\nu^2{}^b$
$\text{PF}_{\text{rms}}$	3–5 keV	$0.281 \pm 0.003$	$0.050 \pm 0.002$	$0.179 \pm 0.008$	3.66
	5–10 keV	$0.351 \pm 0.001$	$0.038 \pm 0.0009$	$0.108 \pm 0.003$	10.85
	10–20 keV	$0.492 \pm 0.002$	$0.039 \pm 0.003$	$0.079 \pm 0.005$	8.89
	20–78 keV	$0.559 \pm 0.007$	$0.059 \pm 0.030$	$0.106 \pm 0.06$	1.72
$c_1/c_0$	3–5 keV	$0.150 \pm 0.002$	$0.028 \pm 0.0004$	$0.186 \pm 0.003$	3.46
	5–10 keV	$0.204 \pm 0.001$	$0.025 \pm 0.0002$	$0.122 \pm 0.001$	9.63
	10–20 keV	$0.313 \pm 0.001$	$0.026 \pm 0.0007$	$0.083 \pm 0.002$	8.27
	20–78 keV	$0.369 \pm 0.004$	$0.037 \pm 0.006$	$0.102 \pm 0.02$	1.77
$c_2/c_0$	3–5 keV	$0.121 \pm 0.002$	$0.024 \pm 0.0003$	$0.197 \pm 0.004$	2.60
	5–10 keV	$0.138 \pm 0.001$	$0.014 \pm 0.0002$	$0.098 \pm 0.001$	3.61
	10–20 keV	$0.145 \pm 0.001$	$0.014 \pm 0.0003$	$0.098 \pm 0.002$	2.81
	20–78 keV	$0.122 \pm 0.004$	$0.028 \pm 0.001$	$0.233 \pm 0.01$	0.98
$c_2/c_1$	3–5 keV	$0.819 \pm 0.02$	$0.149 \pm 0.2$	$0.18 \pm 0.2$	1.59
	5–10 keV	$0.681 \pm 0.006$	$0.048 \pm 0.04$	$0.071 \pm 0.06$	1.25
	10–20 keV	$0.463 \pm 0.004$	$0.034 \pm 0.01$	$0.073 \pm 0.03$	1.27
	20–78 keV	$0.331 \pm 0.01$	$0.071 \pm 0.03$	$0.215 \pm 0.09$	0.72

<sup>a</sup> Standard deviation of the parameter.

<sup>b</sup> Reduced chi-square when fitted with a constant model.

## 4.6 Summary

In this chapter, we investigated the orbital- and spin-phase variabilities of Cen X-3 by analyzing 38.7 ks NuSTAR observation data. The orbital-phase variability is caused by the mixture of two comparable effects: the intrinsic flux variability of  $\sim 10\%$  and the obscuration by an inhomogeneous stellar wind. The spin-phase variability is characterized by the change in the photon index, ranging from 0.72 to 1.16. The spectrum gets harder at the bright spin phases and softer at the dark phases. The Fe emission line and CRSF also exhibit spin-phase variabilities. The equivalent width and intensity of the Fe line negatively correlate with the continuum flux, suggesting the Fe line comes from non-pulsed distant regions from the neutron star. The central energy of the CRSF varies by  $\sim 10\%$  along the spin phase, displaying an enhancement at the pulse maximum. We also found that the pulse profiles are highly stable along the orbital phase within a variation degree of  $\sim 20\%$ , which gives evidence of a highly stable accretion flow of the binary system. Since the observation data analyzed here only covers  $\sim 20\%$  of the whole orbit, we performed an observation covering a longer duration. We perform the same time-

resolved analysis on the observation data in the next chapter.

## Chapter 5

# Broadband X-ray variability of Cen X-3 studied with long-time NuSTAR observation

In Chapter 4, we described the orbital- and spin-phase variabilities of the disk-fed X-ray pulsar Cen X-3 derived from 39 ks ( $\Delta\Phi = 0.215$ ) NuSTAR observation data. The orbital-phase variability was caused by different absorption degrees of inhomogeneous stellar wind and the intrinsic variability of the neutron star, both of which contribute by a factor of  $\sim 10\%$ . However, long-term observations over tens of years have revealed that Cen X-3 shows large variability in luminosity, spectral shape, and pulse fraction, which suggests the emission from the source is far from stable. For example, according to the nine-year observations conducted by the All-Sky Monitor (ASM) onboard RXTE, the soft X-ray flux of Cen X-3 varies by a factor of  $\sim 40$  (Paul et al., 2005). The observations by Proportional Counter Array (PCA) onboard RXTE revealed that the pulse fraction of Cen X-3 varies over time and appears to correlate with the continuum flux (Raichur & Paul, 2008b). Therefore, the flux variability and the spin-phase modulation could have some correlation in terms of a long-time observation. The physical conditions surrounding the neutron star are much more complicated than the mere photo-electric absorption by the stellar wind.

In order to nail down the physical conditions and emission mechanism through the spectral variability of the source, it is necessary to conduct a long and continuous observation. For a binary system, an observation over multiple orbital cycles is potent because it can examine spectral variability between two adjacent orbits. In order to meet such demands, we proposed a NuSTAR observation of Cen X-3 over two orbital cycles with a continuous observation time (PI: Tamba). The broad coverage of energy bands ranging from the soft to hard X-rays realized by NuSTAR will allow us to establish a physical interpretation of the spectral variability of the object. The proposal was accepted by

NuSTAR, and Cen X-3 was observed as an AO7 observation target in 2022 January. In this chapter, we describe the analysis results of the long-time observation data of NuSTAR, focusing on the orbital- and spin-phase variabilities and comparing them with the 2015 NuSTAR results obtained in Chapter 4.

## 5.1 Observation and data reduction

We observed Cen X-3 with NuSTAR from 2022 January 12 to 16 with an elapsed time of 369 ks (ObsID: 30701019002). The elapsed time corresponds to  $\sim 2.04$  cycles of the binary system, calculated from  $P_{\text{orb}} \sim 2.09$  days. We applied general data reduction of NuSTAR on the observation data (see Section 4.2) with `HEASoft` 6.30. Both FPM images presented no stray lights during the observation. The source and background regions are a circle with a radius of  $180''$  from the source center and a rectangle in the off-source region, respectively. The barycentric correction was also applied to the observation data. After the data reduction, we yielded FPMA and FPMB cleaned event data with net exposures of 189 ks. All the temporal and spectral analyses in this chapter and the following chapters were carried out with `HEASoft` 6.30, `Xronos` 6.0, and `XSPEC` 12.12.1.

### 5.1.1 Rough estimation of orbital parameters

Similar to Section 4.2, one needs to search for the orbital parameters during the observation to apply correction of binary modulation. We divided the whole observation data into every 2 ks interval, and searched for the Doppler-shifted spin period at each interval. We applied the epoch-folding search for each interval, in which we folded the data over a range of periods and evaluated chi-square values. The period that yields the maximum chi-square can be interpreted as the spin period, and the variance of the spin period can be calculated by

$$\sigma_p^2 = \frac{3P^3}{\pi^2 \chi^2 T}, \quad (5.1)$$

where  $P$ ,  $\chi^2$ , and  $T$  denote the spin period, chi-square value at that period, and the length of one time bin (Larsson, 1996). The modulation of the Doppler-shifted spin period can be described in terms of the orbital parameters, as presented in equation (4.1).

Figure 5.1 shows the binary modulation of the Doppler-shifted spin period and the best-fit sinusoidal function. The orbital parameters yielded here are

$$\begin{aligned} P_{\text{orb}} &= 2.09 \pm 0.03 \text{ days}, \\ P_{\text{spin}} &= 4.7966 \pm 0.0002 \text{ s}, \\ a_x \sin i &= 40.1 \pm 1.6 \text{ lt-s}, \\ \Phi_{\text{start}} &= -0.16 \pm 0.02. \end{aligned} \quad (5.2)$$



The errors were estimated from the fitting results.  $P_{\text{orb}}$  and  $a_x \sin i$  show consistent values with 2015 NuSTAR data (see Table 4.1), while  $P_{\text{spin}}$  shows a significant spin-up property with a spin-up rate of  $\dot{P} = -3.1 \times 10^{-11} \text{ s s}^{-1}$ . The  $\Phi_{\text{start}} = -0.16$  means that this observation covers an orbital interval of  $-0.16 < \Phi < 1.88$ .

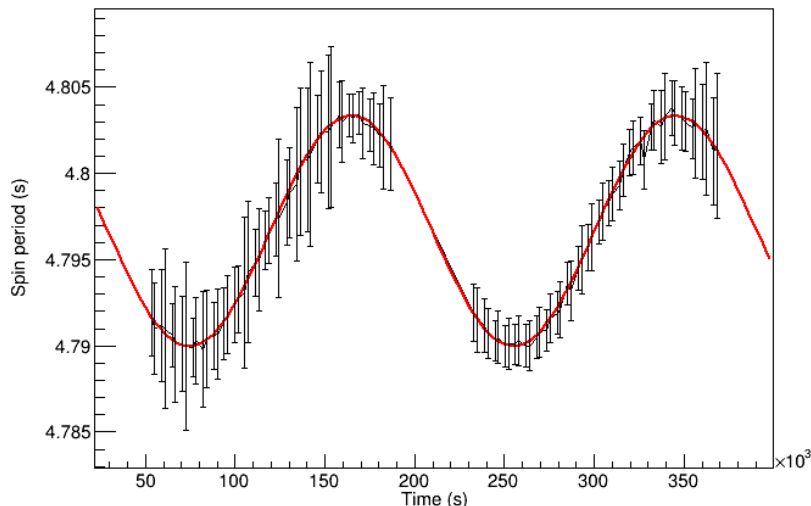


Figure 5.1: Binary modulation of Doppler-shifted spin period. The red line denotes the best-fit sinusoidal function.

### 5.1.2 Precise estimation of orbital parameters

The estimation of the orbital parameters in the previous sub-section is insufficient to perform coherent spin-phase-resolved spectroscopy. This can be evaluated by calculating the peak phase shifts of pulse profiles between the beginning and end of the observation. The shift of the peak phase  $\Delta\phi$  caused by the uncertainty of the spin period determination ( $\Delta P_{\text{spin}}$ ) is

$$\Delta\phi = \frac{T \Delta P_{\text{spin}}}{P_{\text{spin}}^2}, \quad (5.3)$$

where  $T = 369 \text{ ks}$  is the elapsed time of the observation. If we adopt the rough estimation of  $\Delta P_{\text{spin}} = 0.0002 \text{ s}$ , the spin-phase shift during the observation would be  $\Delta\phi \sim 3.2$ , and a spin-phase-resolved analysis over the whole observation time would be impossible.

The precise estimation of the orbital parameters can be carried out using the  $Z_n^2$  test (Buccheri et al., 1983; Brazier, 1994). It is a more sophisticated method than the epoch folding search and was originally developed for pulsar searches in gamma-ray data. Unlike the epoch folding search, it directly utilizes the arrival times of photons for the calculation,

thus being free from the binning ambiguity. The  $Z_n^2$  value is given by

$$Z_n^2 = \frac{2}{N} \sum_{k=1}^n \left[ \left( \sum_{j=1}^N \cos k\phi_j \right)^2 + \left( \sum_{j=1}^N \sin k\phi_j \right)^2 \right], \quad (5.4)$$

where  $N$  and  $\phi_j$  denote the number of arrival photons and the corresponding spin phase of the  $j$ -th photon, respectively. In the absence of a pulsed signal,  $Z_n^2$  is distributed as  $\chi^2$  with  $2n$  degrees of freedom. When  $n = 1$ , the  $Z_n^2$  test corresponds to the Rayleigh test, which is suited for pulse searches of purely sinusoidal signals.  $n = 2$  is frequently used for pulse searches of celestial objects since most objects have more complicated pulse profiles than a purely sinusoidal function.

We performed a  $Z_2^2$  test on the observation data with the four parameters  $P_{\text{orb}}$ ,  $P_{\text{spin}}$ ,  $a_x \sin i$ , and  $\Phi_{\text{start}}$  varying within the ranges described in equations (5.2). The orbital parameters yielding the largest  $Z_2^2$  and their uncertainties are listed in Table 5.1, compared with previously yielded values. The variations of  $Z_2^2$  values as functions of orbital parameters around the peaks are shown in Figure 5.2. The uncertainties of the orbital parameters were evaluated by fitting the  $Z_2^2$  variations with Gaussian functions (red lines in Figure 5.2). The uncertainties of the parameters are much more suppressed compared to the rough estimation (equations 5.2). Especially, the  $1\sigma$  error of  $P_{\text{spin}}$  was improved by order of magnitude, and the peak phase shift can be reduced to  $\Delta\phi \sim 0.3$ .

The binary correction for the observation data was carried out using the parameters listed in the first row of Table 5.1. In order to quantify the pulse peak shift during the observation, we divided the binary corrected observation data into multiple pieces, and generated 3–78 keV pulse profiles for the orbital intervals. We calculated the pulse peak phase for each pulse profile using Fourier transform, which we described in Section 4.4.1. The peak phase of the  $k$ -th Fourier component can be calculated by

$$\phi_{\text{peak}, k} = \frac{1}{2\pi k} \arctan \left( \frac{b_k}{a_k} \right), \quad (5.5)$$

where  $a_k$  and  $b_k$  are the  $k$ -th Fourier coefficients defined in equations (4.11). In Figure 5.3, we present the peak phases of the 1st Fourier component as a function of the orbital phase. Here, we define the zero point of the spin phase so that  $\phi = 0.25$  correspond to the peak phase of the 1st Fourier component in the phase-averaged pulse profile. The peak phase shift is much less than expected from the uncertainty of the spin period determination. In the following analysis, therefore, we assume that the peak phase shift during the observation is  $\Delta\phi < 0.05$ , based on Figure 5.3.

Table 5.1: Orbital parameters of Cen X-3.<sup>a</sup>

Reference	$P_{\text{orb}}$ (days)	$P_{\text{spin}}$ (s)	$a_x \sin i$ (lt-s)	$\Phi_{\text{start}}$
This work (2022 NuSTAR)	2.089(3)	4.796653(23)	39.65(82)	-0.164(2)
This work (2015 NuSTAR) <sup>b</sup>	2.087 (fixed)	4.8026(4)	39.5(20)	0.199(4)
Bildsten et al. (1997)	2.087113936(7) <sup>c</sup>	4.8	39.6612(9)	-

<sup>a</sup> For definition of parameters, see text.

<sup>b</sup> See Table 4.1

<sup>c</sup> At the time of 50506.788423(7) MJD.

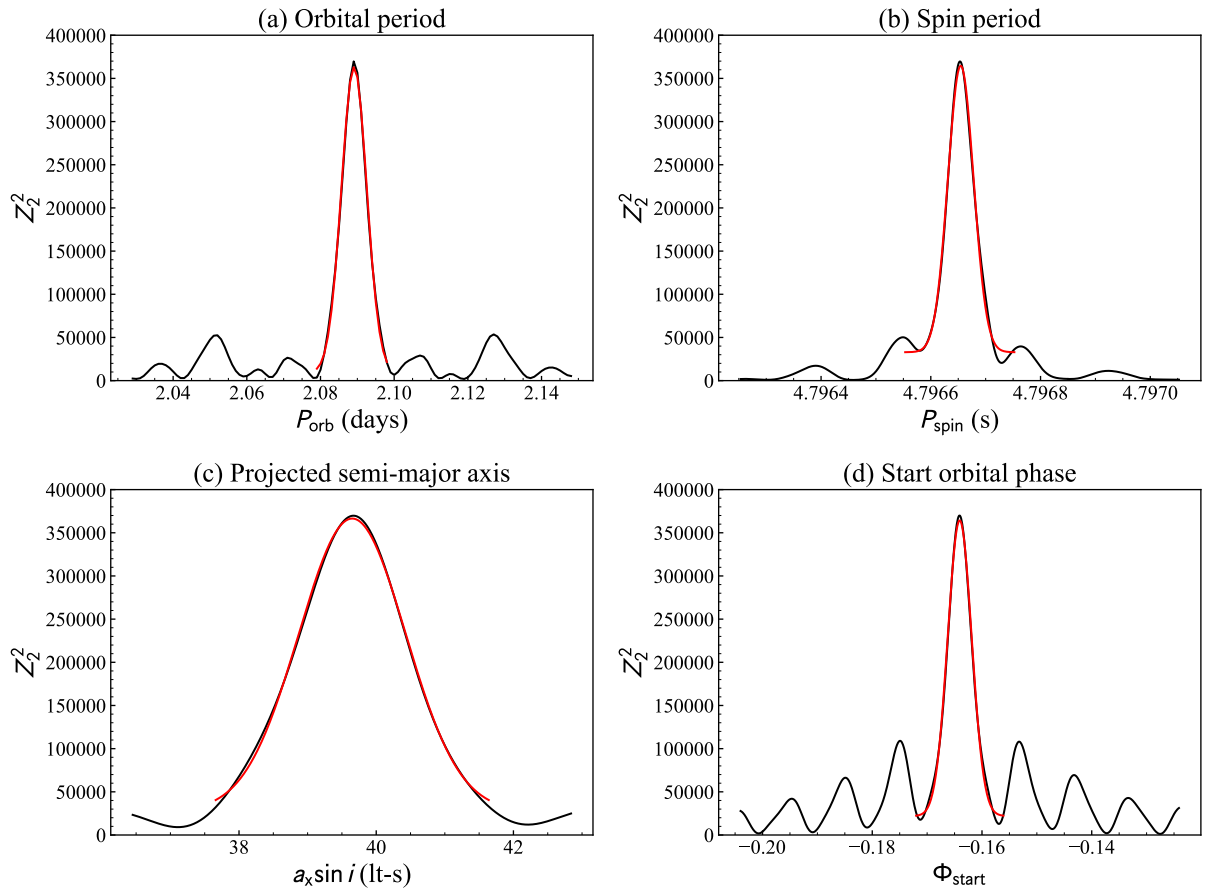


Figure 5.2: Variations of  $Z_2^2$  values around the best-fit parameters for  $P_{\text{orb}}$ ,  $P_{\text{spin}}$ ,  $a_x \sin i$ , and  $\Phi_{\text{start}}$ . The red lines denote the best-fit Gaussian functions.

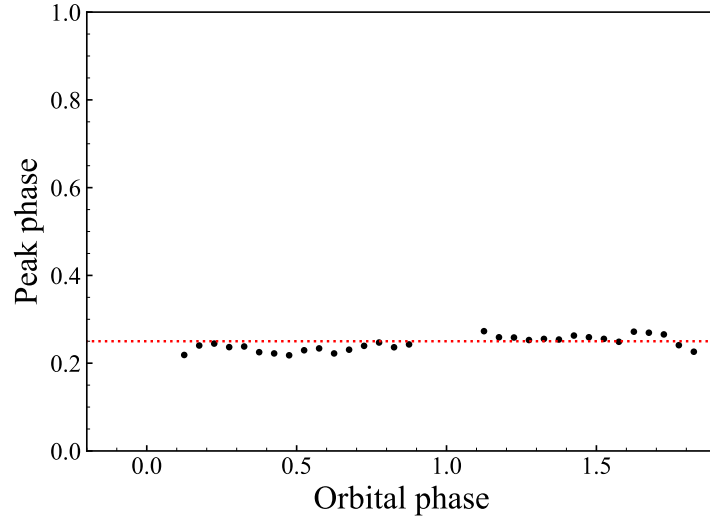


Figure 5.3: Variation of the peak phase of the 1st Fourier component along the orbital phase, generated from 3–78 keV pulse profiles. The red dotted line denotes the peak phase of the phase-averaged pulse profile ( $\phi = 0.25$ ).

### 5.1.3 Definition of orbital intervals

Due to its high inclination angle of  $70.2 \pm 2.7$  deg (Ash et al., 1999), the light curve of Cen X-3 shows a clear eclipsed feature in every cycle. Figure 5.4 shows the 3–78 keV light curve during the observation. The low count rate intervals around  $\Phi = 0.0$  and  $\Phi = 1.0$  can be interpreted as eclipses. Analyzing the summation of FPMA and FPMB light curves, it becomes clear that two orbital intervals of  $-0.100 < \Phi < 0.103$  and  $0.897 < \Phi < 1.096$  have lower count rates than 10 photons/s. The durations of the eclipses are consistent with the optical analysis that revealed 20% of the whole orbit corresponds to the eclipse (Ash et al., 1999). In our analysis, we define the eclipse phases as

$$\begin{aligned} \text{Eclipse 1 :} \quad & -0.10 \leq \Phi \leq 0.10, \\ \text{Eclipse 2 :} \quad & 0.90 \leq \Phi \leq 1.10, \end{aligned} \tag{5.6}$$

which are shown in Figure 5.4.

In the following analysis, we also define other orbital phases than the eclipse as “out-of-eclipse” phases. The out-of-eclipse phases are composed of three intervals, defined as

$$\begin{aligned} \text{Orbit 0 :} \quad & \Phi_{\text{start}} \leq \Phi \leq -0.10, \\ \text{Orbit 1 :} \quad & 0.10 \leq \Phi \leq 0.90, \\ \text{Orbit 2 :} \quad & 1.10 \leq \Phi \leq \Phi_{\text{end}}. \end{aligned} \tag{5.7}$$

$\Phi_{\text{start}} = -0.164$  and  $\Phi_{\text{end}} = 1.880$  are the orbital phases at the start and end of the observation. These definitions are presented in Figure 5.4.

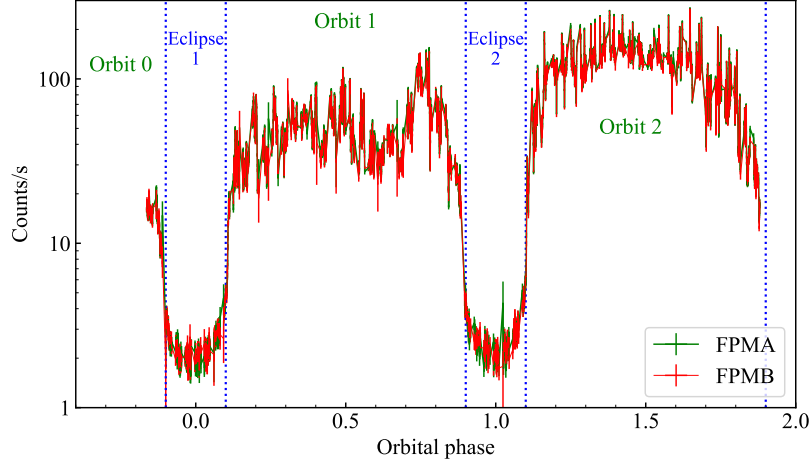


Figure 5.4: 3–78 keV light curve of Cen X-3 during the observation. One bin corresponds to 100 s. The start and end phases of the eclipses are represented by blue dotted line.

## 5.2 Orbital-phase variability

Similar to Section 4.3, we investigated the spectral variability along the orbital phase with the two-orbit observation data of Cen X-3. The whole observation data were divided into multiple orbital intervals. For the out-of-eclipse phases, the duration of an orbital interval is  $\Delta\Phi = 0.005$ , which corresponds to  $\sim 900$  s. For the eclipse phases, one orbital interval was set to a much longer duration due to the lack of photon counts, which is  $\Delta\Phi = 0.05$  corresponding to  $\sim 9$  ks. The whole observation is composed of 337 orbital intervals, and 98 were excluded from the following analysis due to short exposures of  $< 150$  s. In this section, we study the orbital-phase variability using the remaining 239 orbital intervals via light curve analysis and spectroscopy, as carried out in Section 4.3.

### 5.2.1 Energy-resolved light curve

In order to track the orbital-phase variability in different energy bands, we calculated count rates of the 246 orbital intervals for 3–78 keV, 3–5 keV, 5–10 keV, 10–20 keV, and 20–78 keV. The generated light curves are presented in the left panel of Figure 5.5. The right panel of Figure 5.5 shows the hardness ratios among these energy bands. There are characteristic orbital phases located at the ingresses and egresses of the eclipses, in which the hardness ratios become incredibly high. These phases are often called “pre-eclipse dips” and “post-eclipse dips”, considered to be affected by a deep absorption near the

surface of the companion star. Hereafter, we characterize these phases as ingress and egress phases by

$$\begin{aligned} \text{Ingress :} \quad & -0.15 \leq \Phi \leq -0.10, 0.85 \leq \Phi \leq 0.90, 1.85 \leq \Phi \leq \Phi_{\text{end}} \\ \text{Egress :} \quad & 0.10 \leq \Phi \leq 0.15, 1.10 \leq \Phi \leq 1.15, \end{aligned} \quad (5.8)$$

in order to distinguish them from the “normal” out-of-eclipse phases. These definitions are represented by red dotted lines in Figure 5.5.

Table 5.2 presents the average count rates of different orbital intervals for different energy bands. All the energy bands display a common trend that Orbit 2 has higher count rates than Orbit 1. Since the 2015 NuSTAR observation yielded average count rates of 24.5, 83.7, 54.8, and 5.80 counts/s for 3–5, 5–10, 10–20, 20–78 keV, respectively, the analysis in Chapter 4 approximately corresponds to the middle state between Orbit 1 and Orbit 2 (see Section 4.3.1). The count ratios between Orbit 1 and Orbit 2 are different among the energy bands. In 3–78 keV, the count rates of Orbit 1 and Orbit 2 differ by a factor of 2.31. Consulting individual energy bands, the ratios between Orbit 1 and Orbit 2 count rates are 3.62, 2.43, 1.78, 1.55 for 3–5, 5–10, 10–20, 20–78 keV, respectively. The monotonic decrease of the ratios means that the lower energy bands exhibit higher variabilities in the count rate. This trend is reflected in the hardness ratio, as we can see a common feature that Orbit 1 has larger hardness ratios than Orbit 2, as shown in the right panel of Figure 5.5.

In Figure 5.6, we present the hardness ratios as a function of 3–78 keV count rate with the above classification of the orbital intervals. The hardness ratios have clear negative correlations with the count rate, including the prominent hardness ratios of the Ingress & Egress phases. The rough trend of the flux variability is that the low-energy photons are more dominantly variable than high-energy photons, suggested by the monotonic decreases in hardness ratios with the count rate. The qualitative features of the light curve variability are thus identical to those found in Section 4.3.1. The only exception is the eclipse phases, where the hardness ratios are comparable to the normal orbital phases despite the lowest count rates.

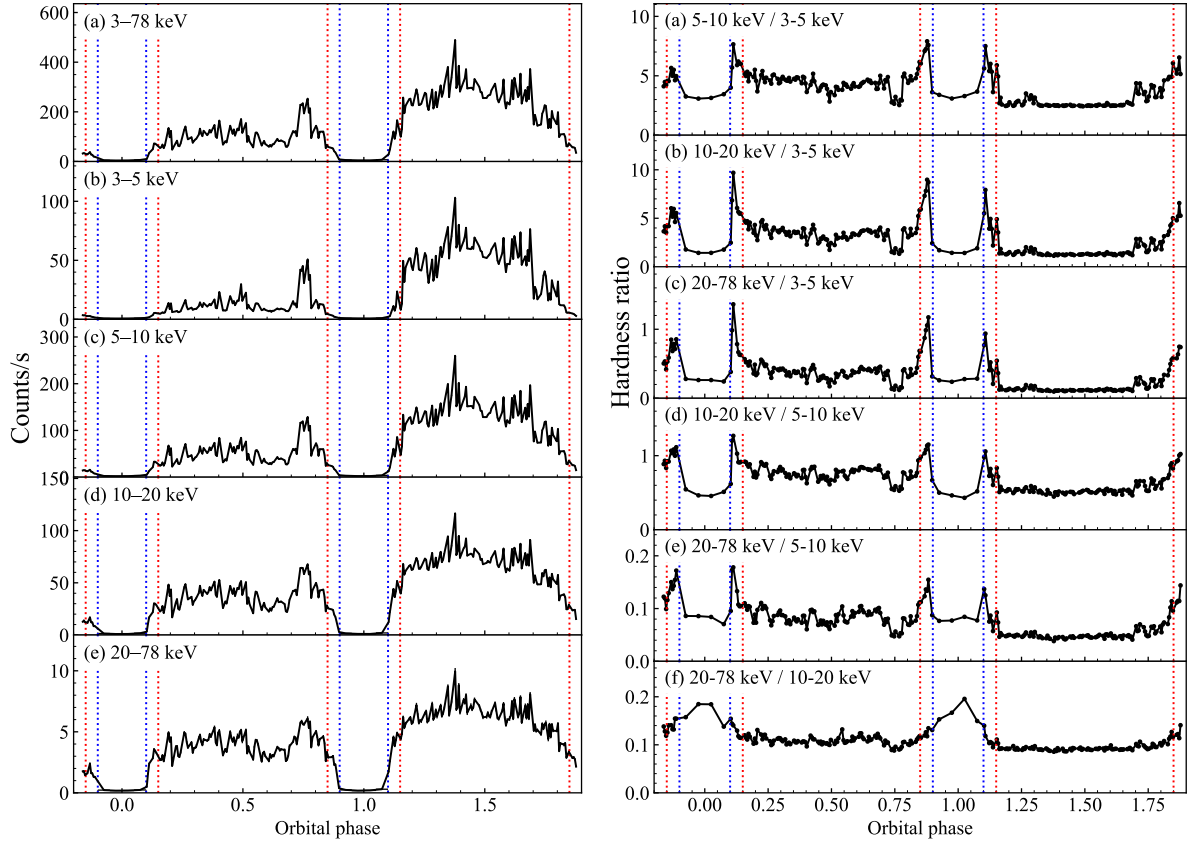


Figure 5.5: Light curves of different energy bands (left) and hardness ratios among the energy bands (right). The blue dotted lines denote the beginnings and ends of the eclipses. The red dotted lines represent the beginnings of ingresses ( $\Phi = -0.15, 0.85, 1.85$ ) and ends of egresses ( $\Phi = 0.15, 1.15$ ).

Table 5.2: Average count rates of different orbital intervals.

Energy band	All <sup>a</sup> (Counts/s)	Orbit 1 (Counts/s)	Orbit 2 (Counts/s)	Ingress & Egress (Counts/s)	Eclipse (Counts/s)
3–78 keV	153	106	245	49.8	5.13
3–5 keV	25.3	12.9	46.7	4.27	0.825
5–10 keV	76.9	51.9	126	22.7	2.74
10–20 keV	46	37.5	66.7	20.3	1.35
20–78 keV	4.56	3.99	6.19	2.44	0.218

<sup>a</sup> Average count rate of all the valid orbital intervals.

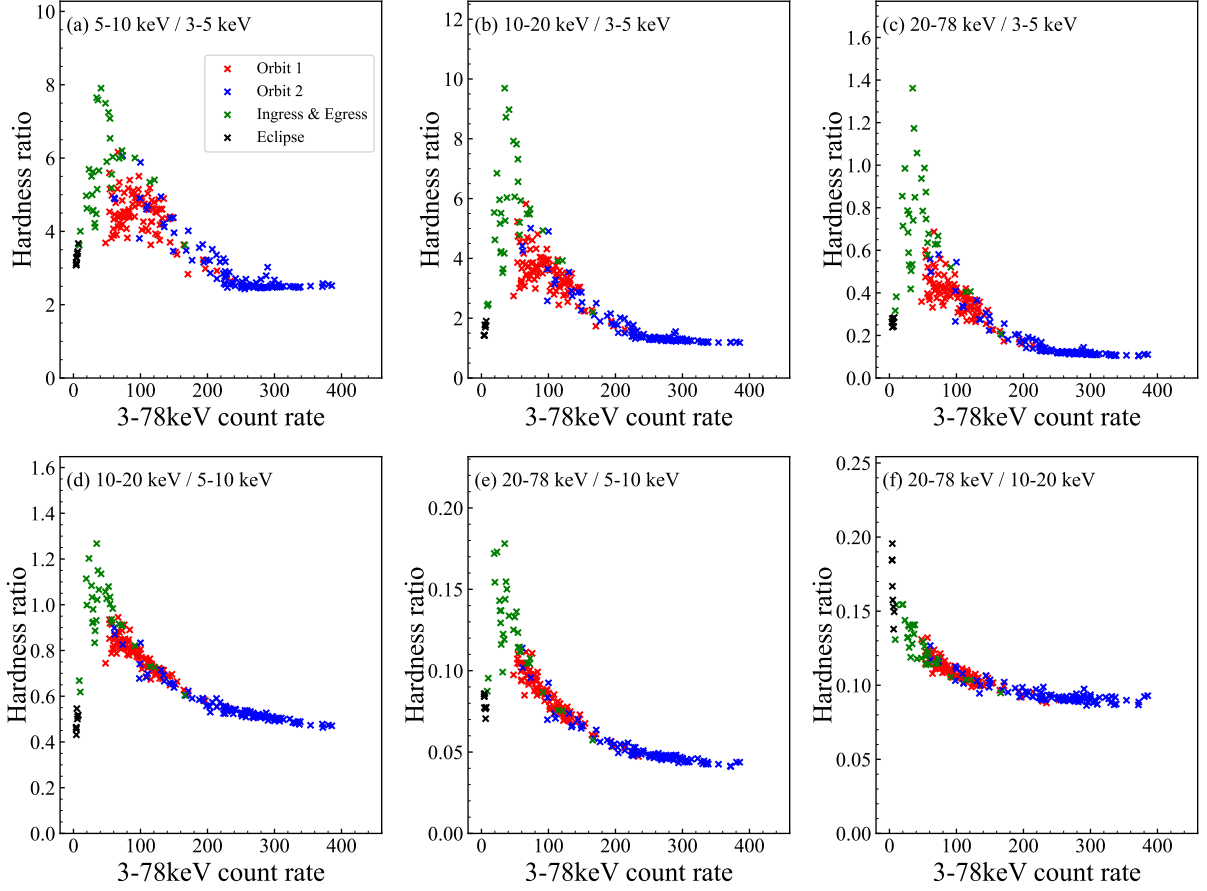


Figure 5.6: Hardness ratios among multiple energy bands as a function of 3–78 keV count rate. Different colors denote different types of orbital intervals, Orbit 1 (red), Orbit 2 (blue), Ingress & Egress (green), and Eclipse (black).

### 5.2.2 Spectral fitting on orbital-phase-resolved spectra

In order to examine the quantitative variability along the orbital phase, we carried out the spectral fitting on the orbital-phase-resolved spectra, generated from each orbital interval. The assumed spectral model is the Fermi-Dirac cut-off accompanied by the Fe line and CRSF components, given by

$$\frac{dN(E)}{dE} \propto f_{\text{phabs}} \times (f_{\text{FDcut}} + f_{\text{gauss}}) \times f_{\text{gabs}}, \quad (5.9)$$

which is identical to equation (4.15). The absorption column density corresponding to the interstellar medium is fixed to  $N_{\text{H}}^{\text{IM}} = 1.1 \times 10^{22} \text{ cm}^{-2}$  (HI4PI Collaboration et al., 2016), and the valid energy band is 4–78 keV, same as Section 4.3.2. Since each spectrum has insufficient photon counts for the determination of the CRSF, we adopted fixed values for the central energy, line width, and strength of the CRSF. These values were derived from



the preliminary fitting of the phase-averaged spectrum. The adopted values were

$$\begin{aligned} E_{\text{cyc}} &= 27.5 \text{ keV}, \\ \sigma_{\text{cyc}} &= 6.31 \text{ keV}, \\ \tau_{\text{cyc}} &= 1.32. \end{aligned} \tag{5.10}$$

In Figure 5.7, we present the best-fit spectral parameters derived from the orbital-phase-resolved spectra. All the spectra were successfully fitted by the model, and yielded acceptable  $\chi^2_\nu$  values with an average value of 1.04. The 4–78 keV absorbed flux varies from  $7.6 \times 10^{-11} \text{ erg s}^{-1} \text{ cm}^{-2}$  to  $9.2 \times 10^{-9} \text{ erg s}^{-1} \text{ cm}^{-2}$ , corresponding to luminosities of  $3.7 \times 10^{35} \text{ erg s}^{-1}$  and  $4.5 \times 10^{37} \text{ erg s}^{-1}$ , respectively. In order to examine the effect of the parameter coupling, we also tried spectral fittings with initial conditions slightly changed from equation (5.9) as follows.

- Fixed the Fe line component ( $E_{\text{Fe}} = 6.4 \text{ keV}$  and  $\sigma_{\text{Fe}} = 0$ )
- Ignored the Fe line band (6–7 keV) with no Fe line component ( $I_{\text{Fe}} = 0$ )
- Fixed the CRSF component to zero ( $\tau_{\text{cyc}} = 0$ )
- Fixed  $\Gamma$
- Fixed  $E_c$

All of these trials yielded worse chi-square values than the initially assumed model except for the last one. The last case, with a fixed  $E_c$ , does not affect the chi-square values. This is due to a strong parameter coupling between  $\Gamma$  and  $E_c$  as shown in Figure 4.2. Although the fixed  $E_c$  resulted in lower variability in  $\Gamma$ , it does not affect the variability of other parameters. Since this analysis is a phenomenological treatment for the spectral variability, we treat equation (5.9) with no constraints other than  $N_{\text{H}}^{\text{IM}} = 1.1 \times 10^{22} \text{ cm}^{-2}$  as the best-fit model.

Figure 5.8 shows the relation between the absorbed flux and the continuum parameters, that is,  $N_{\text{H}}$ ,  $\Gamma$ ,  $E_c$ , and  $E_{\text{f}}$ , for different types of orbital intervals.  $N_{\text{H}}$  varies from 0 to  $2.4 \times 10^{23} \text{ cm}^{-2}$ , but it does not show a clear correlation with the continuum flux. The range of  $N_{\text{H}}$  is comparable to the 2015 NuSTAR data, but the relation with the continuum flux is different between the two observations as a clear negative correlation can be seen in Figure 4.4. Orbit 1 intervals generally have larger  $N_{\text{H}}$  than Orbit 2 intervals, and the Ingress & Egress phases have even larger  $N_{\text{H}}$ , presumably due to the high absorption degree. The photon index  $\Gamma$  also displays a large variation along the orbital phase, ranging from  $-0.37$  to  $1.72$ . Instead of  $N_{\text{H}}$ ,  $\Gamma$  strongly correlates with the continuum flux except for the eclipse phases: softer photon indices in higher-flux phases and harder in lower-flux phases. It is a common trend that Orbit 1 has harder photon indices than Orbit 2. The

photon index becomes extremely hard in the Ingress & Egress phases, while it returns to the soft values of  $\Gamma \sim 1.06 - 1.33$  in the eclipse phases. The variation feature of  $\Gamma$  is similar to that of the hardness ratios shown in Figure 5.5, which suggests that the photon index is the most important parameter that characterizes the variability of the continuum spectrum. The cut-off energy  $E_c$  also has a moderate correlation with the flux, ranging from 19 to 31 keV, but it could be due to the parameter coupling with  $\Gamma$ . The folding energy  $E_f$  does not show significant variability along the orbital phase, keeping its value at  $\sim 4.5$  keV.

The variability of the photon index is, surprisingly, correlated with the flux of all the energy bands. This is shown in Figure 5.8. We can see that the photon index is positively correlated with the absorbed fluxes of 3–5, 5–10, 10–20, 20–78 keV. From this result, we conclude that the variation of the photon index is not due to the parameter coupling with  $N_H$ , because the photoelectric absorption by  $N_H$  could only affect low-energy photons and could not have any correlation with high-energy fluxes. The variability of the photon index is attributed to other physical processes than the pure photoelectric absorption by the stellar wind.

The Fe line component also shows significant variability along the orbital phase. Figure 5.10 presents the relation between the absorbed flux and the Fe line parameters, that is,  $E_{Fe}$ ,  $\sigma_{Fe}$ ,  $I_{Fe}$ , and  $Eqw_{Fe}$ . In the Eclipse phases,  $E_{Fe}$  displays higher values of  $\sim 6.6$  keV than other phases of  $\sim 6.4$  keV. This trend is due to the increased proportion of the highly ionized Fe lines, which are an  $\sim 6.7$  keV line for He-like ions and an  $\sim 7.0$  keV line for H-like ions. The variability of  $E_{Fe}$  is natural because these highly-ionized lines generally originate from the reprocessing by the stellar wind, which is the primary emission component during the Eclipse phases. The line width  $\sigma_{Fe}$  does not show significant variability along the orbital phase, settling at  $\sim 0.3$  keV. The line intensity  $I_{Fe}$  becomes significantly low in the Eclipse and Ingress & Egress phases, but no correlation with the continuum flux is seen in Orbit 1 or 2. The equivalent width ( $Eqw_{Fe}$ ) shows a negative correlation with the flux, particularly in Orbit 1. The Eclipse and Ingress & Egress phases also display large equivalent widths. The average equivalent widths are 0.37 keV, 0.11 keV, 0.44 keV, and 0.85 keV for Orbit 1, Orbit 2, Ingress & Egress, and Eclipse, respectively. The variabilities of the line intensity and equivalent width indicate that the continuum spectrum and the Fe line are not synchronized at all, due to the difference in emission regions. The flux difference between Orbit 1 and Orbit 2 does not induce significant variability in the Fe line because of the comparable line intensity between the two orbits. In the Ingress & Egress phases, both the continuum and the Fe line are significantly reduced, but the continuum is more suppressed than the Fe line because of the enhanced equivalent width.

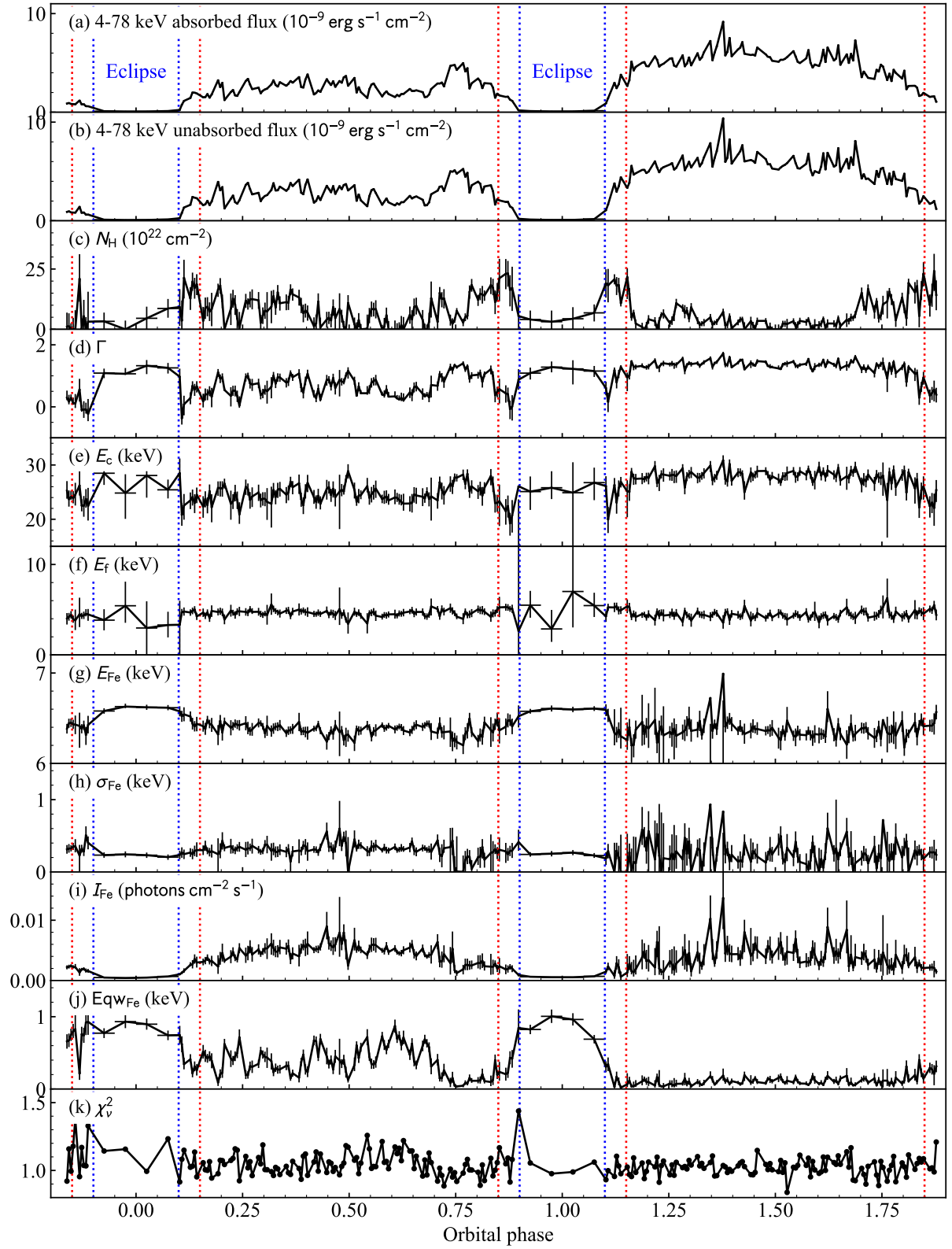


Figure 5.7: Orbital-phase variability of the best-fit spectral parameters derived from 4–78 keV orbital-phase-resolved spectroscopy. See text for the model description and definition of parameters. Error bars represent 90% confidence levels.

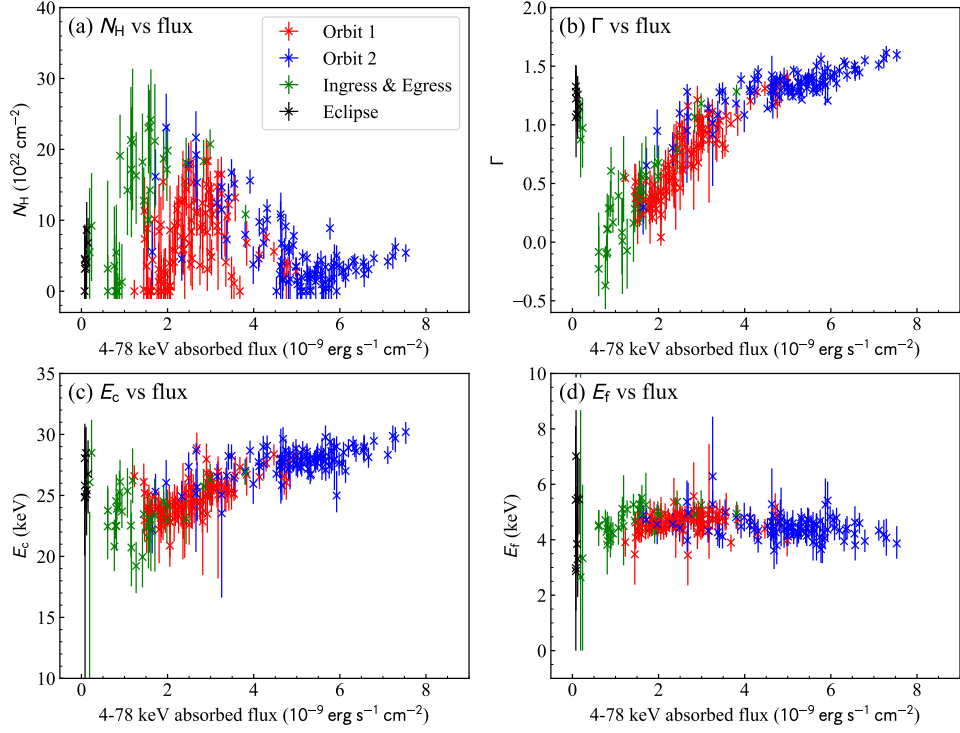


Figure 5.8: Relations between 4–78 keV absorbed flux and continuum parameters along the orbital phase. Error bars represent 90% confidence levels.

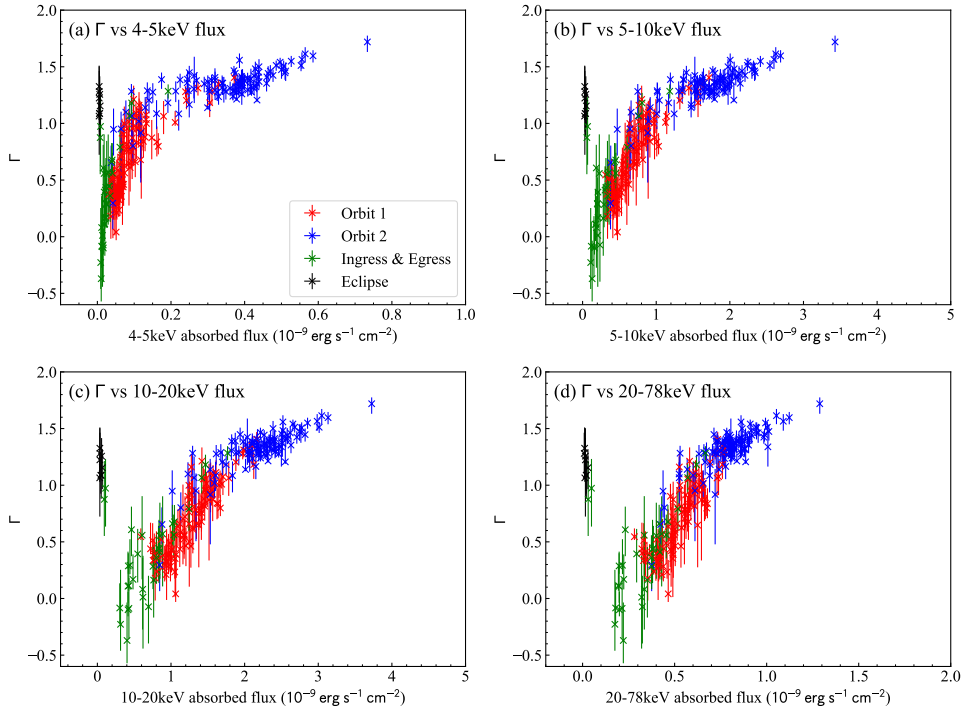


Figure 5.9: Relations between absorbed fluxes of different energy bands and the photon index along the orbital phase. Error bars represent 90% confidence levels.

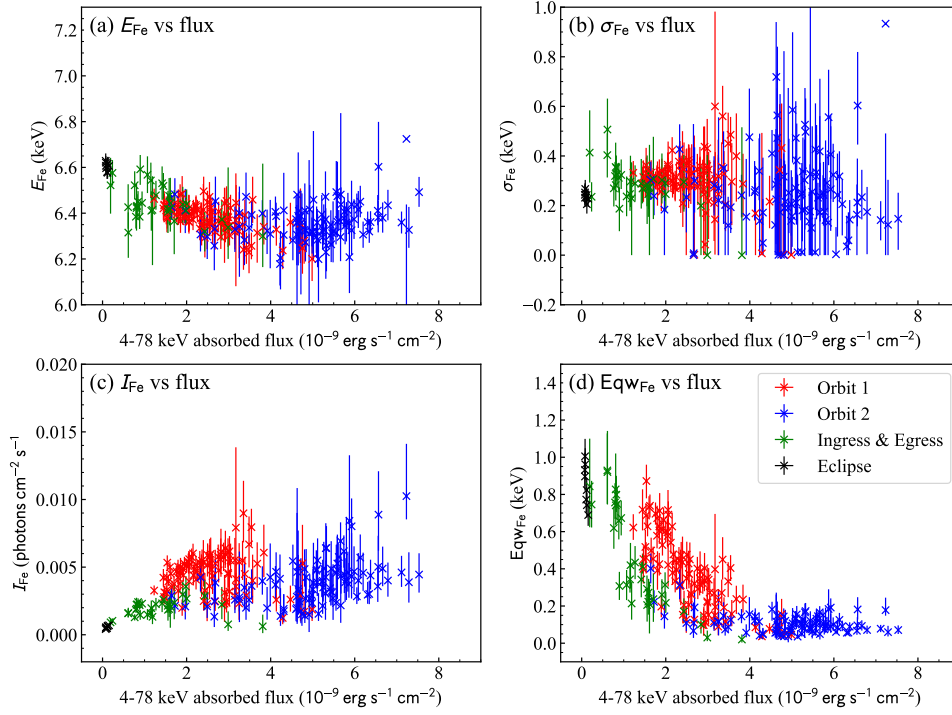


Figure 5.10: Relations between 4–78 keV absorbed flux and Fe line parameters along the orbital phase. Error bars represent 90% confidence levels.

## 5.3 Spin-phase variability

Similar to Section 4.4, we investigated the spin-phase variability through energy-resolved pulse profiles and spin-phase-resolved spectroscopy. The spin-phase-resolved analysis is carried out by summing all the data along the orbital phase. Therefore, we do not consider the difference between Orbit 1 and Orbit 2. The contributions from Eclipse and Ingress & Egress phases would be smeared out due to relatively low count rates.

### 5.3.1 Energy-resolved pulse profiles

We divided 3–78 keV into 18 energy bands and generated energy-resolved pulse profiles by folding them with the spin period of  $P_{\text{spin}} = 4.796653$  s. The spin phase is defined so that the peak phase of the 1st Fourier component for the 3–78 keV pulse profile correspond to  $\phi = 0.25$ , same as Section 5.1.2. Figure 5.11 shows the pulse profiles of the 18 energy bands over two spin periods. All of the pulse profiles show apparent pulsations, and their shapes gradually vary with energy bands. The pulse profile has a double-peaked shape with a moderate pulsation degree in the low-energy bands, while it has a single-peaked profile with a large pulsation degree in the high-energy bands. This is qualitatively the same trend as the 2015 NuSTAR observation (also see Figure 4.5).

In order to evaluate the energy-resolved pulse profiles, we performed the Fourier transform and calculated the parameters of the pulse profiles. A detailed description of the pulse profile analysis is given in Section 4.4.1. The number of the phase bins was set to  $N = 64$ . Figure 5.12 shows the analysis results of the pulse profiles, presenting the rms pulse fraction  $PF_{\text{rms}}$ , and ratios among the Fourier coefficients ( $c_1/c_0$ ,  $c_2/c_0$ , and  $c_2/c_1$ ). The pulse fraction displays a gradual increase with the energy, peaking at  $\sim 40$  keV, as shown in Figure 5.12(a). In the Fe line band ( $\sim 6.4$  keV) and the CRSF band ( $\sim 27$  keV), the pulse fraction becomes lower than the nearby bands by  $\sim 13\%$  and  $\sim 15\%$  respectively, suggesting different spin-phase variations of these two components. The 1st Fourier coefficient shows a similar trend with the pulse fraction (Figure 5.12b). In contrast, the ratio of the 2nd Fourier coefficient is relatively robust to the energy (Figure 5.12c). As a result, the 1st Fourier component becomes more dominant over the 2nd Fourier component as energy increases up to  $\sim 30$  keV (Figure 5.12d). These quantitative trends of the energy-resolved pulse profiles are consistent with those in the 2015 NuSTAR short-time observation data, as shown by the orange dashed lines in Figure 5.12. Thus, the energy dependence of the pulse profiles should be interpreted as a common feature for Cen X-3. The pulse fractions derived from this observation are lower than those of the 2015 data for all energy bands by a factor of  $\sim 10\%$ . This difference can be attributed to the difference in the average luminosity because our long observation includes eclipse phases, ingress & egress, and relatively low-luminosity phases in Orbit 1. All of these orbital phases tend to show lower pulse fractions. The detailed orbital-phase variability of the pulse profile is examined later in Section 5.4.1.

In this observation, we have sufficient photon counts to determine the peak phase of each Fourier component. The results are shown in Figure 5.13. The peak phases of the 1st and 2nd Fourier components exhibit interesting modulations along the energy. The peak of the 1st Fourier component gradually shifts to earlier phases up to the 25 keV turnover and returns to the later phases above 25 keV. The 2nd Fourier component displays a monotonic delay of the peak phase with energy. The peak phases at  $\phi \sim 0.15$  below 10 keV corresponds to the second peak of the pulse profiles emerging at  $\phi \sim 0.65$ . The peak phases of the two components become comparable above 20 keV, which generates sharper profiles around  $\phi \sim 0.25$  than the low-energy pulse profiles. Although the peak phase is sensitive to the accuracy of the orbital parameters, the continuous variations along the energy cannot be generated from the biases of the orbital parameters. The continuous variations support the possibility of significant peak-phase modulations based on different emission processes dependent on the photon energies.

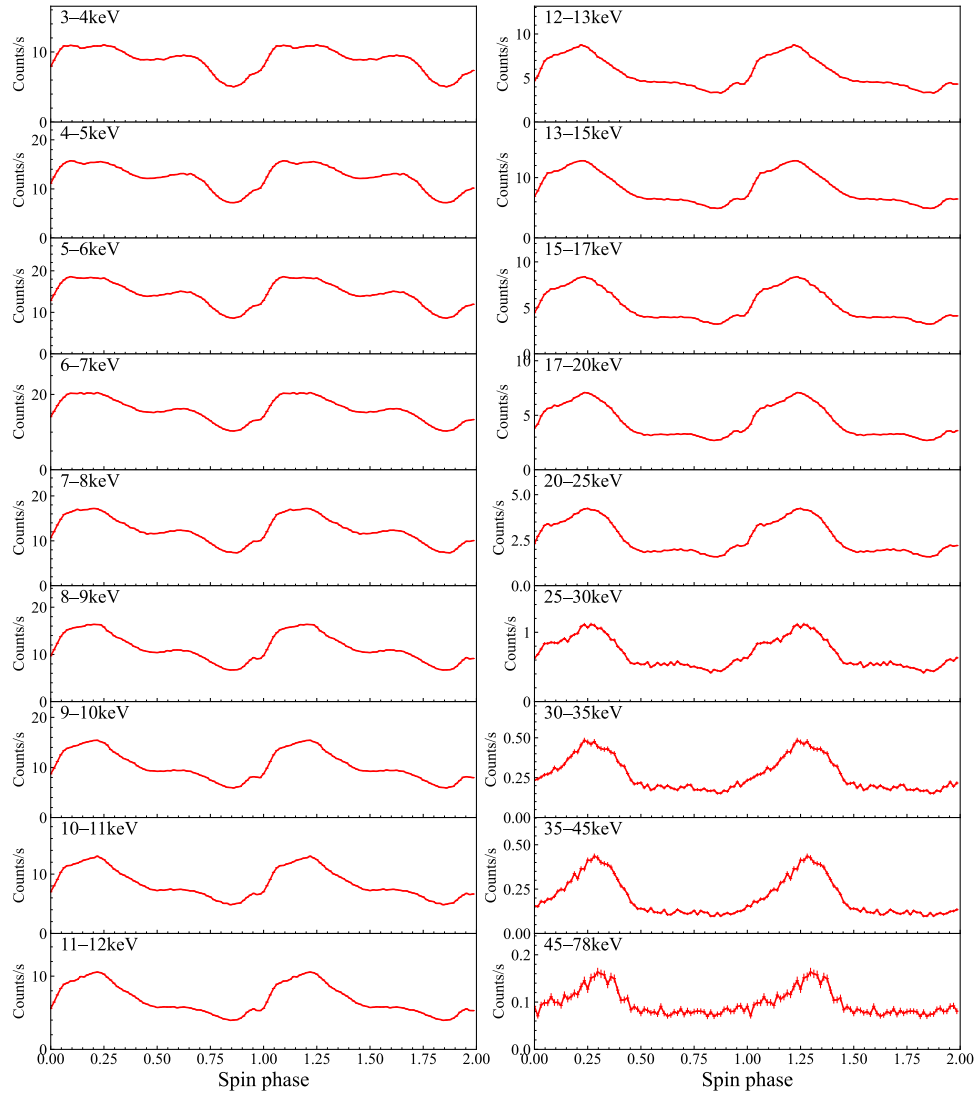


Figure 5.11: Energy-resolved pulse profiles over two spin periods generated for 18 energy bands. The summation of FPMA and FPMB counts are plotted.

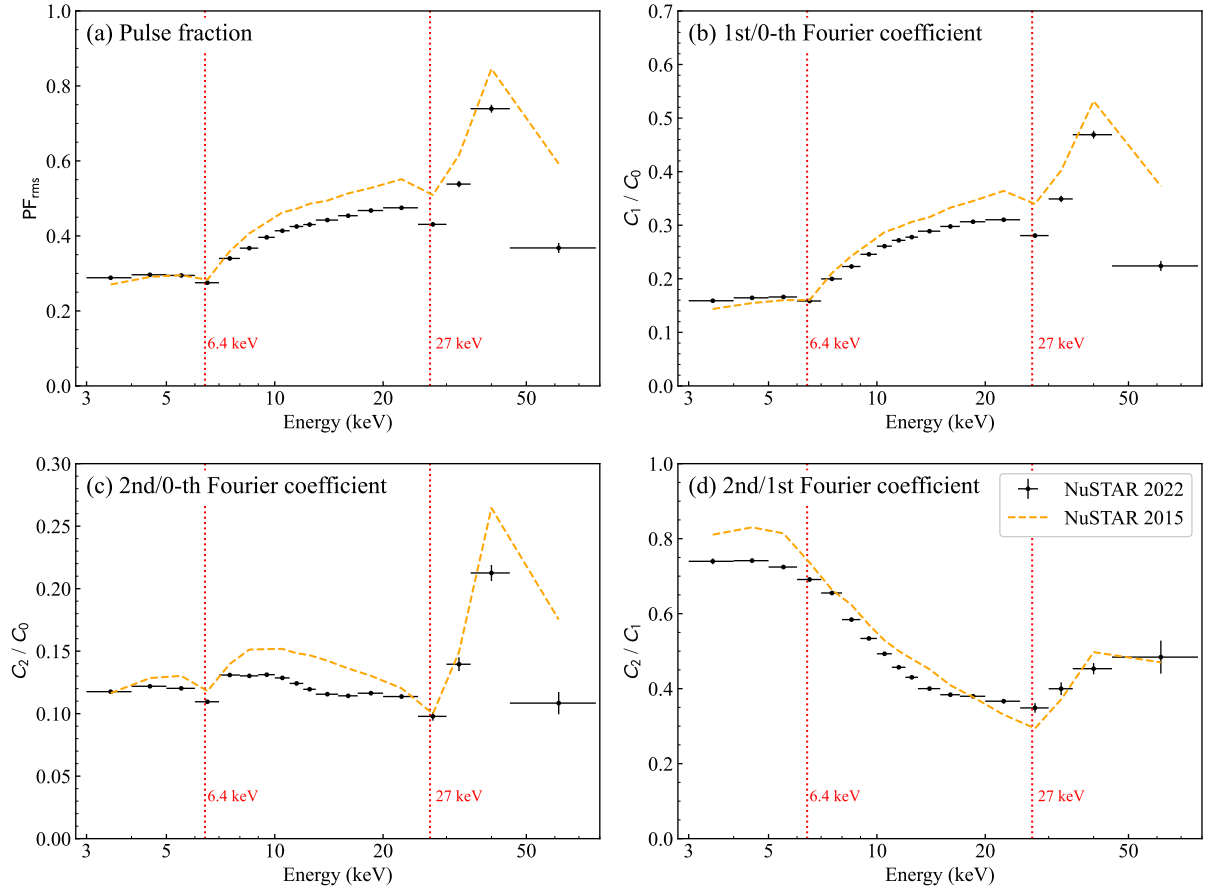


Figure 5.12: Analysis results of energy-resolved pulse profiles. (a)  $PF_{rms}$ , (b)  $c_1/c_0$ , (c)  $c_2/c_0$ , and (d)  $c_2/c_1$  as a function of energy. For comparison, results from the 2015 NuSTAR observation are overlayed by orange dashed lines.

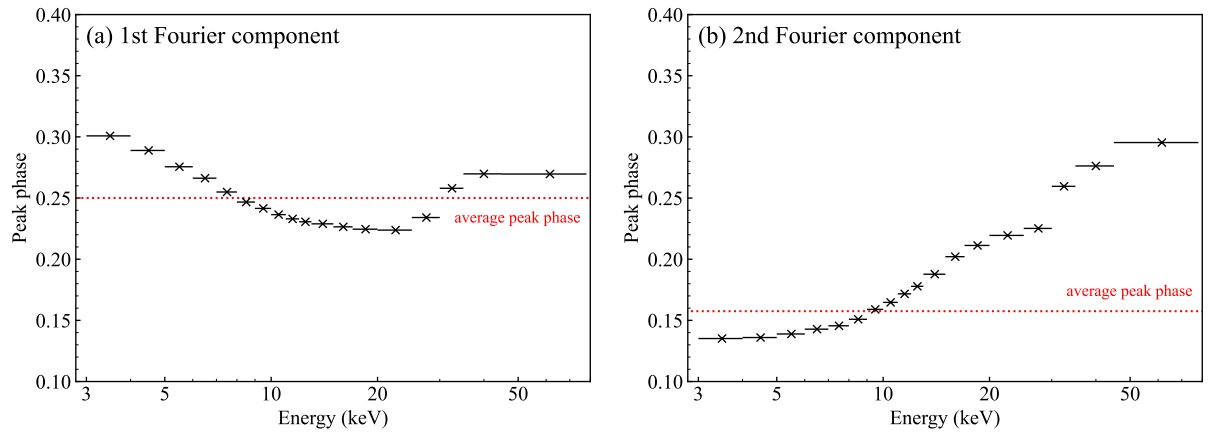


Figure 5.13: Peak phases of energy-resolved pulse profiles. The red dotted lines denote the peak phases of the pulse profile of 3–78 keV,  $\phi = 0.25$  and  $\phi = 0.16$  for the 1st and 2nd Fourier components, respectively.



### 5.3.2 Spectral fitting on spin-phase-resolved spectra

We examined more detailed spin-phase variability by analyzing the spin-phase-resolved spectra. This section takes the same approach as Section 4.4.3. The difference is the statistical richness of the observation data. Since we have much richer statistics than the 2015 NuSTAR data, we divided the whole spin phase into 32 intervals and performed spectral fitting on each spin-phase-resolved spectrum. The assumed model is the Fermi-Dirac cut-off power law with an Fe line and a CRSF, given by equation (4.15). All of the parameters were set free except for  $N_{\text{H}}^{\text{IM}} = 1.1 \times 10^{22} \text{ cm}^{-2}$  (HI4PI Collaboration et al., 2016), and the FPMA and FPMB spectra were analyzed simultaneously by joint fitting.

Figure 5.14 shows the spin-phase variabilities of the best-fit spectral parameters. We tried spectral fitting with both free  $N_{\text{H}}$  and fixed  $N_{\text{H}}$ . In the latter case, the column density is fixed to  $N_{\text{H}} = 3.2 \times 10^{22} \text{ cm}^{-2}$ , which is derived from the phase-averaged spectrum. Both cases of analysis yielded acceptable  $\chi^2_{\nu}$  values with average values of 1.19. The different  $N_{\text{H}}$  does not affect the spin-phase variabilities of other parameters. Hereafter, we adopt the fixed- $N_{\text{H}}$  case as the best-fit model because it is more natural to treat the absorption by the stellar wind as independent of the spin phase. The relations between the spectral parameters and the continuum flux shown in Figure 5.15, 5.16, and 5.17 are plotted for the fixed  $N_{\text{H}}$  model.

Figure 5.15 shows the spin-phase variabilities of the continuum parameters as a function of the continuum flux.  $\Gamma$  shows a clear negative correlation with the flux, ranging from 0.76 to 1.30. In contrast,  $E_{\text{c}}$  and  $E_{\text{f}}$  do not show significant variabilities along the spin phase, settling at  $\sim 26 \text{ keV}$  and  $\sim 4.5 \text{ keV}$ , respectively. The results from the 2015 NuSTAR data are also plotted together. The variabilities of the continuum parameters are consistent between 2022 and 2015 NuSTAR data, as shown in Figure 5.15.

The variabilities of the Fe line parameters as a function of the continuum flux are presented in Figure 5.16.  $E_{\text{Fe}}$  and  $\sigma_{\text{Fe}}$  do not show any significant variability along the spin phase.  $I_{\text{Fe}}$  and  $\text{Eqw}_{\text{Fe}}$  both display negative correlations with the flux. At the pulse maximum, they reach  $\sim 60\%$  and  $\sim 30\%$  of the pulse minimum values, respectively. These variabilities are consistent with the 2015 NuSTAR data, although the absolute intensities are higher in the 2015 data by factors of  $\sim 2$ .

The variabilities of CRSF parameters with the continuum flux are shown in Figure 5.17. Both  $E_{\text{cyc}}$  and  $\sigma_{\text{cyc}}$  show positive correlations with the continuum flux, while  $\tau_{\text{cyc}}$  does not show significant variability due to large uncertainties. The CRSF energy  $E_{\text{cyc}}$  ranges from 25.1 keV to 29.0 keV, corresponding to an  $\sim 15\%$  difference in the magnetic field strength. The line width  $\sigma_{\text{cyc}}$  ranges from 5.0 keV to 7.4 keV, varying by a factor of  $\sim 50\%$ . All three parameters exhibit consistent variabilities with the 2015 data, as shown in Figure 5.17.

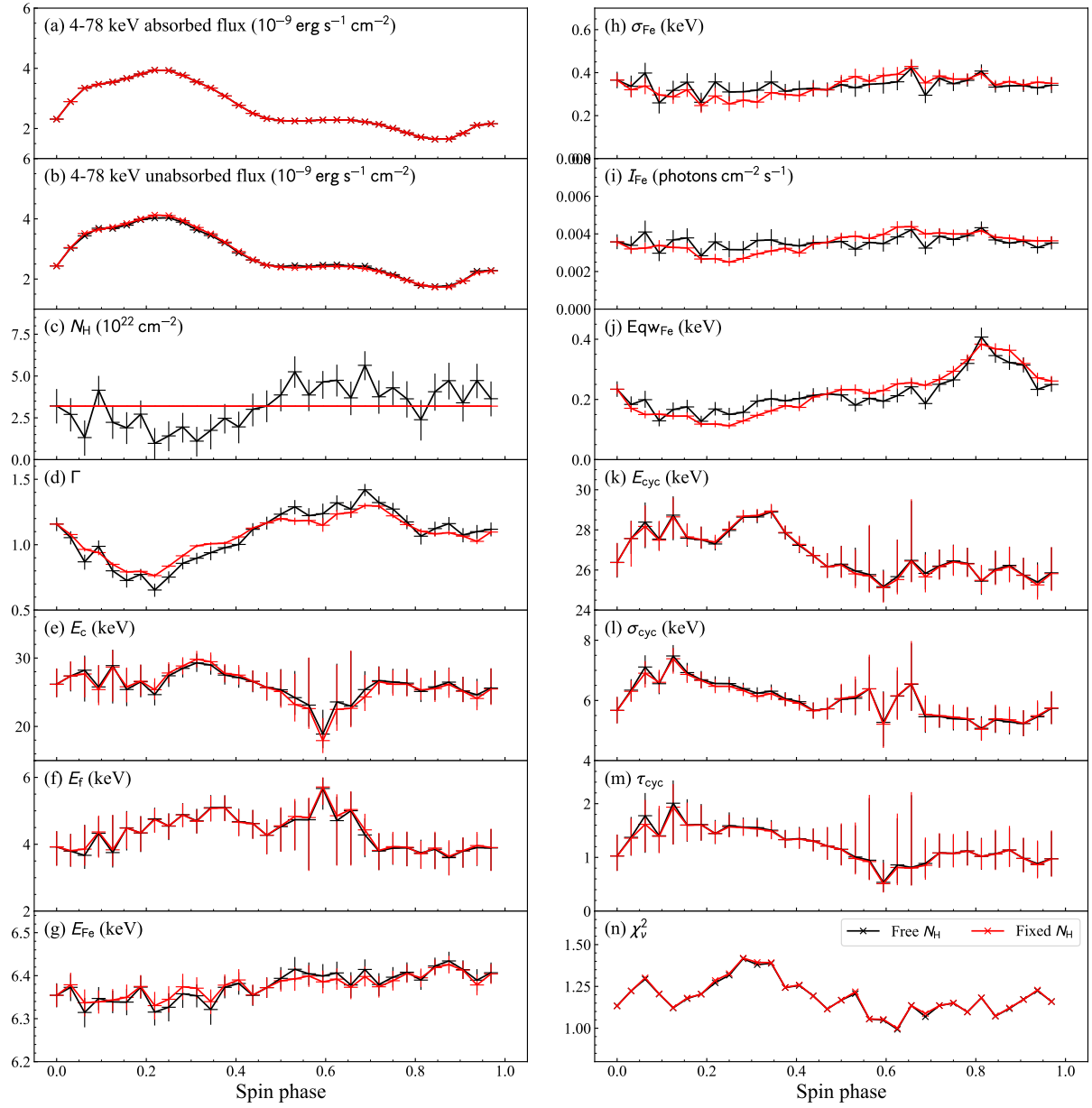


Figure 5.14: Spin-phase variability of the best-fit spectral parameters derived from 4–78 keV spin-phase-resolved spectroscopy. Results with free  $N_{\text{H}}$  and fixed  $N_{\text{H}}$  are plotted together. Error bars represent 90% confidence levels.

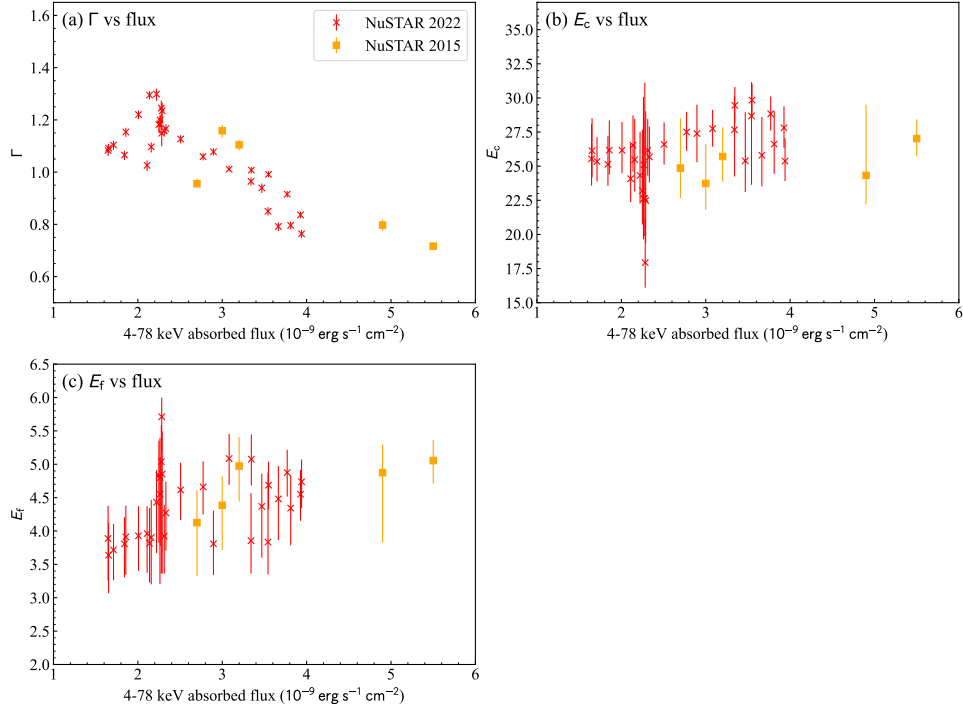


Figure 5.15: Relations between 4–78 keV absorbed flux and continuum parameters along the spin phase for the fixed  $N_{\text{H}}$  model. For comparison, results from the 2015 NuSTAR observation are plotted together by orange-squared points. Error bars represent 90% confidence levels.

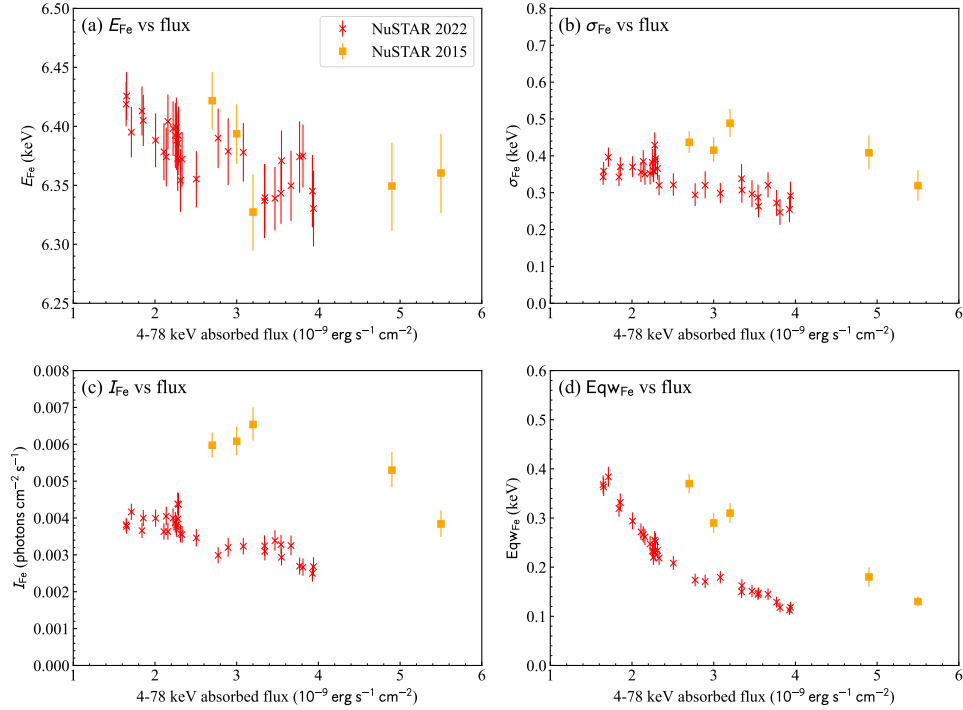


Figure 5.16: Same as Figure 5.15 but for the Fe line parameters.

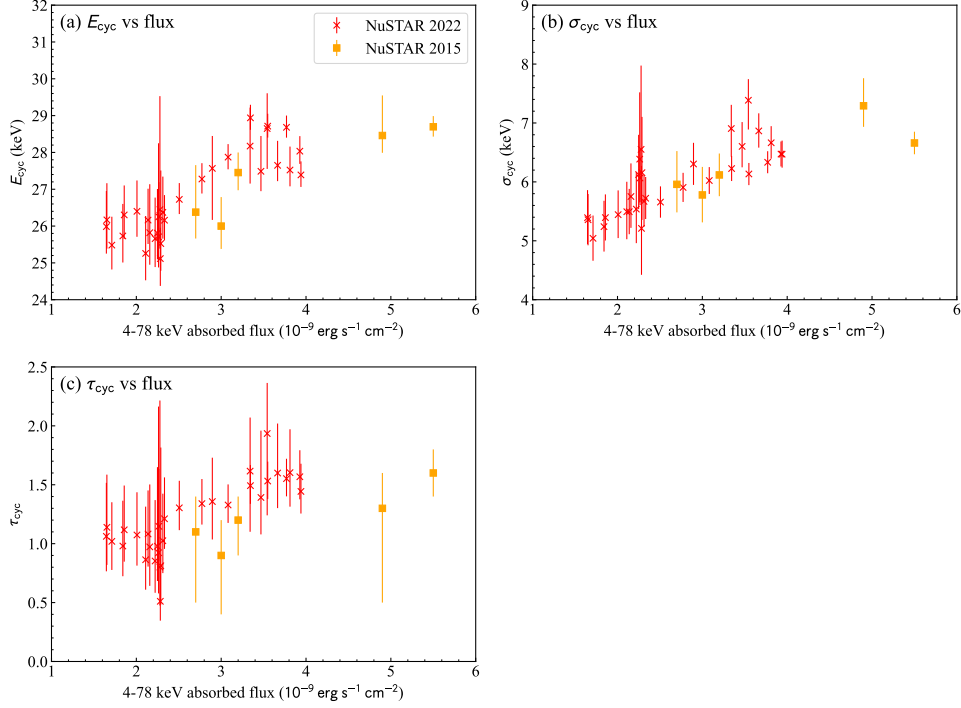


Figure 5.17: Same as Figure 5.15 but for the CRSF parameters.

## 5.4 Doubly-phase-resolved analysis

In Sections 5.2 and 5.3, we investigated the orbital- and spin-phase variabilities, but the effects of either of the orbital and spin phases were integrated and smeared out. It is necessary to give validity to these analyses by showing the orbital-phase variability preserves along the spin phase and vice versa. In this section, we resolve the observation data by the orbital and spin phases by taking a similar approach to Section 4.5. We first examine the orbital-phase variability of the pulse profiles in multiple energy bands to see the relation between the orbital- and spin-phase variabilities. We then perform doubly-phase-resolved spectroscopy to investigate the variabilities of the spectral parameters along the orbital and spin phases. We note that the doubly-phase-resolved spectroscopy is available thanks to the rich observation data over two cycles of the orbital periods.

### 5.4.1 Orbital-phase variability of pulse profiles

We generated orbital-phase-resolved pulse profiles for 3–78, 3–5, 5–10, 10–20, and 20–78 keV. Since Cen X-3 does not show any pulsation in the eclipse phases, we excluded them from this analysis. The division along the orbital phase is made by  $\Delta\Phi = 0.05$ . Similar to Section 4.5.2, we calculated the parameters of the pulse profiles and tracked their variabilities along the orbital phase.

Figure 5.18 shows the variations of pulse profile parameters, that is, the rms pulse fraction ( $PF_{\text{rms}}$ ) and the ratios among 0-th, 1st, and 2nd Fourier coefficients ( $c_1/c_0$ ,  $c_2/c_0$ ,  $c_2/c_1$ ). Contrary to the results from the 2015 NuSTAR observation in Figure 4.11, which show stable pulse profiles along the orbital phase within  $\sim 10\%$  variabilities, the pulse profiles generated from this observation data display significant variations along the orbital phase. Both the contributions from 1st and 2nd Fourier components exhibit certain variabilities along the orbital phase (Figure 5.18b and c), while the ratio between them is stable (Figure 5.18d). The pulse fraction is suppressed in Orbit 1 compared to Orbit 2, by 35% (3–5 keV), 18% (5–10 keV), 10% (10–20 keV), 9% (20–78 keV), calculated from the average values of  $PF_{\text{rms}}$  in Orbit 1 and Orbit 2. Since the mean values of  $PF_{\text{rms}}$  in the 2015 NuSTAR data are 0.28 (3–5 keV), 0.35 (5–10 keV), 0.49 (10–20 keV), and 0.56 (20–78 keV), these values approximately correspond to the maximum levels of Orbit 2 (also see Table 4.3).

Although the orbital-phase variabilities of pulse profiles are similar among all the energy bands, the 3–5 keV pulse profiles display the most prominent variability. The pulse fraction ranges from 0.08 to 0.36, and the low-pulse-fraction phases primarily reside in Orbit 1 or near-eclipse phases. It can be speculated that the low pulse fraction is related to low-flux phases because the orbital-phase intervals in Orbit 1 or near-eclipse phases have relatively low fluxes. Indeed, there are strong correlations between the pulse fraction and the spectral parameters, as shown in Figure 5.19. The high-pulse-fraction phases are associated with high fluxes and soft photon indices, while the low-pulse-fraction phases are associated with low fluxes and hard photon indices.

The correlations between the pulse fraction and spectral parameters strongly support the different variabilities in two emission components: the pulsed and the non-pulsed components. For example, let us consider what happens when the pulse fraction is reduced. It can be naturally speculated that the non-pulsed component becomes dominant over the pulsed component. According to the correlations in Figure 5.19, the observed flux is also reduced, and the photon index becomes hard in this situation. The decreased flux could be a consequence of a suppression of the pulsed component while the non-pulsed component keeps its original flux. The different degrees of suppression between the pulsed and non-pulsed components are attributed to the variability of the photon index. The non-pulsed component is likely to result in a hard photon index. Since the 3–5 keV pulse fraction exhibits the most variability, the non-pulsed component should be dominant in low-energy bands.

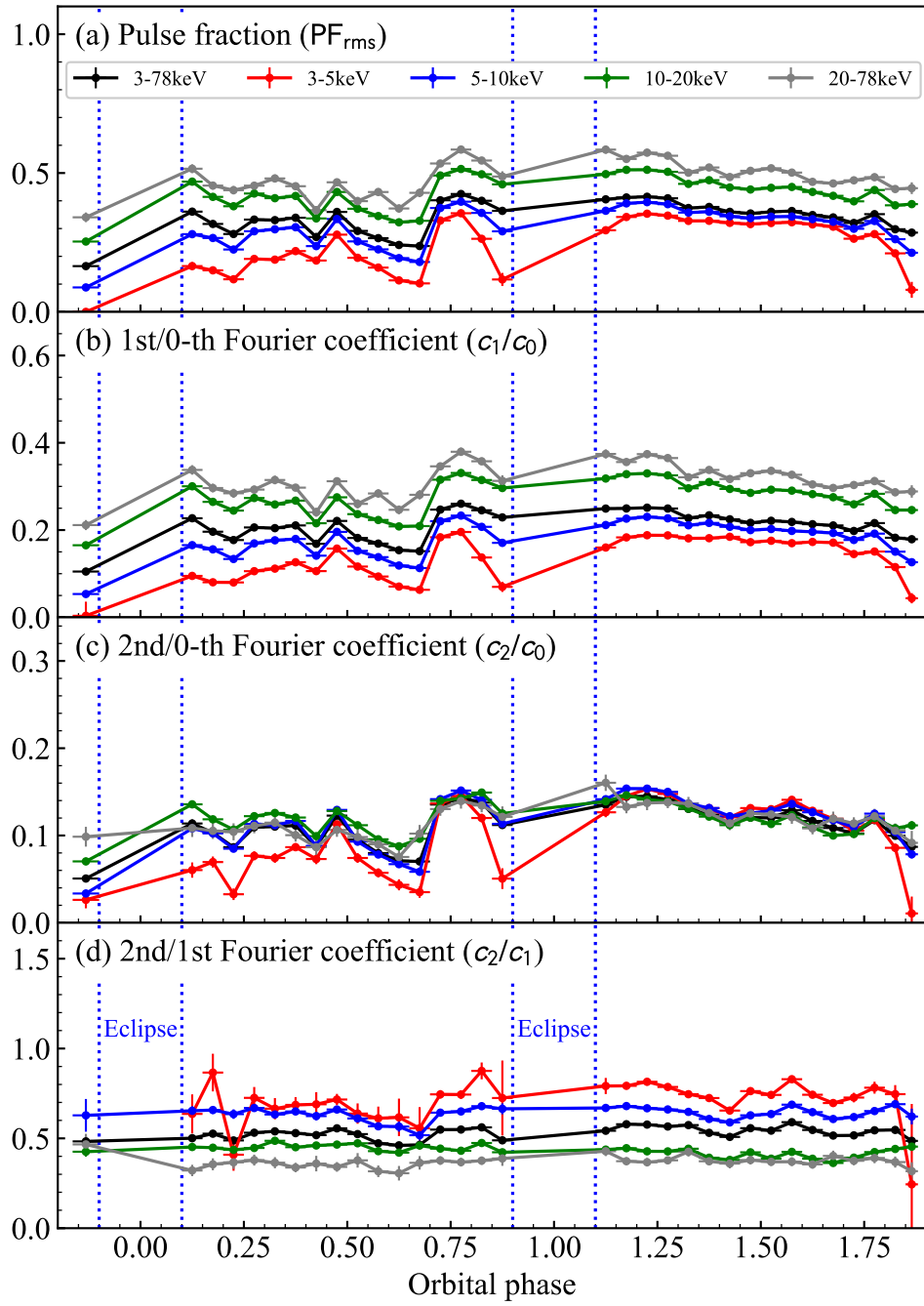


Figure 5.18: Variations of pulse profile parameters along the orbital phase calculated for multiple energy bands. Eclipse phases were excluded because of no pulsed emission.

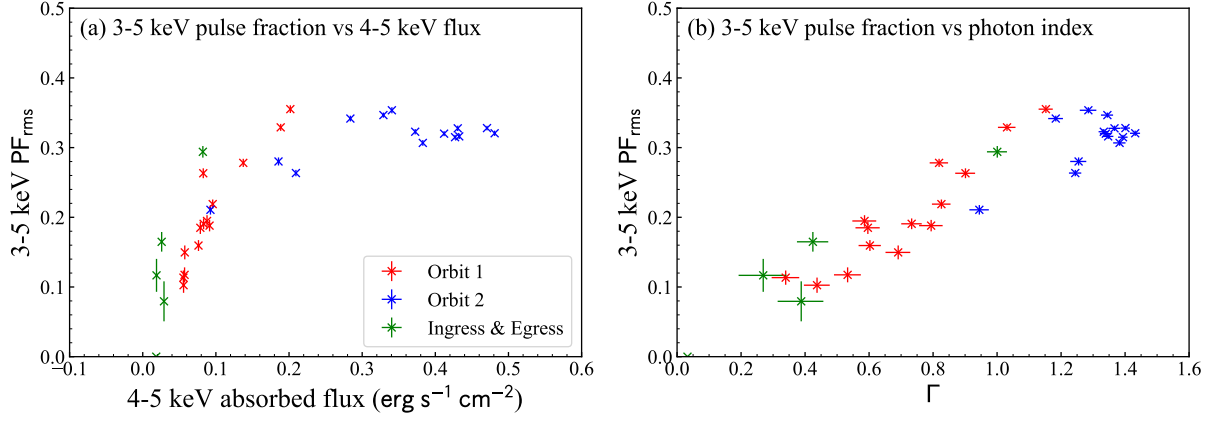


Figure 5.19: Relations between the pulse fraction and continuum spectral parameters along the orbital phase. (left) Relation between 3–5 keV pulse fraction and 4–5 keV absorbed flux. (right) Relation between 3–5 keV pulse fraction and photon index.

### 5.4.2 Doubly-phase-resolved spectroscopy

In order to investigate the spectral variability along both the orbital and spin phases, we performed spectroscopy on doubly-phase-resolved spectra. Since the spectral analysis needs a sufficient count of photons, we carefully determined the manner of the orbital- and spin-phase separations. In this analysis, the orbital phase was divided into intervals with  $\Delta\Phi = 0.04$ , and the eclipse phases were excluded because of no pulsations. The total number of the orbital-phase intervals was 41. The spin phase was divided into eight intervals named intervals A to H, and the definition is presented in Figure 5.20. Each spin-phase interval covers  $\Delta\phi = 0.125$ , and the central phase of interval A corresponds to  $\phi = 0.0$ .

The assumed model is the Fermi-Dirac cut-off power law with a Fe line and a CRSF, given by equation (4.15). The valid energy range is 4–78 keV, and the FPMA and FPMB spectra were fitted simultaneously. In this analysis, we set several parameter constraints on the model, consulting the actual situation of emission. The parameter constraints are as follows.

- $N_{\text{H}}^{\text{IM}}$  was fixed to  $1.1 \times 10^{22} \text{ cm}^{-2}$  (HI4PI Collaboration et al., 2016).
- $N_{\text{H}}$  should be constant along the spin phase. We performed a preliminary fitting on the spin-phase-averaged spectrum of each orbital-phase interval and determined the best-fit  $N_{\text{H}}$ . In the doubly-phase-resolved spectroscopy,  $N_{\text{H}}$  was fixed to these values.
- $E_{\text{Fe}}$  and  $\sigma_{\text{Fe}}$  were assumed to be constant along the spin phase. We fixed these parameters in the same manner as  $N_{\text{H}}$ . This fixture was applied to reduce the

instability of the fitting rather than reflect the physical conditions.

- CRSF parameters ( $E_{\text{cyc}}$ ,  $\sigma_{\text{cyc}}$ ,  $\tau_{\text{cyc}}$ ) were assumed to be constant among the orbital phase and differ among the spin phases. We adopted the best-fit values derived from the spin-phase-resolved spectroscopy in Section 5.3.2, averaging over every four spin-phase intervals. The parameters were fixed to the calculated values.

The remained free parameters consist of the photon index  $\Gamma$ , the cut-off energy  $E_c$ , the folding energy  $E_f$ , the normalization of the continuum, and the normalization of the Fe line ( $I_{\text{Fe}}$ ). The model successfully fitted all the  $41 \times 8$  spectra with acceptable chi-square values. The reduced chi-square values ranged from 0.9 to 1.3 with no distinctive biases, as shown in Figure 5.21.

Figure 5.22 presents the variabilities of the continuum fluxes in different energy bands. In all the panels in Figure 5.22, we can see that the magnitude correlations among different colors are highly preserved along the orbital phase. This indicates that the qualitative features of pulse profiles, such as phases of pulse maximum and pulse minimum, are constant, even though the pulse fractions show certain variations. The spin-phase intervals B (red) and C (blue) have comparable high fluxes in low-energy bands (4–5 and 5–10 keV), while the spin-phase interval C becomes the most prominent pulse maximum in high-energy bands (10–20 and 20–78 keV). This feature is consistent with the peak-phase shift along the energy axis presented in Figure 5.13, reflecting the non-negligible effects of the 2nd Fourier component in the low-energy bands.

Figure 5.23 shows the variabilities of the continuum parameters along the orbital and spin phases. The most characteristic is the variation in the photon index  $\Gamma$ . Similar to the flux variations, the photon index also preserves the relation among different spin phases. The spin-phase interval C (blue) mostly has the hardest photon index among the spin-phase intervals in a specific orbital-phase interval, and G (purple) mostly has the softest one. The cut-off energy  $E_c$  and folding energy  $E_f$  do not show significant variabilities. The only exception is the cut-off energy in spin-phase intervals E (magenta) and F (orange), which show significantly low values compared to other spin-phase intervals. A possible cause is an association with the second peak of the pulse profile around  $\phi \sim 0.65$ .

The doubly-phase-resolved spectroscopy shows that the spectral variability can be mostly characterized by the photon index. In Figure 5.24, we present the relation between the photon index and the continuum flux, plotted for all the doubly-phase-resolved spectra. Each color, representing a spin-phase interval, displays a clear positive correlation between these two parameters. The orbital-phase correlation of each color presents a very similar correlation profile with the spin-phase-averaged profile in Figure 5.8(b). A possible implication would be that the orbital-phase variability can be explained by a unified mechanism that is independent of the spin phase. We discuss possible mechanisms that induce the orbital- and spin-phase variabilities in Chapter 7, particularly focusing



on the variability of the photon index.

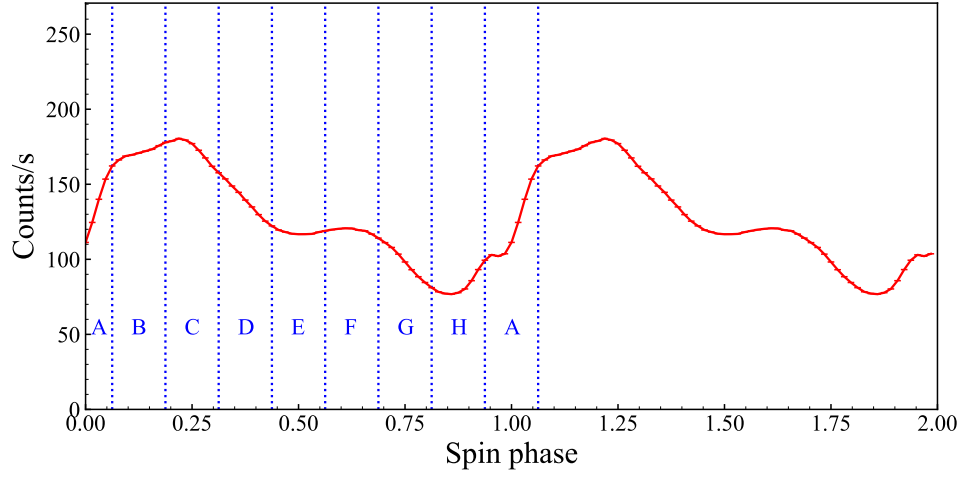


Figure 5.20: Definition of the spin-phase intervals for doubly-phase-resolved spectroscopy, overlaid on the 3–78 keV phase-averaged pulse profile.

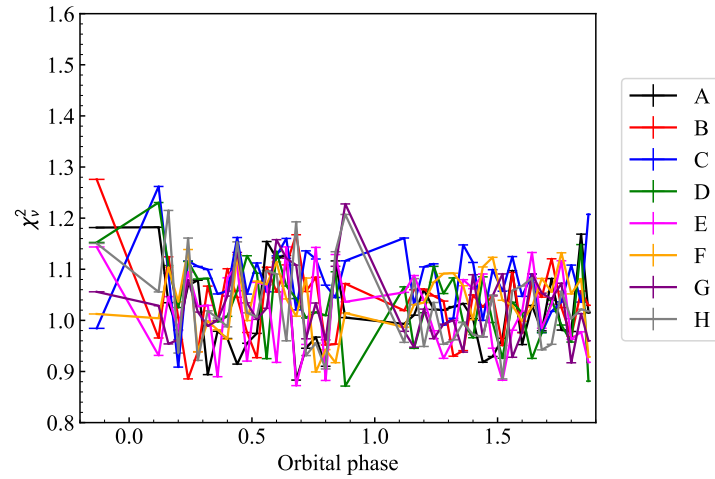


Figure 5.21: Reduced chi-square values of the doubly-phase-resolved spectroscopy. Different colors represent different spin-phase intervals from A to H.

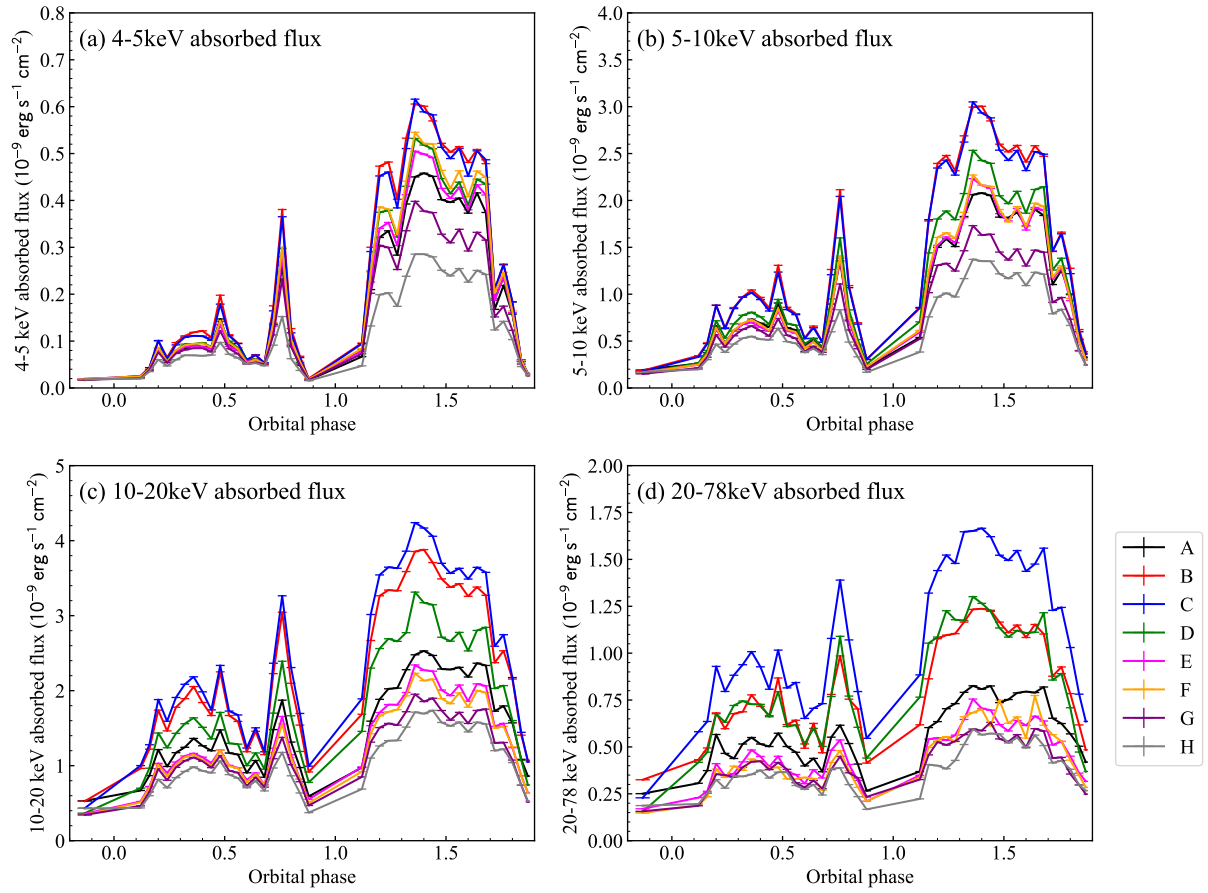


Figure 5.22: Variabilities of fluxes in different energy bands along the orbital and spin phases, derived from the doubly-phase-resolved spectroscopy. Error bars represent 90% confidence levels.

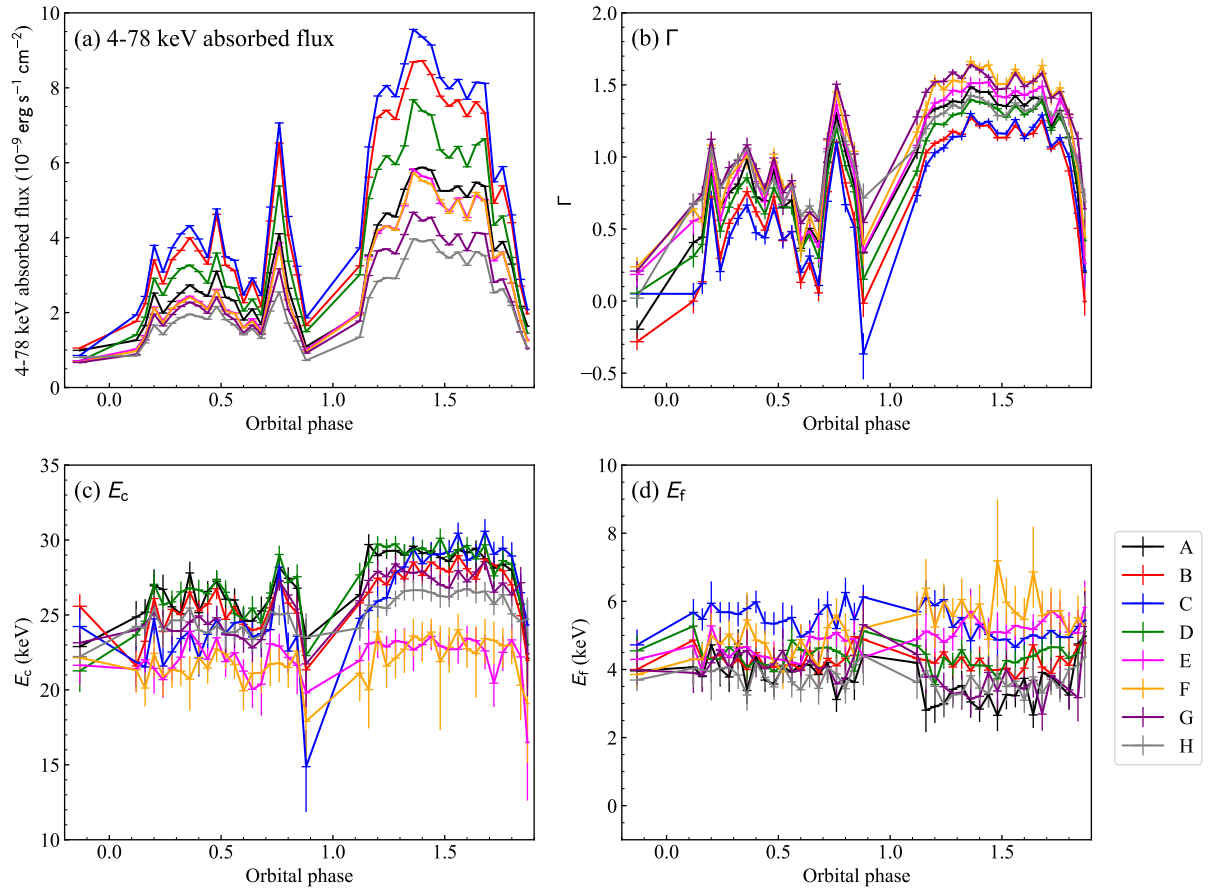


Figure 5.23: Variabilities of the continuum parameters along the orbital and spin phases, derived from the doubly-phase-resolved spectroscopy. Error bars represent 90% confidence levels.

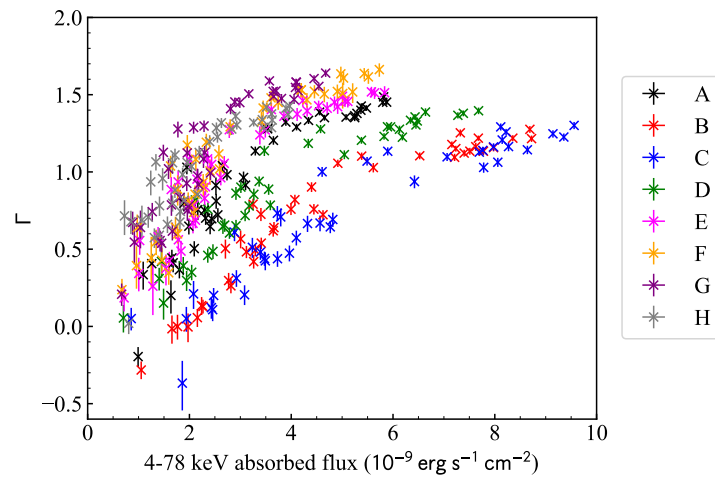


Figure 5.24: Relation between 4–78 keV absorbed flux and the photon index along the orbital and spin phases. Error bars represent 90% confidence levels.

## 5.5 Summary

In this chapter, we investigated the orbital- and spin-phase variabilities of Cen X-3 by analyzing NuSTAR observation data with a much longer exposure than that of Chapter 4. Some of the observational features are consistent with the short observation data, but there are a lot of updates from Chapter 4, thanks to the rich photon counts and long coverage over two orbital periods. The most notable observational feature we found is the photon index variability along the orbital phase. The 4–78 keV luminosity ranges from  $3.7 \times 10^{35} \text{ erg s}^{-1}$  to  $4.5 \times 10^{37} \text{ erg s}^{-1}$ , which can be characterized by the variability in the photon index ranging from -0.37 to 1.72. The photon index gets soft in the high-luminosity phases and hard in the low-luminosity phases, but it returns to soft values of  $\Gamma \sim 1.2$  exceptionally in the eclipse phase. The spin-phase variability is almost consistent with the results in Chapter 4, but the rich observation data allowed us to investigate it with much higher precision. The spin-phase variability of the continuum spectrum is characterized by the photon index, ranging from  $\Gamma = 1.30$  in the pulse minimum and  $\Gamma = 0.76$  in the pulse maximum. The pulse profiles display a gradual shift from a flat-peaked structure to a sharp-peaked structure as energy increases. The Fe line and the CRSF also exhibit spin-phase variabilities. The equivalent width of the Fe line is negatively correlated with the continuum flux, ranging from 0.1 keV to 0.4 keV, suggesting the Fe line emission originates from non-pulsed regions. The central energy, line width, and optical depth of the CRSF positively correlate with the continuum flux. The central energy ranges from 25.1 keV to 29.0 keV, corresponding to an  $\sim 15\%$  difference in the magnetic field strength. The doubly-phase-resolved analysis showed that the pulse profiles have certain variabilities along the orbital phase. The 3–5 keV pulse profile exhibits the most prominent variability, with the pulse fraction ranging from 0.1 to 0.4. The variation of the pulse fraction is synchronized with the continuum flux and photon index. The doubly-phase-resolved spectroscopy confirmed that the relative relations among the spectral parameters of different spin phases do not vary with the orbital phase. It supports the stability of the accretion flow, and the orbital-phase variability is likely caused by extrinsic factors apart from the neutron star. In the following chapter, we examine the soft X-ray properties of Cen X-3 with NICER observation data, particularly focusing on the spectrum below 3 keV, which is out of the NuSTAR coverage.

# Chapter 6

## Soft X-ray variability of Cen X-3 studied with NICER observation

In Chapters 4 and 5, we investigated the spectral variability of Cen X-3 utilizing NuSTAR observation data. However, the valid energy band is limited to  $> 3$  keV, and it is impossible to examine the low-energy features. Cen X-3 is reported to have a soft excess below  $\sim 3$  keV, which is approximated by a blackbody with a temperature of  $kT \sim 0.1$  keV (Burderi et al., 2000). NICER provides large effective areas in 0.2–12 keV and good timing resolution of  $< 300$  ns that is sufficient for the spin-phase-resolved analysis. In this chapter, we investigate the soft X-ray variability of Cen X-3 by analyzing the NICER archival data in 2017.

### 6.1 Observation and data reduction

NICER observed Cen X-3 in 2017 over five days from July 24 to 28 (ObsID: 1034070101–1034070105). About 2% of the duration is devoted to the observation of Cen X-3. We applied calibration and screening processes using the standard pipeline processing tool `nicerl2` contained in `HEASoft`. As a result, the net exposure over the five days was 8.79 ks. We excluded six detectors from the analysis among the 56 detectors, following the recommendation in the NICER Data Analysis Threads<sup>1</sup>. Four of them are disabled detectors at the time of the launch (detector IDs: 11, 20, 22, and 60), and the other two are enabled but noisy detectors (detector IDs: 14 and 34). The light curves and spectra were extracted from the cleaned event file using `XSELECT`, which is also a NASA standard analysis tool. The barycentric correction was applied to the extracted light curves. The response matrix file (RMF) and ancillary response file (ARF), which are necessary to conduct spectral analysis, were generated by `nicerrmf` and `nicerarf`, respectively.

---

<sup>1</sup>[https://heasarc.gsfc.nasa.gov/docs/nicer/analysis\\_threads/](https://heasarc.gsfc.nasa.gov/docs/nicer/analysis_threads/)

The background spectra were modeled and generated by `nibackgen3C50` (for a detailed description, see Section 3.2.3).

Similar to Section 5.1.2, we searched for the orbital parameters by applying a  $Z_2^2$  test on the observation data. The  $Z_2^2$  test returned the following values as the best-fit parameter set.

$$\begin{aligned} P_{\text{orb}} &= 2.087 \text{ days (fixed)}, \\ P_{\text{spin}} &= 4.80078 \pm 0.00005 \text{ s}, \\ a_x \sin i &= 39.66 \text{ lt-s (fixed)}, \\ \Phi_{\text{start}} &= 0.770 \pm 0.005. \end{aligned} \tag{6.1}$$

In the parameter search, we fixed  $P_{\text{orb}}$  and  $a_x \sin i$  to the values in Bildsten et al. (1997) because of the insufficient photon counts. Figure 6.1 shows the NICER light curve for 0.2–12 keV. The observation started at  $\Phi = 0.77$  and stopped at  $\Phi = 2.40$ . Same as Chapter 5, orbital intervals of  $0.9 < \Phi < 1.1$  and  $1.9 < \Phi < 2.1$  were defined as eclipse phases, which display lower count rates than other orbital intervals. The average count rates of the eclipse and out-of-eclipse phases were 9.0 counts/s and 60.4 counts/s, respectively.

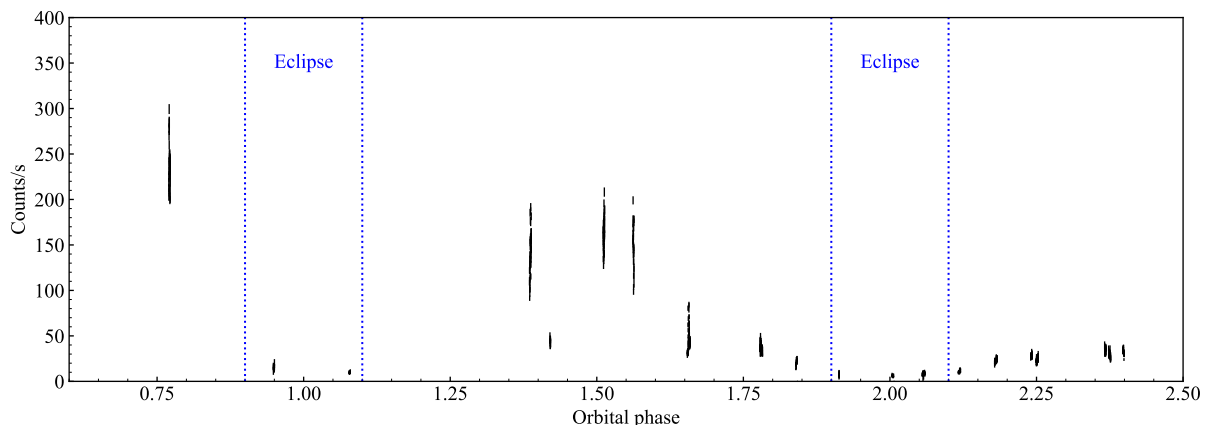


Figure 6.1: 0.2–12 keV NICER light curve of Cen X-3, plotted as a function of orbital phase. The blue dotted lines represent the eclipse phases.

## 6.2 Spectroscopy

In order to investigate the soft X-ray variability of Cen X-3, we divided the NICER observation data into several intervals and performed spectral analysis on each spectrum. The main purpose of this analysis is to evaluate the soft excess component lying below  $\sim 3$  keV. We consulted the light curve and determined the orbital intervals based on the count rate variability. Figure 6.2 shows the definition of the orbital intervals used for

NICER analysis. They are named intervals a, b, c, ..., k, and intervals b and i correspond to the eclipse phases.

As a model description, we adopted a power-law function without a cut-off to reproduce the continuum, as the quasi-exponential cut-off of Cen X-3 is beyond the NICER energy band. We also added a blackbody function and three Gaussian components to reproduce the soft excess component and Fe emission lines (neutral, He-like, and H-like), respectively. The model spectrum is given by

$$\frac{dN(E)}{dE} \propto f_{\text{phabs}} \times [f_{\text{pl}} + f_{\text{bb}} + f_{\text{gauss}} + f_{\text{gauss}} + f_{\text{gauss}}], \quad (6.2)$$

where  $f_{\text{pl}}$  and  $f_{\text{bb}}$  are the power-law function and blackbody function, respectively, given by

$$f_{\text{pl}}(E) = A_{\text{pl}} E^{-\Gamma}, \quad (6.3)$$

$$f_{\text{bb}}(E) = \frac{8.0525 \times E^2}{(kT)^4 [\exp(E/kT) - 1]} \left( \frac{L_{\text{bb}}}{10^{39} \text{ erg s}^{-1}} \right) \left( \frac{D}{10 \text{ kpc}} \right)^{-2}. \quad (6.4)$$

$k$ ,  $T$ ,  $L_{\text{bb}}$ , and  $D$  represent the Boltzmann constant, the blackbody temperature, the blackbody luminosity, and the distance to the source, respectively. The definition of  $f_{\text{gauss}}$  is given in equation (4.8). In the spectral analysis, we set the valid energy band to 0.6–10 keV because of high background levels at  $< 0.6$  keV and  $> 10$  keV. Same as Chapters 4 and 5, the absorption column density by the interstellar medium was set to  $1.1 \times 10^{22} \text{ cm}^{-2}$ . We adopted the Cash statistics (Cash, 1979) in the spectral fitting, which is free from the binning ambiguity, in order to evaluate the three Fe lines accurately.

Figure 6.3 presents the fitting results of the intervals a to k. The spectra were well reproduced by the model and the residuals have no distinctive features. The best-fit parameters are summarized in Table 6.1. The photon index  $\Gamma$  ranges from  $-0.17$  to  $1.14$  in the out-of-eclipse phases, which is a comparable range to the photon indices derived from the 2022 NuSTAR observation (see Figure 5.8b). The positive correlation between the photon index and the continuum flux, seen in the NuSTAR data, still holds for the NICER data. The high-flux phases (a, c, e, f) have softer photon indices of  $\Gamma = 0.86$ – $1.14$ , while the low-flux phases (d, g, h, j, k) have harder photon indices of  $\Gamma = -0.17$ – $0.55$ . In the eclipse phases (b, i), the photon indices return to even softer values of  $\Gamma = 1.7$ ,  $2.2$ , which is also a similar trend to the NuSTAR analysis (Figure 5.7).

The blackbody temperature  $kT$  ranges from  $0.09$  to  $0.25$  keV, which is consistent with the result of previous research of  $kT \sim 0.1$  keV (Burderi et al., 2000). However, the luminosity of the blackbody component has a wide range in our analysis, from  $\sim 10^{35} \text{ erg s}^{-1}$  to  $\sim 10^{38} \text{ erg s}^{-1}$ . Since the blackbody radiation is assumed to originate from the thermal emission of the accretion disk, it is unrealistic to have such a high variability. Moreover, it is unlikely to have a much brighter luminosity than the neutron star ( $\sim 5 \times 10^{37} \text{ erg s}^{-1}$ ; Suchy et al., 2008). A possible cause that induced the unrealistic

results would be the simple treatment of the power-law model. Therefore, we conclude that the current model is no more than a phenomenological treatment, and we need to adopt a more realistic model to explain the physical origin of the soft excess. We discuss it in Chapter 7 by combining the NICER data with the NuSTAR observation data.

The Fe line also exhibits variability along the orbital phase.  $I_{\text{Fe},1}$ ,  $I_{\text{Fe},2}$ , and  $I_{\text{Fe},3}$  in Table 6.1 denote the intensities of the neutral, He-like, and H-like Fe emission lines, respectively. Among the three lines, the neutral Fe line is the most significant and dominant while the H-like Fe line could not be detected in many orbital intervals. The dominance of the neutral Fe line does not hold in the eclipse phases, and the He-like Fe line becomes the most dominant line in these phases (intervals b, i). This trend is consistent with the NuSTAR analysis result, in which the central energy of the Fe line shifts to higher energy in the eclipse phases (see Figure 5.10a). It can be speculated that the neutral Fe line originates from the proximity of the neutron star while the highly-ionized Fe lines originate from distant regions from the neutron star, that is, the scattering by the highly-ionized stellar wind.

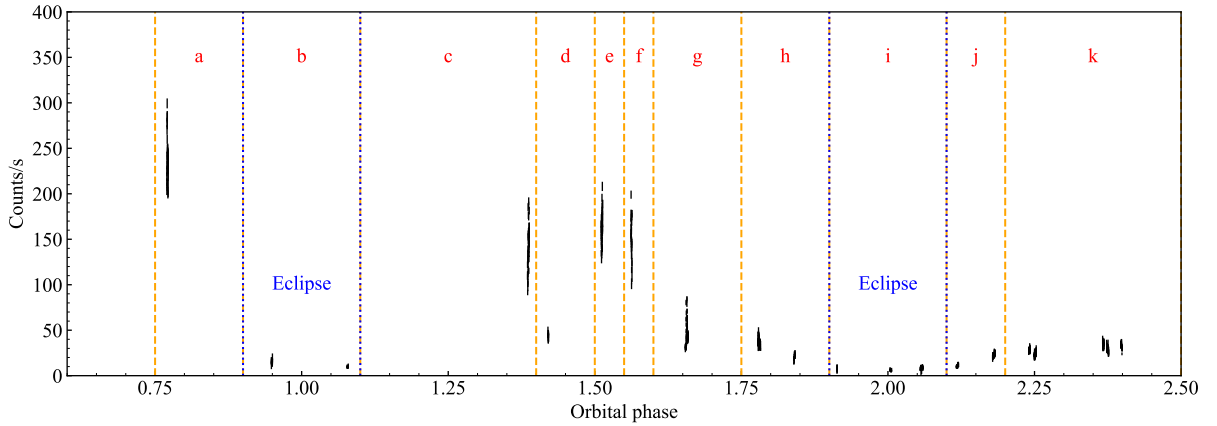


Figure 6.2: Same as Figure 6.1 but overlaid with the definition of the orbital intervals.



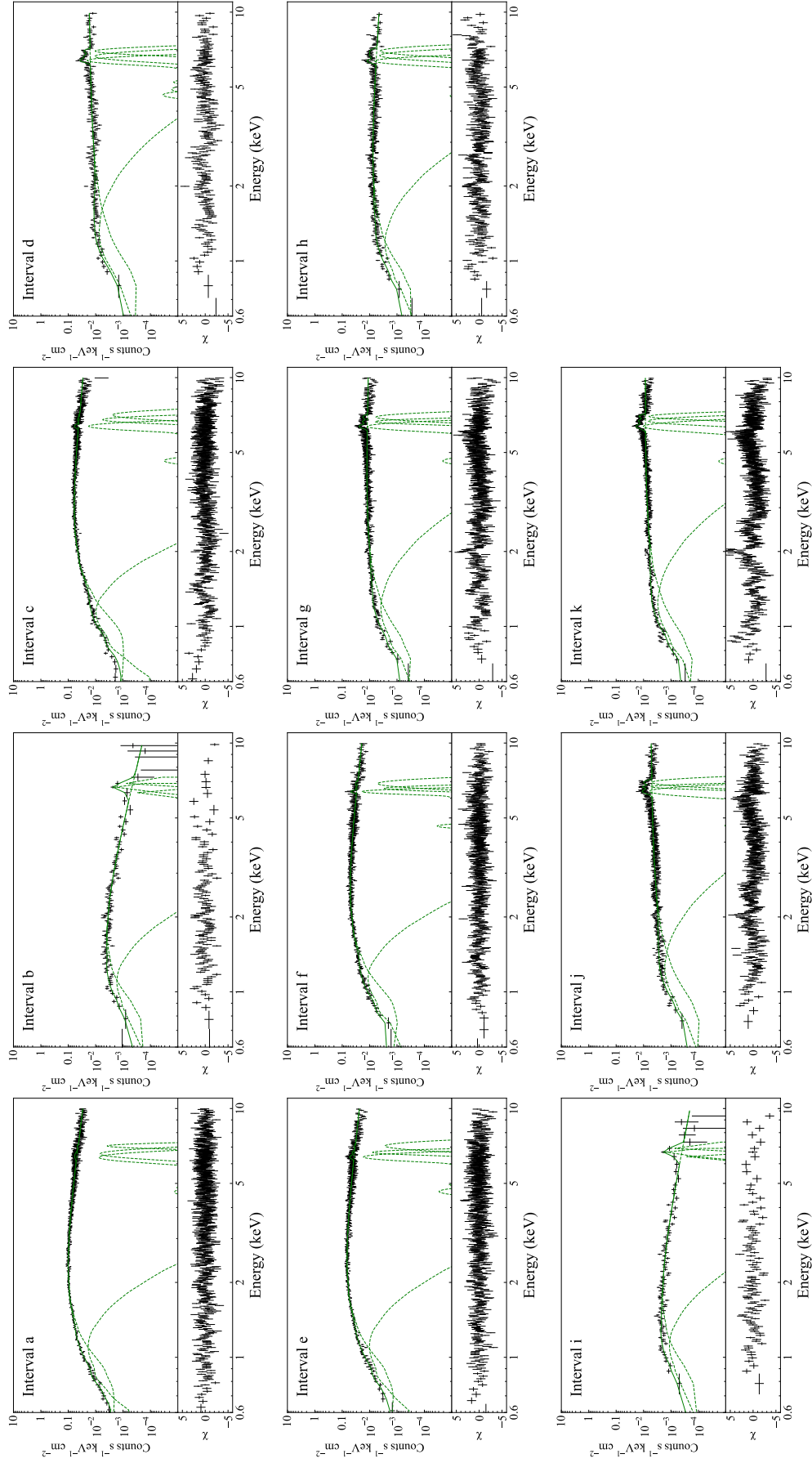


Figure 6.3: Fitting results on orbital-phase-resolved spectra. See text for the model description. The spectra are binned for display purposes, but the fitting was performed utilizing the unbinned data. The bottom panels represent the residuals between the data and the model. The contributions from spectral components are represented by dashed lines.

Table 6.1: Best-fit parameters of spectral fitting.<sup>a</sup>

Interval	$N_{\text{H}}$ ( $10^{22} \text{ cm}^{-2}$ )	$kT$ (keV)	$L_{\text{bb}}^b$ ( $10^{38} \text{ erg s}^{-1}$ )	$\Gamma$	PL flux <sup>c</sup>	$I_{\text{Fe},1}^d$	$I_{\text{Fe},2}^d$	$I_{\text{Fe},3}^d$	C-stat <sup>e</sup>
a	$0.44 \pm 0.06$	$0.109 \pm 0.004$	$0.6 \pm 0.2$	$1.14 \pm 0.03$	$420 \pm 6$	$< 4$	$< 4$	$< 1.4$	943
b	$< 0.28$	$0.12 \pm 0.03$	$0.024 \pm 0.020$	$2.2 \pm 0.2$	$5.9 \pm 0.4$	$0.15 \pm 0.1$	$0.4 \pm 0.2$	$< 0.45$	1035
c	$1.12 \pm 0.07$	$0.089 \pm 0.004$	$4.4 \pm 1.9$	$0.86 \pm 0.03$	$353 \pm 4$	$4.2 \pm 0.9$	$1.3 \pm 0.9$	$< 1.6$	1188
d	$< 0.04$	$0.24 \pm 0.02$	$0.007 \pm 0.001$	$-0.17 \pm 0.09$	$124 \pm 6$	$5 \pm 2$	$< 6$	$< 4$	998
e	$0.47 \pm 0.08$	$0.109 \pm 0.006$	$0.3 \pm 0.1$	$1.01 \pm 0.04$	$310 \pm 4$	$4 \pm 1$	$1.2 \pm 0.7$	$< 1.7$	978
f	$0.66 \pm 0.10$	$0.10 \pm 0.01$	$0.7 \pm 0.4$	$1.00 \pm 0.06$	$251 \pm 2$	$2.9 \pm 0.7$	$< 1.2$	$< 2.5$	954
g	$< 0.02$	$0.18 \pm 0.01$	$0.0063 \pm 0.0009$	$0.18 \pm 0.03$	$95 \pm 2$	$3.0 \pm 0.6$	$1.0 \pm 0.6$	$1.5 \pm 0.5$	1217
h	$< 0.03$	$0.18 \pm 0.02$	$0.005 \pm 0.001$	$0.55 \pm 0.06$	$46 \pm 1$	$1.6 \pm 0.5$	$1.3 \pm 0.7$	$1.2 \pm 0.6$	1129
i	$< 0.3$	$0.14 \pm 0.03$	$0.006 \pm 0.004$	$1.7 \pm 0.2$	$4.3 \pm 0.4$	$0.11 \pm 0.09$	$0.3 \pm 0.1$	$0.24 \pm 0.13$	1037
j	$< 0.02$	$0.21 \pm 0.02$	$0.0019 \pm 0.0002$	$-0.14 \pm 0.05$	$38.7 \pm 0.9$	$1.8 \pm 0.2$	$0.8 \pm 0.2$	$1.4 \pm 0.2$	1201
k	$< 0.01$	$0.21 \pm 0.01$	$0.0035 \pm 0.0003$	$-0.01 \pm 0.03$	$66 \pm 1$	$3.0 \pm 0.2$	$1.6 \pm 0.4$	$1.3 \pm 0.3$	1500

<sup>a</sup> Errors denote 90% confidence levels.

<sup>b</sup> Assuming a distance of 6.4 kpc (Arnason et al., 2021).

<sup>c</sup> 2–10 keV power-law flux in units of  $10^{-11} \text{ erg s}^{-1} \text{ cm}^{-2}$ .

<sup>d</sup>  $I_{\text{Fe},1}$ ,  $I_{\text{Fe},2}$ , and  $I_{\text{Fe},3}$  represent the intensity of neutral, He-like, and H-like Fe emission lines, respectively.

In units of  $10^{-3} \text{ photons s}^{-1} \text{ cm}^{-2}$ .

<sup>e</sup> d.o.f.=964 for all the cases.

### 6.3 Pulse profile

We generated energy-resolved pulse profiles from the NICER observation data, similar to Sections 4.4.1 and 5.3.1. Unlike the NuSTAR observation data, NICER observation is non-continuous and has a much shorter exposure. Therefore, the orbital parameters measured by the  $Z_2^2$  test (equation 6.1) are not accurate enough to perform the coherent spin-phase-resolved analysis. In this analysis, we generated pulse profiles for each orbital interval, defined in Figure 6.2. Among the 11 orbital intervals, coherent pulsations were detected in four intervals (a, c, e, f). The other seven intervals have insufficient photon counts to detect a significant pulsation.

Figure 6.4 presents the energy dependence of the pulse fractions for the four orbital intervals. Although the pulse fractions differ among the orbital intervals, they do not show much variance with the energy below 5 keV, settling at  $\sim 20\%$ . The significant pulsation in the low energy band, especially below 2 keV, indicates the dominance of the pulsed component. If the soft excess component originates from the thermal emission of the accretion disk, it could not have pulsations. Therefore, the luminosity of the soft excess component should be much lower than the neutron star luminosity. As indicated in Section 6.2, the extremely high luminosities of  $L_{\text{bb}}$  seen in several orbital intervals (Table 6.1) do not accurately reflect the actual situation of the emission region.

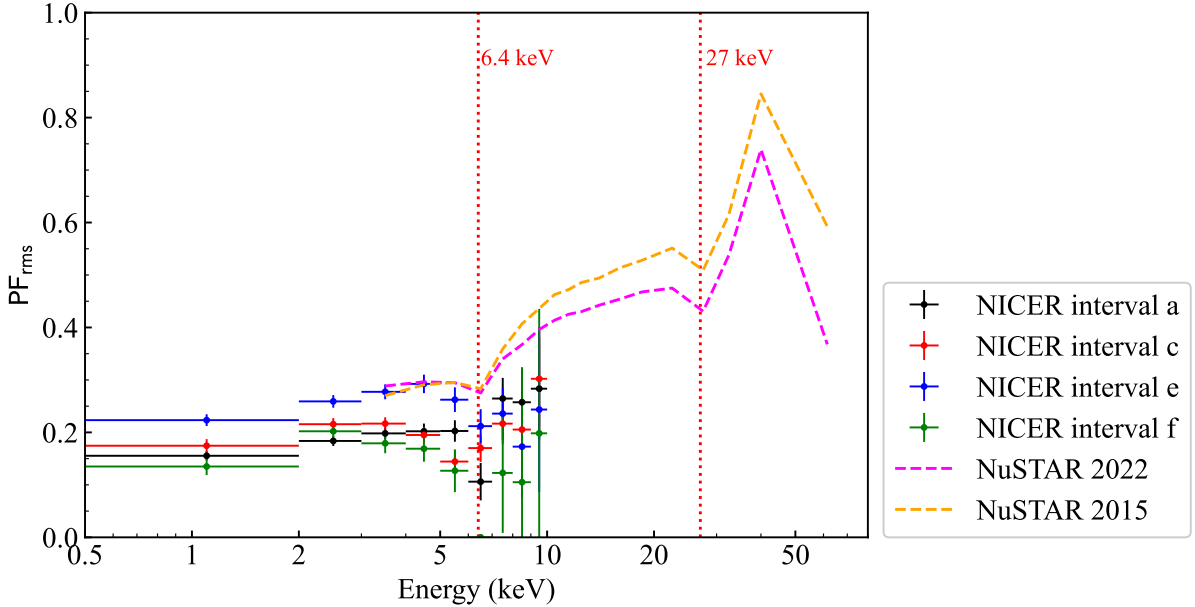


Figure 6.4: Energy dependence of pulse fractions for orbital intervals a, c, e, and f. The NuSTAR results obtained in Chapters 4 and 5 are overlaid for comparison.

## 6.4 Summary

The soft X-ray properties of Cen X-3 became clear in this chapter. The NICER observation data allowed us to determine the spectral properties below 3 keV, which is expressed by an additional blackbody function with a temperature ranging from  $kT = 0.09$  keV to  $kT = 0.25$  keV. The luminosity of the blackbody has a wide range from  $\sim 10^{35}$  erg s $^{-1}$  to  $\sim 10^{38}$  erg s $^{-1}$ . In order to accurately evaluate the luminosity of the blackbody, we need a more physically-motivated model, which we discuss in the next chapter. The pulse profile analysis resulted in a consistent view with the NuSTAR results. The pulsed emission extends down to  $\sim 1$  keV, with a pulse fraction of  $\sim 0.2$ .

# Chapter 7

## Discussions on the circumstellar medium of Cen X-3

Unlike other disk-fed X-ray pulsars (e.g., Her X-1, LMC X-4, SMC X-1), Cen X-3 is a unique source that displays a stochastic spectral variability with no characteristic timescale (e.g., Paul et al., 2005; Raichur & Paul, 2008b). However, a comprehensive study has yet to be carried out on the continuous spectral variability of Cen X-3 up to date because of the highly complicated variations in spectral shape and pulse profile. In Chapters 4, 5, and 6, we presented a detailed analysis on the X-ray observation data of Cen X-3 from soft to hard X-ray bands and investigated orbital-phase variabilities of the spectrum and pulse profile. In this chapter, we give physical interpretations on the continuous orbital-phase variability for the first time. We summarize the analysis results and discuss them from the point of view of the stability of the accretion stream and circumstellar medium of Cen X-3. We note that the detailed analysis on the spin-phase variability, which is related to the structure of the accretion flow, is given later in Chapter 9 together with Her X-1.

### 7.1 Stellar wind obscuration as the main cause of the orbital-phase variability

Possible explanations for the orbital-phase spectral variability would be the variation of the accretion rate or the obscuration by the stellar wind. Indeed, the orbital-phase-resolved spectroscopy on the NuSTAR short-time observation suggests that the contributions from these two effects are comparable, causing  $\sim 10\%$  flux variability respectively (Section 4.3.2). However, the accumulating observational properties obtained in the NuSTAR long observation (Chapter 5) and NICER observation (Chapter 6) allowed us to conclude that the stellar wind obscuration has a much more influence on the orbital-

phase variability than the intrinsic effects. The observational bases on which we support the stellar wind obscuration rather than the intrinsic variability of the accretion rate are summarized as follows.

- The photon index positively correlates with the continuum flux along the orbital phase (Figure 5.8b). If the change in the accretion rate induces the flux variability, the correlation between these two parameters should be negative. A good example is the spectral variability of Vela X-1. The hardening of the spectrum synchronized with the enhanced luminosity is reported, which can be interpreted as the enhancement in the optical depth of Comptonization inside the accretion column (Odaka et al., 2013, 2014). The positive correlation between the photon index and the continuum flux is likely to be induced by other mechanisms than the variability of the accretion rate.
- According to Figure 5.8(b), the photon index becomes significantly hard in all the ingress and egress phases. If the spectral variability is due to the intrinsic factor, it should be independent of the orbital phase. In these phases, the stellar wind absorption becomes large, and the large degree of the absorption could be somehow linked to the hardening of the photon index.
- In the eclipse phases, the photon index returns to soft values comparable to those in the “normal” out-of-eclipse phases,  $\Gamma \sim 1.2$  for the NuSTAR analysis (Figure 5.8b) and  $\Gamma \sim 2.0$  for the NICER analysis (Table 6.1). Since the emission in the eclipse phase originates from the scattering by the stellar wind, the observed spectral shape is similar to the intrinsic spectrum of the neutron star, although the normalization is greatly reduced. It can be speculated that the intrinsic emission from the neutron star is stable and has a photon index of  $1 < \Gamma < 2$ . The harder photon indices in the low-flux phases ( $\Gamma < 1$ ) could be due to extrinsic factors.
- The equivalent width of the Fe line negatively correlates with the continuum flux (Figure 5.10d). The Fe line is considered to be a consequence of the illumination of the circumstellar medium by the neutron star radiation. If the flux variability is due to purely intrinsic factors, the Fe line intensity should be proportional to the continuum flux, which leads to a constant equivalent width. The enhancement of the equivalent width in the low-flux phases suggests that the Fe line flux is less suppressed than the main emission component due to difference in emission region.
- Although the pulse profile shows large orbital-phase variability in the pulse fraction, the ratio between the 1st and 2nd Fourier coefficients is preserved along the orbital phase (Figure 5.18). This result indicates that only the ratio between pulsed emission and non-pulsed emission varies with the orbital phase, and the intrinsic

emission pattern from the neutron star is approximately constant. Such variability should be caused by extrinsic factors rather than the intrinsic variability of the accretion flow.

- The positive correlation between the photon index and the continuum flux still holds even when we focus on a specific spin-phase interval (Figure 5.24). The correlation profiles are similar among all the spin-phase intervals. A possible explanation would be that the orbital-phase variability is caused by extrinsic factors independent of the spin phase.

In order to examine this hypothesis, we need to assume a model function that describes the intrinsic emission from the neutron star. In this analysis, we divided the 2022 NuSTAR observation data into multiple intervals with  $\Delta\Phi = 0.05$  and searched for the photon index variation. We found that the orbital interval of  $\Phi = 1.40\text{--}1.45$  have the softest photon index among all the orbital intervals. Thus, we defined  $\Phi = 1.40\text{--}1.45$  as the “non-obscured” phase and adopted the spectrum in this interval as the intrinsic emission from the neutron star. The best-fit spectral parameters in this interval are summarized in Table 7.1, which we treat as the pure emission from the neutron star. Hereafter, we describe the intrinsic emission spectrum from the neutron star as  $f_{\text{NS}}$ . The mathematical expression is given by

$$f_{\text{NS}} = f_{\text{FDcut}} \times f_{\text{gabs}}, \quad (7.1)$$

where the parameters of  $f_{\text{FDcut}}$  and  $F_{\text{gabs}}$  are fixed to the values listed in Table 7.1. Note that  $f_{\text{NS}}$  does not necessarily reflect the actual emission from the neutron star because we only need to investigate the relative variability among the orbital-phase-resolved spectra.

Table 7.1: Spectral parameters for intrinsic emission from neutron star. <sup>a</sup>

parameter	value
$\Gamma$	1.42
$E_{\text{c}}$ (keV)	28.3
$E_{\text{f}}$ (keV)	4.30
$A_{\text{FDcut}}^a$ (photons $\text{keV}^{-1} \text{ s}^{-1} \text{ cm}^{-2}$ at 1 keV)	0.705
$E_{\text{cyc}}$ (keV)	27.5
$\sigma_{\text{cyc}}$ (keV)	6.31
$\tau_{\text{cyc}}$	1.32

<sup>a</sup> Normalization of the Fermi-Dirac cut-off power law.

## 7.2 Stellar wind model

Before measuring the effect of the stellar wind, we briefly describe the properties of the stellar wind of Cen X-3 derived from previous researches. We assumed a simple radiation-driven wind model based on the CAK model (Castor et al., 1975), in which the velocity profile is given by

$$v(r) = v_{\infty} \left(1 - \frac{R_*}{r}\right)^{\beta}, \quad (7.2)$$

where  $r$ ,  $v_{\infty}$ , and  $R_*$  denote the radial distance from the center of the companion star, the terminal velocity of the wind, and the radius of the companion star, respectively.  $\beta$  is a parameter that determines the wind acceleration. By mass conservation, the density profile is given by

$$n(r) = \frac{\dot{M}_*}{4\pi\mu m_p r^2 v(r)}, \quad (7.3)$$

where  $\dot{M}_*$  is the mass loss rate of the companion star and  $\mu m_p$  is the average gas mass per hydrogen atom.

We adopted the stellar wind parameters of Cen X-3 based on the calculation of previous studies. The radius of the companion star was set to  $R_* = 12.1R_{\odot}$  (Ash et al., 1999). The mass loss rate was calculated from the spectral type of the companion star, which is  $\dot{M}_* \sim 5.3 \times 10^{-7} M_{\odot} \text{ yr}^{-1}$  (Falanga et al., 2015). The terminal velocity of the stellar wind was measured by Wojdowski et al. (2003) utilizing Chandra HETG data, yielding  $v_{\infty} \sim 500 \text{ km s}^{-1}$ . The index of the velocity profile was set to  $\beta = 0.8$ , consulting the typical value suggested by Friend & Abbott (1986). Assuming the solar chemical abundances, we set  $\mu = 1.3$ . We can calculate the number density of the stellar wind at any given point using these parameters.

What we observe is the column density, which is the integration of the number density along the line of sight. Using the inclination angle of  $70.2 \text{ deg}$  (Ash et al., 1999), we calculated the column density  $N_{\text{H}}$  at multiple orbital phases. Figure 7.1 presents the calculation result. In most of the orbital phase, the column density settles at  $\sim 3 \times 10^{22} \text{ cm}^{-2}$ . In the ingress and egress phases, the column density is enhanced to  $N_{\text{H}} \sim 1\text{--}5 \times 10^{23} \text{ cm}^{-2}$ .



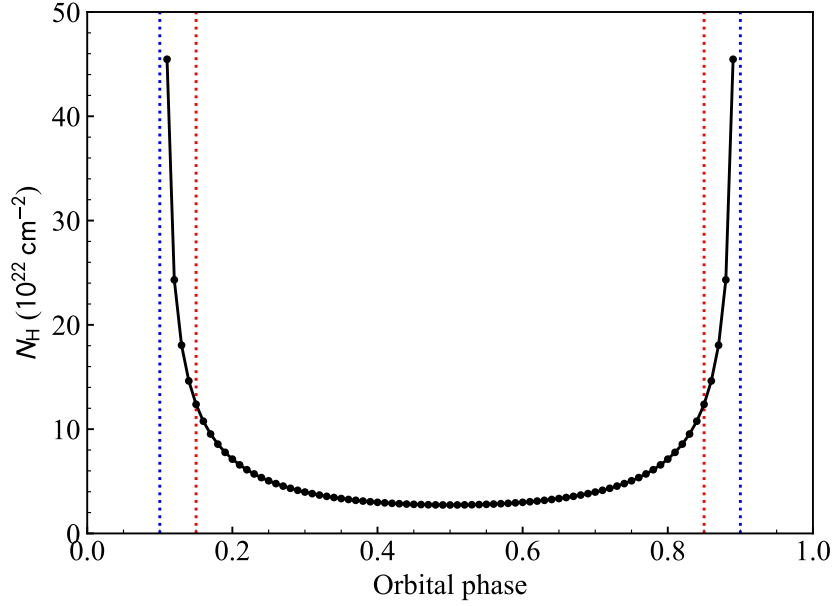


Figure 7.1: Column density of the stellar wind of Cen X-3 as a function of the orbital phase. The stellar wind parameters are  $R_* = 12.1R_\odot$ ,  $\dot{M}_* = 5.3 \times 10^{-7} M_\odot \text{ yr}^{-1}$ ,  $v_\infty = 500 \text{ km s}^{-1}$ ,  $\beta = 0.8$ ,  $\mu = 1.3$ , and an inclination angle of  $70.2^\circ$  (see text). The blue dotted lines represent the beginning and end of the eclipse, and the red dotted lines represent the end of the egress and the start of the ingress.

### 7.3 Physical origins of X-ray emission in eclipse phase

Firstly, we tried to give a physical interpretation of the X-ray spectrum in the eclipse phase. In the eclipse phase, the direct emission from the neutron star is entirely obscured by the companion star, and we only observe the reprocessed photons that are scattered by the highly ionized stellar wind. The enhanced He-like Fe line in the eclipse phase observed in the NICER data (Table 6.1) supports this picture. The spectrum in the eclipse phase gives us a lot of information about the stellar wind, as the reprocessed component is invisible in other phases due to dominant direct emission from the neutron star.

We assumed a simple geometry like Figure 7.2. The photons emitted from the neutron star are scattered by the stellar wind with a column density of  $N_H^{\text{CS}}$ . Then they travel to the observer with the attenuation due to the photoelectric absorption by the stellar wind with a column density of  $N_H^{\text{PE}}$ . The model spectrum is given by

$$\frac{dN}{dE} \propto \exp \left[ - (N_H^{\text{IM}} + N_H^{\text{PE}}) \sigma_{\text{abs}}(E) \right] \times \left[ R_{\text{CS}}(N_H^{\text{CS}}) * f_{\text{NS}} + f_{\text{gauss}} \right], \quad (7.4)$$

where  $R_{\text{CS}}$  represents the convolution model that reproduces the Compton scattering by the stellar wind.  $N_H^{\text{IM}} = 1.1 \times 10^{22} \text{ cm}^{-2}$  denotes the column density of the interstellar

medium.  $f_{\text{NS}}$  is the intrinsic emission from the neutron star defined in equation (7.1) with the fixed parameters listed in Table 7.1.

Since no model is implemented in **XSPEC** that reproduces the convolution function  $R_{\text{CS}}$ , we constructed it with a simulation-based calculation. We utilized a Monte-Carlo simulation library **MONACO** (Odaka et al., 2011), which can calculate physical processes in celestial objects based on three-dimensional geometries. We performed a simulation with a spherical cloud composed of a fully ionized cold plasma with a radial column density of  $N_{\text{H}} = 10^{22} \text{ cm}^{-2}$ . The abundance was set to the solar chemical abundance. The seed photons are emitted from the center of the cloud, and they travel toward outside the cloud, with a part of them experiencing Compton scattering. Figure 7.3 presents a schematic illustration of the simulation setup. We simulated  $10^9$  photons with various incident energies ranging from 3 to 78 keV and generated an energy spectrum outside the spherical cloud. The convolution matrix of the Compton scattering can be constructed from the simulation result, given by

$$R_{\text{CS}}(N_{\text{H}}^{\text{CS}}; E_1, E_2) = \frac{N_{\text{H}}^{\text{CS}}}{10^{22} \text{ cm}^{-2}} \times \frac{N(E_1, E_2, 1)}{N(E_1, E_1, 0) + \int N(E_1, E_2, 1) dE_1}, \quad (7.5)$$

where  $N(E_1, E_2, n)$  denotes the number of photons that have initial energy  $E_1$  and are scattered down to the post energy  $E_2$  via  $n$ -times scattering. Since we only consider the Compton thin regime ( $N_{\text{H}} < 10^{24} \text{ cm}^{-2}$ ), we ignore the multi-scattering, and the convolution matrix can be written in a linear form of  $N_{\text{H}}^{\text{CS}}$ . The convolution can be applied to any spectrum by

$$R_{\text{CS}} * f(E) = \int R_{\text{CS}}(N_{\text{H}}^{\text{CS}}; E', E) f(E') dE'. \quad (7.6)$$

We performed spectral fitting on the spectra of Eclipse 1 ( $-0.1 < \Phi < 0.1$ ) and 2 ( $0.9 < \Phi < 1.1$ ) of the 2022 NuSTAR data (see definition in Figure 5.4) using equation (7.4). Since  $f_{\text{NS}}$  is composed of fixed parameters, the free parameters of the fitting are  $N_{\text{H}}^{\text{PE}}$ ,  $N_{\text{H}}^{\text{CS}}$ , and the three Gaussian parameters ( $E_{\text{Fe}}$ ,  $\sigma_{\text{Fe}}$ ,  $I_{\text{Fe}}$ ). The model successfully reproduced the eclipse spectra, as shown in Figure 7.4. The best-fit parameters are summarized in Table 7.2. Both eclipse phases yielded comparable parameters to each other. Our analysis measured the column densities as  $N_{\text{H}}^{\text{PE}} \sim 1.3 \times 10^{23} \text{ cm}^{-2}$  and  $N_{\text{H}}^{\text{CS}} \sim 2.4 \times 10^{22} \text{ cm}^{-2}$ . These values are reasonable consulting the CAK stellar wind model discussed in Section 7.2. The former value corresponds to the column density at the end of the egress or the start of the ingress (see Figure 7.1). The latter value is consistent with the vertical integration of the hydrogen number density given by

$$\int_{R_*}^{\infty} n(r) dz = 2.4 \times 10^{22} \text{ cm}^{-2}, \quad (7.7)$$

where

$$\begin{aligned} r &= \sqrt{x^2 + y^2 + z^2} \\ x &= 0 \\ y &= R_{\text{sp}}, \end{aligned} \tag{7.8}$$

and  $(x, y, z) = (0, 0, 0)$  corresponds to the center of the companion star.  $R_{\text{sp}} = 1.48R_*$  represents the binary separation of Cen X-3 calculated by Sanjurjo-Ferrín et al. (2021). Therefore, the broadband spectrum of the eclipse phase can be naturally explained by the emission geometry assumed in Figure 7.2. The column densities of the stellar wind measured from the observation are consistent with the stellar wind model constructed by previous observations.

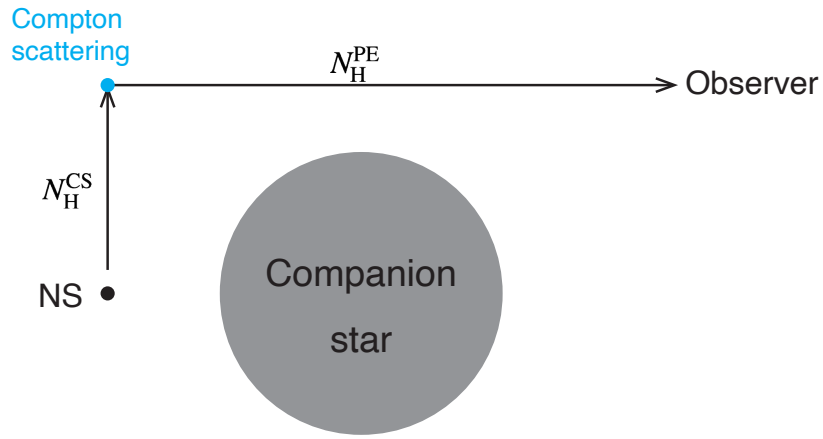


Figure 7.2: Schematic illustration of the emission mechanism during the eclipse phase.

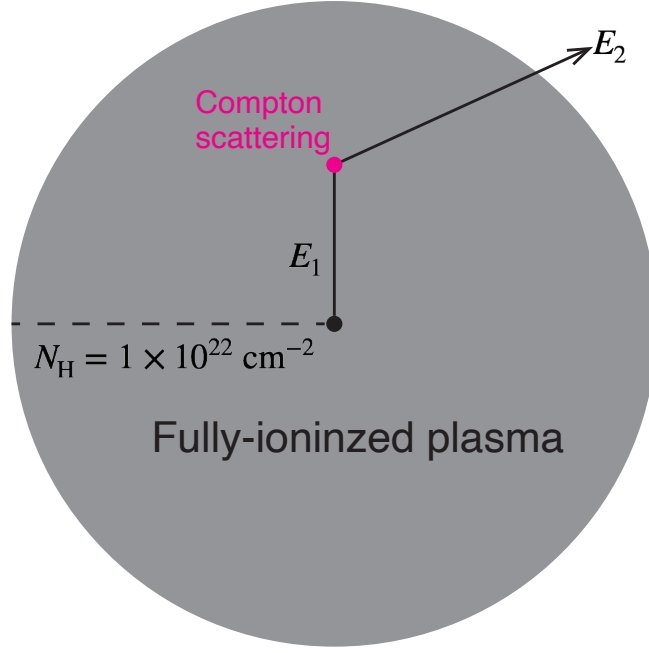


Figure 7.3: Schematic illustration of MONACO simulation setup. The simulation results were utilized for the construction of the convolution matrix in equation (7.5).

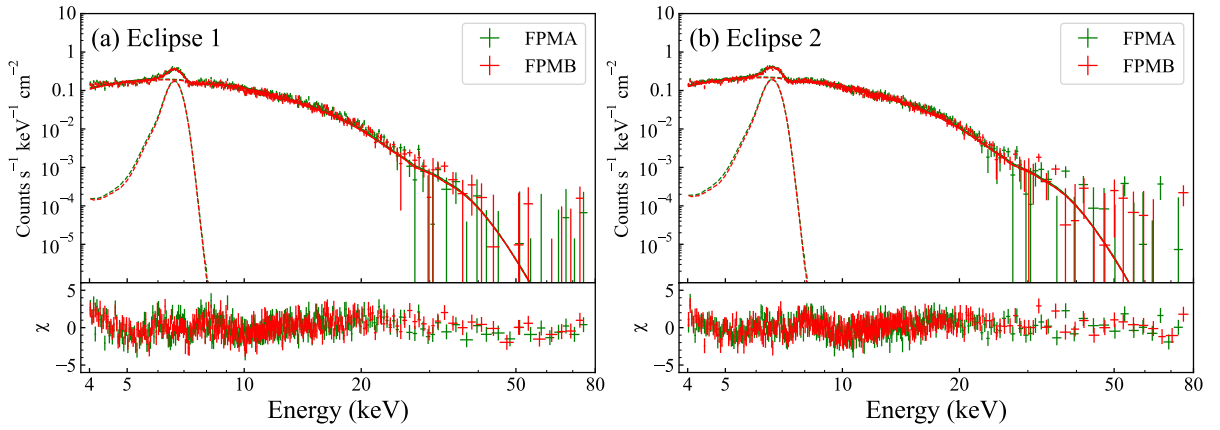


Figure 7.4: Fitting results of eclipse phase spectra. For the model description, see text. The dashed lines represent the Fe line components.

Table 7.2: Best-fit parameters of spectral fitting on eclipse phases.<sup>a</sup>

Interval	$N_{\text{H}}^{\text{PE}}$ ( $10^{22} \text{ cm}^{-2}$ )	$N_{\text{H}}^{\text{CS}}$ ( $10^{22} \text{ cm}^{-2}$ )	$E_{\text{Fe}}$ (keV)	$\sigma_{\text{Fe}}$ (keV)	$I_{\text{Fe}}^b$	$\chi_{\nu}^2$ (d.o.f.)
Eclipse 1	$13.6^{+0.7}_{-0.3}$	$2.25^{+0.01}_{-0.04}$	$6.64^{+0.03}_{-0.003}$	$0.19 \pm 0.02$	$4.8 \pm 0.2$	1.64 (648)
Eclipse 2	$13.4 \pm 0.6$	$2.50 \pm 0.04$	$6.61 \pm 0.01$	$0.22 \pm 0.02$	$5.8 \pm 0.3$	1.11 (668)

<sup>a</sup> Errors denote 90% confidence levels.<sup>b</sup> In units of  $10^{-4} \text{ photons s}^{-1} \text{ cm}^{-2}$ .

## 7.4 Physical origins of X-ray variability in out-of-eclipse phase

### 7.4.1 Physically-motivated spectral model

We first tried to explain the orbital-phase variability solely by the different absorption degrees caused by an inhomogeneous stellar wind. It can be naturally speculated that not only the photoelectric absorption but also the attenuation by Compton scattering plays an important role since the stellar wind is composed of highly ionized plasma. Indeed, the hard X-ray band above 10 keV, where the effect of photoelectric absorption is negligible, displays large flux variability (Figure 5.9). It should be explained by the attenuation due to Compton scattering, in which the scattering cross section is much more robust to the photon energy. We assumed a simple model to examine whether each orbital-phase-resolved spectrum can be explained by the attenuation from the non-obscured spectrum  $f_{\text{NS}}$ . The assumed model is given by

$$\frac{dN}{dE} = \exp \left[ - (N_{\text{H}}^{\text{IM}} + N_{\text{H}}^{\text{PE}}) \sigma_{\text{abs}}(E) \right] \times \exp \left[ - N_{\text{H}}^{\text{CS}} \sigma_{\text{CS}}(E) \right] \times (f_{\text{NS}} + f_{\text{gauss}}), \quad (7.9)$$

where  $N_{\text{H}}^{\text{CS}}$  and  $\sigma_{\text{CS}}(E)$  are the column density responsible for Compton scattering and the cross section of the Compton scattering, respectively.

We tried spectral fitting using equation (7.9) on the orbital-phase-resolved spectra over two orbits derived from the 2022 NuSTAR observation data (see Section 5.2). However, we only succeeded in reproducing spectra above 6 keV, and large discrepancies between the model and data remained for 3–6 keV spectra. Figure 7.5(a) shows an example of the spectral fitting on the 6–78 keV spectrum derived from  $\Phi = 0.195\text{--}0.120$  data in the 2022 NuSTAR data. While the 6–78 keV spectral shape is well reproduced by the attenuation by the photoelectric absorption and Compton scattering, the data well exceeds the model in the 3–6 keV band. This trend was seen in all the orbital-phase-resolved spectra.

In order to fully reproduce the observed spectra, we need to compensate for the residuals between the data and model. The most effective way to do it is to include an additional

component that explains the remained structure of the residuals in the low-energy band. We found that a blackbody function with a temperature of  $kT \sim 0.5$  keV successfully compensates for the residuals. Therefore, we added a blackbody function to equation (7.9) and set the model expression by

$$\begin{aligned} \frac{dN}{dE} = & \exp \left[ - \left( N_{\text{H}}^{\text{IM}} + N_{\text{H}}^{\text{PE}} \right) \sigma_{\text{abs}}(E) \right] \times \exp \left[ - N_{\text{H}}^{\text{CS}} \sigma_{\text{CS}}(E) \right] \times (f_{\text{NS}} + f_{\text{gauss}}) \\ & + \exp \left( - N_{\text{H}}^{\text{IM}} \sigma_{\text{abs}}(E) \right) f_{\text{bb}}, \end{aligned} \quad (7.10)$$

where the blackbody function  $f_{\text{bb}}$  is defined in equation (6.4). Figure 7.5(b) shows an example of fitting with equation (7.10). The residuals in 3–6 keV are successfully compensated for by the blackbody function with a temperature of  $kT = 0.47$  keV, and the residuals have no distinctive features.

We applied the above model to all the orbital-phase-resolved spectra and performed spectral fitting. The spectral parameters are composed of  $N_{\text{H}}^{\text{PE}}$ ,  $N_{\text{H}}^{\text{CS}}$ , the blackbody temperature  $kT$ , the blackbody luminosity  $L_{\text{bb}}$ , and the Fe line parameters. The blackbody luminosity was calculated based on the distance to the source of 6.4 kpc (Arnason et al., 2021). We first fitted the 6–78 keV spectra with equation (7.9) and determined  $N_{\text{H}}^{\text{PE}}$  and  $N_{\text{H}}^{\text{CS}}$ , and then performed fitting with equation (7.10) with fixed  $N_{\text{H}}^{\text{PE}}$  and  $N_{\text{H}}^{\text{CS}}$ . Figure 7.6 presents the fitting results and best-fit spectral parameters along the orbital phase. In some of the bright phases particularly in Orbit 2, the blackbody component is not significantly detected due to the dominance of the main emission. We excluded these orbital phases from the plot of  $kT$  and  $L_{\text{bb}}$ , but they are remained for other spectral parameters. The average value of the reduced chi-squares gives an acceptable value of 1.08, and all the spectra were successfully reproduced by the assumed model (equation 7.10). The flux variability is caused by attenuation due to both the photoelectric absorption and Compton scattering, as one can see larger values of  $N_{\text{H}}^{\text{PE}}$  and  $N_{\text{H}}^{\text{CS}}$  in Orbit 1 than in Orbit 2. The temperature of the blackbody settles around 0.5 keV, with no significant variation along the orbital phase. The yielded blackbody luminosity ranges from  $10^{36}$  erg s $^{-1}$  to  $10^{37}$  erg s $^{-1}$ , although large uncertainties are remained for the most high-flux phases (particularly Orbit 2) due to the relatively less contribution from the blackbody component.

Figure 7.7 presents the relation among spectral parameters. Figure 7.7 (a) and (b) show the correlation between the hydrogen column densities and the continuum flux. The hydrogen column density responsible for the photoelectric absorption ( $N_{\text{H}}^{\text{PE}}$ ) reaches a maximum value of  $\sim 7 \times 10^{23}$  cm $^{-2}$ , and that responsible for the Compton scattering ( $N_{\text{H}}^{\text{CS}}$ ) reaches  $\sim 2.5 \times 10^{24}$  cm $^{-2}$ . The two column densities are almost proportional, as shown in Figure 7.7(c). The relation between two column densities can be approximated by

$$N_{\text{H}}^{\text{CS}} \sim 2.85 N_{\text{H}}^{\text{PE}}, \quad (7.11)$$

which is overlaid on Figure 7.7(c). The Ingress & Egress phases have the most attenuation degree, while the Orbit 2 has the lowest. Figure 7.7(d) shows the relation between the blackbody luminosity and the continuum flux. Although some orbital intervals yielded best-fit parameters with large uncertainties, there appears to be a positive correlation between these two parameters.

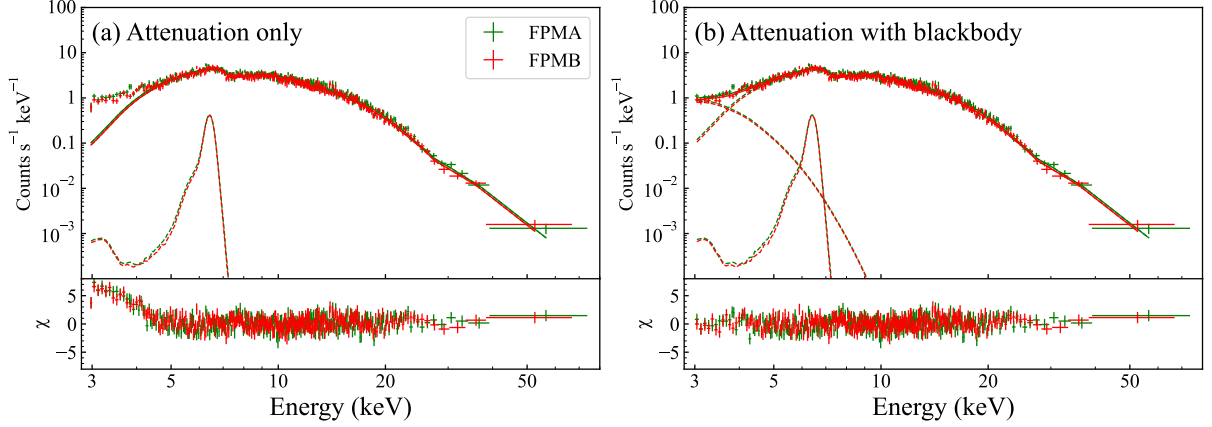


Figure 7.5: Example of spectral fitting based on physically-motivated models for the orbital-phase-resolved spectrum of  $\Phi = 0.195\text{--}0.120$  in 2022 NuSTAR data. (a) Only the attenuation due to the photoelectric absorption and Compton scattering are considered, based on equation (7.9). Fitting was applied to 6–78 keV spectrum. (b) Additional blackbody component with  $kT = 0.47$  keV was included in the fitting, based on equation (7.9). Fitting was applied to 3–78 keV spectrum.

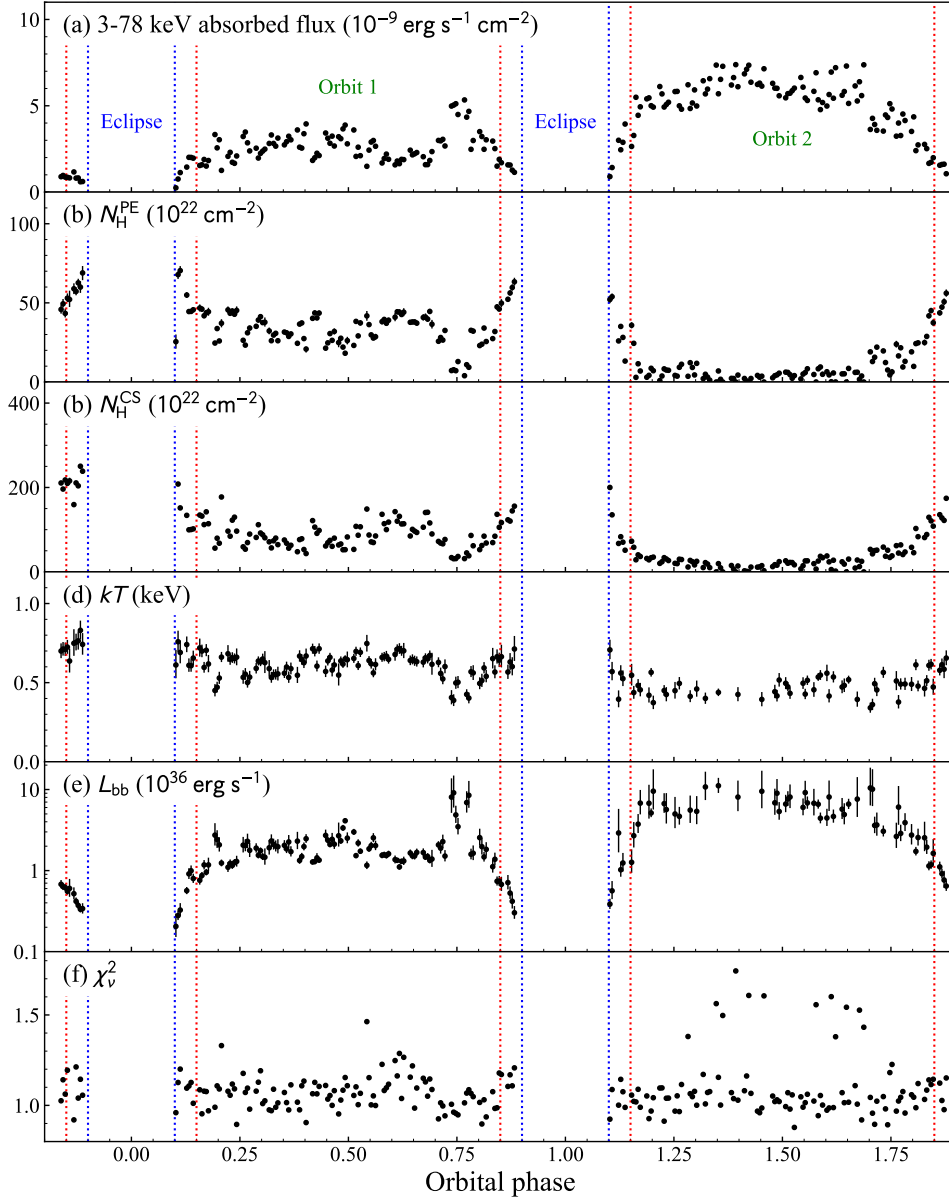


Figure 7.6: Fitting results of orbital-phase-resolved spectra with the physically-motivated spectral model given by equation (7.10).  $kT$  and  $L_{\text{bb}}$  are plotted only for the orbital-phase intervals where the blackbody component is significantly detected. The blue and red dotted lines denote eclipse phases and Ingress & Egress phases, respectively. Error bars represent 90% confidence levels.



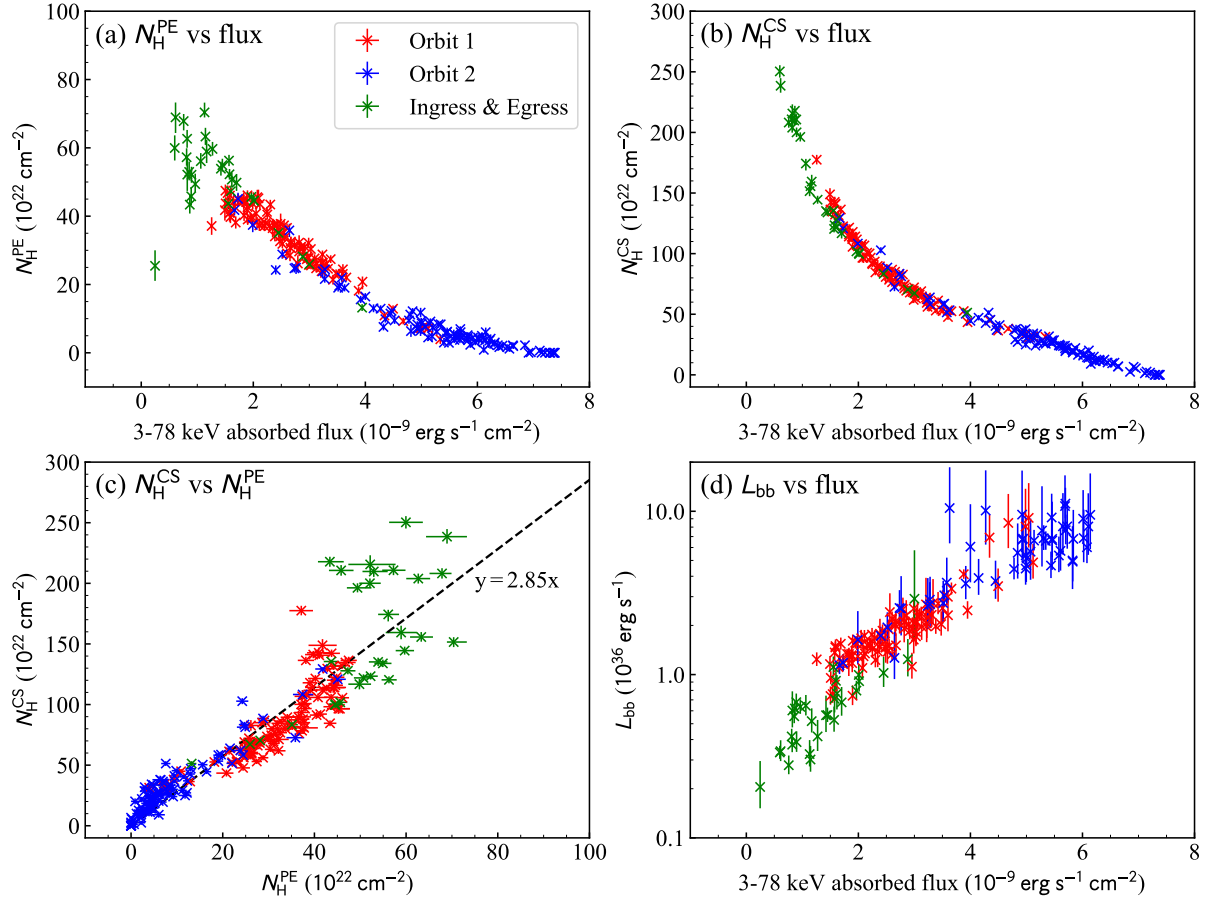


Figure 7.7: Relations among spectral parameters along the orbital phase. The variabilities of the spectral parameters are presented in Figure 7.6. Error bars represent 90% confidence levels.

#### 7.4.2 Physical interpretation of spectral model

The spectral model assumed in the previous subsection successfully reproduced the spectral variability along the orbital phase. The orbital-phase-resolved spectra can be explained by applying attenuation to a fixed intrinsic emission spectrum from the neutron star due to photoelectric absorption and Compton scattering, as well as an additional blackbody component compensating for the low-energy excess. Here, we examine the validity of the spectral model and give physical interpretations on it.

Firstly, the relation between two kinds of hydrogen column density,  $N_{\text{H}}^{\text{PE}}$  and  $N_{\text{H}}^{\text{CS}}$ , supports the spectral model is realistic. They are highly correlated with each other, and the relation is given by equation (7.11). Since the highly variable column densities can be naturally attributed to the absorption by an inhomogeneous stellar wind, the ratio between  $N_{\text{H}}^{\text{PE}}$  and  $N_{\text{H}}^{\text{CS}}$  is determined by the ion fraction of the stellar wind. The spectral fitting yielded an approximately constant ratio between these two column densities, which

suggests the stellar wind clumps responsible for the attenuation are ionized to an almost constant degree.

Secondly, the additional component reproduced by the blackbody function gives a reasonable explanation for the variability of the pulse profile. According to Figure 5.18, the 3–5 keV pulse profile displays larger variability than other energy bands. Moreover, the 3–5 keV pulse fraction is strongly correlated with the continuum flux and the photon index, as shown in Figure 5.19. The low-flux phases with hard photon indices have lower pulse fractions. Figure 7.8 presents the relation between 3–5 keV pulse fraction and 3–5 keV blackbody flux ratio. The negative correlation seen in Figure 7.8 strongly supports that the blackbody component originates from non-pulsed regions apart from the neutron star. The difference in the blackbody flux ratio can be interpreted as different degrees of obscuration by stellar wind between the neutron star and the blackbody emission regions.

Thirdly, the variability in the blackbody luminosity suggests that the blackbody emission originates from the thermal emission from the accretion disk. This can be speculated from the gradual decrease in the blackbody luminosity in the Ingress & Egress phases (Figure 7.6e). The size of the blackbody emission region is comparable to the Ingress & Egress timescale, that is,  $\Delta\Phi = 0.05$  or  $\Delta t \sim 9$  ks. Assuming the binary separation of  $R_{\text{sp}} = 17.9R_{\odot}$  (Sanjurjo-Ferrín et al., 2021), the typical size of the blackbody emission region can be estimated to be  $\sim 3.9 \times 10^{11}$  cm. The size of the accretion disk can be estimated from the size of the Roche lobe around the neutron star, given by (Paczynski, 1971)

$$R_{\text{L}} = 0.462 \left( \frac{M_{\text{ns}}}{M_{*}} \right)^{\frac{1}{3}} R_{\text{sp}} \sim 2.3 \times 10^{11} \text{ cm}, \quad (7.12)$$

where we substitute the masses of the neutron star and the companion star of  $M_{\text{ns}} = 1.34M_{\odot}$  and  $M_{*} = 20.5M_{\odot}$ , respectively. Since the sizes of the blackbody emission region and the accretion disk are comparable, it is natural to interpret the blackbody emission as originating from the accretion disk.

Lastly, the correlation between the blackbody luminosity and the continuum flux (Figure 7.7d) can be interpreted as a partial obscuration of the accretion disk by the stellar wind. The different contribution ratios of the blackbody arises because the typical size of the stellar wind clumps is smaller than that of the accretion disk. When the continuum flux decreases, the stellar wind obscures the whole neutron star and a part of the accretion disk, which in turn results in the enhancement in the blackbody flux ratio, decrease in the absolute luminosity of the blackbody component, and decrease in the pulse fraction. The assumption on the size of the stellar wind clumps is reasonable because the typical timescale of the flux variability is shorter than  $\Delta\Phi = 0.05$  or  $\Delta t \sim 9$  ks, consulting Figure 7.6(a). Moreover, the decrease of the blackbody luminosity by an order of magnitude can be realized with  $N_{\text{H}}^{\text{PE}} = 1 \times 10^{23} \text{ cm}^{-2}$  and  $N_{\text{H}}^{\text{CS}} = 2.85 \times 10^{23} \text{ cm}^{-2}$ , where we assume

$kT = 0.5$  keV and equation (7.11). These values of the column densities are sufficiently lower than the typical values of the measured  $N_{\text{H}}^{\text{PE}}$  and  $N_{\text{H}}^{\text{CS}}$  (see Figure 7.6b and c), which is a strong evidence suggesting that only a part of the accretion disk is obscured by the clumpy stellar wind.

An observational feature that is yet to be explained by this model is the difference between Orbit 1 and Orbit 2. Consulting Figure 7.7(a) and (b), we can see an apparent trend that the amount of stellar wind is larger in Orbit 1 than in Orbit 2. However, our model assumes a randomized distribution of the stellar wind, which could not generate such a difference between two consecutive orbits. One possibility is the sudden change in the mass loss rate of the companion star taking place during the eclipse phase between Orbit 1 and Orbit 2. There is also another possibility of the intrinsic variability of the accretion stream between Orbit 1 and Orbit 2. Nailing down the physical origin of the difference between Orbit 1 and Orbit 2 is beyond the scope of this thesis since it cannot be resolved by the NuSTAR observation data. XRISM (Tashiro et al., 2018), which will be launched in 2023, could solve this problem by investigating the emission and absorption lines originating from the stellar wind and examining the difference in the stellar wind distribution.

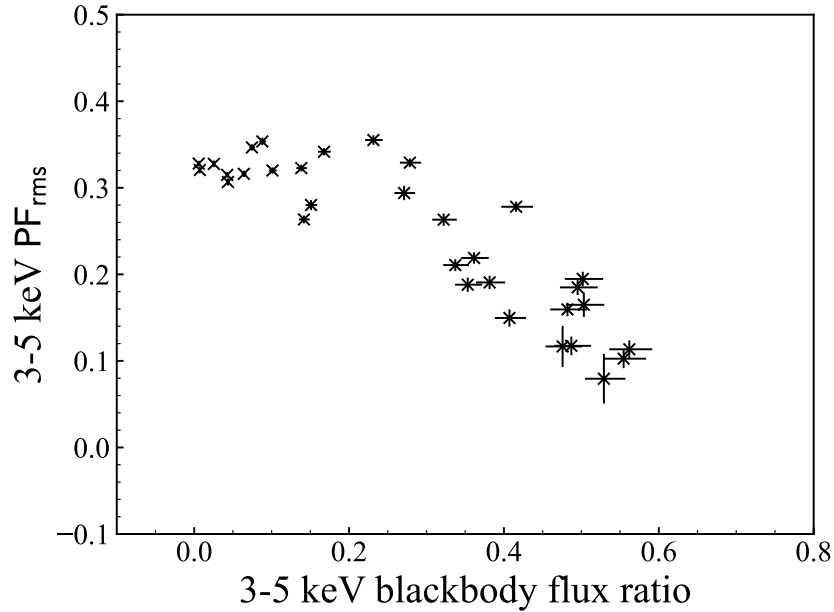


Figure 7.8: Relation between 3–5 keV pulse fraction and 3–5 keV blackbody flux ratio to the continuum flux, plotted for multiple orbital-phase intervals. The former is calculated in Section 5.4.1, and the latter is derived from the spectral parameters yielded in Section 7.4.1.

### 7.4.3 Independence of spin phase

In addition to the investigation of the orbital-phase variability of the spin-phase-averaged spectra, we examined the orbital-phase variability at each spin phase. We adopted the same orbital- and spin-phase divisions as Section 5.4.2. The eight spin-phase intervals are labeled A, B, ..., and H. The assumed model is the same as equation (7.10), but we replaced  $f_{\text{NS}}$  with the intrinsic spectrum at each spin phase, which is extracted from the observation data of the orbital interval of  $\Phi = 1.40\text{--}1.45$  and the corresponding spin phase interval.

Figure 7.9 presents the fitting results derived from the doubly-phase-resolved spectroscopy. The spectra were successfully reproduced by the model, and the average of the reduced chi-squares gives an acceptable value of 1.21. All the parameters,  $N_{\text{H}}^{\text{PE}}$ ,  $N_{\text{H}}^{\text{CS}}$ ,  $kT$ , and  $L_{\text{bb}}$ , do not show significant dependence on the spin phase. Most spectra can be reproduced by the attenuation due to the photoelectric absorption and Compton scattering, with an additional blackbody component with a temperature of  $kT \sim 0.5$  keV and a luminosity of  $10^{36}\text{--}10^{37}$  erg s $^{-1}$ .

Figure 7.10 shows the relations among spectral parameters. The flux attenuation due to the photoelectric absorption and Compton scattering is represented by Figure 7.10(a) and (b), respectively. The maximum values of  $N_{\text{H}}^{\text{PE}}$  and  $N_{\text{H}}^{\text{CS}}$  are  $\sim 7 \times 10^{23}$  cm $^{-2}$  and  $\sim 2.5 \times 10^{24}$  cm $^{-2}$ , respectively, which are consistent with the values yielded in the spin-phase-averaged spectroscopy (Section 7.4.1). The proportional relation between  $N_{\text{H}}^{\text{PE}}$  and  $N_{\text{H}}^{\text{CS}}$  given by equation (7.11) still holds for the spin-phase-resolved analysis, as shown in Figure 7.10(c). The positive correlation between the blackbody luminosity and the continuum flux also has a similar trend to the spin-phase-averaged version. These analysis results indicate that the assumed model is independent of the spin phase, which strongly supports that the attenuation of the continuum flux and the emergence of the blackbody component originate from a distant region from the neutron star.

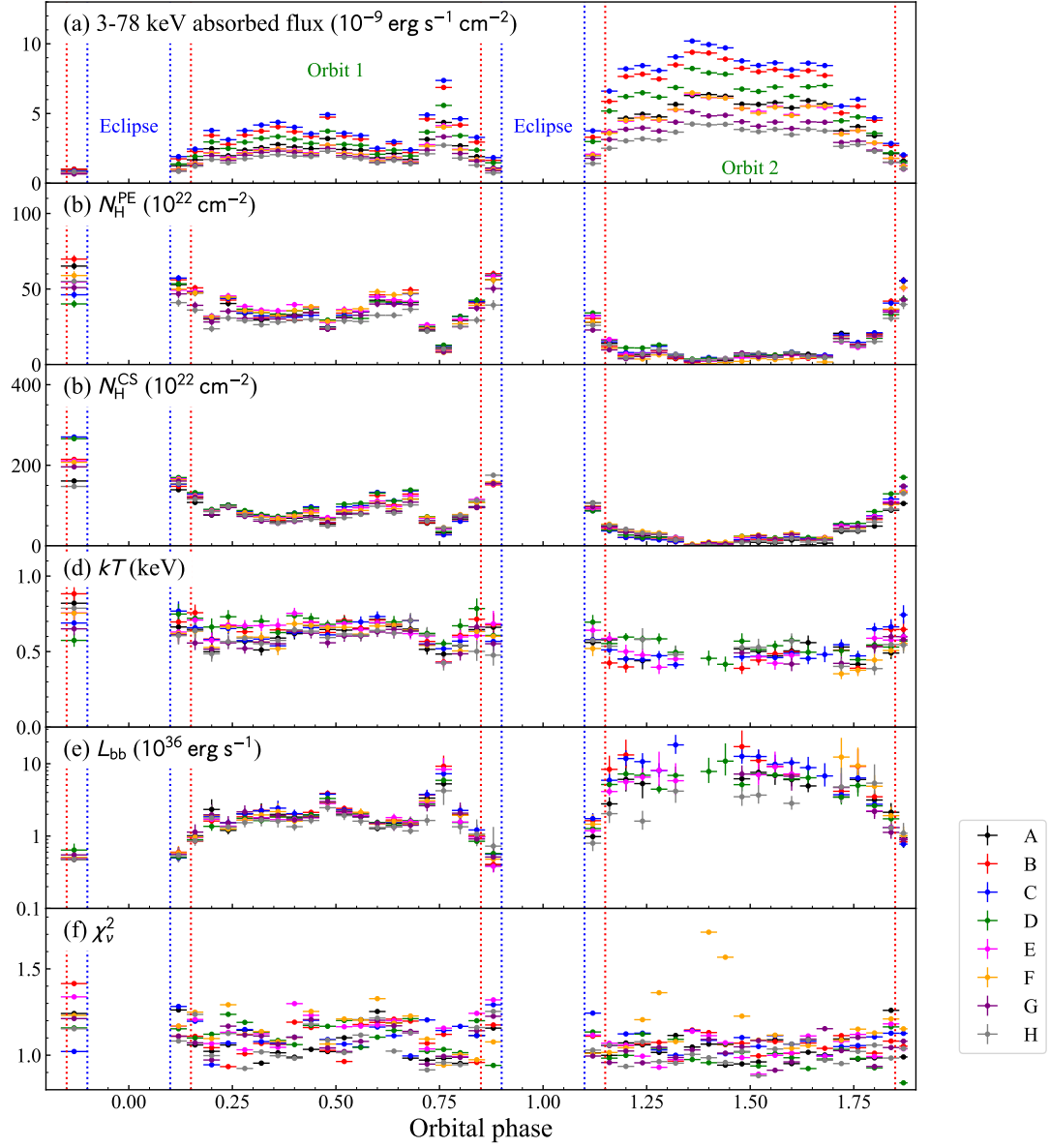


Figure 7.9: Same as Figure 7.6 but plotted for fitting results of doubly-phase-resolved spectra. The definitions of the colors are the same as Figure 5.21.

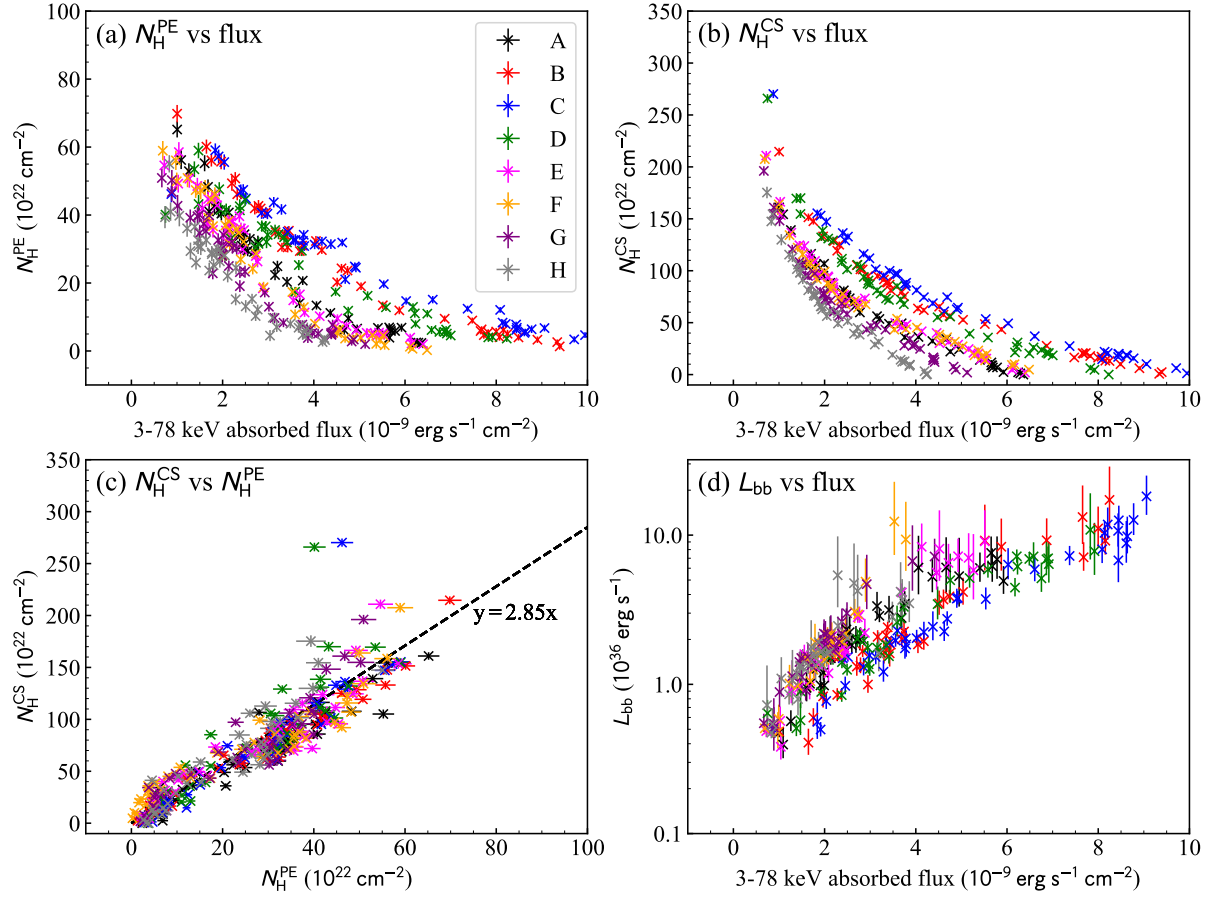


Figure 7.10: Same as Figure 7.7 but plotted for the fitting results of doubly-phase-resolved spectra. The definitions of the colors are the same as Figure 5.21.

#### 7.4.4 Joint fitting on NuSTAR and NICER spectra

In Sections 7.4.1 and 7.4.3, we found that a blackbody function explains the 3–6 keV spectra, particularly when the continuum flux is suppressed. The approximate temperature of the blackbody is  $kT \sim 0.5$  keV. However, this temperature is higher than the reported temperature of the soft excess of  $kT \sim 0.1$  keV (Burderi et al., 2000; Hickox et al., 2004). Moreover, our spectral analysis on the NICER observation data revealed that the temperature of the soft excess ranges from 0.09 to 0.25 keV, which is also lower than the expected 0.5 keV. A possible explanation for this discrepancy is the multiple components of the blackbody with different temperatures. In order to examine this hypothesis, we performed a joint fitting on the NuSTAR and NICER spectra.

We tried to explain the orbital-phase-resolved spectra extracted from the NICER observation data by combining them with NuSTAR spectra. We picked up nine orbital-phase intervals from the 11 intervals defined in Chapter 6, excluding the two intervals corresponding to the eclipse phases (intervals b and i). For the nine intervals, we searched

for suitable NuSTAR orbital intervals that have comparable flux levels with the NICER spectra. We carefully selected the corresponding NuSTAR orbital intervals by comparing 5–10 keV flux levels. The correspondence between NICER and NuSTAR orbital intervals are presented in the first and second columns of Table 7.3. The assumed spectral model is given by

$$\begin{aligned} \frac{dN}{dE} = & \exp \left[ - \left( N_{\text{H}}^{\text{IM}} + N_{\text{H}}^{\text{PE}} \right) \sigma_{\text{abs}}(E) \right] \times \exp \left[ - N_{\text{H}}^{\text{CS}} \sigma_{\text{CS}}(E) \right] \times (f_{\text{NS}} + f_{\text{gauss}}) \\ & + \exp \left( - N_{\text{H}}^{\text{IM}} \sigma_{\text{abs}}(E) \right) (f_{\text{bb}} + f_{\text{bb}}), \end{aligned} \quad (7.13)$$

which is basically the same as equation (7.10) but accompanied by another blackbody component. We denote the temperature and the luminosity of the  $i$ -th blackbody component by  $kT_i$  and  $L_{\text{bb},i}$ , respectively. Same as Section 7.4.1, we first determined  $N_{\text{H}}^{\text{PE}}$  and  $N_{\text{H}}^{\text{CS}}$  with 6–78 keV NuSTAR data, and then utilized these values to determine the blackbody parameters.

Figure 7.11 shows the results of the joint fitting on 0.6–10 keV NICER data and 3–78 keV NuSTAR data. The model successfully reproduced the data in all the orbital-phase intervals, although certain residuals remain due to the slightly different spectral shapes between NuSTAR and NICER data. The best-fit parameters are summarized in Table 7.3. The first blackbody component has a temperature range of 0.1–0.2 keV, while the second one has 0.5–1.0 keV. The luminosities of the first and second blackbody components are comparable, ranging from  $\sim 4 \times 10^{35} \text{ erg s}^{-1}$  to  $\sim 4 \times 10^{36} \text{ erg s}^{-1}$ . The phenomenological spectral analysis on the NICER spectra yielded unrealistic luminosity of the soft excess component up to  $\sim 10^{38} \text{ erg s}^{-1}$  (see Table 6.1), but the physically-motivated model here resulted in more realistic luminosities of the thermal components, which is much more less than the luminosity of the neutron star. The two blackbody components can be interpreted as the emission from a cool region and hot region of the accretion disk. Since the intrinsic luminosity of the neutron star ( $\sim 5 \times 10^{37} \text{ erg s}^{-1}$ ) well exceeds the luminosities of the blackbody components, the hot region of the accretion disk could be naturally interpreted as heated by the illumination from the neutron star.

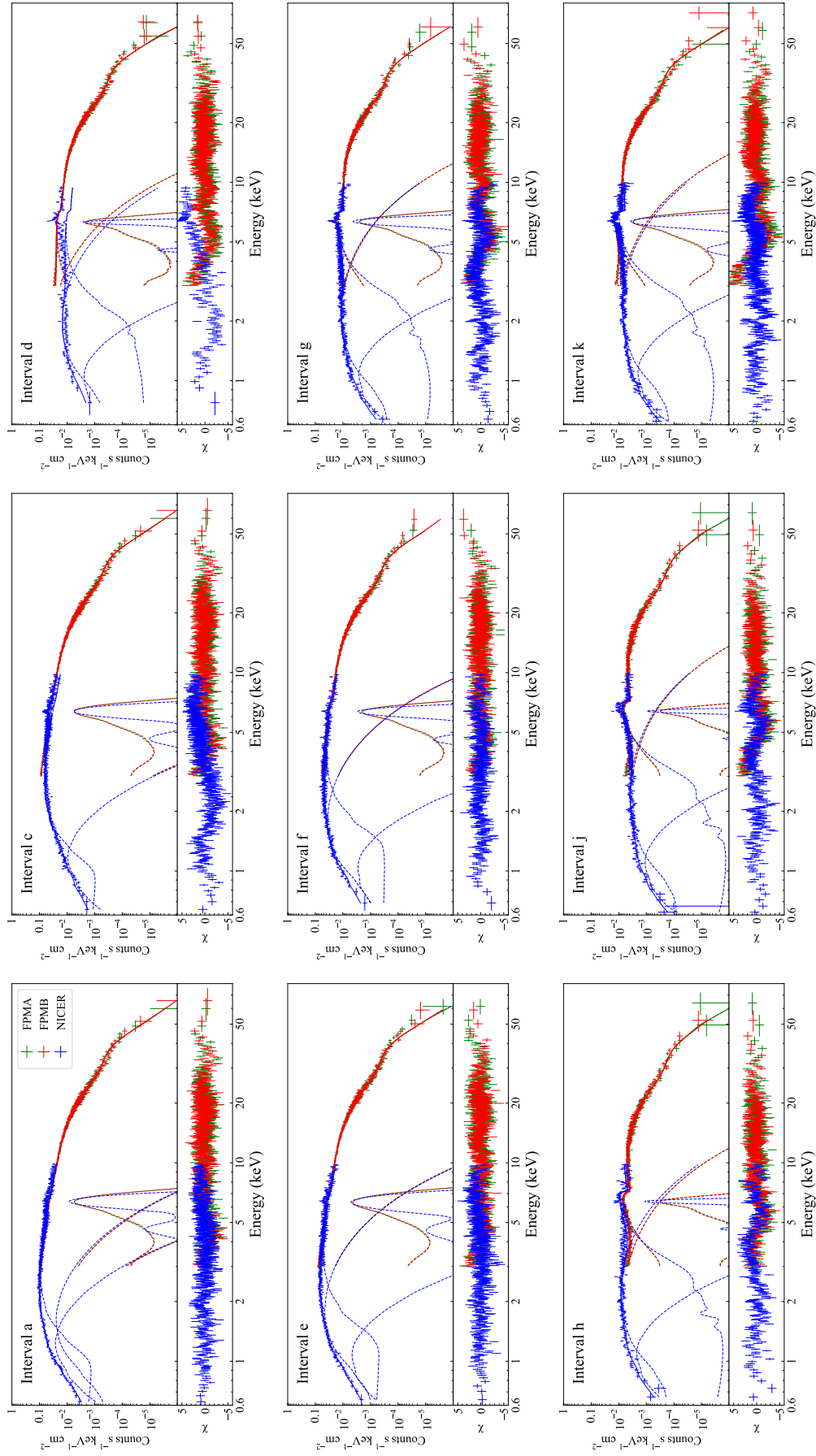


Figure 7.1.1: Results of joint fitting on NuSTAR and NICER spectra. Green, red, and blue data points denote FPMA, FPMB, and NICER spectra, respectively. The contributions from different spectral components are drawn by dashed lines.



Table 7.3: Best-fit parameters of joint spectral fitting.<sup>a</sup>

NICER Interval	NuSTAR $\Phi$	$N_{\text{H}}^{\text{PE}}$ ( $10^{22} \text{ cm}^{-2}$ )	$N_{\text{H}}^{\text{CS}}$ ( $10^{22} \text{ cm}^{-2}$ )	$kT_1$ (keV)	$L_{\text{bb},1}$ ( $10^{36} \text{ erg s}^{-1}$ )	$kT_2$ (keV)	$L_{\text{bb},2}$ ( $10^{36} \text{ erg s}^{-1}$ )	$\chi^2_{\nu}$ (d.o.f.)
a	1.40–1.45	$1.9 \pm 0.4$	$2.3 \pm 0.7$	$< 0.20$	$3.4 \pm 0.2$	$< 0.40$	$1.6 \pm 0.1$	1.24 (1725)
c	1.40–1.45	$1.9 \pm 0.4$	$2.3 \pm 0.7$	$0.17 \pm 0.01$	$2.5 \pm 0.2$	-	-	1.95 (1730)
d	0.70–0.75	$16.8^{+0.4}_{-0.2}$	$53.3^{+0.8}_{-0.7}$	$0.12 \pm 0.01$	$3.6^{+2.0}_{-1.2}$	$0.64 \pm 0.01$	$2.53^{+0.08}_{-0.07}$	1.88 (1236)
e	1.50–1.55	$4.4 \pm 0.4$	$16.4 \pm 0.7$	$0.13^{+0.02}_{-0.01}$	$2.6^{+1.1}_{-0.7}$	$0.52 \pm 0.01$	$3.53 \pm 0.08$	1.24 (1696)
f	1.20–1.25	$6.1 \pm 0.4$	$27.8 \pm 0.8$	$0.12 \pm 0.01$	$2.4^{+1.3}_{-0.9}$	$0.52 \pm 0.01$	$2.80 \pm 0.07$	1.09 (1538)
g	0.30–0.35	$30.2 \pm 0.5$	$72 \pm 1$	$0.13 \pm 0.01$	$1.3 \pm 0.2$	$0.78 \pm 0.01$	$1.12 \pm 0.02$	1.63 (1563)
h	1.85–1.88	$48.1 \pm 0.9$	$138 \pm 2$	$0.14 \pm 0.01$	$0.65^{+0.17}_{-0.14}$	$0.78 \pm 0.01$	$0.59 \pm 0.01$	1.43 (1136)
j	1.85–1.88	$48.1 \pm 0.9$	$138 \pm 2$	$0.14 \pm 0.01$	$0.38^{+0.08}_{-0.07}$	$0.94 \pm 0.01$	$0.43 \pm 0.01$	1.66 (1233)
k <sup>b</sup>	0.55–0.60	$33.4 \pm 0.5$	$97 \pm 1$	0.14	0.9	0.9	1.01	2.19 (1768)

<sup>a</sup> Errors denote 90% confidence levels.

<sup>b</sup> For NICER interval k, errors of blackbody parameters are not evaluated due to the large discrepancy between data and model.

## 7.5 Physical pictures of circumstellar medium of Cen X-3

In the previous sections, we investigated the physical origins of the X-ray spectral variability of Cen X-3 along the orbital phase. In this section, we summarize our findings and compare them with previous researches based on other observation data.

### 7.5.1 Summary of emission geometry

The spectral analysis based on the physically-motivated model in Section 7.4 revealed that the orbital-phase spectral variability of Cen X-3 is mainly caused by the different attenuation degrees by the inhomogeneous stellar wind. In addition to the attenuation of the intrinsic emission from the neutron star, two blackbody components exist in the soft X-ray band, which explains the spectral variability below  $\sim 6$  keV. In the low-flux phases, where the attenuation by the stellar wind is significant, only a part of the blackbody emission is suppressed because of the large size of the accretion disk compared to the typical clump size of the stellar wind. The emission geometry derived here is summarized in Figure 7.12 by a schematic illustration. We note that these results can be only obtained from a careful investigation of the continuous spectral variability along the orbital phase. Otherwise, the emergence of the blackbody component in the low-flux phases would be smeared out and observed as a apparently hardening of the photon index.

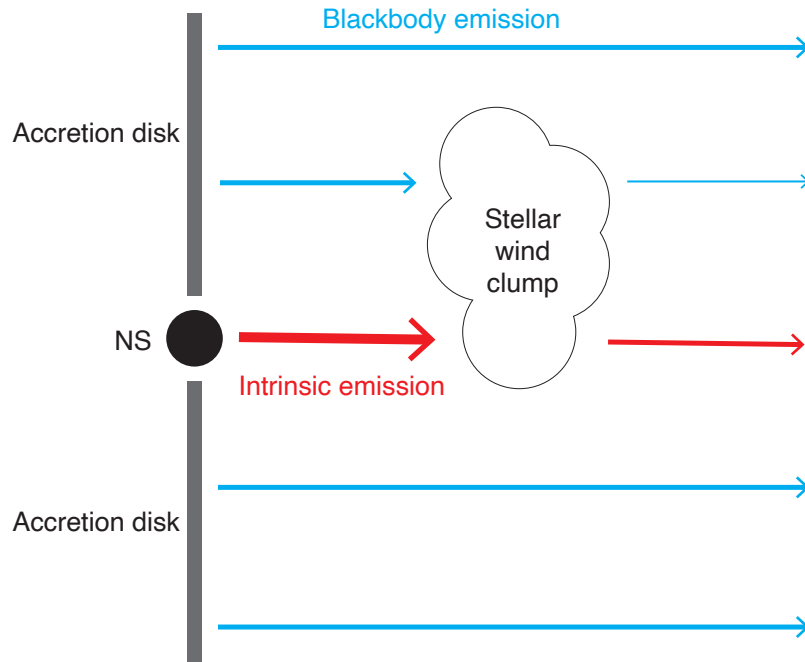


Figure 7.12: Schematic illustration of X-ray emission geometry of Cen X-3.

### 7.5.2 Clumpy stellar wind

The typical hydrogen column density responsible for the attenuation of the neutron star emission was measured to be  $\sim 10^{24} \text{ cm}^{-2}$ . This value is higher than estimated from the stellar wind model calculated in Section 7.2 and Figure 7.1. Such an enhancement in the column density is often interpreted as a consequence of a clumpy stellar wind. From the variability of the absorption degrees, one can estimate the typical size and density of the stellar wind clumps. In Cen X-3, the neutron star is orbiting the companion star with a velocity of  $v = 4.4 \times 10^7 \text{ cm s}^{-1}$ , and thus the typical size of the clumps can be calculated by

$$R_c = v P_{\text{orb}} \Delta\Phi = 8 \times 10^{10} \left( \frac{\Delta\Phi}{0.01} \right) \text{ cm}, \quad (7.14)$$

where  $\Delta\Phi$  is the typical timescale of the flux variability. From the flux variability seen in Figure 4.3 and Figure 5.7, the typical timescale of the variability is  $\Delta\Phi \sim 0.01$ . The typical size of the clumps is smaller than the size of the accretion disk (equation 7.12), consistent with the partial obscuration of the accretion disk discussed above. The typical hydrogen number density of the clumps is given by

$$n_c = \frac{N_H}{R_c} = 1 \times 10^{13} \left( \frac{N_H}{10^{24} \text{ cm}^{-2}} \right) \left( \frac{\Delta\Phi}{0.01} \right)^{-1} \text{ cm}^{-3}. \quad (7.15)$$

The typical value of the observed hydrogen column density is  $N_H \sim 10^{24} \text{ cm}^{-2}$  from Figure 7.6. We note that the above estimation is based on a simplified assumption, where the velocity of the stellar wind and the distance between the neutron star and the stellar wind are not taken into account.

The typical size and number density of the clumps give reasonable values compared to the estimation for Vela X-1, a wind-fed X-ray pulsar with a similar companion star to Cen X-3. It was conducted by Odaka et al. (2013), in which the size and number density of the stellar wind clumps are estimated to be  $R_c \sim 2 \times 10^{11} \text{ cm}$  and  $n_c \sim 7 \times 10^{11} \text{ cm}^{-3}$ , respectively. The sizes of the clumps are comparable between the two objects. The clump density of Cen X-3 is larger than that of Vela X-1 by order of magnitude. An enhancement in the clump density by order of magnitude can be naturally generated by the interaction between the moving neutron star and the stellar wind (e.g., Friend & Castor, 1982; Blondin et al., 1991). The most notable difference between Cen X-3 and Vela X-1 is the distance between the neutron star and the companion star, where the binary separations are  $17.9R_\odot$  (Sanjurjo-Ferrín et al., 2021) and  $53.4R_\odot$  (van Kerkwijk et al., 1995) for Cen X-3 and Vela X-1, respectively. The relatively small binary separation of Cen X-3 could induce more interactions between the neutron star and the stellar wind, forming a denser clump.

We also found that the stellar wind is highly ionized, and the effect of the Compton scattering is significant on the attenuation of the neutron star emission. The highly ionized

stellar wind is a widely agreed picture of an X-ray pulsar with a massive companion star. Indeed, the spectral analysis on the eclipse phases revealed that the H-like and He-like Fe lines are dominant over the neutral Fe line (Section 6.2 and 7.3), which indicates that the Fe atoms are highly stripped due to ionization. Wojdowski et al. (2001) performed a detailed analysis on the eclipse spectrum of Cen X-3 observed by ASCA and confirmed that the stellar wind is highly ionized by the illumination from the neutron star with an ionization parameter (Tarter et al., 1969) of  $\xi = 10^3\text{--}10^4$ . We note that the simple treatment of the calculation of the attenuation with  $N_{\text{H}}^{\text{PE}}$  and  $N_{\text{H}}^{\text{CS}}$  does not necessarily measure the ionization state of the stellar wind. A possible effect that is not considered in our analysis is the Compton down scattering, which changes the traveling photon energy downwards and possibly affects the spectral shape.

### 7.5.3 Accretion disk

Our analysis on the orbital-phase variability of Cen X-3 revealed that the blackbody emission from the accretion disk becomes dominant when the intrinsic emission from the neutron star is suppressed due to the obscuration by the stellar wind. The extra emission in the soft X-ray band is composed of two blackbody components with different temperatures of  $\sim 0.1$  keV and  $\sim 0.5$  keV. Assuming a standard accretion disk proposed by Shakura & Sunyaev (1973), the temperature of the accretion disk at a given distance from the central object  $r$  is expressed by

$$T_{\text{c}} \sim 1.4 \times 10^4 \left( \frac{\dot{M}}{10^{16} \text{ g s}^{-1}} \right)^{3/10} \left( \frac{M_{\text{ns}}}{M_{\odot}} \right)^{1/4} \left( \frac{r}{10^{10} \text{ cm}} \right)^{-3/4} \text{ K}. \quad (7.16)$$

Substituting  $\dot{M} = 3.2 \times 10^{17} \text{ g s}^{-1}$ ,  $M_{\text{ns}} = 1.34 M_{\odot}$ , and  $r = 3 \times 10^8 \text{ cm}$ , corresponding to the Alfvén radius of Cen X-3, yields  $T_{\text{c}} \sim 5.9 \times 10^5 \text{ K}$  or  $kT_{\text{c}} \sim 0.05 \text{ keV}$ . This temperature is consistent with the lower-temperature blackbody of  $\sim 0.1 \text{ keV}$  confirmed in the joint fitting of NuSTAR and NICER data (Section 7.4.4). The higher-temperature blackbody presumably originates from the heated region of the accretion disk by the illumination from the neutron star. Since the luminosity of the blackbody is  $\sim 10^{36} \text{ erg s}^{-1}$ , the X-ray irradiation from the neutron star of  $5 \times 10^{37} \text{ erg s}^{-1}$  is sufficient to transfer the energy to the accretion disk.

As suggested by several previous studies, the inner region of the accretion disk is the most likely candidate for the emission region of the neutral Fe line. For example, Ebisawa et al. (1996) found that the intensity of the neutral Fe line varies with the spin phase, which suggests that the Fe line originates from the proximity of the neutron star. Kohmura et al. (2001) analyzed RXTE data of Cen X-3 and detected a time delay of the Fe line by  $0.39 \pm 0.10 \text{ ms}$ , which corresponds to the travel time from the neutron star to the inner region of the accretion disk. Figure 7.13 presents the relation between the Fe

line intensity and the blackbody luminosity, derived from the analysis on the NuSTAR observation data (Section 7.4.1). Although large uncertainties remain on the intensity of the Fe line, these two parameters appear to have a positive correlation. This result supports the idea that the accretion disk is the main emission region of the Fe line. A more sophisticated research on the Fe line should be performed by XRISM (Tashiro et al., 2018), which has a much better energy resolution in the soft X-ray band and will be launched in 2023.

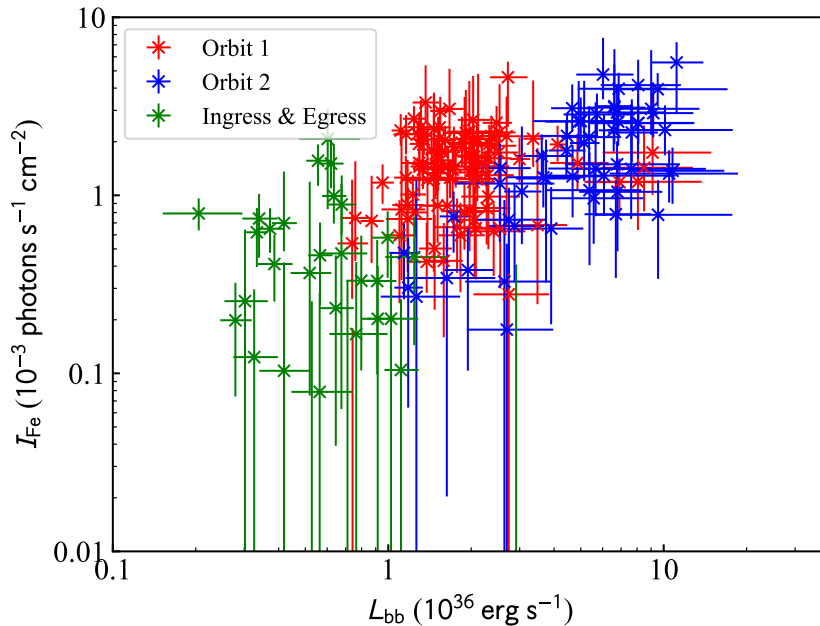


Figure 7.13: Relation between Fe line intensity and blackbody luminosity derived from the orbital-phase-resolved spectroscopy on the NuSTAR observation data. Error bars represent 90% confidence levels.

#### 7.5.4 Stability of accretion flow

Our study on the orbital-phase variability of Cen X-3 has revealed that the main cause of the spectral variability is the obscuration by the stellar wind. The intrinsic variability of the neutron star emission due to the variation of the accretion rate is much less than that, which is natural for a disk-fed X-ray pulsar. The stable accretion rate of Cen X-3 is also suggested by several previous observations. A long-term observation on the light curve obtained by the all-sky monitor onboard Ginga revealed that there is no correlation between the X-ray luminosity and the spin-up rate of the neutron star (Tsunemi et al., 1996). This observational property supports that the variability of the observed flux does not correlate with the change in the accretion rate. According to the 5–12 keV light curve observation over ten years by the all-sky monitor onboard RXTE, there appears to be a maximum luminosity of Cen X-3 that may correspond to the Eddington luminosity (Paul

et al., 2005; Raichur & Paul, 2008b). They also pointed out the possibility of the stable accretion rate near the Eddington luminosity. Moreover, a Suzaku observation over one orbit of Cen X-3 revealed that the flux decreases (dips) emerging in the out-of-eclipse phases are caused by the clumpy stellar wind rather than the change of the accretion rate, consulting the variability of the Fe line (Naik et al., 2011). All of these results are strong evidence for a stable accretion flow.

Some previous studies, however, detected certain variability in the accretion rate. In an XMM-Newton observation covering the orbital phase of  $\Phi = 0.36\text{--}0.80$ , the count ratio between 3–10 keV and 0.2–3 keV photons do not show any significant variance over the observation, although the continuum flux varies to a certain degree (Sanjurjo-Ferrín et al., 2021). This flux variability can be attributed to the pure intrinsic variability of the accretion flow, presumably originating from the change in the accretion rate. The estimated flux variability is  $\sim 10\%$ , which would be smeared out in our NuSTAR long-time observation. The variability in unabsorbed flux detected in the short-time NuSTAR observation data in Section 4 may correspond to the intrinsic variability of the accretion flow, because our analysis revealed that the 10% variation of the unabsorbed flux does not correlate with the absorption column density (Figure 4.4b).

## Chapter 8

# Broadband X-ray variability of Her X-1 studied with NuSTAR observation

In Chapter 7, we discussed the circumstellar medium of Cen X-3 based on the orbital-phase spectral variability derived from X-ray observations. We have yet to investigate the structure and physical processes of the accretion flow from the spin-phase variability of the X-ray emission. In such an investigation, a comparison with other X-ray pulsars would be helpful because the analysis result based on one object would be greatly affected by the factors unique to that object. We picked up Hercules X-1 (Her X-1) as an ideal source to perform the same analysis as Cen X-3 because its luminosity, spectral shape, orbital period, and spin period are all comparable to Cen X-3. It is widely agreed that Her X-1 has a disk-fed accretion mechanism very similar to Cen X-3. SMC X-1 and LMC X-4 also provide similar accretion sites to Cen X-3, but the large distances from the earth result in relatively insufficient photon counts for investigating spectral variability. In this chapter, we apply our analysis method of searching for the orbital- and spin-phase variabilities on Her X-1 observation data with the same method as Chapters 4 and 5.

### 8.1 Overview of Her X-1

Her X-1 is one of the brightest and most studied X-ray pulsars in our galaxy. It was first discovered by Uhuru as a pulsating X-ray source with a period of  $\sim 1.24$  s (Tananbaum et al., 1972; Giacconi et al., 1973). It is a unique source because the optical companion is not a massive star, unlike other X-ray pulsars. In the binary system, a  $1.5M_{\odot}$  neutron star is orbiting a  $2.2M_{\odot}$  A/F-type star HZ Her (Crampton & Hutchings, 1974; Middleditch & Nelson, 1976; Reynolds et al., 1997) with an orbital period of  $\sim 1.7$  day (Deeter et al., 1981; Staubert et al., 2009b). The companion star has a radius of  $\sim 2.6\text{--}3.0 \times 10^{11}$  cm

(Leahy & Abdallah, 2014), and the binary separation is estimated to be  $\sim 3 \times 10^{11}$  cm (Cheng et al., 1995). This object is sometimes classified into a low mass X-ray binary (LMXB) but is mostly interpreted as an intermediate mass X-ray binary (IMXB). The eclipse phase lasts for 5.5 hours every orbit due to the nearly edge-on configuration with a large inclination angle of  $85\text{--}88^\circ$ . The orbit has a small eccentricity of  $4.2 \times 10^{-4}$  (Staubert et al., 2009b). The distance from the earth is estimated to be 6.1 kpc (Reynolds et al., 1997; Leahy & Abdallah, 2014).

Although Her X-1 does not have a massive star as a companion star, it is classified as a disk-fed X-ray pulsar by other observational properties. The most notable property is the superorbital modulation (see Section 2.3.4) speculated from 35-day variability of the light curve (Parmar et al., 1985; Vrtillek et al., 1994; Parmar et al., 1999; Staubert et al., 2009a). The superorbital modulation of Her X-1 is considered to originate from the precession of a warped accretion disk (e.g., Pringle, 1996; Ogilvie & Dubus, 2001; Ramsay et al., 2002; Zane et al., 2004). The accretion onto the neutron star is considered to be stable, but it is periodically obscured by the precession of the accretion disk. In the “main-on” period, which is the brightest phase in the superorbital modulation lasting for 11 days, the luminosity of the source reaches  $4 \times 10^{37}$  erg s $^{-1}$ . Such a high luminosity is also typical for a disk-fed X-ray pulsar with a radiation-dominated shock inside the accretion column. The strong magnetic field predicted by the CRSF in the spectrum is another evidence for a highly magnetized neutron star. The CRSF exists at 35–40 keV, which corresponds to a magnetic field of  $\sim 3 \times 10^{12}$  G. The long-term variability in the central energy of the CRSF exhibits a positive correlation with the source luminosity (Staubert et al., 2007) and a gradual decay (Staubert et al., 2016, 2017).

## 8.2 Observation and data reduction

Her X-1 was observed by NuSTAR more than ten times from 2012 to 2021. Among these observation data, we picked up an observation data set that corresponds to the bright phase of the superorbital modulation (ObsID: 300601012002) since we need rich photon counts to investigate the spectral variability. The observation was carried out on 2021 May 17 with a duration of 62.7 ks. Figure 8.1 shows the 2–20 keV light curve of MAXI<sup>1</sup> (Matsuoka et al., 2009) around the observation date. It shows the 35-day variability of Her X-1 originating from the superorbital modulation. The NuSTAR observation we selected corresponds to the peak of the main-on phase, as represented by the red dotted line in Figure 8.1. We applied a standard data reduction of NuSTAR with `HEASoft` 6.30, similar to Chapters 4 and 5. The source and background regions are a circle with a radius of  $180''$  from the source center and a rectangle in the off-source region, respectively. The

---

<sup>1</sup>taken from <http://maxi.riken.jp/top/lc.html>



data reduction yielded cleaned event data with net exposures of 24.3 ks for FPMA and FPMB.

We applied a binary correction to the arrival time of the cleaned event data, the same as the Cen X-3 analysis. The method is based on the  $Z_2^2$  test, same as Section 5.1.2. Since the observation covers only a part of the whole orbit of Her X-1, we fixed the orbital period  $P_{\text{orb}}$  and the projected semi-major axis  $a_x \sin i$  to the value listed in Wilson et al. (1997). The best-fit values of the spin period  $P_{\text{spin}}$  and start orbital phase  $\Phi_{\text{start}}$  are presented in Table 8.1, and the variation of  $Z_2^2$  values along the parameters are shown in Figure 8.2. The yielded spin period was  $P_{\text{spin}} = 1.237711$  s, and the start orbital phase of  $\Phi_{\text{start}} = 0.153$  means the 62.7 ks observation covers an orbital-phase interval of  $\Phi = 0.153$ – $0.427$ . Figure 8.3 shows the shift of the peak phase along the orbital phase, derived from the peak phase of the 1st Fourier component of 3–78 keV pulse profiles (equation 5.5). The peak phase does not shift significantly within the observation duration, with a typical deviation of  $\Delta\phi < 0.01$ . It renders validity to the coherent spin-phase-resolved analysis.

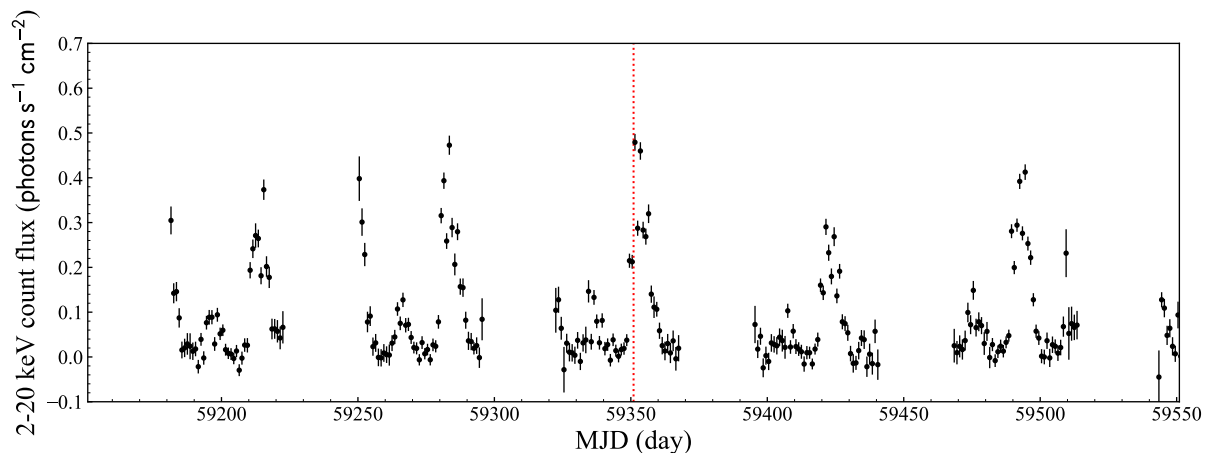


Figure 8.1: MAXI light curve of Her X-1 with one-day bin. The red dotted line corresponds to the NuSTAR observation date.

Table 8.1: Orbital parameters of Her X-1.<sup>a</sup>

$P_{\text{orb}}$ (days)	$P_{\text{spin}}$ (s)	$a_x \sin i$ (lt-s)	$\Phi_{\text{start}}$
$1.700167446^b$ (fixed)	$1.237711(8)$	$13.18549^b$ (fixed)	$0.153(3)$

<sup>a</sup> Derived from the NuSTAR observation data at the time of 59351.109337319 MJD.

<sup>b</sup> Based on Wilson et al. (1997).

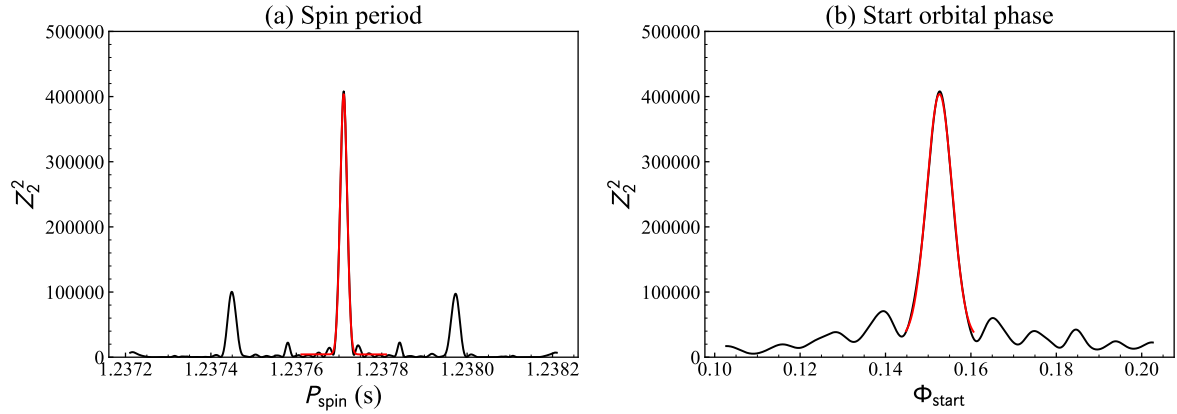


Figure 8.2: Variations of  $Z_2^2$  values around the best-fit parameters for  $P_{\text{spin}}$  and  $\Phi_{\text{start}}$ . The red lines denote the best-fit Gaussian functions.

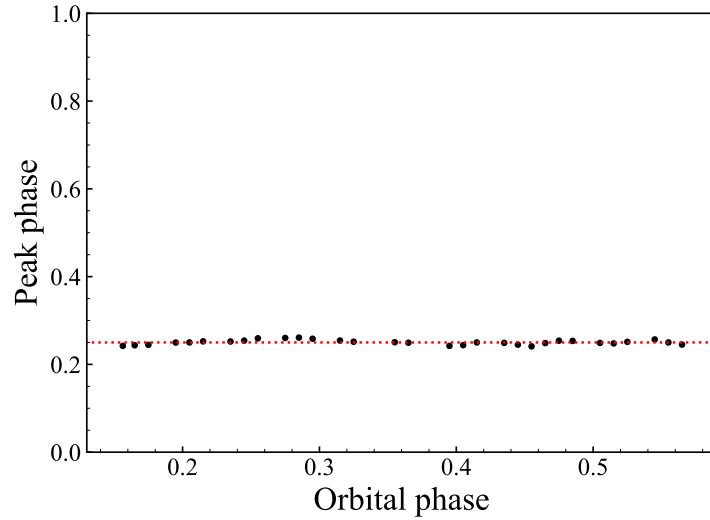


Figure 8.3: Variation of the peak phase of the 1st Fourier component along the orbital phase, generated from 3–78 keV pulse profiles. The red dotted line denotes the peak phase of the phase-averaged pulse profile ( $\phi = 0.25$ ).

### 8.3 Orbital-phase variability

We first investigated the orbital-phase variability of Her X-1 within the observation duration. Since the companion star of Her X-1 does not have a strong stellar wind, the short-term variability compared to the superorbital modulation is considered to be negligible. We examine the variability via light curves and spectral analysis, as conducted in Sections 4.3 and 5.2. We divided the whole observation data into 84 pieces with each orbital interval covering  $\Delta\Phi = 0.005$  or  $\Delta t = 734$  s. 35 out of 84 orbital intervals were

excluded due to short exposures of  $< 150$  ms, and the following analysis was applied to the remaining 49 orbital intervals.

### 8.3.1 Energy-resolved light curve

We generated energy-resolved light curves from the 49 orbital intervals for 3–5, 5–10, 10–20, and 20–78 keV bands. The left panel of Figure 8.4 shows the light curves of the multiple energy bands. Unlike the Cen X-3 case, the orbital-phase variability seen from the light curves is very small. We also examined the variabilities of the hardness ratios among these energy bands, as presented in the right panel of Figure 8.4. The relations among different energy bands are preserved constant over the orbital phase. Table 8.2 shows the statistical parameters derived from the energy-resolved light curves. The variation degrees, evaluated by the ratio of the standard deviation to the average, are at most 3.5%. These results show that both the effect of the stellar wind and the intrinsic variability of the neutron star emission are nearly negligible, affecting the observed flux only by  $< 3.5\%$ .

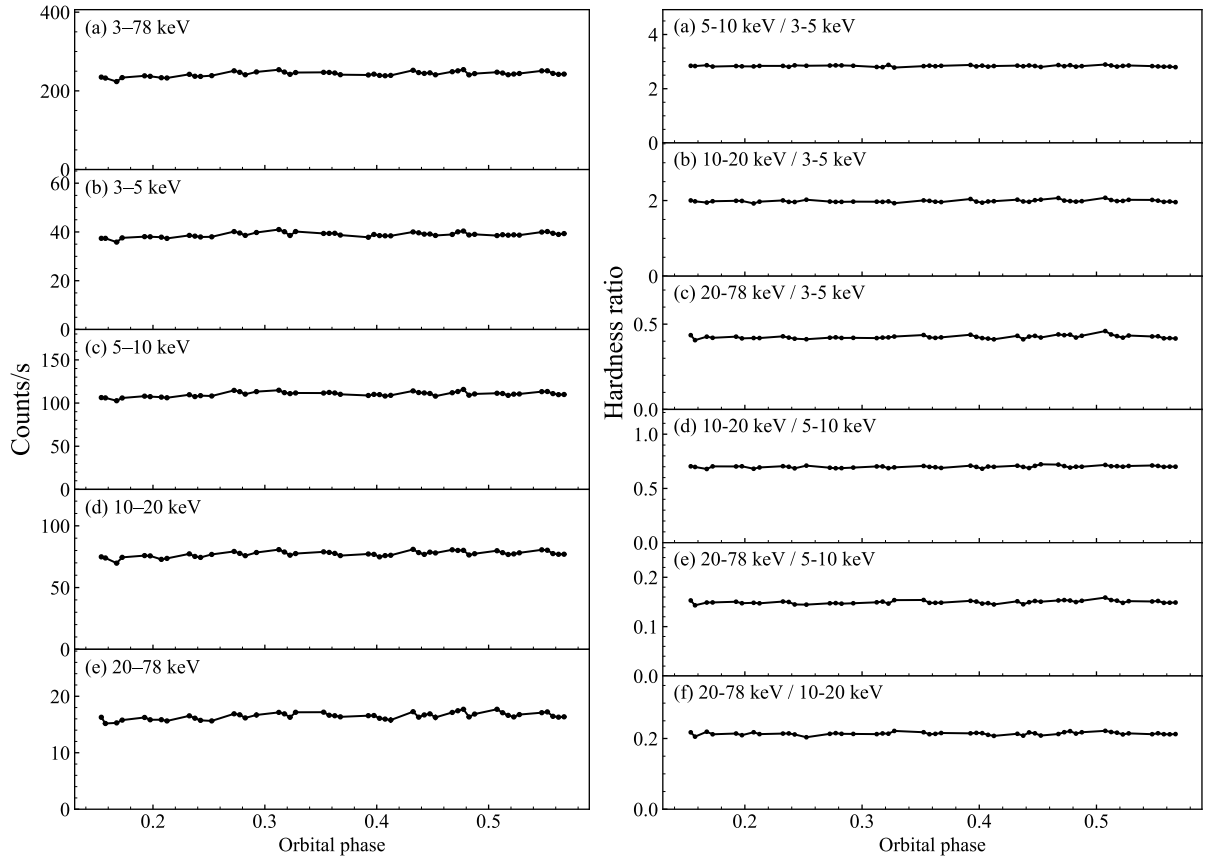


Figure 8.4: Light curves of different energy bands (left) and hardness ratios among the energy bands (right).

Table 8.2: Statistical parameters of energy-resolved light curves.

Energy band	mean <sup>a</sup> (Counts/s)	$\sigma^b$ (Counts/s)	$\sigma/\text{mean}$
3–78 keV	243	6.13	2.52%
3–5 keV	38.9	0.957	2.46%
5–10 keV	110	2.64	2.39%
10–20 keV	77.2	2.22	2.88%
20–78 keV	16.5	0.578	3.50%

<sup>a</sup> Average value of the count rates.

<sup>b</sup> Standard deviation of the count rates.

### 8.3.2 Orbital-phase-resolved spectroscopy

We performed a spectral analysis on the orbital-phase-resolved data in order to examine the variability of the spectral shape. We first tried to evaluate the phase-averaged spectrum by a typical phenomenological model described by equation (4.15). We assumed  $N_{\text{H}}^{\text{IM}} = 1.5 \times 10^{20} \text{ cm}^{-2}$  for the photoelectric absorption by the interstellar medium, based on HI4PI Map (HI4PI Collaboration et al., 2016).

Figure 8.5 shows the result of the spectral fitting on the phase-averaged spectrum. The observed spectrum was well reproduced by the model with an acceptable reduced chi-square of  $\chi_{\nu}^2 = 1.37$ . The best-fit parameters are summarized in Table 8.3. The 3–78 keV flux is  $7.45 \times 10^{-9} \text{ erg s}^{-1} \text{ cm}^{-2}$ , corresponding to a luminosity of  $3.3 \times 10^{37} \text{ erg s}^{-1}$ . We did not detect any additional absorption by the stellar wind, with an upper limit of  $N_{\text{H}} < 0.8 \times 10^{20} \text{ cm}^{-2}$ . The continuum parameters are typical to disk-fed X-ray pulsars, giving a harder photon index, higher cut-off energy, and comparable folding energy to Cen X-3. The Fe line is also detected significantly with a comparable line intensity and equivalent with Cen X-3. The CRSF parameters are also comparable to Cen X-3, but Her X-1 has a little higher central energy than Cen X-3.

In order to examine the variability of the spectral shape, we applied spectral fitting on each orbital-phase-resolved spectrum, with spectral parameters fixed to the values in Table 8.3. We only freed parameters representing the normalization of each component, that is, the continuum flux, the Fe line intensity  $I_{\text{Fe}}$ , and the optical depth of CRSF  $\tau_{\text{cyc}}$ . Figure 8.6 presents the results of the spectral fitting. The fitting yielded acceptable reduced chi-square values with an average value of 1.00. The 3–78 keV flux varies by 2.8%, and  $I_{\text{Fe}}$  and  $\tau_{\text{cyc}}$  do not show any significant variability along the orbital phase. Therefore, all the orbital-phase-resolved spectra can be reproduced by the variation in the normalization factor of the continuum.

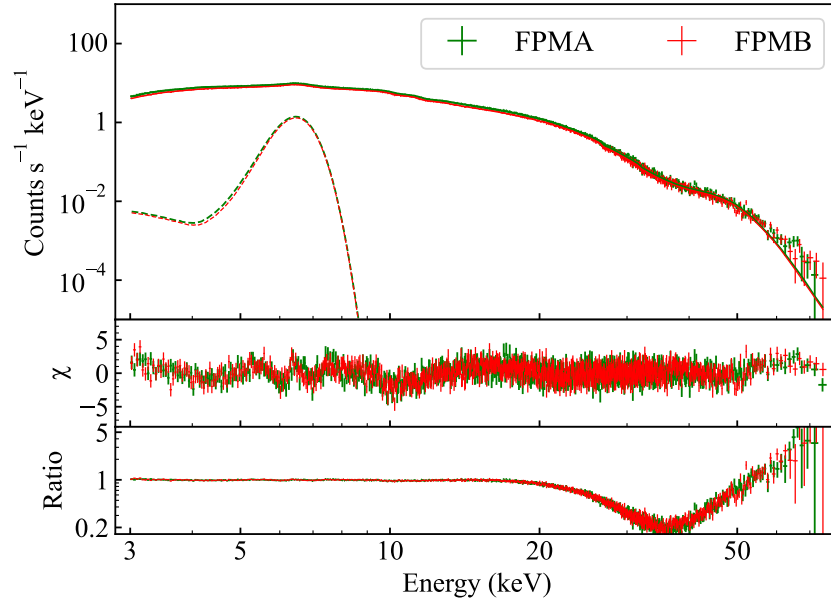


Figure 8.5: Fitting result of 3–78 keV phase-averaged spectra. The contributions of the Fe emission line are plotted by dashed lines. The middle panel shows the residuals between data and model. The bottom panel shows the contribution of the CRSF by plotting ratios between data and model without CRSF.

Table 8.3: Best-fit parameters of phase-averaged spectrum.<sup>a</sup>

Parameter <sup>b</sup>	Value
$N_{\text{H}}^{\text{IM}}$ ( $10^{20} \text{ cm}^{-2}$ )	1.5 (fixed)
$N_{\text{H}}$ ( $10^{20} \text{ cm}^{-2}$ )	$< 0.8$
$\Gamma$	$0.960 \pm 0.003$
$E_{\text{c}}$ (keV)	$36.9^{+0.9}_{-0.8}$
$E_{\text{f}}$ (keV)	$5.1 \pm 0.2$
$E_{\text{Fe}}$ (keV)	$6.48 \pm 0.01$
$\sigma_{\text{Fe}}$ (keV)	$0.40 \pm 0.02$
$I_{\text{Fe}}$ ( $10^{-3} \text{ photons cm}^{-2} \text{ s}^{-1}$ )	$5.5 \pm 0.2$
$\text{Eqw}_{\text{Fe}}^{\text{c}}$ (keV)	$0.19 \pm 0.01$
$E_{\text{cyc}}$ (keV)	$36.3 \pm 0.2$
$\sigma_{\text{cyc}}$ (keV)	$7.3 \pm 0.1$
$\tau_{\text{cyc}}$	$1.6 \pm 0.1$
Flux <sup>d</sup> ( $10^{-9} \text{ erg s}^{-1} \text{ cm}^{-2}$ )	$7.45 \pm 0.05$
$\chi^2_{\nu}$ (d.o.f.)	1.37 (1848)

<sup>a</sup> Errors denote 90% confidence levels.

<sup>b</sup> For the definitions of the parameters, see equations (4.6), (4.7), (4.8), (4.15), and (4.16).

<sup>c</sup> The equivalent width of the Fe line.

<sup>d</sup> 3–78 keV absorbed flux.

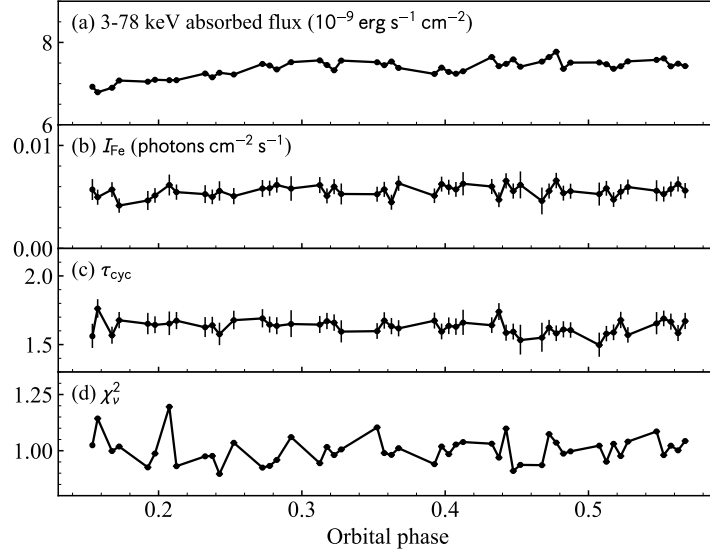


Figure 8.6: Orbital-phase variability of spectral parameters. See text for the detailed model expression and fitting method.

## 8.4 Spin-phase variability

Similar to Sections 4.4 and 5.3, we investigated the spin-phase variability of Her X-1 by energy-resolved pulse profiles and spin-phase-resolved spectroscopy.

### 8.4.1 Energy-resolved pulse profile

We divided 3–78 keV NuSTAR data into 18 energy bands and generated pulse profiles for all the energy bands by folding the light curves with  $P_{\text{spin}} = 1.237711$  s. The spin phase is defined so that the peak of the 1st Fourier component in 3–78 keV pulse profile correspond to  $\phi = 0.25$ , same as the Cen X-3 analysis. Figure 8.7 presents the 18 pulse profiles over two spin periods. All the pulse profiles show apparent pulsations, exhibiting a gradual change in the profile shape with energy. In low energy bands, the profiles have two peaks at  $\phi \sim 0.1$  and  $\phi \sim 0.4$  but do not have a peak at  $\phi \sim 0.25$ . As energy increases, the two-peaked shape declines, and the pulse profile shifts to a single-peaked profile with a peak phase of  $\phi \sim 0.25$ . The boundary can be seen in the 8–9 keV pulse profile, where three peaks exist in one pulse profile at  $\phi \sim 0.1, 0.25, 0.4$ . In the latter half of the spin period ( $\phi > 0.5$ ), we can see a small peak around  $\phi \sim 0.65$ , which is less significant than Cen X-3 pulse profiles (see Figure 5.11).

We also carried out a detailed analysis on the energy-resolved pulse profiles based on the Fourier transform. The detailed analysis method is presented in Section 4.4.1. Figure 8.8 shows the energy dependence of the pulse fraction and Fourier coefficients. The pulse fraction displays a gradual increase from 0.6 to 1.0 as energy goes up with the exceptions of two energy bands, corresponding to Fe emission line and CRSF bands represented by red dotted lines (Figure 8.8a). The pulse fraction becomes lower than nearby bands by  $\sim 12\%$  and  $\sim 21\%$  for Fe line and CRSF bands, respectively, which are comparable to the Cen X-3 case (Section 5.3.1). The decrease in pulse fraction is seen in both the 1st and 2nd Fourier coefficients (Figure 8.8b and c). Figure 8.8(d) shows the ratio between the 1st and 2nd Fourier coefficient. It shows that the 1st Fourier component becomes significantly dominant at the CRSF band, suggesting that the CRSF strength is more likely to vary as a single-peaked profile along the spin phase.

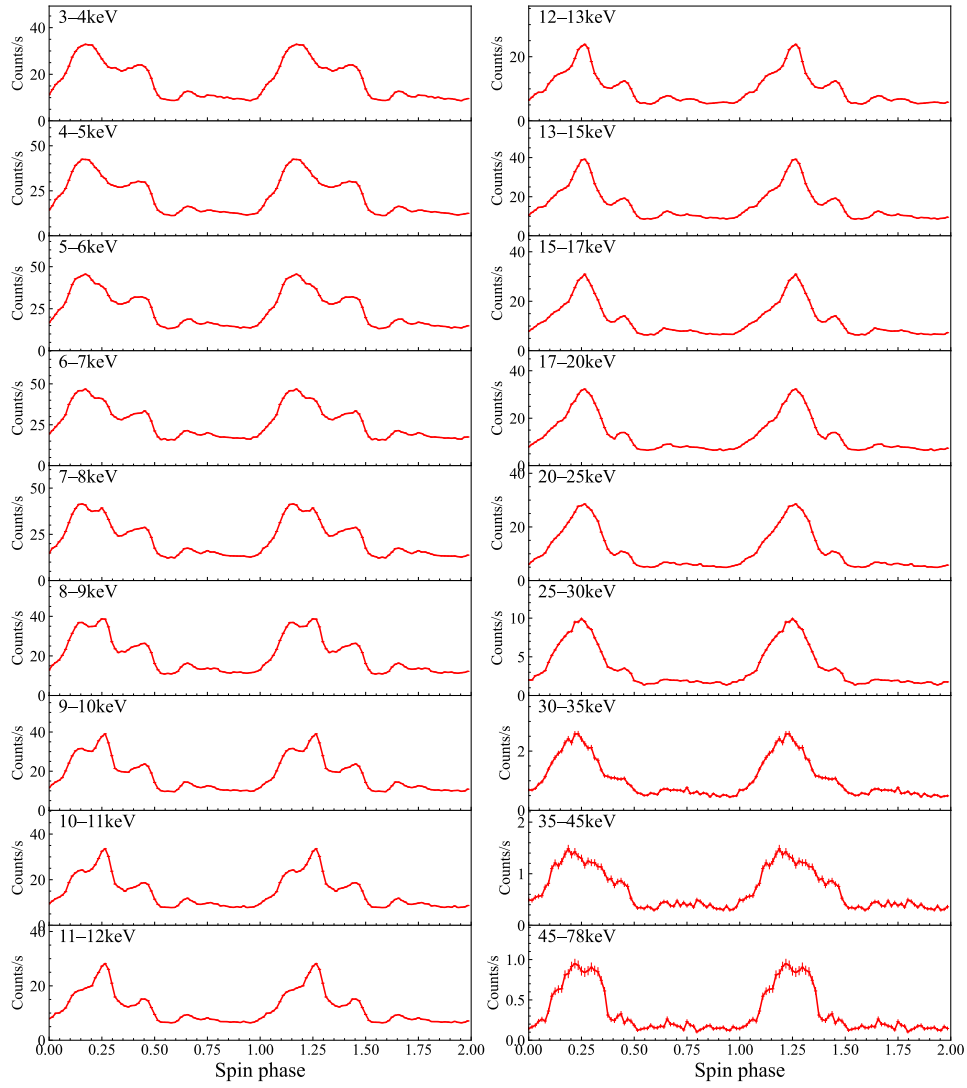


Figure 8.7: Energy-resolved pulse profiles over two spin periods generated for 18 energy bands. The summation of FPMA and FPMB counts are plotted.



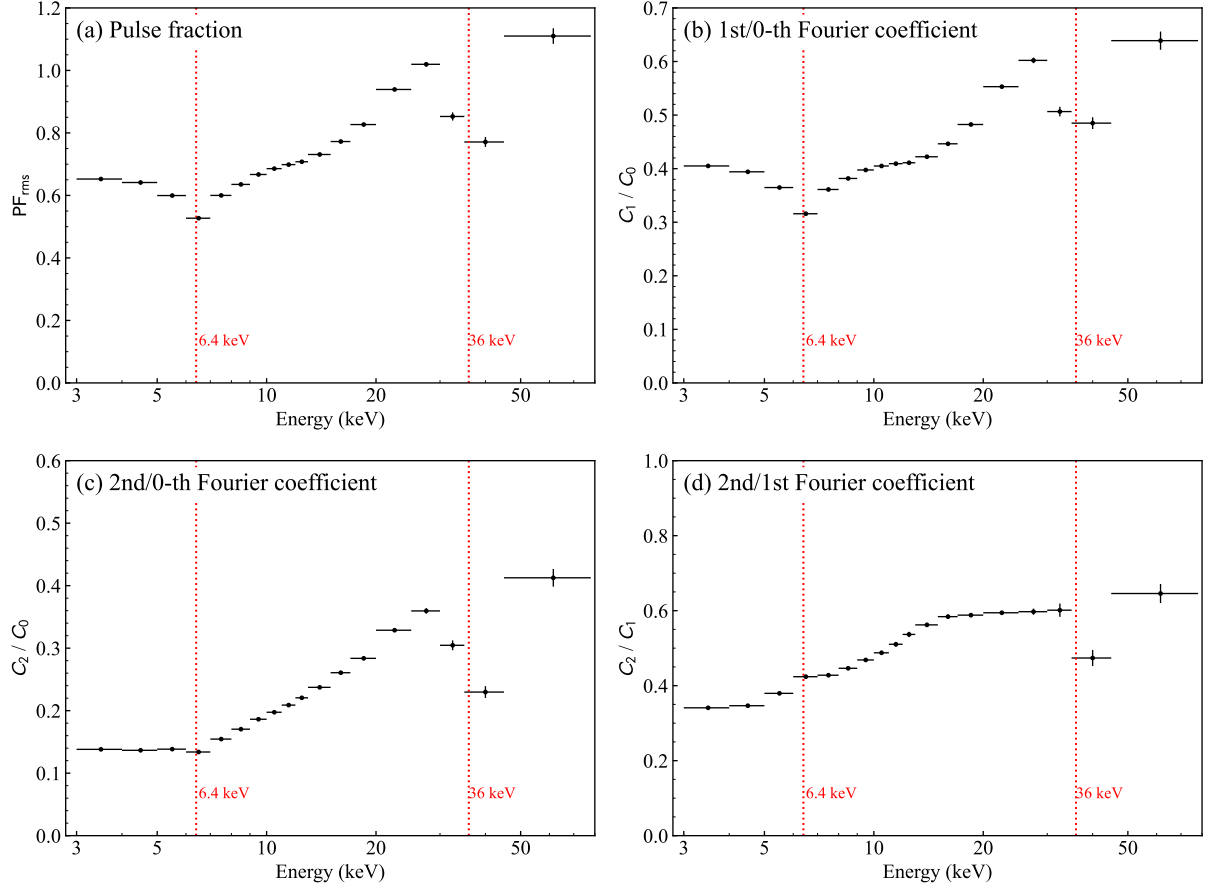


Figure 8.8: Analysis results of energy-resolved pulse profiles. (a)  $PF_{\text{rms}}$ , (b)  $c_1/c_0$ , (c)  $c_2/c_0$ , and (d)  $c_2/c_1$  as a function of energy. The red dotted lines represent energies corresponding to the Fe emission line (6.4 keV) and the CRSF central energy (36 keV).

#### 8.4.2 Spin-phase-resolved spectroscopy

In order to investigate the spin-phase spectral variability in detail, we performed spectral fitting to the spin-phase-resolved spectra. We divided the whole spin phase into eight intervals. We adopted the same definition of spin-phase intervals as Figure 5.20, labeled by A, B, ..., and H. The assumed spectral model is the same as the phase-averaged spectroscopy in Section 8.3.2, given by equation (4.15).

Figure 8.9 shows the fitting results of the spin-phase-resolved spectroscopy, and the best-fit parameters are summarized in Table 8.4. The model basically reproduces the observed spectra except for the spin-phase interval C, where large residuals remain in 3–5 keV. The evaluation of Fe line also faces troubles in bright phases (intervals B, C, and D), as the emission line is not significant enough to determine spectral parameters. These discrepancies between data and model should be examined by a more statistically rich observation with a finer division of the spin phase. In this section, we only focus on the

variability of the CRSF parameters since the basic properties of the spin-phase variability at each energy band can be adequately examined by the energy-resolved pulse profiles. Figure 8.9 shows that the structures of the CRSF are well reproduced by the spectral model.

Figure 8.10 shows the spin-phase variability of the CRSF parameters. The central energy  $E_{\text{cyc}}$  ranges from 31.9 to 37.6 keV, corresponding to an  $\sim 18\%$  difference in the magnetic field strength. It displays a significant enhancement in the pulse maximum (interval C). The line width  $\sigma_{\text{cyc}}$  also appears to increase to 7 keV at the pulse maximum, although it has large uncertainties in the latter half of the spin period. The optical depth ranges from 0.7 to 2.2, and also peaks at the pulse maximum. These trends of CRSF parameters, the increased central energy, line width, and optical depth at the pulse maximum, are similar to those of Cen X-3 (see Section 5.3.2).

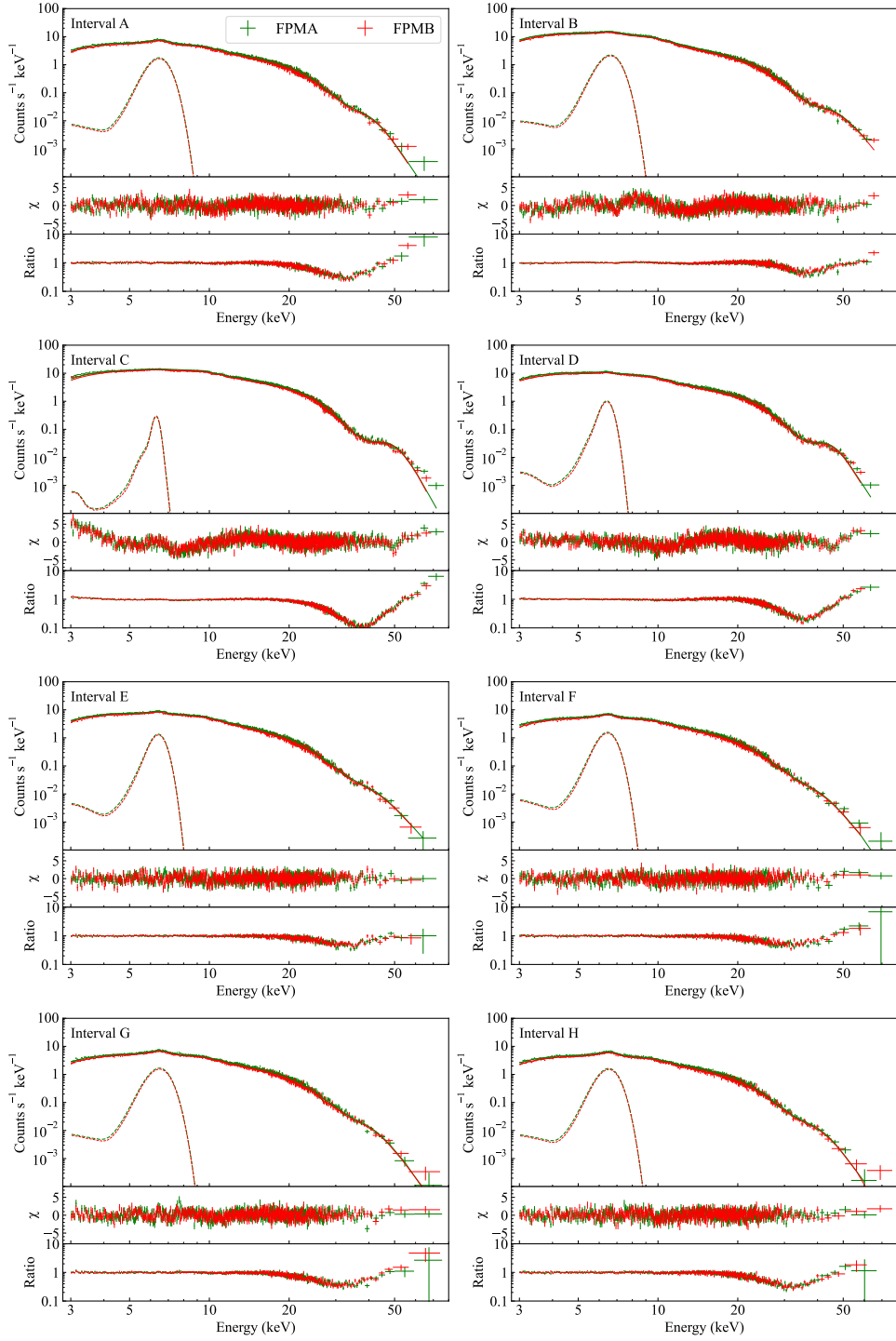


Figure 8.9: Fitting results of spin-phase-resolved spectroscopy. The contributions of emission lines are plotted by dashed lines. The middle panels show residuals between the data and model. The bottom panels show the contributions of the CRSF by plotting ratios between data and model without CRSF.

Table 8.4: Best-fit parameters of spin-phase-resolved spectroscopy.<sup>a</sup>

Spin-phase interval	A	B	C	D	E	F	G	H
$\Gamma$	$1.00 \pm 0.01$	$1.05^{+0.02}_{-0.01}$	$0.71 \pm 0.01$	$1.07 \pm 0.01$	$0.95^{+0.03}_{-0.02}$	$0.86 \pm 0.02$	$0.89^{+0.01}_{-0.02}$	$0.95^{+0.01}_{-0.02}$
$E_c$ (keV)	$32.8^{+2.4}_{-1.9}$	$27.3^{+1.0}_{-0.5}$	$39.8^{+0.9}_{-0.9}$	$39.2^{+0.8}_{-0.7}$	$26.0^{+3.5}_{-1.7}$	$26.6^{+3.7}_{-1.9}$	$30.4^{+4.8}_{-2.7}$	$31.8^{+3.9}_{-2.8}$
$E_f$ (keV)	$4.2^{+0.5}_{-0.6}$	$8.6^{+0.2}_{-0.3}$	$4.7 \pm 0.3$	$4.5 \pm 0.3$	$6.5^{+0.3}_{-0.7}$	$5.6^{+0.4}_{-0.7}$	$4.9^{+0.6}_{-1.1}$	$4.5^{+0.7}_{-1.0}$
$E_{\text{Fe}}$ (keV)	$6.47 \pm 0.03$	$6.62 \pm 0.03$	$6.31 \pm 0.13$	$6.42 \pm 0.04$	$6.43 \pm 0.03$	$6.46 \pm 0.03$	$6.50 \pm 0.03$	$6.53 \pm 0.02$
$\sigma_{\text{Fe}}$ (keV)	$0.48 \pm 0.04$	$0.50$ (fixed) <sup>c</sup>	$0.05^{+0.14}_{-0.05}$	$0.24^{+0.07}_{-0.06}$	$0.31 \pm 0.05$	$0.41 \pm 0.04$	$0.50 \pm 0.03$	$0.47 \pm 0.03$
$I_{\text{Fe}}$ ( $10^{-3}$ photons $\text{cm}^{-2} \text{s}^{-1}$ )	$7.9 \pm 0.4$	$10.1 \pm 0.5$	$0.5 \pm 0.3$	$2.8 \pm 0.4$	$4.4 \pm 0.4$	$6.2 \pm 0.4$	$7.8^{+0.3}_{-0.4}$	$7.2 \pm 0.4$
$\text{Eqw}_{\text{Fe}}^c$ (keV)	$0.39 \pm 0.02$	$0.23 \pm 0.01$	$0.01 \pm 0.01$	$0.08 \pm 0.01$	$0.17 \pm 0.02$	$0.33 \pm 0.02$	$0.42 \pm 0.02$	$0.45 \pm 0.02$
$E_{\text{cyc}}$ (keV)	$32.4^{+1.0}_{-0.8}$	$36.9 \pm 0.4$	$37.6 \pm 0.3$	$35.4 \pm 0.3$	$33.0^{+0.8}_{-0.7}$	$31.6^{+1.3}_{-0.7}$	$32.0^{+1.8}_{-1.0}$	$31.9^{+1.4}_{-0.9}$
$\sigma_{\text{cyc}}$ (keV)	$6.3 \pm 0.4$	$5.1 \pm 0.3$	$7.1 \pm 0.1$	$5.7^{+0.1}_{-0.2}$	$6.7^{+1.0}_{-0.7}$	$6.6^{+1.0}_{-0.9}$	$6.9^{+0.8}_{-0.7}$	$6.5 \pm 0.6$
$\tau_{\text{cyc}}$	$1.2^{+0.4}_{-0.3}$	$0.9 \pm 0.1$	$2.2 \pm 0.1$	$1.7 \pm 0.1$	$0.7^{+0.4}_{-0.2}$	$0.7^{+0.5}_{-0.3}$	$1.0^{+0.7}_{-0.3}$	$1.2^{+0.6}_{-0.4}$
Flux <sup>b</sup> ( $10^{-9}$ erg $\text{s}^{-1} \text{cm}^{-2}$ )	$4.9 \pm 0.1$	$11.0^{+0.2}_{-0.1}$	$15.4 \pm 0.2$	$9.1 \pm 0.1$	$5.9 \pm 0.1$	$4.5 \pm 0.1$	$4.6 \pm 0.1$	$4.0 \pm 0.1$
$\chi^2_{\nu}$ (d.o.f.)	$1.11$ (1158)	$1.60$ (1387)	$1.93$ (1474)	$1.51$ (1338)	$1.06$ (1190)	$1.09$ (1136)	$1.12$ (1143)	$1.14$ (1105)

<sup>a</sup> Errors denote 90% confidence levels.

<sup>b</sup> 3–78 keV absorbed flux.

<sup>c</sup> Fixed due to large uncertainties.

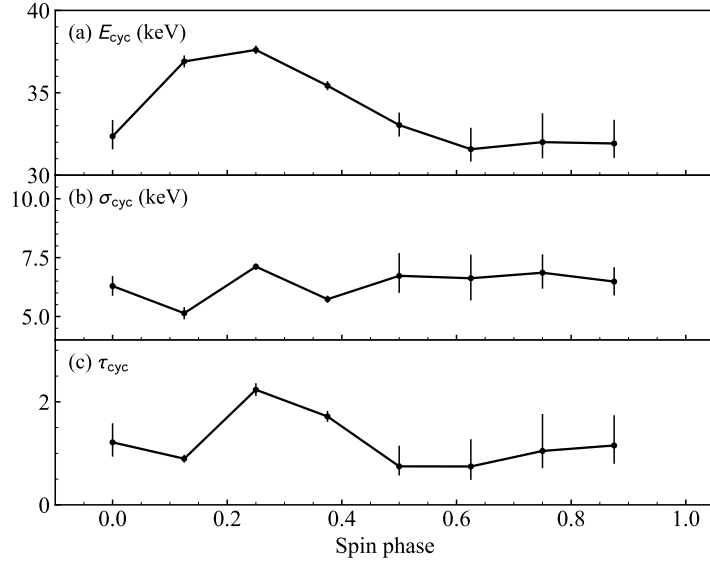


Figure 8.10: Spin-phase variability of CRSF parameters derived from spectral fitting.

## 8.5 Variability of pulse profile

Finally, we investigate the variability of the pulse profile along the orbital phase. It is suggested that the accretion flow is highly stable because of the low variability of the flux along the orbital phase (Section 8.3). Here, we examine the stability of the pulsed beam pattern by investigating the variability of the pulse profile parameters. The detailed expression for the analysis method is presented in Section 4.5.2.

We calculated pulse profile parameters at each of 49 orbital intervals defined in Section 8.3. Figure 8.11 presents the orbital-phase variability of the pulse profile parameters for multiple energy bands. We did not detect any significant variability in the pulse fraction and ratios among the Fourier coefficients. We can conclude that the pulse profile is highly stable along the orbital phase, which gives us the legitimacy to conduct a spin-phase-resolved analysis without caring about the dependence on the orbital phase.

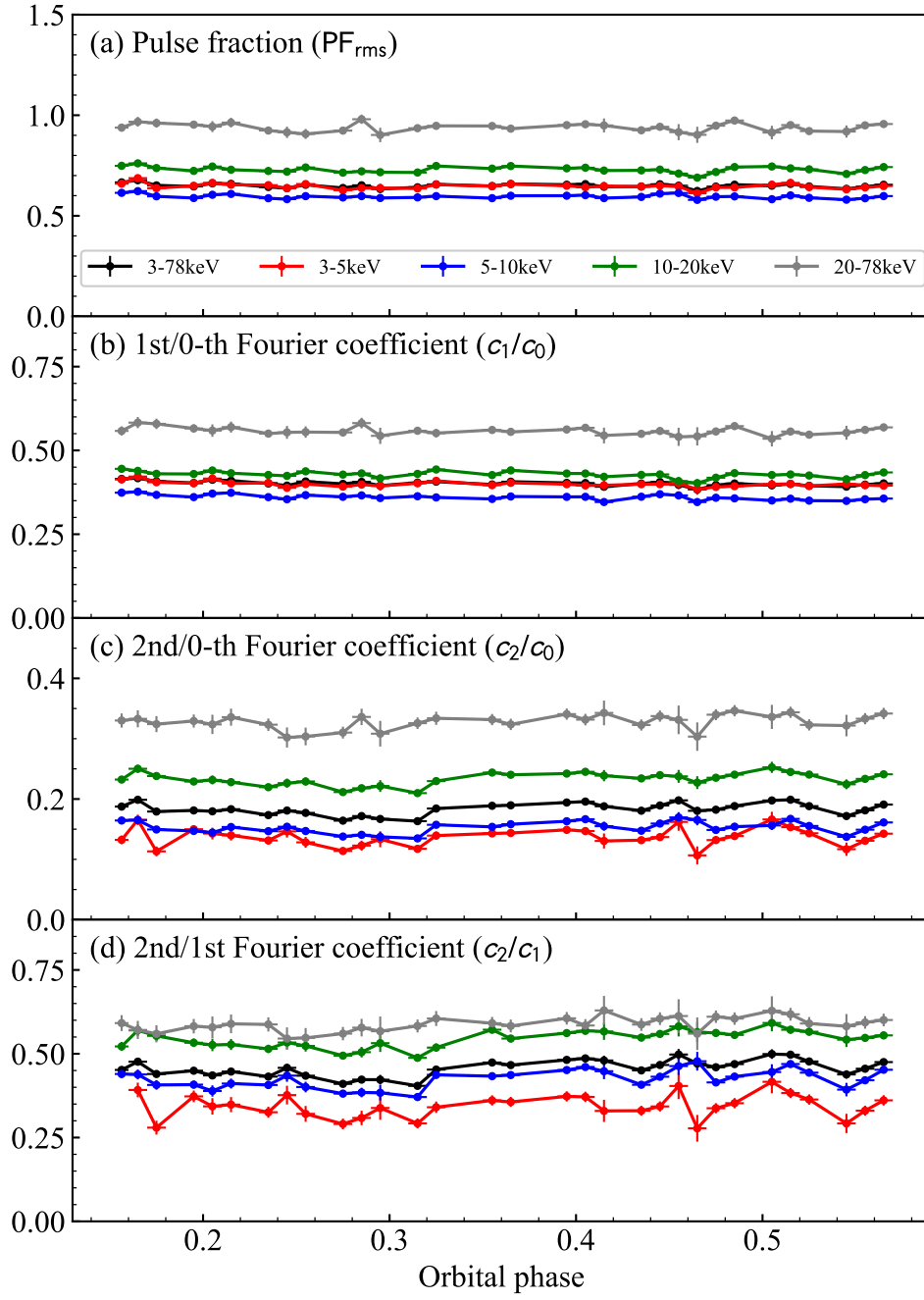


Figure 8.11: Variations of pulse profile parameters along the orbital phase calculated for multiple energy bands.

# Chapter 9

## Discussions on the accretion flow onto highly magnetized neutron stars

In addition to the orbital-phase variability discussed in Chapter 7, we have investigate the spin-phase variability of disk-fed X-ray pulsars through the observation data of Cen X-3 and Her X-1. The spin-phase variability, characterized by pulse profiles and spin-phase-resolved spectra, reflects the unique environment in the accretion sites of X-ray pulsars particularly affected by the strong magnetic field. In this chapter, we mainly focus on the pulse profiles of these two objects and give physical interpretations to the observational properties obtained in the previous chapters. We also discuss the spin-phase-resolved spectra, mainly focusing on the variabilities of the CRSF.

### 9.1 Summary of pulse profile properties of Cen X-3 and Her X-1

We investigated the spin-phase variabilities through energy-resolved pulse profiles in the analysis of Cen X-3 and Her X-1 observation data. The accurate shapes of pulse profiles are presented in Figure 5.11 and Figure 8.7 for Cen X-3 and Her X-1, respectively. For both cases, the shapes of pulse profiles display gradual changes with energy. In order to examine the similarities and differences in pulse profile properties between these objects, we picked up three representative energy bands, 3–4, 9–10, and 20–25 keV. Figure 9.1 shows the pulse profiles in these energy bands for the two sources. Here, we summarize the qualitative properties of pulse profiles and discuss possible physical interpretations.

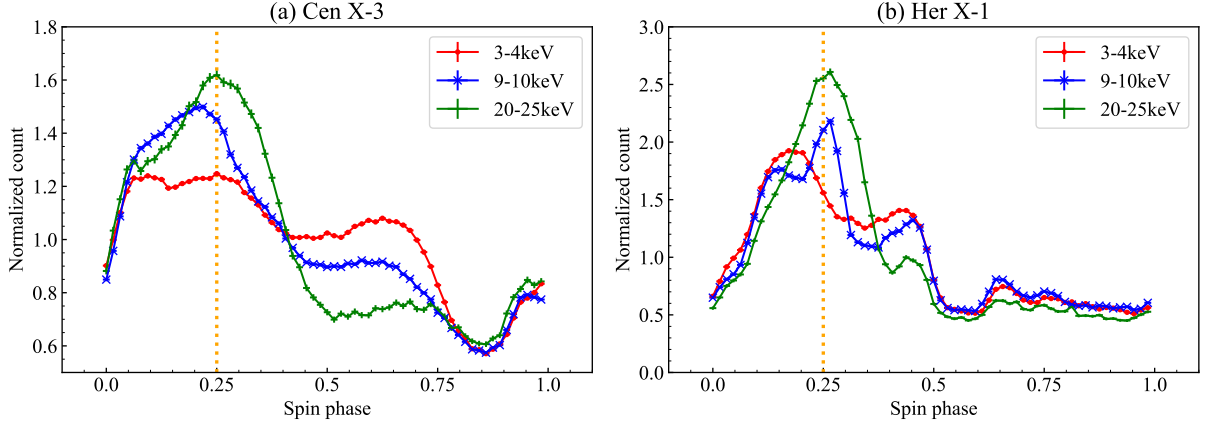


Figure 9.1: Energy dependence of pulse profiles of (a) Cen X-3 and (b) Her X-1. Pulse profiles of different energy bands are plotted with different colors. For the sake of comparison, the pulse profiles are normalized by the average value of the count rates. The vertical orange lines denote the pulse maxima of  $\phi = 0.25$ .

### 9.1.1 Pulse maximum

It is widely agreed that high-luminosity pulsars like Cen X-3 and Her X-1 form optically thick accretion columns above the magnetic poles. The radiation-dominated shock is formed inside the column, which decelerates the accretion flow, and the kinetic energy is converted to radiation via bulk and thermal Comptonization (see Section 2.4). Generally, the radiation from the accretion column is classified into two types depending on the emission regions. One is the “pencil beam”, a sharp X-ray radiation from the top of the column. The other is the “fan beam”, which is a widespread X-ray radiation from the wall of the column. The pulse maximum of a single-peaked pulse profile is generally considered to correspond to the center of the pencil beam because the fan beam needs two separate peaks at symmetrical phases.

In Cen X-3 and Her X-1 cases, we can infer that the pulse maximum corresponds to the center of the pencil beam. For both sources, the 20–25 keV pulse profile has a sharp peak at  $\phi = 0.25$  and no other prominent peaks, as shown in Figure 9.1. Since the pencil beam distributes around the magnetic axis, the angle between the magnetic axis and line of sight reaches a minimum at the spin phase of  $\phi = 0.25$ . The low-energy pulse profiles, however, do not show apparent peaks at  $\phi = 0.25$ . In Cen X-3, the 3–4 keV pulse profile displays a flat profile at  $0.1 < \phi < 0.3$ . This trend was already examined by the pulse profile analysis, detected as low pulse fractions (Figure 5.12a) and peak phase shifts (Figure 5.13) in low-energy bands. In Her X-1, the 3–4 keV pulse profile is even more characteristic, which shows two separate peaks at  $\phi \sim 0.15$  and  $\phi \sim 0.40$ . This feature is also reflected as suppressed pulse fractions in low-energy bands (Figure 8.8a). We can attribute the flatness or separated peaks around the pulse maximum to the



contributions from the fan-beam component. A possible explanation for the observational properties of pulse profiles is that the widespread fan beam has more contribution in low-energy bands than in high-energy bands. Indeed, West et al. (2017) shows that the fan beam is dominant in low-energy bands while the pencil beam becomes more dominant in high-energy bands up to the cyclotron energy, through a simulation-based study on the accretion column model of Becker & Wolff (2007).

### 9.1.2 Asymmetry around pulse maximum

In both Cen X-3 and Her X-1, the pulse profiles are not completely symmetrical about the pulse maximum. The low-energy bands appear to show more asymmetrical profiles than the high-energy bands, as seen in Figure 9.1. We evaluated the symmetrical degrees of the pulse profiles by calculating the count ratios between symmetrical phases about the pulse maximum ( $\phi = 0.25$ ). The count ratio can be calculated by

$$\text{Count ratio} = \frac{p(\phi)}{p(0.5 - \phi)} \quad (0.25 < \phi < 0.5), \quad (9.1)$$

where  $p(\phi)$  denotes the pulse profile. Figure 9.2 presents count ratios representing symmetrical degrees.

The asymmetry of the pulse profiles can be approximated by a Gaussian-like absorption function. We evaluated the profiles in Figure 9.2 by

$$\frac{p(\phi)}{p(0.5 - \phi)} = \exp \left\{ -\tau_{\text{abs}} \exp \left[ -\frac{(\phi - \phi_{\text{abs}})^2}{2\sigma_{\text{abs}}^2} \right] \right\}. \quad (9.2)$$

The physical meaning of the equation is the absorption by a spatially expanded material whose angular distribution is Gaussian.  $\tau_{\text{abs}}$ ,  $\phi_{\text{abs}}$ , and  $\sigma_{\text{abs}}$  denote the optical depth at the center, central phase of absorption, and width of the absorption profile, respectively. Table 9.1 presents these three parameters derived from fitting on the pulse profiles of Cen X-3 and Her X-1. The optical depth at the center of the absorption profile is 0.2–0.5, corresponding to a hydrogen column density of  $3\text{--}8 \times 10^{23} \text{ cm}^{-2}$  when Compton scattering is assumed.

The most possible candidate for the physical origin of the asymmetric pulse profile is the obscuration by a warped accretion disk. This can be shown by the superorbital variability of the pulse profile. It is widely known that the Her X-1 pulse profile is highly transient along the superorbital phase (Scott et al., 2000; Ramsay et al., 2002; Brumback et al., 2021). Figure 9.3 shows one example of pulse profile variability of Her X-1 along the superorbital phase, presented in Scott et al. (2000). Note that  $\phi \sim 1.1$  in Figure 9.3 is the pulse maximum and corresponds to  $\phi = 0.25$  in our analysis. In the brightest phase, the pulse profile is similar to our analysis, with a large peak at  $\phi \sim 1.05$  and a small peak at  $\phi \sim 1.2$  forming an asymmetric pulse profile. However, the difference between

the two peaks vanishes in the dark phases. Therefore, it is strongly suggested that the asymmetrical profile in the Her X-1 pulse profile originates from the geometrical effect of the precessing accretion disk. Although no superorbital motion is detected for Cen X-3, the disk-fed accretion site is confirmed, and it is also possible to form asymmetric pulse profiles by the effect of the accretion disk.

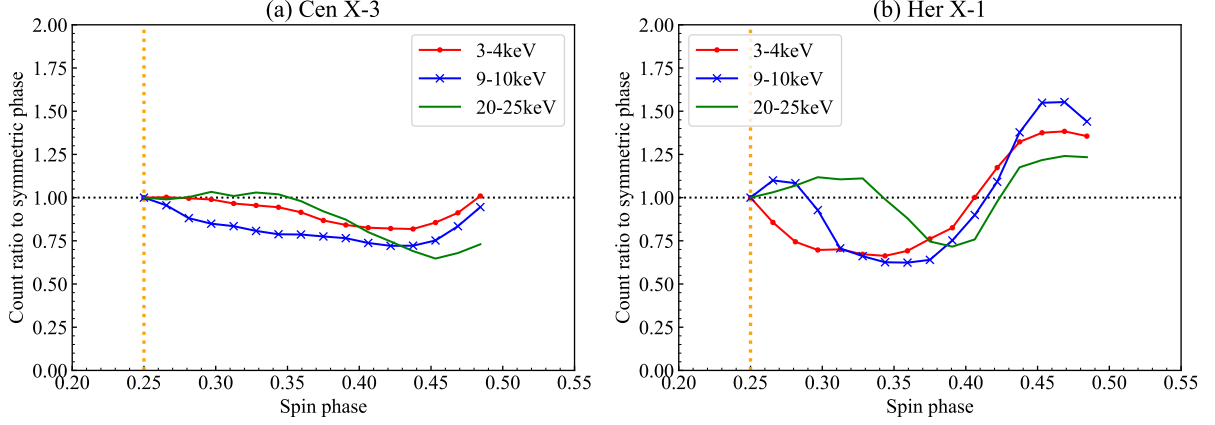


Figure 9.2: Symmetrical degrees of pulse profiles, investigated for  $0.25 < \phi < 0.50$ . The y-axis denotes the count ratio to the symmetrical phase, given by equation (9.1).

Table 9.1: Parameters of pulse profile obscuration.<sup>a</sup>

Source	Energy band	$\tau_{\text{abs}}$	$\phi_{\text{abs}}$	$\sigma_{\text{abs}}$
Cen X-3	3–4 keV	0.21	0.41	0.042
	9–10 keV	0.31	0.39	0.072
	20–25 keV	0.42	0.45	0.041
Her X-1	3–4 keV	0.44	0.33	0.041
	9–10 keV	0.55	0.35	0.030
	20–25 keV	0.36	0.39	0.020

<sup>a</sup> Based on equation (9.2).

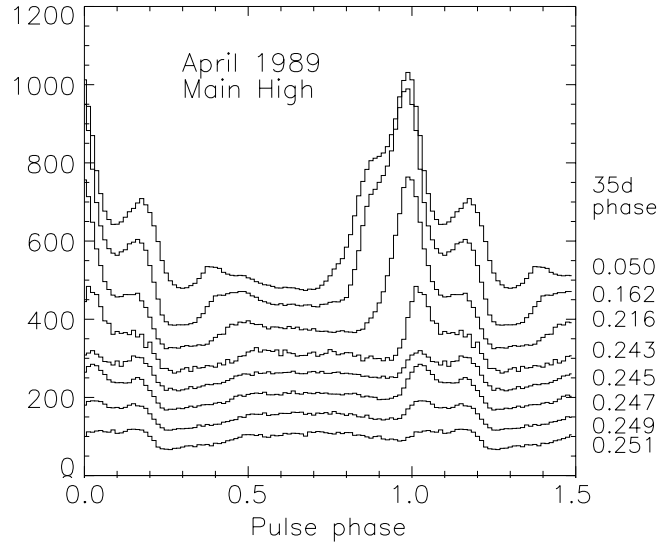


Figure 9.3: Difference in Her X-1 pulse profiles along the superorbital phase, observed by Ginga. 9.3–14 keV Ginga data from eight superorbital phases are plotted together. Taken from Scott et al. (2000).

### 9.1.3 Emission from dipole configuration

Since the neutron star is accompanied by two magnetic poles, one could observe the contribution from the two accretion columns depending on the relation among the spin axis, magnetic axis, and line of sight. In such an object, a smaller peak than the main peak can be seen in the antipodal phase of the main peak. This feature is seen in both Cen X-3 and Her X-1, as the pulse profiles in Figure 9.1 exhibit small peaks at  $\phi \sim 0.65$ . Cen X-3 shows more apparent peaks, while those of Her X-1 pulse profiles are almost smeared out in the non-pulsed component. It can be speculated that the configuration of Cen X-3 is more likely to result in the observation of the opposite side of the accretion column, while Her X-1 mostly has one side of the columns faced to the observer. There is a large energy difference in the antipodal peak, particularly in Cen X-3 pulse profiles. The low-energy bands have more prominent antipodal peaks than the high-energy bands. It is natural because the contribution from the antipodal column should be composed of the widespread fan beam rather than the narrow pencil beam, which is more dominant in low-energy bands.

Assuming an utterly antipodal configuration of the magnetic poles, it is strange that the peak phase is not located at  $\phi = 0.75$  but at  $\phi \sim 0.65$ . The displacement from the antipodal configuration of Cen X-3 was investigated by Kraus et al. (1996). They pointed out the possibility of the distorted antipodal configuration by  $\sim 10^\circ$ . The recent IXPE observation based on the spin-phase variability of X-ray polarization also derived a similar result (Tsygankov et al., 2022). Another possible effect would be the asymmetric pulse

profiles around  $\phi = 0.75$  caused by the obscuration due to a warped accretion disk, as pointed out in Section 9.1.2. For further investigation on the peak phase of the antipodal peaks, we need to investigate the long-term variability of pulse profiles in detail, which is beyond the scope of this thesis.

## 9.2 Physical model of X-ray emission from accretion column

In Section 9.1, we have summarized the qualitative properties of pulse profiles found in Cen X-3 and Her X-1. The most notable is the energy difference in the shape around the pulse maximum. The qualitative interpretation can be easily given as discussed in Section 9.1.1, but no quantitative explanation based on a three-dimensional view of physical processes has been established. In this section, we construct a simulation-based framework that can reproduce the three-dimensional view of the emission processes in the highly magnetized accretion column.

We used a Monte-Carlo simulation framework MONACO (Odaka et al., 2011) to calculate the emission processes in the accretion column. It can reproduce three-dimensional plasma with physical parameters such as number density, bulk velocity, magnetic field, ionization degree, and electron temperature. It then simulates interactions between photons and plasma based on physical processes such as photo-excitation, photo-absorption, and Compton scattering. The simulation of the accretion columns in X-ray pulsars was already carried out by Odaka et al. (2014), which successfully reproduced the variability in the spin-phase-averaged spectra of a wind-fed X-ray pulsar Vela X-1. However, the spin-phase-resolved emission profile has yet to be studied with MONACO because Vela X-1 is highly transient due to the effect of the stellar wind capture. In this thesis, we aim to investigate the anisotropy of the emission by reproducing the observed pulse profiles with the three-dimensional simulation.

### 9.2.1 Simulation setup

Figure 9.4 shows the schematic view of the simulation setup for the accretion column. We constructed a column geometry with a radius and height of  $r_0$  and  $h$ , respectively. The column is filled with a fully-ionized plasma falling onto the neutron star with a bulk velocity  $v_z$ . The plasma has a radial optical depth of  $\tau$  and an electron temperature of  $kT_e$ . Although the velocity and the radial optical depth in the accretion column depend on the height from the neutron star surface (equation 2.24), we adopted a one-zone model for simplicity. The one-dimensional study of the accretion column in West et al. (2017) shows that the most observed emission comes from the limited region around the sonic

point, and thus the one-zone approximation is not far from the actual situation of the emitting region.

The whole system is magnetized with a uniform magnetic field of  $B_z$ . Seed photons are originated uniformly in the accretion column, and the bulk and thermal Comptonization in the column is calculated by the framework. Here, the cross section of the Comptonization is suppressed by the strong magnetic field, as shown by equation (2.17). In our simulation, the cross section is based on equation (2.17) with  $\sigma_T$  converted to the Klein-Nishina Compton scattering cross section (Klein & Nishina, 1929). The scattered seed photons escape from either the ceiling or the wall of the column after experiencing Compton scattering, and are recorded as pencil beam or fan beam, respectively.

The seed photons originate from thermal bremsstrahlung, cyclotron radiation inside the accretion column, and blackbody emission from the surface of the neutron star, as reviewed in Section 2.4.3. It is shown that thermal bremsstrahlung is the most dominant process for the seed photon generation, and the effects of the other two processes are negligible (e.g., Wolff et al., 2016; West et al., 2017). In our simulation, we treat thermal bremsstrahlung as the only process to generate seed photons. We first generate seed photons with a power-law distribution with a photon index of  $\Gamma = 1$ , and correct the output spectrum by assigning different weights on the output events so that the initial energy distribution follow thermal bremsstrahlung. In specific, the statistical weight of each event  $w(E_{\text{ini}})$  is given by

$$w(E_{\text{ini}}) = \frac{\tau^2 k T_e \exp(-E_{\text{ini}}/k T_e) E_{\text{ini}}^{-1}}{E_{\text{ini}}^{-1}}, \quad (9.3)$$

where  $E_{\text{ini}}$  is the energy of each seed photon. The output spectrum can be generated by applying the statistical weight to each event.

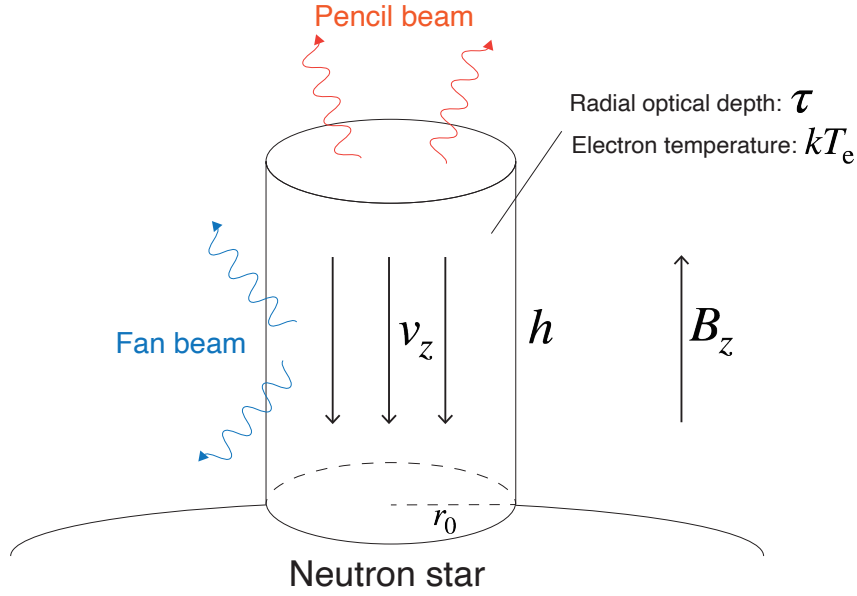


Figure 9.4: Schematic illustration of the simulation setup for an accretion column on the magnetic pole.

## 9.2.2 Simulation parameters

There are several simulation parameters in the simulation of the accretion column. We need to constrain these parameters as consistent with the physical picture of disk-fed X-ray pulsars. Here, we examine each of the simulation parameters and describe how we treat them in the simulation.

### Magnetic field

The magnetic field strength  $B_z$  is an important parameter that determines the suppression of the Comptonization cross section and affects the formation of the CRSF. We set the magnetic field strength as consistent with the detected CRSF central energy  $E_{\text{cyc}}$  at the pulse maximum, which are 29.0 keV and 37.6 keV for Cen X-3 and Her X-1, respectively (see Sections 5.3.2 and 8.4.2). The adopted values are  $2.38 \times 10^{12}$  G and  $3.25 \times 10^{12}$  G for Cen X-3 and Her X-1, respectively.

### Bulk velocity

The bulk velocity  $v_z$  determines the efficiency of bulk Comptonization, which generates the high-energy photons exceeding the electron temperature. In the radiation-dominated accretion column, these high-energy photons are generated above the sonic point because the accretion flow is highly decelerated due to radiation pressure under the sonic point.

The accretion flow moves approximately at the free-fall velocity given by

$$v_{\text{ff}} = \sqrt{\frac{2GM_{\text{ns}}}{R_{\text{ns}}}} = 1.9 \times 10^{10} \left( \frac{M_{\text{ns}}}{1.4M_{\odot}} \right)^{1/2} \left( \frac{R_{\text{ns}}}{10 \text{ km}} \right)^{-1/2} \text{ cm s}^{-1}. \quad (9.4)$$

In this simulation, we adopted  $v_z = 2 \times 10^{10} \text{ cm s}^{-1}$ . We also confirmed that the high-energy spectral feature could not be reproduced by  $v_z$  smaller than  $2 \times 10^{10} \text{ cm s}^{-1}$ .

### Electron temperature

The electron temperature  $kT_e$  is a parameter that regulates thermal Comptonization. It affects the cut-off feature of the spectrum and the flattening feature in the low-energy bands. It is known that the folding energy ( $E_f$ ) of the Fermi-Dirac cut-off power law approximately corresponds to the electron temperature in unsaturated Comptonization (e.g., Rybicki & Lightman, 1979). The folding energy of the phase-averaged spectrum is  $\sim 5 \text{ keV}$  for both Cen X-3 and Her X-1 (Tables 7.1 and 8.3). We tried multiple electron temperatures from 3 to 10 keV with an interval of 1 keV to reproduce the cut-off feature and low-energy flattening of the spectrum, and confirmed that  $kT_e = 5 \text{ keV}$  gives the most appropriate spectral feature for both Cen X-3 and Her X-1. Therefore, we adopted  $kT_e = 5 \text{ keV}$  in the simulation.

### Radial optical depth

The radial optical depth determines the average number of scattering and the escaping time from the column, which affects the photon index of the spectrum. We tried multiple optical depths from  $\tau = 1$  to  $\tau = 1000$  ( $\tau = 1, 3, 10, 30, 100, 300, 1000$ ) and confirmed that the optical depth does not affect spectral shape significantly when  $\tau \gtrsim 10$ . It is natural because the photons and the electrons could sufficiently reach the equilibrium after the photons experience  $\tau^2 = 100$  times scattering. Instead of the correspondence to the emitted spectrum, the optical depth should be constrained by the energy conservation of the accretion flow. The mass accretion rate can be expressed by

$$\dot{M} = \frac{\tau m_p \pi r_0 v_z}{\sigma_T}, \quad (9.5)$$

where the accretion rate should be balanced with the X-ray luminosity  $L_x$  by

$$L_x = \frac{GM_{\text{ns}}\dot{M}}{R_{\text{ns}}}. \quad (9.6)$$

The accretion rate calculated from the X-ray luminosity is  $2\text{--}3 \times 10^{17} \text{ g s}^{-1}$  for both Cen X-3 and Her X-1.  $\tau = 10$  and  $r_0 = 10^5 \text{ cm}$  give a good correspondence to the estimated accretion rate with  $\dot{M} = 1.6 \times 10^{17} \text{ g s}^{-1}$ . Compared to the typical neutron star radius of  $10^6 \text{ cm}$ ,  $r_0 = 10^5 \text{ cm}$  is a reasonable value for the radius of the accretion column. Therefore, we adopted  $\tau = 10$  in our simulation.

## Column radius and height

In the simulation of the accretion column, the absolute values of the column radius  $r_0$  and height  $h$  do not affect the simulation result. The absolute value of the column radius should be estimated from equation (9.5). Instead, the ratio between radius and height, expressed by  $h/r_0$ , plays an important role in the simulation. It affects the efficiency of bulk Comptonization, and also has a significant influence on the direction of the emitted photons. Since we adopt a one-zone model, the height of the column effectively corresponds to the height where the X-ray emission becomes negligible.

There are roughly two possibilities for the relation between the radius and height. One is the “flat” column with  $h/r_0 \sim 1$ , and the other is the “elongated” column with  $h/r_0 \gg 1$ . We examined both possibilities by consulting the emission profile obtained from the simulation. Here, we define the emission profile as the angular distribution of the X-ray emission from the column with respect to the magnetic axis, normalized to the count rate per unit solid angle. In emission profiles,  $0^\circ$  corresponds to the direction of the magnetic axis and center of the pencil beam.

Figure 9.5 shows the emission profiles obtained from different  $h/r_0$  values, plotted for 3–4 keV and 9–10 keV. In the flat column ( $h/r_0 = 1$ ), the pencil beam forms a sharp peak around  $0^\circ$  in the 3–4 keV emission profile, while it does not form a significant peak in the 9–10 keV emission profile. However, such a sharp peak in low-energy pulse profiles is not detected for Cen X-3 and Her X-1. Rather, the low-energy pulse profiles show suppressed emission in the direction of the magnetic axis, as shown in Figure 9.1. In the elongated column ( $h/r_0 = 10$ ), the suppressed emission around  $0^\circ$  can be seen in the 3–4 keV emission profile due to a more dominant fan beam component. This is because it is more difficult for photons to escape from the top of the column when the column is elongated. Therefore, we adopted the elongated geometry of the accretion column as an appropriate configuration. It is also suggested in the one-dimensional model of Becker & Wolff (2007) that the height of the accretion column is much longer than the radius (e.g., West et al., 2017). We tried multiple  $h/r_0$  values ( $h/r_0 = 1, 3, 10, 30, 100$ ) and found that  $h/r_0 = 10$  gives the most similar spectral shape to the observed spectra of Cen X-3 and Her X-1.



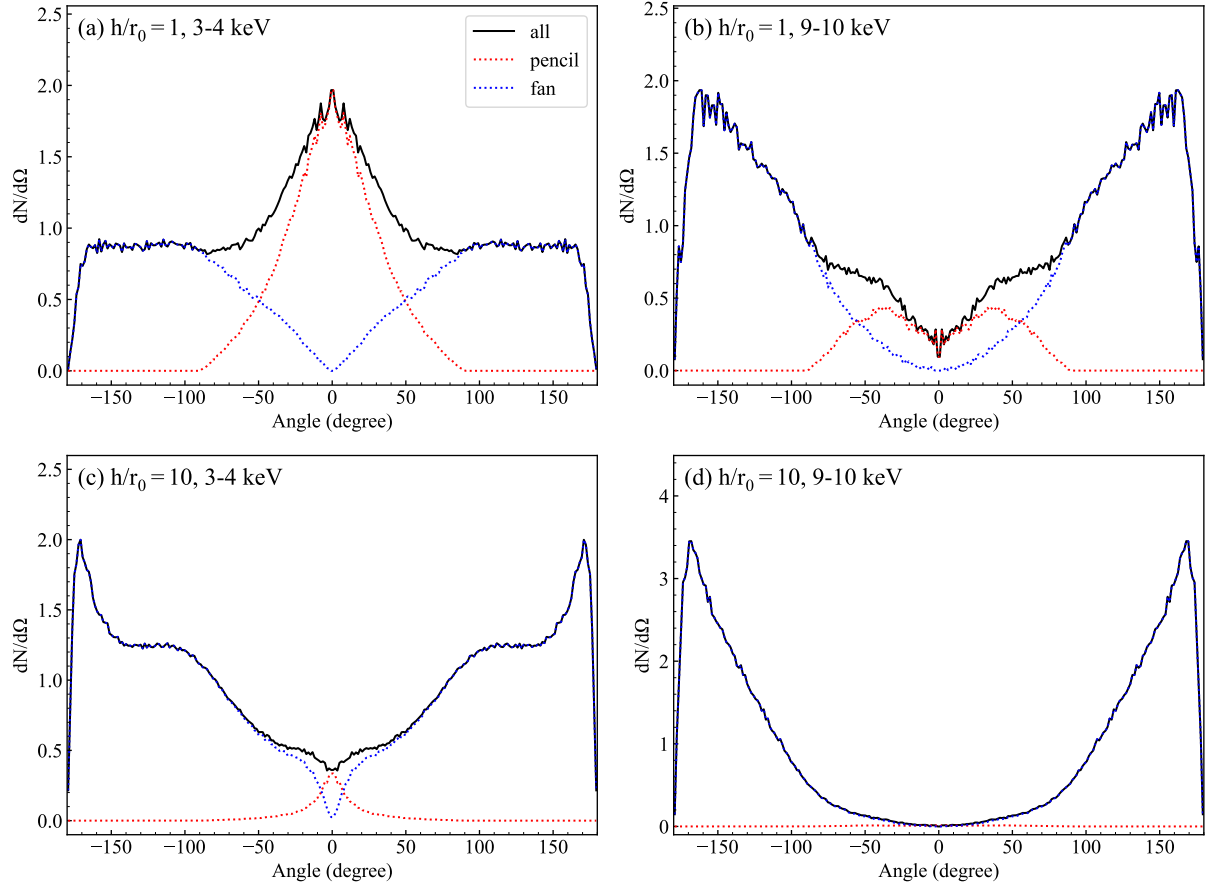


Figure 9.5: 3–4 keV and 9–10 keV emission profiles derived from the Monte-Carlo simulation. The upper and lower panels represent emission from a flat column with  $h/r_0 = 1$  and an elongated column with  $h/r_0 = 10$ . The contributions from pencil and fan beams are plotted by red and blue dotted lines, respectively. The other simulation parameters are  $B_z = 3.25 \times 10^{12}$  G,  $v_z = 2 \times 10^{10}$  cm s $^{-1}$ ,  $kT_e = 5$  keV, and  $\tau = 10$ .

### 9.2.3 Energy spectrum

We simulated the emission from the accretion column with the simulation parameters fixed to the values described in the previous section. Figure 9.6 shows the comparison between the energy spectra derived from the observation and simulation, plotted for Cen X-3 and Her X-1. We adopted the spin-phase-averaged spectrum at  $\Phi = 1.40$ – $1.45$  in the 2022 NuSTAR observation data (Chapter 5) as the reference spectrum of Cen X-3 (also see discussion in Section 7.1). The observed spectrum of Her X-1 was taken from the phase-averaged spectrum of the 2021 NuSTAR data (Chapter 8) without any filter. The simulation and observation spectra well agree with each other below 20 keV for Cen X-3 and 10 keV for Her X-1. There are discrepancies between the observation and simulation in the hard X-ray band, but we could not find more appropriate solutions with the simplified one-zone model. What we aim to investigate is the energy dependence of

the pulse profile shape around the pulse maximum, which shows large variability below 10 keV, and the agreement shown in Figure 9.6 is enough to serve our goal. The following analysis adopts the simulation setup discussed here.

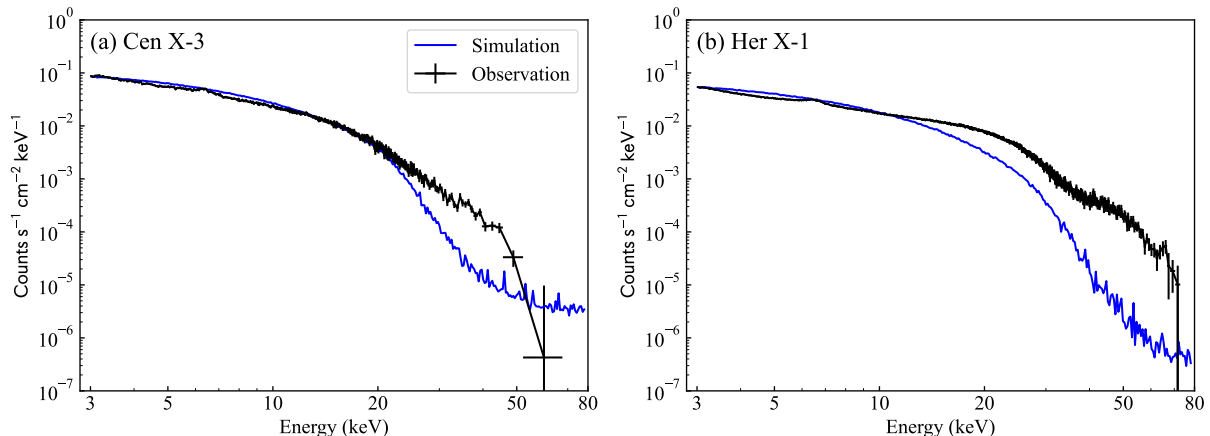


Figure 9.6: Comparison of energy spectra between observation and simulation, plotted for Cen X-3 and Her X-1. The adopted simulation parameters are presented in Section 9.2.2.

## 9.3 Modeling of pulse profile

In Section 9.2, we constructed a simulation-based model for a highly magnetized accretion flow and successfully reproduced the observed energy spectra of Cen X-3 and Her X-1. Our goal is to reproduce the energy-dependent anisotropy of the X-ray emission, which is observed as pulse profiles. In this section, we aim to model the pulse profiles of Cen X-3 and Her X-1 using the constructed simulation setup. Since the emission profiles presented in Figure 9.5 do not match the observed pulse profile at all, we need to apply some reprocessing to them to compare with the observation. We first describe the reprocessing we applied and then present the comparison between simulation results and observation data.

### 9.3.1 Effects of reflection from neutron star surface

We start from the emission profiles presented in Figure 9.5. In the previous section, we mentioned that the elongated geometry of the column (Figure 9.5c, d) is appropriate for reproducing observed pulse profiles. This is because of the dented feature around  $0^\circ$  shown in the 3–4 keV emission profile, which is qualitatively consistent with the suppressed emission of low-energy pulse profiles at the pulse maximum. In such a geometry, the fan beam is the dominant emission component, and it is mostly beamed downwards due to the bulk motion of the accretion flow toward the neutron star. The beaming effect

is more prominent in high-energy bands, as shown in Figure 9.5(c) and (d), because bulk Comptonization is more important to generate high-energy photons. The observed pulse profiles, however, display that a sharp peak should be generated around the pulse maximum or in the direction of the magnetic axis.

The most plausible way to solve this problem is the inclusion of the reflection component. Since there is a solid surface on the neutron star, the fan beam photons emitted downwards should mostly hit the surface. A large part of these photons would be reflected by the surface and consequently observed as a sharp beam around the magnetic axis. We set an additional geometry that imitates the reflection from the neutron star surface. We approximated the neutron star surface by a slab-like column just below the accretion column, with a radius of  $10^6$  cm and a vertical optical depth of  $\tau = 2$ . The former value is based on the typical neutron star radius, and the latter value was set to reflect photons effectively. We set the slab composed of fully ionized plasma with an electron temperature of  $kT_e = 0.5$  keV, typical of neutron star surface temperature, and did not apply any magnetic field.

Figure 9.7 shows the emission profiles after we added the reflection components. The suppressed emission at the magnetic axis is successfully reproduced in the 3–4 keV emission profile, while a sharply peaked structure is generated in the 9–10 keV emission profile. The qualitative features around the pulse maximum of the energy-resolved pulse profiles can be reproduced by the summation of the pencil, fan, and reflection components. It becomes clear that the pencil beam contributes very little to the emission. The fan beam and the reflection component is comparable in the 3–4 keV emission profile, and they are balanced to generate a relatively flat profile around the magnetic axis. The reflection component becomes dominant in the 9–10 keV emission profile because the emission from the accretion column is more beamed toward the neutron star surface, and it forms a sharp peak around the magnetic axis. The little contribution from the pencil beam was already suggested by the one-dimensional accretion column model (see Figure 2 of West et al., 2017), but we point out the importance of the reflection component for the first time, from the point of view of the observed pulse profiles.

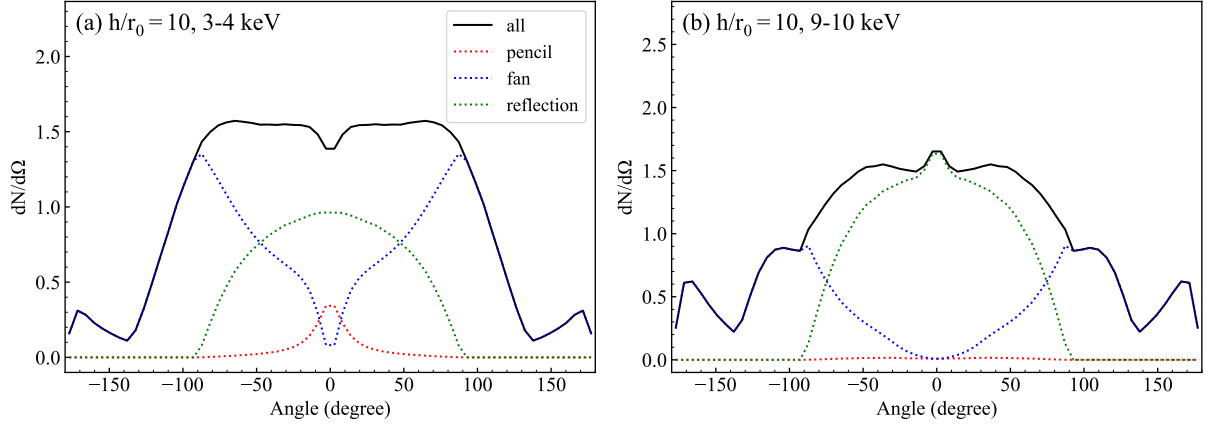


Figure 9.7: 3–4 keV and 9–10 keV emission profiles derived from the Monte-Carlo simulation with reflection components. The contributions from the pencil beam, fan beam, and reflection are plotted by red, blue, and green dotted lines, respectively. The geometrical configuration of the column is  $h/r_0 = 10$ , and other simulation parameters are the same as Figure 9.5.

### 9.3.2 Generation of pulse profile

Since the qualitative feature of observed pulse profiles was successfully reproduced owing to the inclusion of the reflection effects, we next try to generate pulse profiles from the emission profiles and compare them with the observation. The most important effect for the pulse profile generation is the geometrical configuration among the spin axis, magnetic axis, and line of sight. Figure 9.8 presents a schematic illustration of the relation among these three axes. We define two parameters,  $\alpha$  and  $\beta$ . The former represents the angle between the spin axis and magnetic axis, and the latter represents the angle between the spin axis and line of sight. The emission profiles presented in Figure 9.7 correspond to pulse profiles with  $\alpha = 90^\circ$  and  $\beta = 90^\circ$ . With any given  $\alpha$  and  $\beta$ , we can generate a pulse profile by reconstructing the emission profile consulting the configuration in Figure 9.8.

We simulated  $3 \times 10^8$  photons and generated emission profiles with simulation setups of Cen X-3 and Her X-1. We generated pulse profiles with various  $\alpha$  and  $\beta$  and searched for the configuration where the generated pulse profiles agree with observation data. We only focused on the pulse profile shape around the pulse maximum, and limited the spin phase for comparison to  $0.0 < \phi < 0.5$ . This is because the spin phase out of this range could be affected by the other side of the column, which needs a more sophisticated model. The asymmetry of the observed pulse profiles discussed in Section 9.1.2 cannot be reproduced by our simulation setup. Thus, we only focused on  $0.0 < \phi < 0.25$ , and we attribute the discrepancy between data and model in the latter half of the pulse profile to the phenomenological Gaussian-like absorption feature presented in Table 9.1.

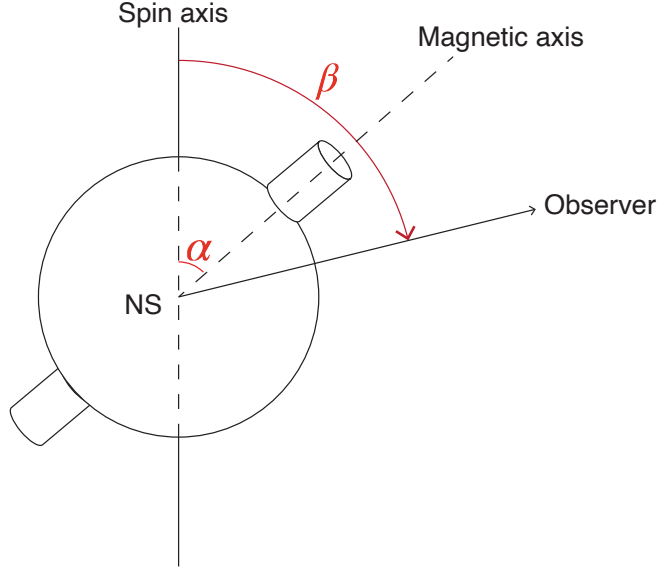


Figure 9.8: Geometrical configuration among spin axis, magnetic axis, and line of sight.  $\alpha$  denotes the angle between spin axis and magnetic axis, and  $\beta$  represents the angle between spin axis and line of sight.

### 9.3.3 Modeling of Her X-1 pulse profiles

Since Her X-1 has more distinctive features in pulse profiles than Cen X-3, we first aim to model the Her X-1 pulse profiles. Our aim is to reproduce the characteristic features around the pulse maximum, where the low-energy pulse profiles display split peaks, and the high-energy pulse profiles show a single-peaked structure. Since the shift of the peak shape occurs below 10 keV, and the energy spectrum shows a good agreement between the data and model only below 10 keV (Figure 9.6), we mainly focused on 3–10 keV pulse profiles. We divided 3–10 keV into seven energy bands, with each band covering 1 keV, and treated 10–78 keV as one unified band.

We compared the pulse profiles of the above eight energy bands with various  $\alpha$  and  $\beta$  values. The pulse profiles generated by the simulation were applied a linear transform so that they match the observation data. The linear conversion was applied by two free parameters,  $a$  and  $b$ , given by

$$p_{\text{data}}(\phi) = ap_{\text{model}}(\phi) + b, \quad (9.7)$$

where  $p_{\text{data}}(\phi)$  and  $p_{\text{model}}(\phi)$  are the observed and simulated pulse profiles, respectively. The first parameter  $a$  compensates for the difference in the normalization between data and model, and the second parameter  $b$  compensates for the difference in the pulse fraction. Ideally,  $a$  should be constant among energy bands, and  $b$  should equal zero, but our simplified model needs these two parameters to make simulated pulse profiles matched to the observation data.

Figure 9.9 shows one example where the simulation well reproduces the observation data. The geometrical configuration is  $\alpha = 90^\circ$  and  $\beta = 90^\circ$ . The free parameters  $a$  and  $b$  are listed in Table 9.2. The suppressed emission at the pulse maximum seen in low-energy pulse profiles was successfully reproduced by the simulation. The gradual growth of the sharp peak at the pulse maximum as energy increases can be seen in the simulated pulse profiles. When the energy reaches 9–10 keV or 10–78 keV, the simulated pulse profiles reproduce the single sharp peak at the pulse maximum. We can see that the fan beam and reflection component are comparable in 3–4 keV, but the reflection component gradually becomes dominant as energy goes up, and the 10–78 keV pulse profile is almost solely composed of the reflection component. The free parameters in Table 9.2 show that the quantitative reproduction of the pulse profiles is still underway, because  $a$  differs by an order of magnitude among energy bands and  $b$  displays negative values. The most prominent is 10–78 keV, where  $b = -663.4$  is unrealistic compared to the average count rate of  $\sim 150$  photons  $\text{s}^{-1}$ . This can be solved by generating a sharper peak at the pulse maximum in the simulation, which could be explained by the magnetic field in the reflection site or anisotropic obscuration by the accretion disk. However, further investigation is beyond the scope of this thesis.

We found that other geometrical configurations with  $\alpha = \beta$  can reproduce the similar trend of pulse profiles shown in Figure 9.9. This is because the suppressed emission at the pulse maximum needs a coincidence of the magnetic axis and line of sight, which leads to the observation of the top of the column at the pulse maximum. Other configurations with  $|\alpha - \beta| \geq 10^\circ$  could not reproduce this feature. Therefore, we conclude that the geometrical configuration of Her X-1 is limited to  $|\alpha - \beta| < 10^\circ$ .

Table 9.2: Free parameters of Her X-1 pulse profile modeling.<sup>a</sup>

Energy band	$a$	$b$
3–4keV	$2.4 \times 10^{-9}$	−15.3
4–5keV	$4.5 \times 10^{-9}$	−15.3
5–6keV	$5.9 \times 10^{-9}$	−5.9
6–7keV	$1.6 \times 10^{-9}$	−47.5
7–8keV	$2.4 \times 10^{-8}$	−60.4
8–9keV	$2.7 \times 10^{-8}$	−49.3
9–10keV	$3.9 \times 10^{-8}$	−58.4
10–78keV	$1.0 \times 10^{-7}$	−663.4

<sup>a</sup> With a geometrical configuration of  $\alpha = 90^\circ$  and  $\beta = 90^\circ$ .

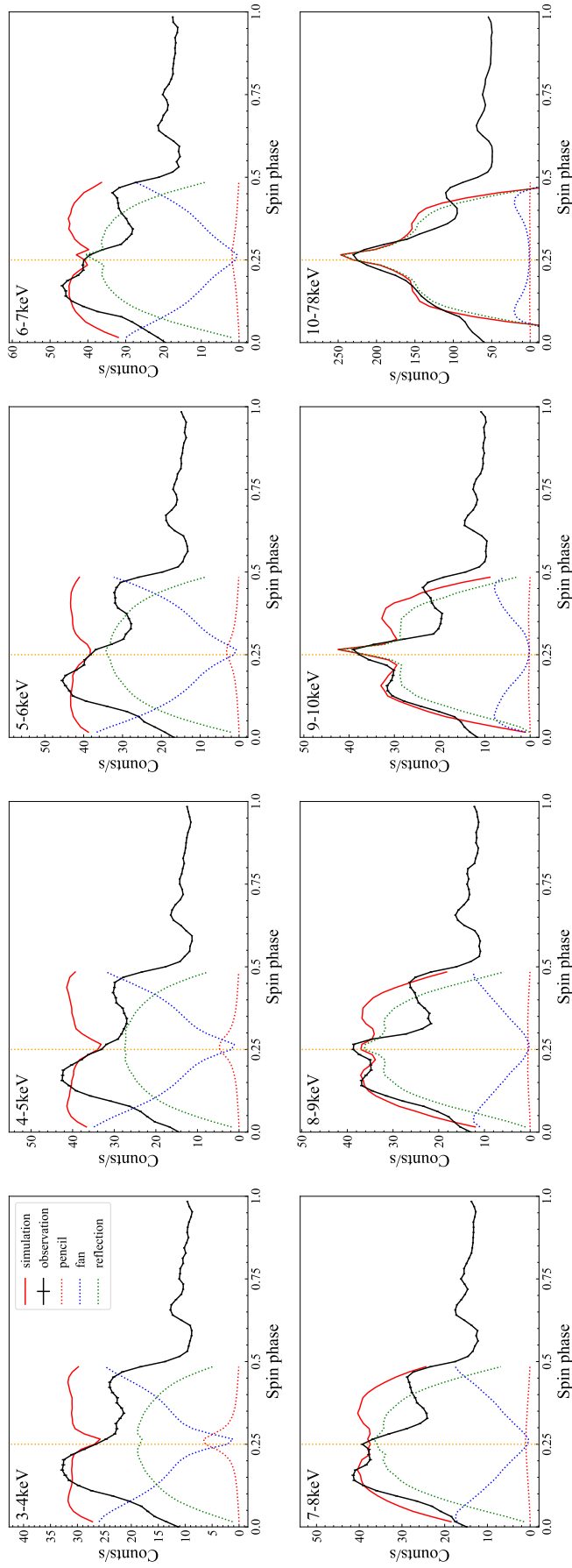


Figure 9.9: Results of pulse profile modeling on Her X-1. The vertical orange lines represent the pulse maximum of  $\phi = 0.25$ . The geometrical configuration is  $\alpha = 90^\circ$  and  $\beta = 90^\circ$ . The free parameters  $a$  and  $b$  are listed in Table 9.2.

### 9.3.4 Modeling of Cen X-3 pulse profiles

Similar to Section 9.3.3, we performed pulse profile modeling on the Cen X-3 observation data. The adopted energy bands are the same as those of Her X-1 modeling. We fixed one of the free parameters to  $b = 0$  since Cen X-3 pulse profiles do not have complex features like Her X-1. Therefore, the difference in the pulse fraction can be reproduced in this modeling.

Figure 9.10 presents one example of geometrical configurations where the simulation well reproduces the observation data,  $\alpha = 90^\circ$  and  $\beta = 30^\circ$ . The free parameters used in the modeling are listed in Table 9.3. Although there are no distinctive features in Cen X-3 pulse profiles, the flatness around the pulse maximum seen in low-energy bands and the sharpness in high-energy bands were successfully reproduced by the simulation. This trend can be explained in terms of the contribution ratio of the fan beam and reflection component. In 3–4 keV, the fan beam component is a little more dominant over the reflection, and the different angular distributions of these two components balance and generate a flat pulse profile. The reflection component gradually becomes dominant over the fan beam as energy increases, and eventually results in a sharp peak, as seen in the 10–78 keV pulse profile.

Since Cen X-3 pulse profiles have a relatively smooth shape, the limitation of the geometrical configuration is difficult. Many patterns of  $\alpha$  and  $\beta$  can reproduce the observed pulse profiles. However, the alignment of the magnetic axis and line of sight with  $|\alpha - \beta| < 10^\circ$  results in a failure of the modeling because it leads to a suppressed structure at the pulse maximum in low-energy bands, as seen in the Her X-1 pulse profiles. Therefore, we conclude that the magnetic axis and line of sight are misaligned by  $> 10^\circ$  in Cen X-3.

Table 9.3: Free parameters of Cen X-3 pulse profile modeling.<sup>a</sup>

Energy band	$a$	$b$
3–4 keV	$5.4 \times 10^{-9}$	0
4–5 keV	$1.2 \times 10^{-8}$	0
5–6 keV	$2.1 \times 10^{-8}$	0
6–7 keV	$3.5 \times 10^{-8}$	0
7–8 keV	$4.3 \times 10^{-8}$	0
8–9 keV	$5.6 \times 10^{-8}$	0
9–10 keV	$7.3 \times 10^{-8}$	0
10–78 keV	$9.3 \times 10^{-8}$	0

<sup>a</sup> With a geometrical configuration of  $\alpha = 90^\circ$  and  $\beta = 30^\circ$ .



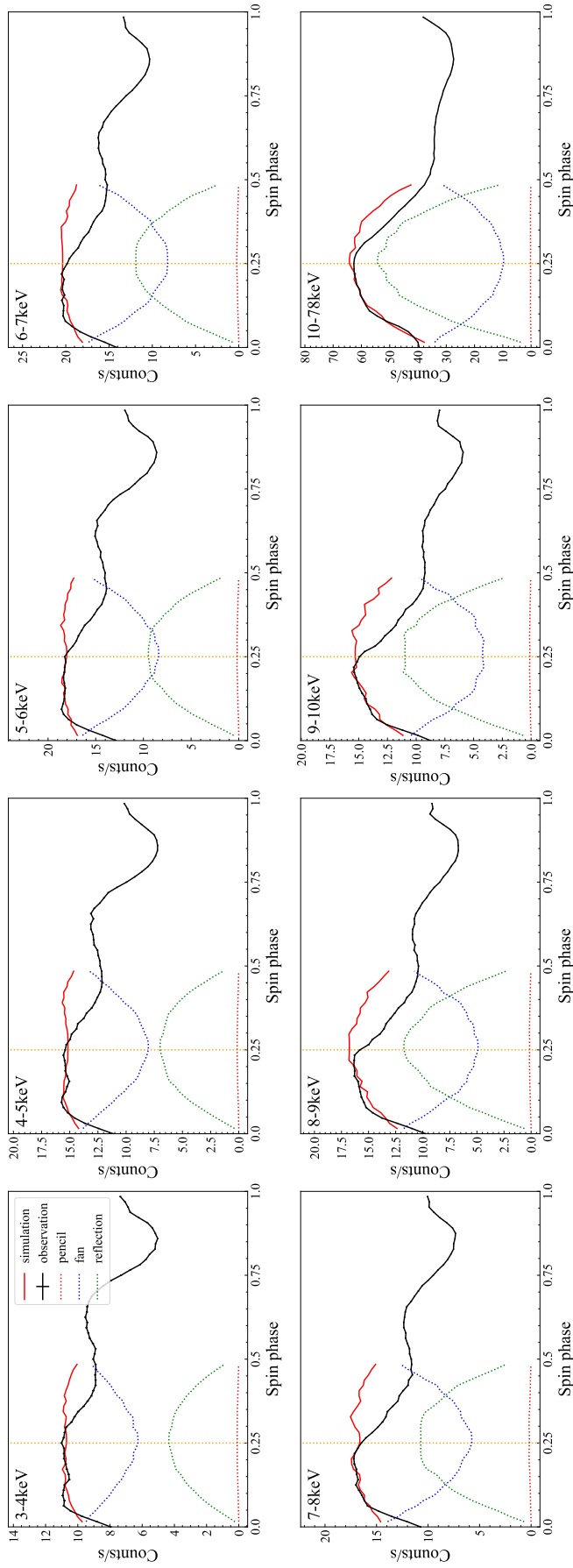


Figure 9.10: Results of pulse profile modeling on Cen X-3. The vertical orange lines represent the pulse maximum of  $\phi = 0.25$ . The geometrical configuration is  $\alpha = 90^\circ$  and  $\beta = 30^\circ$ . The free parameters  $a$  and  $b$  are listed in Table 9.3.

## 9.4 Three-dimensional structures of accretion flow

In previous sections, we modeled the observed pulse profiles of Cen X-3 and Her X-1 based on the Monte-Carlo simulation of a highly magnetized accretion column in order to give a physical interpretation to the spin-phase variability of these objects. In this section, we summarize our findings and compare them with previous studies. We also discuss the spin-phase variability of the spectrum, focusing on the variability of the CRSF.

### 9.4.1 Summary of pulse profile modeling

The modeling of pulse profiles based on the physical model has revealed that the energy dependence of the peak shape can be reproduced by the different compositions of the fan beam and reflection component. Figure 9.11 presents a schematic illustration of the emission anisotropy with different energy bands. The photons whose energies are comparable to the electron temperature do not have strong beaming effects toward the neutron star surface, and the emission is composed of a mixture of the direct fan beam and reflection component. It is because these photons are mostly generated via thermal Comptonization rather than bulk Comptonization, leading to a less beaming effect. The photons whose energies exceed the electron temperature, on the other hand, exhibit strong beaming effects downwards since they are mostly generated from bulk Comptonization. It leads to the formation of a dominant reflection component over direct fan beam.

We also succeeded in giving limitations on the geometrical configuration between the magnetic axis and line of sight. In Her X-1, the magnetic axis and line of sight are highly aligned with  $\lesssim 10^\circ$ . This is based on the split feature in low-energy pulse profiles, which could only originate from the suppressed fan beam in the direction of the magnetic field. In Cen X-3, such a split feature was not detected in pulse profiles, which suggests that the magnetic axis and line of sight are misaligned with  $\gtrsim 10^\circ$ . The difference in the pulse profile shapes between Her X-1 and Cen X-3 originates from the different geometrical configurations between the magnetic axis and line of sight.

Recently, the three-dimensional configurations of X-ray pulsars have been investigated by observing X-ray polarization from these sources, thanks to the launch of IXPE (Weiskopf et al., 2016). Her X-1 and Cen X-3 were also observed by IXPE, and the results were reported by Doroshenko et al. (2022) and Tsygankov et al. (2022), respectively. They mainly measure the magnetic obliquity, corresponding to  $\alpha$  in Figure 9.8, through the spin-phase variability of the polarization angle and the polarization degree. However, the X-ray polarimetry could not measure the angle between the spin axis and line of sight ( $\beta$  in Figure 9.8) for these sources. Since we give limitations to the values of  $|\alpha - \beta|$ , we can further constrain the geometrical configuration of the neutron star by combining them with the IXPE results.

Doroshenko et al. (2022) argues that the magnetic obliquity of Her X-1 is  $12 \pm 4$  degree according to the IXPE observation. They also suggest that the spin axis of the neutron star and the angular momentum of the binary motion is misaligned by at least  $20^\circ$ . Since the inclination angle of Her X-1 is  $85\text{--}88^\circ$  and our analysis derived  $|\alpha - \beta| < 10^\circ$ , the spin axis should be misaligned from the angular momentum of the binary motion by  $\sim 70^\circ$ . This is consistent with the misaligned larger than  $20^\circ$ . Tsygankov et al. (2022) argues that the magnetic obliquity of Cen X-3 is  $17^\circ$ . Since we estimated  $|\alpha - \beta| \gtrsim 10^\circ$ , the angle between the spin axis and line of sight is larger than  $27^\circ$ . As the inclination angle of Cen X-3 is estimated to be  $72^\circ$  (Ash et al., 1999), the misalignment between the spin axis and the angular momentum of the binary motion can be estimated to be smaller than  $45^\circ$ . Since the low-energy pulse profiles of Cen X-3 exhibit significant contributions from the other pole (see Section 9.1.3), further estimation of the geometrical configuration could be carried out by evaluating them, but it is beyond the scope of this thesis.

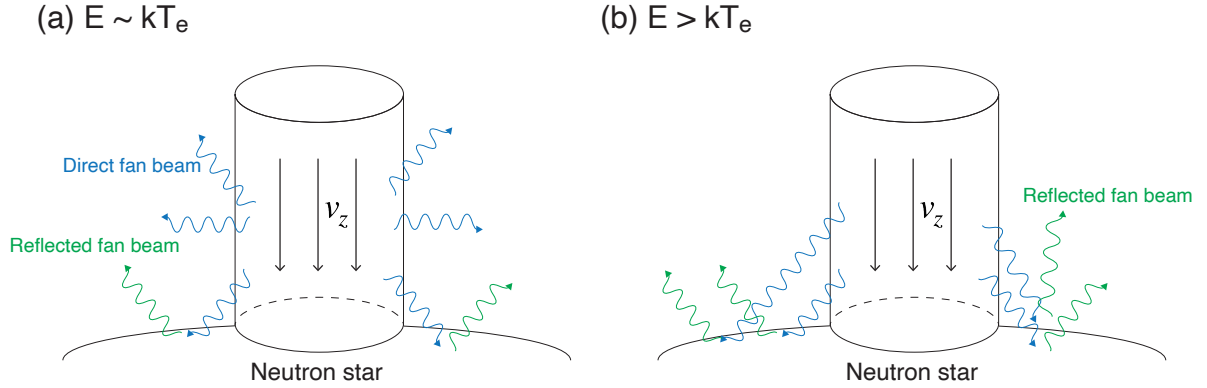


Figure 9.11: Schematic illustration of the emission mechanism from an accretion column for (a) photons with comparable energies to the electron temperature and (b) photons with energies exceeding the electron temperature. The former emission is composed of a mixture of the fan beam and reflection, while the latter is mostly composed of reflection.

#### 9.4.2 Origin of CRSF

In NuSTAR observation data, we detected the spin-phase variabilities for both Cen X-3 and Her X-1. The central energy of the CRSF has a positive correlation with the continuum flux, and is enhanced to the highest value at the pulse maximum (Figures 5.17 and 8.10). The CRSF central energy  $E_{\text{cyc}}$  ranges from 25.1 keV to 29.0 keV and from 31.9 keV to 37.6 keV for Cen X-3 and Her X-1, respectively. The variation degree is 15% and 18% for Cen X-3 and Her X-1, respectively, which corresponds to the variability of the corresponding magnetic field strength. Such variability is often attributed to the different emission regions inside the accretion column. However, an elongated configuration of the

accretion column confirmed in the pulse profile modeling (see Section 9.2.2) does not allow such a small variability. Assuming a dipole magnetic field, the magnetic field strength inside the accretion column decays by  $z^{-3}$  toward the top of the column. The magnetic field strength can be decayed by 20% with a vertical distance of  $\sim 7 \times 10^4$  cm, which is too small compared to the typical height of the accretion column ( $\sim 10^6$  cm). Moreover, we revealed that most photon emission originates from the reflected fan beam. In such a situation, the CRSF would be smeared out due to the reflection process, a large difference in the magnetic field strength, or Doppler broadening inside the accretion column.

One possibility that explains the CRSF variability is the generation of the CRSF at the neutron star surface. In this hypothesis, the CRSF generated in the accretion column is smeared out, and instead, the magnetic field on the neutron star surface generates another CRSF that is observed. This hypothesis is consistent with our simulation result that most high-energy photons are generated via reflection from the neutron star surface. The variability in the CRSF central energy can also be explained reasonably. Assuming a dipole configuration, the magnetic field strength at the surface of the neutron star is given by

$$B = 0.5B_0\sqrt{1 + 3\cos^2\theta}, \quad (9.8)$$

where  $\theta = 0$  corresponds to the magnetic pole and  $B_0$  is the magnetic field strength at the magnetic pole. The variability in the surface magnetic field strength is at most 50%. Therefore, the variation degrees of 15% for Cen X-3 and 18% for Her X-1 can be naturally explained by the difference in the surface magnetic field.

The neutron star surface as the origin of the CRSF was already suggested by Poutanen et al. (2013). Figure 9.12 shows a schematic illustration of this hypothesis. In this hypothesis, a low accretion rate forms a low accretion column, which illuminates only the proximity of the magnetic pole. The observed CRSF consequently has a high central energy (Figure 9.12a). A high accretion rate, on the other hand, forms a high accretion rate, which illuminates a large part of the neutron star surface. The observed CRSF is then shifted to the lower energy (Figure 9.12b). This hypothesis is confirmed by a long-term observation of an X-ray pulsar V 0332+53 as a negative correlation between the CRSF energy and the observed luminosity (Lutovinov et al., 2015). In Cen X-3 and Her X-1 cases, this feature was observed as a positive correlation between the flux and CRSF energy within the spin period. We conclude that the observed CRSFs of Cen X-3 and Her X-1 originate from the reflection at the neutron star surface, and the spin-phase variabilities are caused by the difference in the magnetic field strength at the surface.

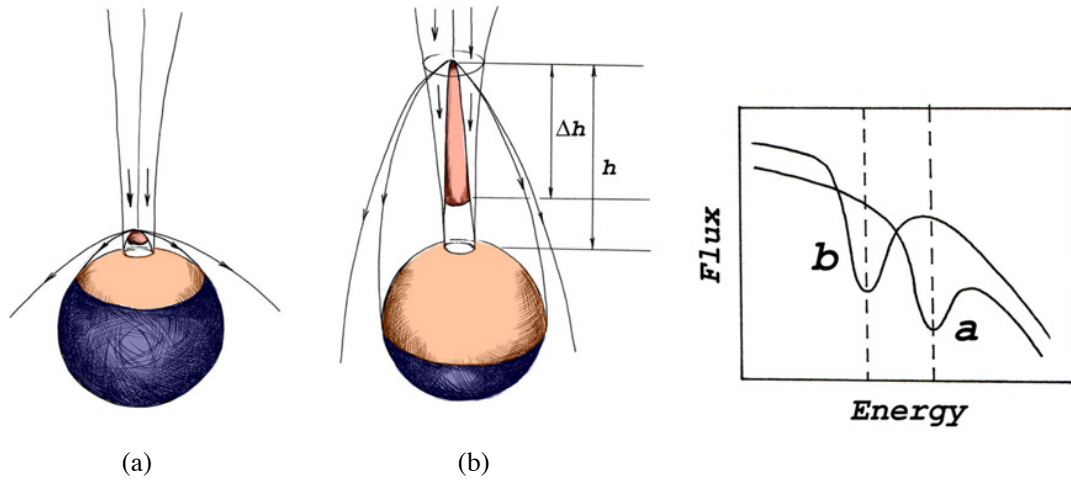


Figure 9.12: Schematic illustration of CRSF generation on the neutron star surface, taken from Poutanen et al. (2013).

# Chapter 10

## Conclusions

We investigated the structure of the circumstellar medium and the three-dimensional pictures of the accretion flow by analyzing time variabilities of the X-ray emission from accreting neutron stars. We analyzed the observation data of two representative disk-fed X-ray pulsars, Cen X-3 and Her X-1. Our analysis focused on the X-ray variabilities along the orbital and spin phases, which reflect the structure of the circumstellar medium and highly magnetized accretion flow, respectively.

We first analyzed spectra, light curves, and pulse profiles of Cen X-3 utilizing NuSTAR and NICER observation data covering 0.6–78 keV and investigated the orbital- and spin-phase variabilities. The broadband observation data allowed us to derive the following conclusions.

- The orbital-phase variability is characterized by the photon index. It varies from  $-0.37$  to  $1.72$  and correlates with the 4–78 keV luminosity ranging from  $3.7 \times 10^{35} \text{ erg s}^{-1}$  to  $4.5 \times 10^{37} \text{ erg s}^{-1}$ . The photon index becomes soft in the high-luminosity phases and hard in the low-luminosity phases. The photon index returns to soft values of  $\Gamma \sim 1.2$  in the eclipse phases. The two consecutive orbits displayed an apparent difference; the first orbit is characterized by low fluxes and hard photon indices while the second is by high fluxes and soft photon indices.
- The spin-phase variability of the continuum is characterized by a monotonic increase in pulse fraction with the energy. It is also characterized as a variability in the photon index ranging from  $\Gamma = 1.30$  in the pulse minimum to  $\Gamma = 0.76$  in the pulse maximum. The peak phase of the pulse profiles displays a gradual shift with the energy. This is a consequence of the gradual transition in pulse profile peak structure; a flat-peaked structure in low-energy bands gradually shifts to a sharp-peaked structure in high-energy bands.
- The Fe line and the CRSF exhibit spin-phase variabilities. The equivalent width of the Fe line is negatively correlated with the continuum flux, ranging from 0.1 keV

to 0.4 keV, suggesting the Fe line emission originates from non-pulsed regions. The central energy, line width, and optical depth of the CRSF positively correlate with the continuum flux. The central energy ranges from 25.1 keV to 29.0 keV, corresponding to an  $\sim 15\%$  difference in the magnetic field strength.

- The pulse fraction varies along the orbital phase. The 3–5 keV pulse profiles show the most prominent variability, ranging from 0.1 to 0.4 in out-of-eclipse phases. The suppressed pulse fractions are synchronized with the low continuum fluxes and hard photon indices.
- The orbital-phase variability characterized by the photon index variation is preserved when we focus on a specific spin phase. The relative relations among the spectral parameters of different spin phases do not vary with the orbital phase. It suggests that the accretion flow is stable, and the obscuration by the circumstellar medium causes the orbital-phase variability.

The rich observation data and detailed analysis of time variability allowed us to establish a physical picture of the circumstellar medium of Cen X-3, which could not be resolved by a simple spectral analysis. The accumulating observational properties on the orbital-phase variability suggest that the orbital-phase variability is caused by attenuation due to a clumpy stellar wind, and the intrinsic emission from the neutron star is stable. The eclipse-phase spectra can be explained based on scattering by a stellar wind with a column density of  $N_{\text{H}}^{\text{CS}} \sim 2.4 \times 10^{22} \text{ cm}^{-2}$ . The spectra in the out-of-eclipse phases can be reproduced by the attenuation by the stellar wind applied to a fixed intrinsic emission from the neutron star. The apparent hardening of the photon index in low-flux phases is compensated for by adding blackbody components representing the thermal emission from the accretion disk. The maximum column density of the stellar wind clumps is  $N_{\text{H}}^{\text{PE}} = 7 \times 10^{23} \text{ cm}^{-2}$  for photoelectric absorption and  $N_{\text{H}}^{\text{CS}} = 2.5 \times 10^{24} \text{ cm}^{-2}$  for Compton scattering. The typical size and hydrogen number density of the stellar wind clumps are roughly estimated to be  $R_{\text{c}} \sim 8 \times 10^{10} \text{ cm}$  and  $n_{\text{c}} \sim 1 \times 10^{13} \text{ cm}^{-3}$ , respectively. The thermal emission from the accretion disk consists of two blackbody components with temperatures of  $kT \sim 0.1 \text{ keV}$  and  $kT \sim 0.5 \text{ keV}$  and luminosities of  $\sim 10^{36} \text{ erg s}^{-1}$ . The blackbody with the higher temperature is most probably generated by the irradiation from the neutron star. The suppressed pulse fraction in low-flux phases can be naturally explained by a partial obscuration of the accretion disk due to the smaller size of the stellar wind clumps than the accretion disk ( $\sim 2.3 \times 10^{11} \text{ cm}$ ).

In order to investigate the three-dimensional pictures of the highly magnetized accretion flow based on the spin-phase variability, we analyzed the observation data of another X-ray pulsar, Her X-1, for comparison with Cen X-3. We applied the same analysis framework as Cen X-3 to the NuSTAR observation data of Her X-1 and derived the following

conclusions.

- Her X-1 does not show significant orbital-phase variability within the 62.7 ks observation. The 3–78 keV flux variability is only 2.8%, with an average luminosity of  $3.3 \times 10^{37} \text{ erg s}^{-1}$ . No significant variability in spectral parameters other than the flux was detected, suggesting that both the accretion flow and the circumstellar medium are stable.
- The energy-resolved pulse profiles of Her X-1 display a gradual change as energy increases. In low-energy bands below  $\sim 7 \text{ keV}$ , the profile around the pulse maximum has split two peaks, and the emission at the pulse maximum is suppressed. As energy goes up to  $\sim 10 \text{ keV}$ , the split feature disappears with an emergence of a single-peaked structure. This trend is qualitatively similar to Cen X-3 pulse profiles but more distinctive in Her X-1 pulse profiles.
- The CRSF parameters exhibit spin-phase variabilities. The central energy, the line width, and the optical depth are all enhanced in the pulse maximum. The central energy ranges from 31.9 keV to 37.6 keV, corresponding to an  $\sim 18\%$  difference in the magnetic field strength.

Finally, we estimated the three-dimensional pictures of the accretion flow onto the highly magnetized neutron star, which could not be investigated with the conventional accretion column model. We focused on the observed spin-phase variabilities of Cen X-3 and Her X-1, particularly on the energy dependence of the pulse profiles. In order to reproduce the observed pulse profiles, we constructed a simulation framework that calculates bulk and thermal Comptonization inside a magnetized accretion column. Although our model adopts a simplified one zone model with a uniform velocity, the comparison between the simulation results and the observation data allowed us to reach the following pictures of the accretion flows in Cen X-3 and Her X-1.

- Both Cen X-3 and Her X-1 have elongated accretion columns with a height-to-radius ratio of  $h/r_0 \sim 10$ . The typical values of the radius and height are  $r_0 \sim 1 \text{ km}$  and  $h \sim 10 \text{ km}$ , respectively.
- For both Cen X-3 and Her X-1, the X-ray emission from the accretion column is composed of the fan beam and the reflection from the neutron star surface, and the pencil beam is almost negligible. The low-energy emission comparable to the electron temperature of the accretion flow is composed of a mixture of the fan beam and the reflection. The reflection component gradually becomes dominant over the fan beam as energy increases.
- The difference in observational properties between Cen X-3 and Her X-1 originates from different geometrical configurations between the magnetic axis and line of sight.



These two axes are misaligned by  $> 10^\circ$  in Cen X-3 while they are highly aligned by  $< 10^\circ$  in Her X-1.

- The observed CRSFs in these two sources are most probably generated by the reflection at the neutron star surface rather than in the accretion column.

As a future prospect, the launch of XRISM satellite will enable us to further extend this study. Since it is an X-ray observatory with an extremely good energy resolution, we can obtain much more information by analyzing the variability of emission and absorption lines. For example, the column density of the stellar wind obscuring the neutron star could be measured by observing emission and absorption lines. This can be used as a cross-check with the estimation from the continuum spectrum derived in this study. One thing that is not clarified in this study is the flux difference between two consecutive orbits in the NuSTAR long observation. Orbit 1 appears to display more stellar wind absorption than Orbit 2, but there is also a possibility of an intrinsic variability between these two orbits. Such uncertainties can be solved by measuring emission and absorption lines. Moreover, an investigation on the spin-phase variability of the emission lines could tell us more about the geometrical structure of the accretion column. We assume the accretion column is composed of fully ionized plasma, but this assumption is not based on any apparent observational properties. If the emission line from the accretion column is observed, we can estimate the height of the accretion column, mass, and radius of the neutron star by measuring the gravitational redshift of the emission lines. This leads to a further constraint on the three-dimensional structure of the accretion column, which was only roughly estimated to be  $h/r_0 \sim 10$  in this study. Combining the broadband study performed in this thesis with the future line study will lead to a more precise estimation of the structure of the accretion flow and circumstellar medium of the accreting neutron star.

# Bibliography

- Alonso-Hernández, J., Fürst, F., Kretschmar, P., Caballero, I., & Joyce, A. M. 2022, *A&A*, 662, A62, doi: 10.1051/0004-6361/202141774
- An, H., Archibald, R. F., Hascoët, R., et al. 2015, *ApJ*, 807, 93, doi: 10.1088/0004-637X/807/1/93
- Arnason, R. M., Papei, H., Barmby, P., Bahramian, A., & Gorski, M. D. 2021, *MNRAS*, 502, 5455, doi: 10.1093/mnras/stab345
- Arons, J., Klein, R. I., & Lea, S. M. 1987, *ApJ*, 312, 666, doi: 10.1086/164912
- Ash, T. D. C., Reynolds, A. P., Roche, P., et al. 1999, *MNRAS*, 307, 357, doi: 10.1046/j.1365-8711.1999.02605.x
- Bachetti, M., Harrison, F. A., Walton, D. J., et al. 2014, *Nature*, 514, 202, doi: 10.1038/nature13791
- Bartels, J., Heck, N. H., & Johnston, H. F. 1939, *Terrestrial Magnetism and Atmospheric Electricity (Journal of Geophysical Research)*, 44, 411, doi: 10.1029/TE044i004p00411
- Basko, M. M., & Sunyaev, R. A. 1976, *MNRAS*, 175, 395, doi: 10.1093/mnras/175.2.395
- Becker, P. A. 1992, *ApJ*, 397, 88, doi: 10.1086/171769
- . 1998, *ApJ*, 498, 790, doi: 10.1086/305568
- Becker, P. A., & Wolff, M. T. 2005, *ApJ*, 630, 465, doi: 10.1086/431720
- . 2007, *ApJ*, 654, 435, doi: 10.1086/509108
- Bildsten, L., Chakrabarty, D., Chiu, J., et al. 1997, *ApJS*, 113, 367, doi: 10.1086/313060
- Blondin, J. M., Stevens, I. R., & Kallman, T. R. 1991, *ApJ*, 371, 684, doi: 10.1086/169934
- Boella, G., Butler, R. C., Perola, G. C., et al. 1997, *A&AS*, 122, 299, doi: 10.1051/aas:1997136

- Bradt, H. V., Rothschild, R. E., & Swank, J. H. 1993, *A&AS*, 97, 355
- Brazier, K. T. S. 1994, *MNRAS*, 268, 709, doi: 10.1093/mnras/268.3.709
- Brumback, M. C., Hickox, R. C., Fürst, F. S., et al. 2021, *ApJ*, 909, 186, doi: 10.3847/1538-4357/abe122
- Buccheri, R., Bennett, K., Bignami, G. F., et al. 1983, *A&A*, 128, 245
- Burderi, L., Di Salvo, T., Robba, N. R., La Barbera, A., & Guainazzi, M. 2000, *ApJ*, 530, 429, doi: 10.1086/308336
- Bykov, A. M., & Krasil'Shchikov, A. M. 2004, *Astronomy Letters*, 30, 309, doi: 10.1134/1.1738153
- Canuto, V., Lodenguai, J., & Ruderman, M. 1971, *Phys. Rev. D*, 3, 2303, doi: 10.1103/PhysRevD.3.2303
- Cash, W. 1979, *ApJ*, 228, 939, doi: 10.1086/156922
- Castor, J. I., Abbott, D. C., & Klein, R. I. 1975, *ApJ*, 195, 157, doi: 10.1086/153315
- Cheng, F. H., Vrtillek, S. D., & Raymond, J. C. 1995, *ApJ*, 452, 825, doi: 10.1086/176351
- Chodil, G., Mark, H., Rodrigues, R., et al. 1967, *PhRvL*, 19, 681, doi: 10.1103/PhysRevLett.19.681
- Corbet, R. H. D. 1986, *MNRAS*, 220, 1047, doi: 10.1093/mnras/220.4.1047
- Crampton, D., & Hutchings, J. B. 1974, *ApJ*, 191, 483, doi: 10.1086/152988
- Daugherty, J. K., & Harding, A. K. 1986, *ApJ*, 309, 362, doi: 10.1086/164608
- Day, C. S. R., Nagase, F., Asai, K., & Takeshima, T. 1993, *ApJ*, 408, 656, doi: 10.1086/172625
- Deeter, J. E., Boynton, P. E., & Pravdo, S. H. 1981, *ApJ*, 247, 1003, doi: 10.1086/159110
- Doroshenko, V., Poutanen, J., Tsygankov, S. S., et al. 2022, *Nature Astronomy*, doi: 10.1038/s41550-022-01799-5
- Ebisawa, K., Day, C. S. R., Kallman, T. R., et al. 1996, *PASJ*, 48, 425, doi: 10.1093/pasj/48.3.425
- Enoto, T., Kisaka, S., & Shibata, S. 2019, *Reports on Progress in Physics*, 82, 106901, doi: 10.1088/1361-6633/ab3def

- Falanga, M., Bozzo, E., Lutovinov, A., et al. 2015, *A&A*, 577, A130, doi: 10.1051/0004-6361/201425191
- Friend, D. B., & Abbott, D. C. 1986, *ApJ*, 311, 701, doi: 10.1086/164809
- Friend, D. B., & Castor, J. I. 1982, *ApJ*, 261, 293, doi: 10.1086/160340
- Gaia Collaboration, Prusti, T., de Bruijne, J. H. J., et al. 2016, *A&A*, 595, A1, doi: 10.1051/0004-6361/201629272
- Gendreau, K. C., Arzoumanian, Z., & Okajima, T. 2012, in *Society of Photo-Optical Instrumentation Engineers (SPIE) Conference Series*, Vol. 8443, *Space Telescopes and Instrumentation 2012: Ultraviolet to Gamma Ray*, ed. T. Takahashi, S. S. Murray, & J.-W. A. den Herder, 844313, doi: 10.1117/12.926396
- Giacconi, R., Gursky, H., Kellogg, E., et al. 1973, *ApJ*, 184, 227, doi: 10.1086/152321
- Giacconi, R., Gursky, H., Kellogg, E., Schreier, E., & Tananbaum, H. 1971, *ApJL*, 167, L67, doi: 10.1086/180762
- Giacconi, R., Gursky, H., Paolini, F. R., & Rossi, B. B. 1962, *PhRvL*, 9, 439, doi: 10.1103/PhysRevLett.9.439
- Gnedin, Y. N., & Syunyaev, R. A. 1974, *Soviet Journal of Experimental and Theoretical Physics*, 38, 51
- Harrison, F. A., Craig, W. W., Christensen, F. E., et al. 2013, *ApJ*, 770, 103, doi: 10.1088/0004-637X/770/2/103
- Heemskerk, M. H. M., & van Paradijs, J. 1989, *A&A*, 223, 154
- Heger, A., Fryer, C. L., Woosley, S. E., Langer, N., & Hartmann, D. H. 2003, *ApJ*, 591, 288, doi: 10.1086/375341
- Hewish, A., Bell, S. J., Pilkington, J. D. H., Scott, P. F., & Collins, R. A. 1968, *Nature*, 217, 709, doi: 10.1038/217709a0
- HI4PI Collaboration, Ben Bekhti, N., Flöer, L., et al. 2016, *A&A*, 594, A116, doi: 10.1051/0004-6361/201629178
- Hickox, R. C., Narayan, R., & Kallman, T. R. 2004, *ApJ*, 614, 881, doi: 10.1086/423928
- Hu, C.-P., Chou, Y., Wu, M.-C., Yang, T.-C., & Su, Y.-H. 2011, *ApJ*, 740, 67, doi: 10.1088/0004-637X/740/2/67

- Hutchings, J. B., Cowley, A. P., Crampton, D., van Paradijs, J., & White, N. E. 1979, *ApJ*, 229, 1079, doi: 10.1086/157042
- Iaria, R., Di Salvo, T., Robba, N. R., et al. 2005, *ApJL*, 634, L161, doi: 10.1086/499040
- Igoshev, A. P., Popov, S. B., & Hollerbach, R. 2021, *Universe*, 7, 351, doi: 10.3390/universe7090351
- Inoue, H. 1985, *Space Sci. Rev.*, 40, 317, doi: 10.1007/BF00212905
- Israel, G. L., Belfiore, A., Stella, L., et al. 2017, *Science*, 355, 817, doi: 10.1126/science.aai8635
- Jansen, F., Lumb, D., Altieri, B., et al. 2001, *A&A*, 365, L1, doi: 10.1051/0004-6361:20000036
- Joye, W. A., & Mandel, E. 2003, in *Astronomical Society of the Pacific Conference Series*, Vol. 295, *Astronomical Data Analysis Software and Systems XII*, ed. H. E. Payne, R. I. Jedrzejewski, & R. N. Hook, 489
- King, A., Lasota, J.-P., & Kluźniak, W. 2017, *MNRAS*, 468, L59, doi: 10.1093/mnrasl/slx020
- Klein, O., & Nishina, T. 1929, *Zeitschrift fur Physik*, 52, 853, doi: 10.1007/BF01366453
- Klein, R. I., Jernigan, J. G., Arons, J., Morgan, E. H., & Zhang, W. 1996, *ApJL*, 469, L119, doi: 10.1086/310277
- Kohmura, T., Kitamoto, S., & Torii, K. 2001, *ApJ*, 562, 943, doi: 10.1086/323848
- Kompaneets, A. S. 1957, *Soviet Journal of Experimental and Theoretical Physics*, 4, 730
- Kondo, K., Dotani, T., & Inoue, H. 2021, *PASJ*, 73, 286, doi: 10.1093/pasj/psaa120
- Kraus, U., Blum, S., Schulte, J., Ruder, H., & Meszaros, P. 1996, *ApJ*, 467, 794, doi: 10.1086/177653
- Krzeminski, W. 1974, *ApJL*, 192, L135, doi: 10.1086/181609
- Lamb, F. K., Pethick, C. J., & Pines, D. 1973, *ApJ*, 184, 271, doi: 10.1086/152325
- Larsson, S. 1996, *A&AS*, 117, 197
- Laurent, P., & Titarchuk, L. 1999, *ApJ*, 511, 289, doi: 10.1086/306683
- Leahy, D. A., & Abdallah, M. H. 2014, *ApJ*, 793, 79, doi: 10.1088/0004-637X/793/2/79

- Liu, Q., Wang, W., Chen, X., et al. 2022, MNRAS, 516, 5579, doi: 10.1093/mnras/stac2646
- Lutovinov, A. A., Tsygankov, S. S., Postnov, K. A., et al. 2017, MNRAS, 466, 593, doi: 10.1093/mnras/stw3058
- Lutovinov, A. A., Tsygankov, S. S., Suleimanov, V. F., et al. 2015, MNRAS, 448, 2175, doi: 10.1093/mnras/stv125
- Makishima, K., Mihara, T., Nagase, F., & Tanaka, Y. 1999, ApJ, 525, 978, doi: 10.1086/307912
- Manchester, R. N., Hobbs, G. B., Teoh, A., & Hobbs, M. 2005, AJ, 129, 1993, doi: 10.1086/428488
- Martin, R. G., Nixon, C., Armitage, P. J., Lubow, S. H., & Price, D. J. 2014, ApJL, 790, L34, doi: 10.1088/2041-8205/790/2/L34
- Matsuoka, M., Kawasaki, K., Ueno, S., et al. 2009, PASJ, 61, 999, doi: 10.1093/pasj/61.5.999
- McClintock, J. E., Rappaport, S., Joss, P. C., et al. 1976, ApJL, 206, L99, doi: 10.1086/182142
- Middleditch, J., & Nelson, J. 1976, ApJ, 208, 567, doi: 10.1086/154638
- Mihara, T. 1995, PhD thesis, The University of Tokyo
- Mihara, T., Makishima, K., & Nagase, F. 1998, Advances in Space Research, 22, 987, doi: 10.1016/S0273-1177(98)00128-8
- Mushtukov, A., & Tsygankov, S. 2022, arXiv e-prints, arXiv:2204.14185. <https://arxiv.org/abs/2204.14185>
- Mushtukov, A. A., Nagirner, D. I., & Poutanen, J. 2016, Phys. Rev. D, 93, 105003, doi: 10.1103/PhysRevD.93.105003
- Mushtukov, A. A., Portegies Zwart, S., Tsygankov, S. S., Nagirner, D. I., & Poutanen, J. 2021, MNRAS, 501, 2424, doi: 10.1093/mnras/staa3809
- Mushtukov, A. A., Suleimanov, V. F., Tsygankov, S. S., & Poutanen, J. 2015, MNRAS, 454, 2539, doi: 10.1093/mnras/stv2087
- Nagase, F. 1989, PASJ, 41, 1

- Nagase, F., Corbet, R. H. D., Day, C. S. R., et al. 1992, *ApJ*, 396, 147, doi: 10.1086/171705
- Naik, S., Paul, B., & Ali, Z. 2011, *ApJ*, 737, 79, doi: 10.1088/0004-637X/737/2/79
- Odaka, H., Aharonian, F., Watanabe, S., et al. 2011, *ApJ*, 740, 103, doi: 10.1088/0004-637X/740/2/103
- Odaka, H., Khangulyan, D., Tanaka, Y. T., et al. 2013, *ApJ*, 767, 70, doi: 10.1088/0004-637X/767/1/70
- . 2014, *ApJ*, 780, 38, doi: 10.1088/0004-637X/780/1/38
- Ogilvie, G. I., & Dubus, G. 2001, *MNRAS*, 320, 485, doi: 10.1046/j.1365-8711.2001.04011.x
- Okajima, T., Soong, Y., Balsamo, E. R., et al. 2016, in *Society of Photo-Optical Instrumentation Engineers (SPIE) Conference Series*, Vol. 9905, *Space Telescopes and Instrumentation 2016: Ultraviolet to Gamma Ray*, ed. J.-W. A. den Herder, T. Takahashi, & M. Bautz, 99054X, doi: 10.1117/12.2234436
- Olausen, S. A., & Kaspi, V. M. 2014, *ApJS*, 212, 6, doi: 10.1088/0067-0049/212/1/6
- Paczynski, B. 1971, *ARA&A*, 9, 183, doi: 10.1146/annurev.aa.09.090171.001151
- Parmar, A. N., Oosterbroek, T., dal Fiume, D., et al. 1999, *A&A*, 350, L5. <https://arxiv.org/abs/astro-ph/9909039>
- Parmar, A. N., Pietsch, W., McKechnie, S., et al. 1985, *Nature*, 313, 119, doi: 10.1038/313119a0
- Paul, B., & Naik, S. 2011, *Bulletin of the Astronomical Society of India*, 39, 429. <https://arxiv.org/abs/1110.4446>
- Paul, B., Raichur, H., & Mukherjee, U. 2005, *A&A*, 442, L15, doi: 10.1051/0004-6361:200500177
- Petre, R., & Serlemitsos, P. J. 1985, *ApOpt*, 24, 1833, doi: 10.1364/AO.24.001833
- Pettersen, J. A. 1975, *ApJL*, 201, L61, doi: 10.1086/181942
- Pfeiffer, H. P., & Lai, D. 2004, *ApJ*, 604, 766, doi: 10.1086/381967
- Poutanen, J., Mushtukov, A. A., Suleimanov, V. F., et al. 2013, *ApJ*, 777, 115, doi: 10.1088/0004-637X/777/2/115

- Pringle, J. E. 1996, MNRAS, 281, 357, doi: 10.1093/mnras/281.1.357
- Raichur, H., & Paul, B. 2008a, ApJ, 685, 1109, doi: 10.1086/591037
- . 2008b, MNRAS, 387, 439, doi: 10.1111/j.1365-2966.2008.13251.x
- Ramsay, G., Zane, S., Jimenez-Garate, M. A., den Herder, J.-W., & Hailey, C. J. 2002, MNRAS, 337, 1185, doi: 10.1046/j.1365-8711.2002.06002.x
- Remillard, R. A., Loewenstein, M., Steiner, J. F., et al. 2022, AJ, 163, 130, doi: 10.3847/1538-3881/ac4ae6
- Reynolds, A. P., Quaintrell, H., Still, M. D., et al. 1997, MNRAS, 288, 43, doi: 10.1093/mnras/288.1.43
- Ribó, M., Peracaula, M., Paredes, J. M., Núñez, J., & Otazu, X. 2001, in ESA Special Publication, Vol. 459, Exploring the Gamma-Ray Universe, ed. A. Gimenez, V. Reglero, & C. Winkler, 333–336
- Rybicki, G. B., & Lightman, A. P. 1979, Radiative processes in astrophysics
- Sanjurjo-Ferrín, G., Torrejón, J. M., Postnov, K., et al. 2021, MNRAS, 501, 5892, doi: 10.1093/mnras/staa3953
- Santangelo, A., del Sordo, S., Segreto, A., et al. 1998, A&A, 340, L55
- Schreier, E., Levinson, R., Gursky, H., et al. 1972, ApJL, 172, L79, doi: 10.1086/180896
- Schwarm, F. W., Schönherr, G., Falkner, S., et al. 2017, A&A, 597, A3, doi: 10.1051/0004-6361/201629352
- Scott, D. M., Leahy, D. A., & Wilson, R. B. 2000, ApJ, 539, 392, doi: 10.1086/309203
- Shakura, N. I., & Sunyaev, R. A. 1973, A&A, 24, 337
- Staubert, R., Klochkov, D., Fürst, F., et al. 2017, A&A, 606, L13, doi: 10.1051/0004-6361/201731927
- Staubert, R., Klochkov, D., Postnov, K., et al. 2009a, A&A, 494, 1025, doi: 10.1051/0004-6361:200810743
- Staubert, R., Klochkov, D., Vybornov, V., Wilms, J., & Harrison, F. A. 2016, A&A, 590, A91, doi: 10.1051/0004-6361/201527955
- Staubert, R., Klochkov, D., & Wilms, J. 2009b, A&A, 500, 883, doi: 10.1051/0004-6361/200911690



- Staubert, R., Shakura, N. I., Postnov, K., et al. 2007, *A&A*, 465, L25, doi: 10.1051/0004-6361:20077098
- Staubert, R., Trümper, J., Kendziorra, E., et al. 2019, *A&A*, 622, A61, doi: 10.1051/0004-6361/201834479
- Staubert, R., Ducci, L., Ji, L., et al. 2020, *A&A*, 642, A196, doi: 10.1051/0004-6361/202038855
- Strüder, L., Briel, U., Dennerl, K., et al. 2001, *A&A*, 365, L18, doi: 10.1051/0004-6361:20000066
- Suchy, S., Pottschmidt, K., Wilms, J., et al. 2008, *ApJ*, 675, 1487, doi: 10.1086/527042
- Suleimanov, V. F., Mushtukov, A. A., Ognev, I., Doroshenko, V. A., & Werner, K. 2022, *MNRAS*, 517, 4022, doi: 10.1093/mnras/stac2935
- Sunyaev, R. A., & Titarchuk, L. G. 1980, *A&A*, 86, 121
- Swank, J. H. 1999, *Nuclear Physics B Proceedings Supplements*, 69, 12, doi: 10.1016/S0920-5632(98)00175-3
- Takeshima, T., Dotani, T., Mitsuda, K., & Nagase, F. 1991, *PASJ*, 43, L43
- Tamba, T., Odaka, H., Tanimoto, A., et al. 2022, *ApJ*
- Tanaka, Y. 1986, in *IAU Colloq. 89: Radiation Hydrodynamics in Stars and Compact Objects*, ed. D. Mihalas & K.-H. A. Winkler, Vol. 255, 198, doi: 10.1007/3-540-16764-1\_12
- Tananbaum, H., Gursky, H., Kellogg, E. M., et al. 1972, *ApJL*, 174, L143, doi: 10.1086/180968
- Tarter, C. B., Tucker, W. H., & Salpeter, E. E. 1969, *ApJ*, 156, 943, doi: 10.1086/150026
- Tashiro, M., Maejima, H., Toda, K., et al. 2018, in *Society of Photo-Optical Instrumentation Engineers (SPIE) Conference Series*, Vol. 10699, *Space Telescopes and Instrumentation 2018: Ultraviolet to Gamma Ray*, ed. J.-W. A. den Herder, S. Nikzad, & K. Nakazawa, 1069922, doi: 10.1117/12.2309455
- Tendulkar, S. P., Hascöet, R., Yang, C., et al. 2015, *ApJ*, 808, 32, doi: 10.1088/0004-637X/808/1/32
- Thalhammer, P., Bissinger, M., Ballhausen, R., et al. 2021, *A&A*, 656, A105, doi: 10.1051/0004-6361/202140582

- Thébault, E., Finlay, C. C., Beggan, C. D., et al. 2015, *Earth, Planets and Space*, 67, 79, doi: 10.1186/s40623-015-0228-9
- Tjemkes, S. A., Zuiderwijk, E. J., & van Paradijs, J. 1986, *A&A*, 154, 77
- Tomar, G., Pradhan, P., & Paul, B. 2021, *MNRAS*, 500, 3454, doi: 10.1093/mnras/staa3477
- Trowbridge, S., Nowak, M. A., & Wilms, J. 2007, *ApJ*, 670, 624, doi: 10.1086/522075
- Truemper, J., Pietsch, W., Reppin, C., et al. 1978, *ApJL*, 219, L105, doi: 10.1086/182617
- Tsunemi, H., Kitamoto, S., & Tamura, K. 1996, *ApJ*, 456, 316, doi: 10.1086/176652
- Tsygankov, S. S., Doroshenko, V., Poutanen, J., et al. 2022, arXiv e-prints, arXiv:2209.02447. <https://arxiv.org/abs/2209.02447>
- van der Meer, A., Kaper, L., van Kerkwijk, M. H., Heemskerk, M. H. M., & van den Heuvel, E. P. J. 2007, *A&A*, 473, 523, doi: 10.1051/0004-6361:20066025
- van Kerkwijk, M. H., van Paradijs, J., Zuiderwijk, E. J., et al. 1995, *A&A*, 303, 483. <https://arxiv.org/abs/astro-ph/9505070>
- Ventura, J. 1979, *Phys. Rev. D*, 19, 1684, doi: 10.1103/PhysRevD.19.1684
- Verner, D. A., Ferland, G. J., Korista, K. T., & Yakovlev, D. G. 1996, *ApJ*, 465, 487, doi: 10.1086/177435
- Vrtilek, S. D., Mihara, T., Primini, F. A., et al. 1994, *ApJL*, 436, L9, doi: 10.1086/187621
- Walter, R., & Ferrigno, C. 2017, in *Handbook of Supernovae*, ed. A. W. Alsabti & P. Murdin, 1385, doi: 10.1007/978-3-319-21846-5\_74
- Walter, R., Lutovinov, A. A., Bozzo, E., & Tsygankov, S. S. 2015, *A&ARv*, 23, 2, doi: 10.1007/s00159-015-0082-6
- Watanabe, S., Sako, M., Ishida, M., et al. 2006, *ApJ*, 651, 421, doi: 10.1086/507458
- Weisskopf, M. C., Ramsey, B., O'Dell, S., et al. 2016, in *Society of Photo-Optical Instrumentation Engineers (SPIE) Conference Series*, Vol. 9905, *Space Telescopes and Instrumentation 2016: Ultraviolet to Gamma Ray*, ed. J.-W. A. den Herder, T. Takahashi, & M. Bautz, 990517, doi: 10.1117/12.2235240
- West, B. F., Wolfram, K. D., & Becker, P. A. 2017, *ApJ*, 835, 130, doi: 10.3847/1538-4357/835/2/130

- White, N. E., Swank, J. H., & Holt, S. S. 1983, *ApJ*, 270, 711, doi: 10.1086/161162
- Wijers, R. A. M. J., & Pringle, J. E. 1999, *MNRAS*, 308, 207, doi: 10.1046/j.1365-8711.1999.02720.x
- Wilson, R. B., Scott, D. M., & Finger, M. H. 1997, in *American Institute of Physics Conference Series*, Vol. 410, *Proceedings of the Fourth Compton Symposium*, ed. C. D. Dermer, M. S. Strickman, & J. D. Kurfess, 739–743, doi: 10.1063/1.54004
- Winkler, C., Courvoisier, T. J. L., Di Cocco, G., et al. 2003, *A&A*, 411, L1, doi: 10.1051/0004-6361:20031288
- Wojdowski, P., Clark, G. W., Levine, A. M., Woo, J. W., & Zhang, S. N. 1998, *ApJ*, 502, 253, doi: 10.1086/305893
- Wojdowski, P. S., Liedahl, D. A., & Sako, M. 2001, *ApJ*, 547, 973, doi: 10.1086/318425
- Wojdowski, P. S., Liedahl, D. A., Sako, M., Kahn, S. M., & Paerels, F. 2003, *ApJ*, 582, 959, doi: 10.1086/344821
- Wolff, M. T., Becker, P. A., Gottlieb, A. M., et al. 2016, *ApJ*, 831, 194, doi: 10.3847/0004-637X/831/2/194
- Zane, S., Ramsay, G., Jimenez-Garate, M. A., Willem den Herder, J., & Hailey, C. J. 2004, *MNRAS*, 350, 506, doi: 10.1111/j.1365-2966.2004.07660.x

# Acknowledgement

First of all, I would like to express my gratitude and respect to Prof. Aya Bamba. She has given me a lot of valuable advice and taught me what scientific research is about during the five years of my graduate course. Her friendly character has always encouraged me and taught me how enjoyable a research life is. I also express my deepest thank to Assistant Prof. Hirokazu Odaka, who has lectured me construction of simulator, data analysis method, and scientific writing. MONACO plays an essential part in this thesis, which was developed by him. He has also given me a lot of advice about my future career.

In my study of accreting neutron stars, the coauthors have been very helpful to me. Atsushi Tanimoto is a good adviser to me, who kindly answers my questions about technical problems. He is also a core member of MONACO, and gave me a lot of valuable information about simulation. Hiromasa Suzuki has been a good friend of me, and helped me in correcting my English when I wrote an observation proposal. I learned a lot of techniques from Satoshi Takashima in writing analysis scripts.

I would like to thank the members of Bamba group, Yuuki Wada, Tomoaki Kasuga, Yuki Aizawa, Kosuke Hatauchi, Takahiro Minami, Taihei Watanabe, Sorato Nammoku, Masahiro Ichihashi, Toshiya Iwata, and Shota Arai. Discussions and seminars with them are very helpful because they have taught me interesting ideas and stories about their research fields. I would like to thank our laboratory secretaries, Kuniko Kono and Haduki Kutsuma. Out of Bamba group, I would like to express special thanks to Chris Done. I had a discussion with her in December 2022, which was very helpful to my doctoral dissertation.

I am grateful to my colleagues in the faculty of physics, especially to Wataru Yokojima, Takumi Hayashi, Kosaku Ono, Yuta Tarumi, Yutaka Tsuzuki, and Tenyo Kawamura. They have always been good friends of me. I could not accomplish my thesis without support of my family.

I acknowledge NuSTAR team and NuSTAR Science Operation Center for the arrangement of our observation. They gave feedback on our proposal on Cen X-3, simulated the stray light effect on the observation, and arranged the schedule of the observation. The comprehensive X-ray study on Cen X-3 could not have been accomplished without these supports. This work is supported by the Japan Society for the Promotion of Science

(JSPS) Research Fellowship for Young Scientist No. 20J20050.

Tsubasa Tamba,  
March 2023